

Patient-specific Modeling and Quantification of the Heart Valves from Multimodal Cardiac Images

RAZVAN IOAN IONASEC

DISSERTATION

SIEMENS

Siemens Corporate Research



Fakultät für Informatik
Technische Universität München

TECHNISCHE UNIVERSITÄT MÜNCHEN
Lehrstuhl für Informatikanwendungen in der Medizin

Patient-specific Modeling and Quantification of the Heart Valves from Multimodal Cardiac Images

Razvan Ioan Ionasec

Vollständiger Abdruck der von der Fakultät für Informatik der Technischen Universität
München zur Erlangung des akademischen Grades eines

Doktors der Naturwissenschaften (Dr. rer. nat.)

genehmigten Dissertation.

Vorsitzender: Univ.-Prof. Dr. Hans-Joachim Bungartz

Prüfer der Dissertation:

1. Univ.-Prof. N. Navab, Ph.D.
2. Prof. Nicholas Ayache, Ph.D.
INRIA, Sophia Antipolis, France
3. Dr. Dorin Comaniciu
Siemens Corporate Research, Princeton NJ, USA

Die Dissertation wurde am 30.06.2010 bei der Technischen Universität München
eingereicht und durch die Fakultät für Informatik am 28.09.2010 angenommen.

Abstract

As decisions in cardiology increasingly rely on non-invasive methods, fast and precise image analysis tools have become a crucial component of the clinical workflow. Especially when dealing with complex cardiovascular disorders, such as valvular heart disease, advanced imaging techniques have the potential to significantly improve treatment outcome as well as to reduce procedure risks and correlated costs.

This thesis concentrates on three aspects: physiological heart valve modeling, algorithms for patient-specific parameter estimation from multimodal images and advanced applications for clinical management of heart valve disease. In particular, a novel physiological model of the complete valvular apparatus is introduced, which captures a large spectrum of morphologic, dynamic and pathologic variations. A robust learning-based framework is proposed to estimate the patient-specific model parameters from cardiac medical scans, mainly transesophageal echocardiography, cardiac computed tomography and cardiac magnetic resonance imaging.

This original model-driven approach enables a multitude of advanced clinical applications including quantitative valvular analysis, shape-based diagnosis and patient selection as well as computational decision support for valve replacement and repair procedures. In comparison to the gold standard methods, which manually process 2D images, the automatic 4D model-based concept provides fast, precise, reproducible and comprehensive valve quantification. Moreover, in case of emerging percutaneous and minimal invasive valve interventions, cardiac surgeons and interventional cardiologists can substantially benefit from the automated patient selection and virtual valve implantation approaches presented in this thesis. The algorithms proposed in this thesis are validated through extensive quantitative and clinical experiments involving over 476 patients treated in leading medical centers around the world.

Zusammenfassung

Da Entscheidungen in der Kardiologie in zunehmendem Maße durch nicht-invasive Methoden gestützt werden, sind schnelle und präzise Bildanalysewerkzeuge zu einem wichtigen Bestandteil klinischer Arbeitsabläufe geworden. Insbesondere im Umgang mit den komplexen Erkrankungen des kardiovaskulären Systems, wie etwa Herzklappenerkrankungen, bergen moderne bildgebende Verfahren das Potential sowohl Behandlungsergebnisse bedeutsam zu verbessern als auch prozedurale Risiken und verbundene Kosten zu senken.

Diese Arbeit konzentriert sich auf drei Aspekte: physiologische Modellierung von Herzklappen, Algorithmen zur Schätzung patientenspezifischer Parameter aus multimodalen Bildern sowie weiterführende Anwendungen für das klinische Management von Herzklappenerkrankungen. Hierzu wird ein neues physiologisches Modell des gesamten Herklappenapparats vorgestellt, der ein umfangreiches Spektrum morphologischer, dynamischer und pathologischer Variationen erfasst. Ein robustes lernbasiertes Framework zur Schätzung patientenspezifischer Modellparameter aus medizinischen Akquisitionen des Herzens wurde erarbeitet, hauptsächlich Transesophageale Echokardiographie, Computertomographie sowie Magnetresonanztomographie.

Der originäre modellgetriebene Ansatz ermöglicht eine Vielzahl fortgeschrittener Anwendungen wie etwa die quantitative Analyse von Herzklappen, formenbasierte Diagnose und Patientenauswahl als auch rechnergestützte Entscheidungsunterstützung für Ersatz und Reparatur von Herzklappen. Das automatische 4D modellbasierte Konzept bietet eine schnelle, genaue, reproduzierbare und umfassende Quantifikation von Herzklappen im Gegensatz zum Gold Standard, der auf manuelle Verarbeitung von 2D Bildern basiert. Besonders im Hinblick auf entstehende perkutane und minimal invasive Behandlungsmethoden können Herzchirurgen und interventionelle Kardiologen erheblich von den in dieser Arbeit vorgestellten Verfahren zur Patientenauswahl und für den virtuellen Herklappenersatz profitieren. Das vorgestellte Framework wird durch umfangreiche quantitative und klinische Experimente validiert, welche über 476 Patienten einbeziehen, die in weltweit führenden Kliniken behandelt wurden.

Acknowledgments

I would like to thank my advisors, Nassir Navab from TUM and Dorin Comaniciu from Siemens, for teaching me everything about research, enlightening my path, and trusting in my success. Dorin, I appreciate your motivation when I faced my deepest frustrations and your continuous "pushing" to exceed expectations. Nassir, I thank you for accepting me into a prestigious academic department and providing me with invaluable advice during the key moments of my studies. I would also like to express my sincere gratitude to Dr. Nicholas Ayache for being part of my committee and for his considerable effort on revising my dissertation.

I have spent the last few years in Siemens' offices in Erlangen, Germany and Princeton, United States. I took frequent trips to CAMP at TUM in Munich, performed a multitude of customer visits, attended numerous international conferences, and visited clinical collaborators from leading cardiac centers around the world. During this time I have had the privilege to work together with a number of savvy students, from whom, I can proudly say, that the best are still working in our group: Ingmar Voigt, Dime Vitanovski and Sasa Grbic. Many other colleagues at SCR have provided valuable input to this work, including: Kevin Zhou, Martin Huber, Yang Wang, Viorel Mihalef, Sharma Puneet, Oliver Kutter, Yefeng Zheng, Terrence Chen, Alexey Tsymbal, and Fabian Moecheren. In addition, I am truly grateful to my colleagues from the Siemens Healthcare divisions, who believed in the technology described in this thesis and financed the research activity: Helene Houle, Mike Sekins and Art Schenck (US), Matthiass John, Jan Boese and Klaus Klingenberg (AX), Bernhardt Dominik, Fernando Vega-Higuera and Michael Scheuring (CT), and Edgar Mueller (MR).

I am very grateful to Bogdan Georgescu, one of the principal research scientists at SCR, for sharing his vast knowledge and experience with me ever since I started this journey. Bogdan, I cannot thank you enough for everything I learned from you, but nonetheless, also for the fun tennis matches, which I used to lose . . . on purpose.

Many thanks to: Adrian Barbu, who guided my first steps at SCR and for our friendship ever since, Ciprian Raileanu for the most careful proof-reading and valuable comments, Yang Wang for our productive discussion on various computer vision topics and our

joint work and publications, and to the people from CAMP for their significant support.

This dissertation was supported by excellent clinical collaborations with major clinics and extraordinary physicians: Mani Vannan and Anna Callaja (OSU), Joseph Schoepf (MUSC), Andrew Taylor (GOSH), Allen Everett and David Yuh (JHU), Ruediger Lange and Gernot Brockmann (DHM), Giacomo Pongiglione (OPBG), Gillam Linda (CUMC), Feroze Mahmood (BIDMC) and Sunil Mankad (MAYO).

Finally, I owe immeasurable acknowledgements to my mom, for making everything possible in the first place, to Nicole for always being on my side as the richest source of motivation, positivity and happiness in my life, and to Simone for calling me "Dr. Raz" already in my first PhD. year. A big "thank you" goes as well to all my friends and family members who contributed one way or another to this thesis.

Princeton, June 2010

Contents

1	Introduction	1
1.1	Motivation	1
1.2	Aims	2
1.3	Contributions	3
1.4	Outline of the Thesis	4
2	Background	7
2.1	The Human Heart	7
2.1.1	Morphology	7
2.1.2	Dynamics	8
2.2	Physiology of the Heart Valves	10
2.2.1	Aortic Valve	10
2.2.2	Mitral Valve	11
2.2.3	Tricuspid Valve	12
2.2.4	Pulmonary Valve	13
2.3	Clinical Pathology of Valvular Heart Disease	13
2.3.1	Aortic Stenosis and Regurgitation	14
2.3.2	Mitral Stenosis and Regurgitation	15
2.3.3	Right-Side Valve Disease	17
2.4	Treatment of Valvular Disease	17
2.4.1	Heart Valve Surgery	18
2.4.2	Percutaneous Valve Therapy	20
2.5	Imaging Modalities	22
2.5.1	X-Ray and Angiography	23
2.5.2	Cardiac Computed Tomography	24
2.5.3	Cardiovascular Magnetic Resonance	25
2.5.4	Echocardiography	25
2.5.5	Nuclear Cardiology	27
2.6	Overview of Medical Image Analysis	27

2.6.1	Image Reconstruction and Enhancement	28
2.6.2	Computer Vision in Medical Imaging	28
2.6.3	Machine Learning in Medical Imaging	29
2.6.4	Computation Modeling and Simulation	31
2.7	Conclusions	31
3	Physiological Modeling and Parametrization	33
3.1	Models of Cardiac Structures	33
3.1.1	Chamber and Related Models	34
3.1.2	Valve Models	35
3.2	Hierarchical Valvular Model	36
3.2.1	Aortic Valve	38
3.2.2	Mitral Valve	38
3.2.3	Tricuspid Valve	39
3.2.4	Pulmonary Valve	39
3.3	Global Location and Rigid Motion	39
3.3.1	Parameterization	39
3.3.2	Anatomical Definition	40
3.4	Non-Rigid Landmark Motion Model	42
3.4.1	Parameterization	42
3.4.2	Anatomical Definition	43
3.5	Comprehensive Valvular Model	46
3.5.1	Parameterization	46
3.5.2	Anatomical Definition	46
3.6	Spatio-Temporal Consistency	49
3.7	Patient-Population Models	50
3.7.1	Trajectory Models	50
3.7.2	Active Shape Models	54
3.7.3	Conditioned Multi-linear Principal Component Analysis	56
3.8	Conclusions	58
4	Patient-specific Parameter Estimation	61
4.1	Model-based Paradigm	61
4.1.1	Object Localization	63
4.1.2	Motion Estimation	64
4.1.3	Boundary Delineation	65
4.2	Discriminative Learning Methods	66
4.2.1	Boosting Algorithms	66
4.2.2	Image Features	69
4.2.3	Training, Testing and Space Marginalization	74
4.3	Object Localization and Rigid Motion Estimation	76
4.3.1	Location Estimation	76
4.3.2	Robust Motion Aggregation	77
4.4	Trajectory Spectrum Learning for Non-Rigid Motion Estimation	78
4.4.1	Problem Formulation	79

4.4.2	Search Space Marginalization	80
4.4.3	Learning in Marginal Trajectory Spaces	80
4.4.4	Motion Trajectory Estimation	82
4.5	Comprehensive Model Estimation	83
4.5.1	Estimation in Cardiac Key Phases	84
4.5.2	Motion Estimation	85
4.6	Results	86
4.6.1	Data Set	86
4.6.2	Ground Truth	87
4.6.3	Performance of the Object Localization and Rigid Motion Estimation	89
4.6.4	Performance of the Non-Rigid-Landmark Motion Estimation	90
4.6.5	Performance of the Comprehensive Valve Model Estimation	92
4.6.6	Inter-modality and Inter-user Variability Analysis	93
4.6.7	Overall Performance Results	94
4.7	Conclusions	94
5	Clinical Applications	97
5.1	Quantitative and Qualitative Analysis	97
5.1.1	Model-based Valvular Quantification	98
5.1.2	Results on Left-Side Valve Measurements	100
5.1.3	Results on Right-Side Valve Measurements	104
5.1.4	Discussion	105
5.2	Computer Aided Diagnosis, Patient Selection and Case Retrieval	106
5.2.1	Learning Discriminative Distance Functions	106
5.2.2	Diagnosis and Severity Assessment of Aortic Valves	108
5.2.3	Patient Selection in PPVI	110
5.2.4	Results	111
5.2.5	Discussion	113
5.3	Computational Decision Support for Percutaneous Valve Procedures	113
5.3.1	Clinical Scope	113
5.3.2	Workflow Overview	114
5.3.3	Patient-Specific Anatomical Modeling and Estimation	114
5.3.4	Device Modeling and In-Silico Deployment	116
5.3.5	Experimental Results	118
5.3.6	Discussion	121
6	Conclusions	123
6.1	Summary	123
6.2	Discussion and Future Work	124
A	Patient-Specific Modeling of Left Heart Anatomy, Dynamics and Hemodynamics from High Resolution 4D CT	129
B	Cross-modality Assessment and Planning for Pulmonary Trunk Treatment using CT and MRI imaging	137

C List of Authored Publications and Patents	147
Abbreviations	159
References	169

CHAPTER 1

Introduction

The unprecedented increase in life expectancy over the current and past century unveiled the most dangerous enemy of the humanity: today, Cardiovascular Disease (CVD) causes approximately 30% of deaths worldwide, and nearly 40% in high-income regions. Besides devastating social implications, CVD generated in 2009 \$475.3 billions in health expenses in the United States alone, compared to \$228 billions for all cancer cases [96].

In response, medicine is continuously equipping itself with innovative technology to provide the best possible treatment. Among many others, breakthroughs in surgical and interventional therapy, as well as non-invasive investigation techniques, completely revolutionized healthcare. This pioneering trend is going to be amplified in the future, forcing the integration of interdisciplinary research into effective solutions to fight CVD.

1.1 Motivation

Valvular Heart Disease (VHD) which affects 2.5% of the global population and requires yearly over 100,000 surgeries in the United States alone, is a representative instance for the growing public health problem provoked by CVD. Yet, heart valve operations are the most expensive and riskiest cardiac procedures, with an average cost of \$141,120 and 4.9% in-hospital death rate [96].

Decisions in valvular disease management increasingly rely on non-invasive imaging, with echocardiography currently regarded as the key evaluation technique. Precise morphological and functional knowledge about the valvular apparatus is highly esteemed today and considered a prerequisite for the entire clinical workflow including diagnosis, therapy-planning, surgery or percutaneous intervention as well as patient monitoring and follow-up. Nevertheless, most non-invasive investigations to date are based on two-dimensional images, user-dependent processing and manually performed, potentially inaccurate measurements [19].

Paradoxically, the quality of acquired information, as well as the accessibility and cost effectiveness of each medical imaging modality has radically improved over the past decades. Techniques like Transesophageal Echocardiography (TEE), cardiac Computed Tomography (CT) and Cardiovascular Magnetic Resonance (CMR) imaging, enable now dynamic four dimensional scanning of the beating heart over the whole cardiac cycle. Such volumetric time-resolved data encode comprehensive structural and dynamic information, which however is barely exploited in clinical practice, due to its size and complexity as well as the lack of appropriate medical systems.

The progress in medical imaging is matched by important advances in surgical techniques, bioprosthetic valves, robotic surgery and percutaneous interventions, which have led to a twofold increase in the number of valve procedures performed in the United States since 1985 [1]. According to the Millennium Research Group, percutaneous heart valve therapies will dominate the future and cover up to 41.1% of all valve procedures by 2012. Powerful computer-aided tools for extensive non-invasive assessment, planning and guidance are mandatory to continuously decrease the level of invasiveness and maximize effectiveness of valve therapy.

The sociological impact of CVD and VHD, along with recent disruptive innovations in imaging and therapy, mobilized a tremendous scientific effort worldwide geared towards multi-scale modeling and simulation of the human anatomy and physiology. Vast projects such as the Virtual Physiological Human and the IUPS Physiome promote a technological framework, which integrates anatomical, physical and biochemical models to enable a holistic view on the human organism. The expected outcome of this global initiative is to advance healthcare towards a more personalized preventive and predictive approach.

1.2 Aims

Given the major trends presented in the previous section 1.1, this dissertation is focused on exploiting patient-specific models of the heart valve physiology estimated from multi-modal images to progress the clinical management of VHD patients. The following aims are pursued:

- Define a mathematical model of the aortic, mitral, tricuspid and pulmonary valves as well as the ascending aorta and pulmonary artery, which captures complex anatomical, dynamical and pathological variations.
- Develop learning-based methodologies for fast and robust patient-specific parameter estimation from multi-modal cardiac images, including TEE, cardiac CT and CMR techniques.
- Design a computational framework for advanced quantitative and qualitative analysis of valvular morphology and function in isolation, and also combined with relevant patient-population representations.
- Provide an experimental environment for therapeutical outcome prediction in interventional valvular procedures and support holistic computational modeling of the integrated cardiovascular system.

1.3 Contributions

The major contributions of this thesis along with the corresponding publications are summarized in the following:

- As part of this dissertation, we incrementally develop a novel physiological model of the valvular heart apparatus, which captures the complete morphology and dynamics as well as pathologic variations. The first representation of the aortic valve was proposed in [72], followed by the mitral valve [180], the aortic-mitral coupling [74], pulmonary trunk [178] and ascending aorta [62]. Subsequently, the complete model of the cardiac valvular system was introduced in [61]. The focus was particularly on the derivation of an appropriate hierarchical parameterization along with physiological constraints to handle the inherent complexity. Furthermore, an anatomically-driven sampling scheme is employed to address the fundamental problem of point correspondence across time and individuals.
- To estimate patient-specific model parameters from cardiac images, a learning-based framework was developed and applied to multi-modal data. We proposed a novel trajectory spectrum learning algorithm and novel local-spatial-temporal features, that support simultaneous extraction of location and motion of non-rigid objects [76]. The journal publication [75], describes in detail a fully automatic pipeline for complete model parameters estimation from cardiac CT and TEE volume sequences, while [178] treats the estimation of the pulmonary valve from CMR. Robustness and effectiveness were demonstrated in extensive experiments on 476 patients affected by various valvular diseases.
- Based on the estimated patient-specific model, we introduced an automatic 4D quantification method for clinical analysis of valvular morphology and function. Automated measurements of the real three-dimensional anatomy and temporal variations, not existent before, support a new paradigm of model-driven cardiac evaluation. The first clinical evaluation to prove the accuracy and time-effectiveness of the approach compared model-based aortic valve area to manual planimetry from cardiac CT [71, 55]. In [32] the automated quantification is validated for aortic root assessment from volumetric 3D TEE and CT, while in [26] we focused on valve and root dimensions in patient affected by aortic regurgitation.
- Onward research resulted in a number of techniques for therapeutical decision support of emerging percutaneous procedures related to shape-based diagnosis patient selection and simulation of prosthetic valve implantation. In particular, we leveraged the patient-specific representations of individuals to learn discriminative distance functions across patient-populations and applied those for aortic and mitral valve shape-based classification [73] and automated patient selection for percutaneous pulmonary valve implantation [181]. By combing the physiological models with mechanical representations of devices, in [179] a computational framework for transcatheter aortic valve implantation was proposed.

Besides the above enumerated contributions, related research was conducted to extract complete anatomical and dynamical information about the pulmonary trunk from sparse CMR images [177]. Furthermore, the integration of the valvular models with representations of the heart chambers previously developed in our group, resulted in the first patient-specific model of the complete heart to incorporate anatomy, dynamics and hemodynamics, which contains explicit valvular information. In [108] and [70] we described hemodynamic simulations and blood flow analysis for left-side valvular pathologies, while [107] presents results on the full heart.

Prototype systems based on the technology presented in this thesis are installed in multiple leading cardiac centers around the world for clinical evaluation purposes. To a large extent, the technology described here has been protected by various Siemens divisions.

1.4 Outline of the Thesis

This thesis concentrates around three interrelated subjects, namely a unified mathematical representation of the heart valves, the estimation of patient-specific model parameters from multimodal images and clinical applications for advance analysis and treatment of valvular heart disease. A brief description of individual chapters included in this work is presented in the following:

Chapter 2: Background

The first part of chapter 2 provides the reader with the necessary medical and clinical background of the cardiac system, with emphasis on the heart valves. Brief descriptions of physiological aspects, relevant for modeling, as well as valvular disease and existent treatment options, define the domain specific concepts. The chapter concludes by presenting relevant imaging modalities for cardiac scanning and the role of medical image analysis in supporting advanced healthcare.

Chapter 3: Physiological Modeling and Parameterization

This chapter describes in detail the proposed physiological model of the heart valves morphology and dynamics. A unified mathematical representation is incrementally introduced, starting with a global location model and ending with a comprehensive model of the complete valvular apparatus. In the last part of this chapter the focus moves from models of individuals towards statistical models of patient-populations.

Chapter 4: Patient-specific Parameter Estimation

In this chapter, a novel algorithmic framework is introduced to estimate patient-specific model parameters from cardiac images. After an overview on discriminative learning methods, specific algorithms for detection of location, shape and motion of the heart valves are described in detail. The chapter ends with experiments and performance eval-

uation of the new algorithms.

Chapter 5: Clinical Applications

The technology described in the preceding chapters is directly applied in order to support clinical management of patients with valvular heart disease. Three different applications are introduced, including morphological and functional valve analysis, patient selection for percutaneous valve treatment, and virtual implantation of prosthetic heart valves.

Chapter 6: Conclusions

Chapter 6 concludes the thesis with a summary of the presented methods, their benefits and impact in the clinical environment, as well as future outlook.

Throughout history, humans have discovered countless ways to analyze and describe the fascinating organ, which is regarded as the foundation of life, the source of all action: the heart. In this chapter the reader is provided with the elementary concepts on its morphology, function and pathological implications. The content is specialized to accommodate pathophysiological aspects of the heart valves, the main focus of this dissertation. State-of-the-art cardiac imaging techniques and major advances in valves treatments, together with medical image analysis technology, are introduced in the second part of the chapter.

2.1 The Human Heart

The human heart is a muscular organ located in the central thoracic cavity underneath the sternum, which is pumping blood by repeated, rhythmic contractions. It is conically shaped about the size of a fist, weights between 200-450 grams, and measures 12cm along its major axis, and 7cm at its widest point. A double-layered membrane, the pericardium, surrounds the heart like a sac and attaches it to the sternum and diaphragm. Electrical impulses send from the sinoatrial node travel through the muscle fibers causing the heart to contract on average 72 times per minute. As a result blood is pumped through the cardiovascular system, transporting oxygen and nutrition to the entire body.

2.1.1 Morphology

The hollow heart muscle is divided along the main axis by the interatrial interventricular septum into a cylindrical left and crescent shaped right side. Each side is further divided into an upper and lower chamber, forming the atria and ventricles (see figure 2.1(a)).

- The Left Atrium (LA) is the smallest chamber with a capacity of approximately 45ml at rest and accepts four pulmonary veins connected to the lungs. Its separation from the left ventricle occurs through the bicuspid, mitral valve.

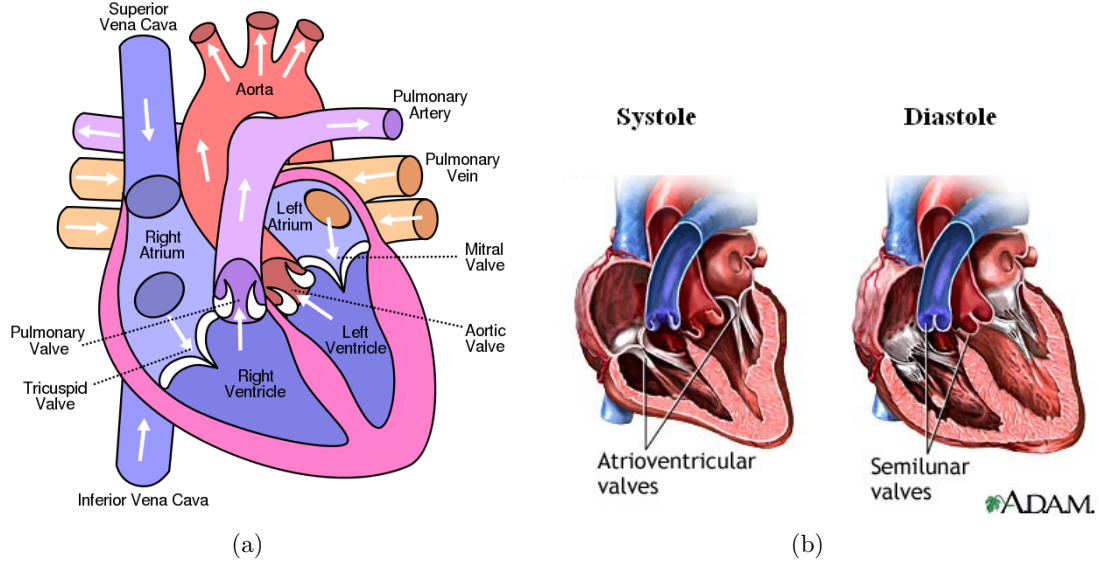


Figure 2.1: (a) Diagram of the human heart showing the chambers, valves and great vessels - by Wapcaplet in Sodipodi. (b) Diagram of the systole and diastole showing the opening and closing of the heart valves - by A.D.A.M. inc.

- The Right Atrium (RA) is connected to the entire venous system through the superior and inferior caval veins and has a volume of about 63ml. Its junction with the right ventricle is formed by the tricuspid valve.
- Extending from atrio-ventricular to the ventriculo-arterial junction, the Left Ventricle (LV) has a capacity of 100ml. Its inner wall, called endocardium, is demarcated by fine trabeculations and two prominent papillary muscles that support the two leaflets of the mitral valve and its tendinous cords. The aorta emerges out of the left ventricle passing through the semi-lunar aortic valve. From the ascending aorta, above the level of the aortic valve, two ostia connect the left and right coronary arteries to the coronary circulation.
- As with the left ventricle, the muscular of the Right Ventricle (RV) extends from the right side atrio-ventricular to the ventriculo-arterial junction and holds up to 130ml. The inlet portion of the right ventricle is limited by the tricuspid valve, while its outlet is connected to the pulmonary artery through the pulmonary valve.

2.1.2 Dynamics

The heart beats at an average frequency of 1.20Hz and passes two major phases to complete a cardiac cycle, the systole and diastole (see figure 2.1(b)). During diastole the ventricles relax until the inside pressure drops below the atrial pressure, which opens the atrioventricular, mitral and tricuspid valves. Blood flows from the atria to fill the ventri-

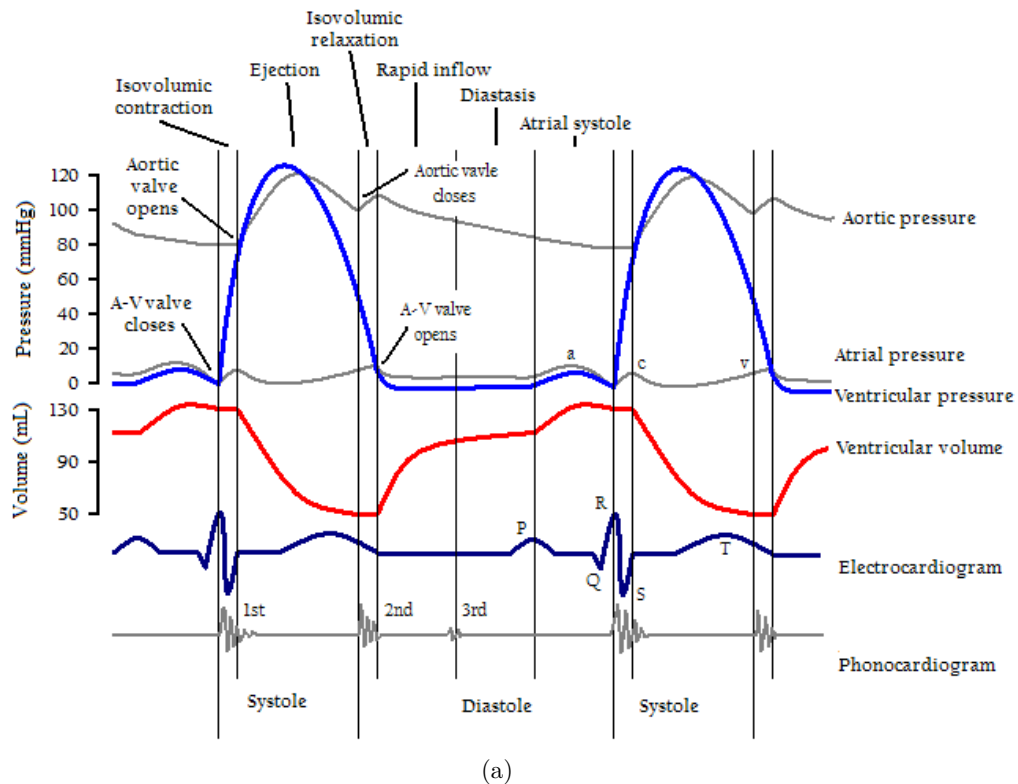


Figure 2.2: Diagram of events in the left-side heart during the cardiac cycle - by DestinyQx in Wikipedia

cles at an approximate velocity of 0.7m/sec. At the beginning of the systole, an electric stimulus causes the muscles of the lower chambers to contract. The drastically pressure increase to around 30mmHg and 130mmHg in the right and left ventricle, respectively, closes the atrioventricular valves (see figure 2.2(a)). The semilunar, aortic and pulmonary valves, open as ventricular surpasses the arterial pressure. Blood flows via the pulmonary valve into the pulmonary artery and to the lungs as well as through the aortic valve into the aorta and the body. After peak-ejection, ventricular pressure drops, closing the semilunar valves. The cardiac cycle ends with the loading of the right and left atria by the superior and inferior caval veins, and pulmonary veins respectively.

The heart pumps blood in parallel through the systemic and pulmonary circulation. In the first circuit, oxygenated blood is transported towards the body due to the left ventricle contraction and returns deoxygenated to the right atrium. The right ventricle circulates the deoxygenated blood through the lungs, which returns oxygenated into the left atrium.

The reader is referred to Hurst's [121] and Braunwald's [91] reference textbooks in cardiology and Wilcox et al. [188] cardiac surgery book for a comprehensive compilation of medical and clinical information about the heart.

2.2 Physiology of the Heart Valves

Scientific knowledge about the heart valves can be traced back to Leonardo da Vinci in the 14th century, who described the anatomy of the aortic and mitral valves in great detail. Many discoveries followed, especially during the 20th century, when precise observation instruments like the electrocardiogram, X-ray and other evaluation methods lead to an in-depth understanding of the pathophysiology of the heart valves.

Today it is well known that the fibrous skeleton of the heart is formed by four cardiac valves: the Aortic Valve (AV), Mitral Valve (MV), Tricuspid Valve (TV) and Pulmonary Valve (PV) (see figure 2.3). The first two are semilunar shaped and located at the interface of the heart with the main arteries, while the latter separate atria from ventricles and are referred to as atrioventricular valves. Over an average lifespan of 3×10^9 cardiac cycles, the valves regulate the blood hemodynamics by ensuring unidirectional flow within the heart and towards the rest of organism.

2.2.1 Aortic Valve

Indeed, there is still no consensus on the best way to describe the aortic valve anatomy [7]. However, its central anatomic structures are the aortic root and the three valvular leaflets also called cusps. The root provides the supporting structures for the leaflets and forms the bridge between the left ventricle and the ascending aorta (see figure 2.4(a)). It extends from the basal attachments of the leaflets within the left ventricle, defined as the hinge points, to the sinutubular junction. The diameter at the hinge points is normally about equal to that of the ascending aorta and the sinutubular junction (see figure 2.4(b)). From a geometric perspective, the aortic root is a cylinder with three wall dilatations referred to as sinuses of the valsava or valvular sinuses.

The three aortic leaflets are avascular and attached to the root on the semilunar structures within the valvular sinuses (see figure 2.4(c)). They can be thought of as shirt pockets with one edge stitched to the shirt and one free of attachment. These attachment structures interlink at the level of the sinutubular junction forming the three commissures. Each cusp presents a fibrous core, which is thickened at the center of the free edge denoted

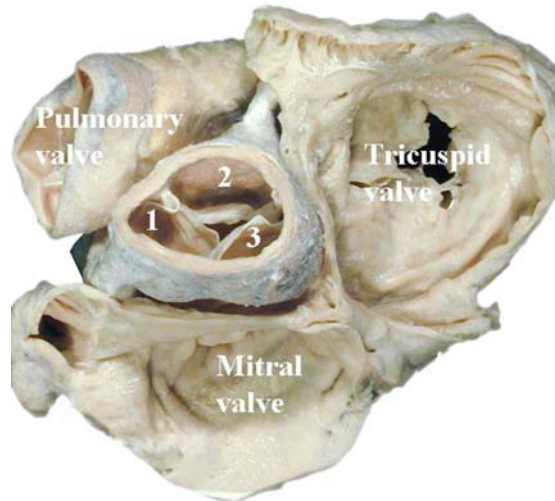


Figure 2.3: The four cardiac valves centered on the aortic valve, which builds the cornerstone of the fibrous extension. Reproduced with permission of the author and the European Association for Cardio-Thoracic Surgery from: Anderson RH. The surgical anatomy of the aortic root. Multimedia Man Cardiothorac Surg doi:10.1510/mmcts.2006.002527.

by the leaflet tip. The left and right coronary arteries arise from two of the three aortic sinuses underneath the sinutubular junction. Thus, the leaflets are named accordingly as being the left coronary leaflet, right coronary leaflet and none coronary leaflet. They are similar sized, but truly equal in only approximately 10% of the hearts.

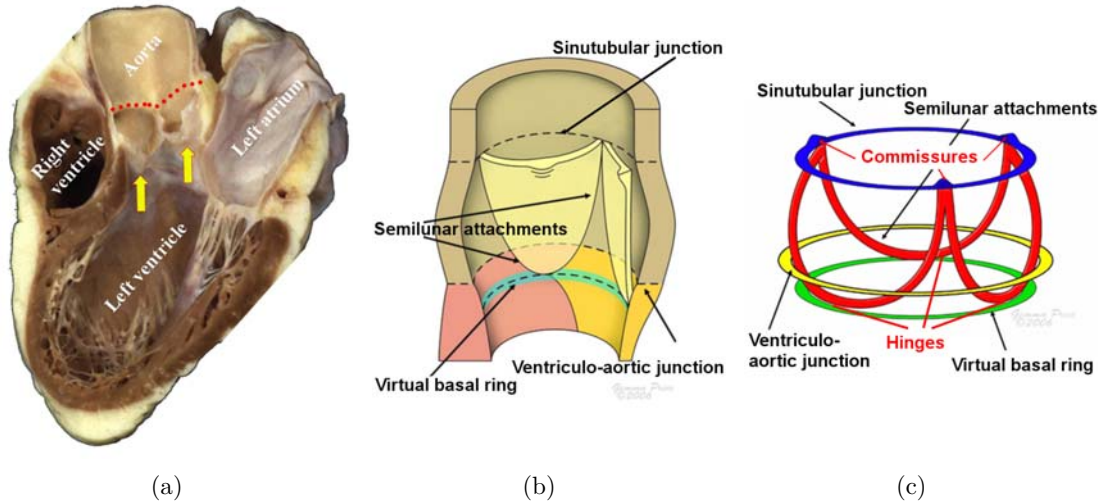


Figure 2.4: (a) Parasternal long axis section through the heart showing the aortic root at the centerpiece of the heart. (b) Cartoon of a bisected aortic root illustrating its cylindrical shape and the leaflets attachments. (c) Cartoon of an idealized aortic root presenting the commissures and hinges as well as the semilunar attachments. Reproduced with permission of the author and the European Association for Cardio-Thoracic Surgery from: Anderson RH. The surgical anatomy of the aortic root. Multimedia Man Cardiothorac Surg doi:10.1510/mmcts.2006.002527.

The AV function is to facilitate unidirectional blood flow, from the LV to the ascending aorta. Under systolic contraction, the pressure in the left ventricular exceeds that of the aorta forcing the leaflets to open parallel to the sinuses wall. In diastole, the aortic leaflets collapse together with their coaptation being sustained by the hydrostatic pressure of the supported column of blood.

2.2.2 Mitral Valve

The mitral valve is located between the left ventricle and left atrium and consists of four central components: the anterior and posterior leaflet, the annulus and the subvalvular apparatus (see figure 2.5(a)). The latter two connect the valve to the LV endocardium. The annulus is a ring-like fibrous entity with a three-dimensional shape resembling a saddle with the middle portions of the anterior annulus being elevated out of the annular plane towards the LA and merging into the aortic mitral curtain. Unlike the other three valves, the mitral valve contains only two leaflets. The anterior leaflet is larger and semicircular,

and through the aortic mitral curtains, which end in the left and right fibrous trigone, it partially separates the ventricular inflow and outflow tracts (see figure 2.5(b)). The posterior leaflet is rectangular and divided through slits into several scallops. Multiple nomenclatures exist, but most commonly the scallops are named P1 to P3 with opposing segments A1 to A3 (see figure 2.5(c)) [8]. The anterior leaflet is normally twice the height of the posterior but has half its annular length. The mitral commissures are the points where both leaflet's free edges join, not coinciding with the mitral annulus. The subvalvular apparatus consists of the chordae tendineae arise from the papillary muscles and extend in a fan-like array to insert into the free edge of both leaflets.

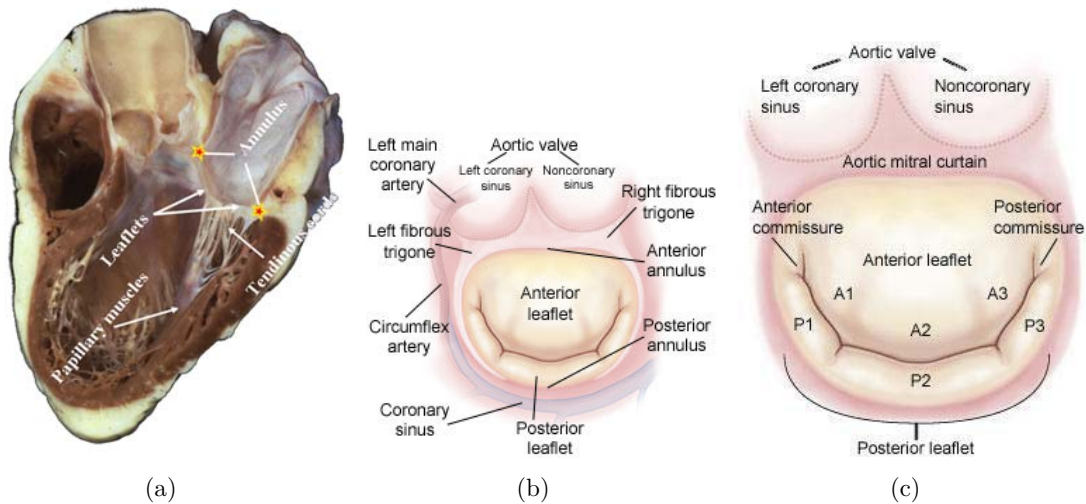


Figure 2.5: (a) Parasternal long axis section through the heart showing the complex mitral valve structure. (b) Cartoon depicting the anterior and posterior leaflets viewed from the left atrium. (c) Cartoon illustrating the mitral valve scallops. Reproduced with permission of the author and the European Association for Cardio-Thoracic Surgery from: Anderson RH. The surgical anatomy of the aortic root. Multimedia Man Cardiothorac Surg doi:10.1510/mmcts.2006.002147 and [30]

The competent mitral valve function is complex and requires optimal interaction between all its components and associated chambers. Its function is to allow blood to flow only one way, from the LA to the LV, separating them hemodynamically. It is opened by the increasing pressure in the left atrium, which is pushing down the leaflets during diastole, and remains closed due to the ventricular pressure during systole.

2.2.3 Tricuspid Valve

The right atrioventricular valve, the tricuspid valve, positioned between the right ventricle and atrium, comprises the annulus, leaflets and subvalvular apparatus. A normal tricuspid valve presents three sail-like leaflets: septal, anterior and posterior. Usually the largest and most mobile is the anterior leaflet, which forms the intracavitary curtain that partially

separates the inflow and outflow tract of the RV. While the anterior leaflet is stable, the posterior and septal leaflets vary in size and position, with the former being the least mobile due to its direct chordal attachments to the septum. The tricuspid annulus forms the supporting structure of the leaflets. Similar to the mitral valve, the free leaflet edges are anchored to the papillary muscles of the right ventricle by chordae tendineae. Tricuspid chordae may also insert directly into the right-ventricle wall. The function of the tricuspid valve is to regulate the blood flow from the right atrium to the right ventricle, staying closed during systole and opened during diastole.

2.2.4 Pulmonary Valve

Anatomically identical in shape with the aortic valve, the pulmonary valve is attached to the muscular infundibulum of the right ventricle. Unlike the left-side valves, which are connected through the fibrous continuum, the pulmonary and tricuspid valves are separated by infundibular muscle. As it is difficult to describe the leaflets directly, these are named according to their relationship to the AV. Two of the aortic valve leaflets attached to the septum always face two corresponding leaflets of the pulmonary valve, which are referred to as left and right facing leaflets. The third is the none facing leaflet. The valvular leaflets coapt in diastole and retract into the sinuses during ventricular systole allowing unrestricted blood flow towards the pulmonary artery.

To date, most data on valvular morphology and function has been obtained by experimental studies on explanted valves or using animal models [37], with small numbers of cases across publications. Standard dimensions provided in the literature vary considerably [87] and there is no consensus on the best way to describe the valvular physiology [7]. The methodology presented in this thesis enables for comprehensive, efficient and reproducible analysis of the valvular apparatus through non-invasive and in-vivo experiments. Thus, it can contribute to a better understanding of the physiology and pathological changes of the heart valves, and potentially consolidate the existent medical knowledge.

2.3 Clinical Pathology of Valvular Heart Disease

While the heart valves regulate the blood flow during the cardiac cycle, two major problems may affect their proper function: stenosis or regurgitation. The condition in which valves fail to open fully because of narrowing, stiffening, thickening fusion or blockage is called stenosis. Conversely, a condition of defective closing, which causes ejected blood to leak backwards, is referred to as insufficiency, incompetence or regurgitation. In some cases both dysfunctions may coexist, but either symptom is sufficient to increase the workload on the heart, which gradually becomes weaker and inefficient. Untreated valvular heart disease eventually results in heart failure and even sudden death. VHD is a frequent symptom, with a prevalence of 2.5% among the global population [122].

VHD may be congenital or acquired later in life such as rheumatic, endocarditis and degenerative malfunctions. Abnormalities present from birth can affect all valves, but the most common congenital malformation is the bicuspid aortic valve, in which the valve possesses only two instead of three leaflets. The defect causes the valve to be more prone to infection, or degenerative disorders.

In the ages before antibiotics were commonly available, VHD was mainly provoked by rheumatic fever, a streptococcal bacterial infection, which often affects children between 5 and 15 years. Although, rheumatic heart disease drastically decreased in developed regions, it still affects some 20 million Americans and remains a serious problem in developing countries. The damage caused by the autoimmune response to the bacteria determines leaflets to stick together or become rigid and thickened.

Another inflammatory condition that progressively degenerates the valve tissue is infective endocarditis. Usually originating from streptococci and staphylococci of untreated infection elsewhere in the body, it forms warty nodules, produce holes and can completely disrupt valve function. Although rare in normal and healthy individuals, patients with artificial mechanical valves are at major risk.

The population aging phenomenon in developed countries made degenerative syndromes the most common type of VHD. From a series of metabolic changes encountered in elderly, valve tissue losses, becomes weak and in addition allows calcium deposits, which decreases the hemodynamic performance of the affected anatomy.

2.3.1 Aortic Stenosis and Regurgitation

Aortic valve stenosis is identified as an obstruction to the left ventricular outflow tract, supra-valvular or subvalvular that has three principal causes: congenital bicuspid valve, degenerative calcification and rheumatic heart disease. Bicuspid aortic valve is the most common congenital valve disease with a prevalence of 1.4% from the global population and 54,800 new cases yearly in the United States [96] (see figure 2.6(a) and 2.6(d)). Although two or one leaflet valves can function normally, these are under increased risk for infections and degenerative disease, as 75% of calcified aortic valves for the 15-65 age group are bicuspid or unicuspid. Age related calcification is the most common form of aortic stenosis associated with a 50% increased risk for cardiac mortality due the congestive heart failure and sudden death (see figure 2.6(b) and 2.6(e)). Leaflet stiffening and commissural fusion from rheumatic fever continues to be a major problem on a worldwide basis.

Aortic stenosis severity is determined from the degree of obstruction where symptomatic and severe cases have an aortic valve area $< 1.0\text{cm}^2$, moderate stenosis $1.0 - 1.5\text{cm}^2$, mild $1.5 - 2.0\text{cm}^2$ and normal between 3.0 and 4.0cm^2 . Severe obstruction is characterized by an aortic jet velocity $> 4\text{m/sec}$ and mean systolic gradient exceeding 40mmHg . Echocardiography is the standard approach to evaluate aortic stenosis with Doppler jet velocity measurements considered the main predictors of severity.

Aortic regurgitation is primarily caused by aortic root dilatation and aortic leaflet disease (see figure 2.6(c) and 2.6(f)). Enlargements of the aortic root and ascending aorta may be age related, due to bicuspid anatomy or genetic disorders e.g. Marfan syndrome. Those normally result in dilated aortic annuli with leaflet separation and ultimately insuf-

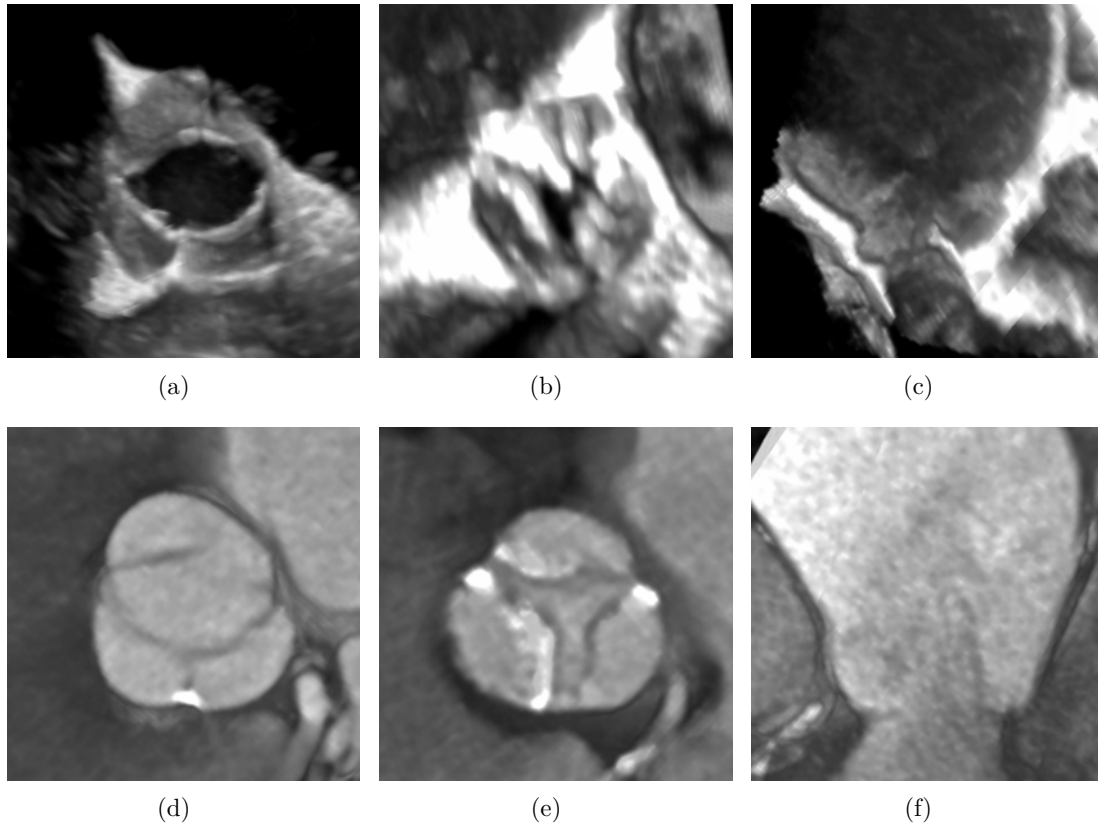


Figure 2.6: Examples of aortic valve disease: bicuspid aortic valve from TEE (a) and CT (d), stenotic aortic valve with calcification from TEE (b) and CT (e), and dilated aortic root with valve regurgitation from TEE (c) and CT (f).

iciency. Vegetation, endocarditis, rheumatic fever and calcified valves may also interfere with the proper coaptation of the aortic cusps. To provide hemodynamic compensation to the chronic blood leakage, the LV end-diastolic volume gradually increases. The breaking point is reached when the mass augmentation and wall thickening fails to keep pace with the additional workload, which provokes soaring end-systolic wall stress and fault ejection fraction.

Echocardiography is indicated for assessment of structural changes, LV end-diastolic and end-systolic dimensions, ejection fraction and ventricular mass. In addition, CMR provides accurate quantification of the regurgitant orifice volume as well as antegrade and retrograde flow volumes in the ascending aorta.

2.3.2 Mitral Stenosis and Regurgitation

The predominant origin of mitral stenosis is rheumatic fever, with a prevalence of 1 case per 100,000 in the US and Europe, and 35 per 100,000 in Africa. The dysfunction

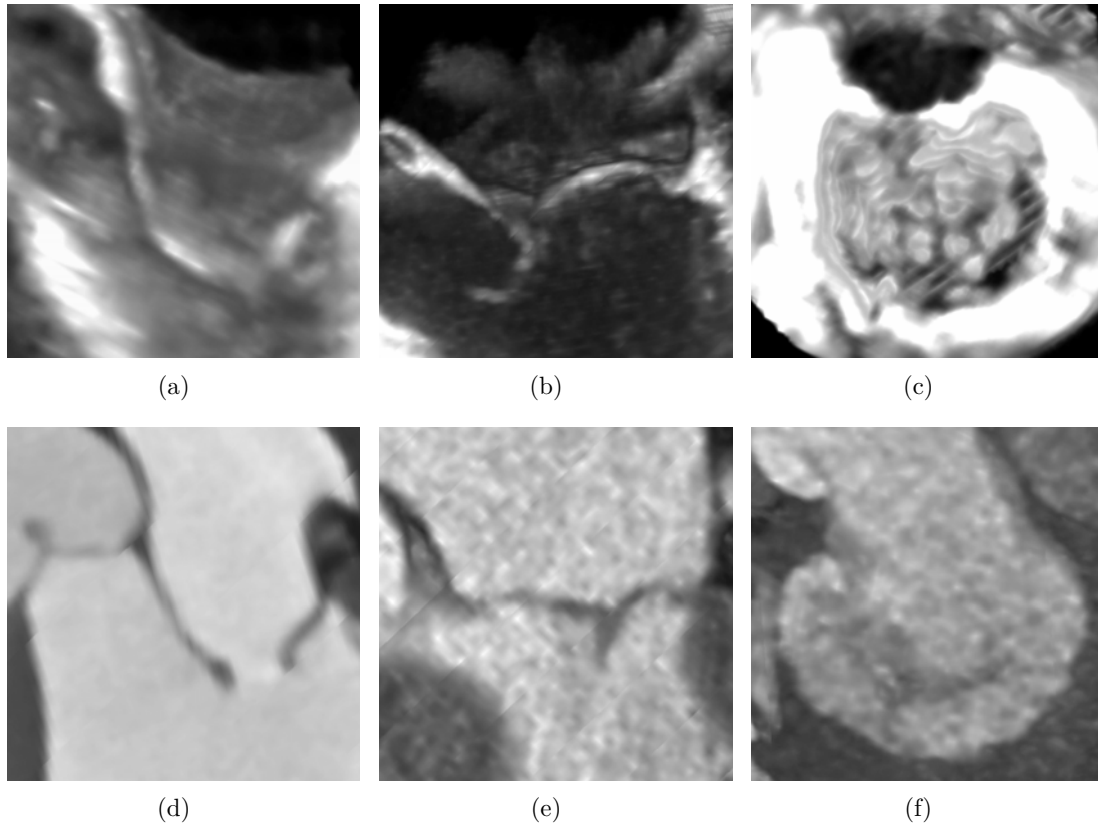


Figure 2.7: Examples of mitral valve disease: stenotic mitral valve from TEE (a) and CT (d), mitral valve prolapse from TEE (b) and CT (e), and mitral valve regurgitation from TEE (c) and CT (f).

is characterized through leaflet thickening, commissural fusion and chordal shortening while calcification further accentuates the pathologic valve function (see figure 2.7(a) and 2.7(d)). The stenosis severity is expressed by the degree of valve opening obstruction, quantified via the mitral valve orifice area in diastole. In normal adults the cross-sectional area is $4 - 6\text{cm}^2$, as for mild stenosis case 2cm^2 . To compensate for the reduced opening, a gradient pressure is needed to propel blood from the LA to the LV. In severe cases with an orifice of 1cm^2 , an atrioventricular pressure gradient of 20mmHg is required for normal cardiac output, which raises atrial pressure and generates pulmonary artery hypertension and other adverse hemodynamic effects. Echocardiography is the most accurate approach to diagnose mitral stenosis, where mitral valve area is calculated by direct planimetry or from Doppler pressure gradients.

Unlike stenosis, the etiology of mitral valve insufficiency is multiple. Mitral valve prolapse due to lengthening or rupture of the chordae tendineae and papillary muscle disease is the most common cause of mitral regurgitation (see figure 2.7(b) and 2.7(e)). Second leading source is the result of ischemic LV dysfunction and cardiomyopathy, both

provoking mitral annular dilatation with reduced systolic constriction and valve closing (see figure 2.7(c) and 2.7(f)). Degenerative calcification and rheumatic fever are other causes for mitral incompetence.

The volume of mitral backflow depends on the regurgitant orifice and pressure gradient between LV and LA. The LV compensates by emptying more completely and increasing preload. As a result its end-diastolic volume increases, which enlarges the mitral annulus and therefore the regurgitant orifice, creating a vicious circle.

Echocardiography plays a central role in mitral regurgitation assessment and severity quantification. It measures high velocity jets in the left atrium during systole characterized by the jet width and atrium size. Another common indicator is the proximal isovelocity surface area (PISA), which measures the flow at one moment in time and may not reflect average performance.

2.3.3 Right-Side Valve Disease

Tricuspid valve stenosis is rather infrequent and never occurs in isolation. Tricuspid regurgitation is mostly functional and not primarily related to leaflet pathology but rather right ventricular dilatation, distortion of the subvalvular apparatus or tricuspid annular dilatation. Severe cases are associated with adverse outcomes and important impact on survival in patients with concomitant cardiovascular disease.

Pulmonary valve stenosis occurs to 80% in isolation, from which 90% of cases are related to congenital disease, such as Tetralogy of Fallot. Balloon valvuloplasty is the procedure of choice in children and adults in severe or symptomatic patients. Paradoxically, adverse consequences of repair are the principal cause of pulmonary valve regurgitation, which progressively provokes right ventricular dysfunction and congestive heart failure.

The reference textbook [122] provides complete information on the valvular heart disease subject. Additionally, both the European Society of Cardiology [167] and the American College of Cardiology [19] supply clinical guidelines for the management of patients with valvular heart disease. In general, the evaluation workflow for VHD patients involves non-invasive imaging using a combination of Transthoracic Echocardiography (TTE), TEE, cardiac CT and CMR techniques. However, most of the decisions are currently based on two-dimensional reconstructed images, user-dependent processing and manually performed, potentially inaccurate measurements. One major contribution of this thesis, mainly covered in section 5.1, involves an automated model-based analysis paradigm that can benefit the diagnosis and assessment of valvular pathologies with precise 4D quantification.

2.4 Treatment of Valvular Disease

As no specific medication prevents the progression of VHD, invasive repair and replacement of defected valves is currently the standard therapy. The first operation on the mitral

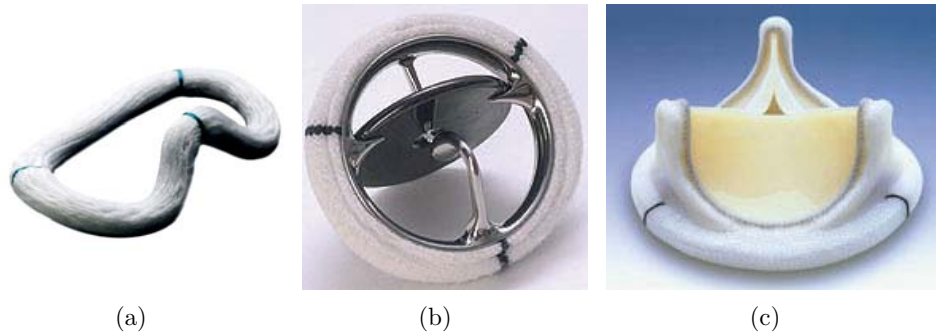


Figure 2.8: (a) GeoForm Annuloplasty Ring, Edwards Lifescience, Irvine CA. (b) Hall Easy-Fit Mechanical Prosthesis, Medtronic, Minneapolis MN. (c) Carpentier-Edwards PERIMOUNT Pericardial Bioprosthesis, Edwards Lifescience, Irvine CA.

valve by Dr. Elliot Cutler was performed in 1923, but it wasn't until the 1950s, when the invention of the heart-lung machine marked the beginning of the modern era of cardiac surgery. Progressive improvements in prosthetic valves, started by the Starr-Edwards ball-in-cage prosthesis in 1961, and corresponding advancements in surgical repair techniques over the past five decades have established open heart valve surgery as the most popular treatment to date. According to the American Heart Association, in 2009, over 100,000 valve procedures were performed alone in the United States [96]. Section 2.4.1 presents an overview on existent surgical repair and replacement techniques.

Despite continuous advancements, valve surgery is the most expensive among all cardiovascular procedures, with associated costs averaging \$141,200 and having the highest in-hospital death rate, 4.9%. Due to the high operative risk, estimated using the EuroSCORE - European System for Cardiac Operative Risk Evaluation and STS- Society of Thoracic Surgeons score, over 30% of the symptomatic patients are currently denied traditional surgery [122]. A less invasive and potentially safer valve treatment has been recently enabled through intravascular procedures. Those, so called, percutaneous techniques are rapidly evolving opening a new era in valvular therapy and are expected to cover up to 41.1% of all procedures by 2012 (Millennium Research Group 2008). Section 2.4.2 introduces the most promising percutaneous treatment approaches to date.

2.4.1 Heart Valve Surgery

Heart valve surgery is an open heart operation executed under general anesthesia. Sternotomy is performed and the pericardium is pierced to secure access to the heart, while the blood is routed through the cardiopulmonary bypass to maintain normal circulation. Depending on the specific physiopathology, affected valves are either repaired or replaced with a prosthetic substitute.

Aortic Valve Repair: An appreciation for the complex anatomy and understanding of the benefits in preserving natural structures, led to an expansion of reconstructive

surgery techniques over the past decades. The Ross operation originally described in 1967 is considered the apogee of true restoration, as it preserves the complete natural anatomy. Experienced surgeons can replace diseased aortic valves with a pulmonary autografts and restore optimal hemodynamics and physical activity. Due to the inherent complexity, the Ross procedure is currently reserved for specialized centers and young patients that justify a life expectancy greater than 25 years.

In the early 1990s Tirone Davis and Sir Magdi Yacoub proposed the reconstruction of the aortic root with preservation of the native leaflets. The choice of the graft tube, the leaflet resection or tailoring and their symmetrical re-suspension is acknowledge to be as much art as it is science. A standardized quantitative approach to patient selection and procedure planning could potentially improve therapy success and enable operation beyond reference centers.

In moderate root disease cases, the valvular orifice can be narrowed by simple commisuroplasty. Knots are placed on the aorta outside on the left-noncoronary fibrous aspect to reduce aortic valve regurgitation. More sophisticated approaches include leaflet shortening and bicuspid to three-leaflet valves conversions, with major application in pediatric cardiology.

Mitral Valve Repair: Mitral repair became a clinical reality in 1983 due to the pioneering work of Dr. Carpentier. His landmark article the "French correction" [29] describes mitral valve repair stabilized with a ring prosthesis. Today, mitral valve repair is considered a widespread and safe procedure recommended in symptomatic and asymptomatic patients with positive post-operative prediction.

The majority of patients suffer from dysfunction of one or more segments associated with ruptured or elongated prolapsing chords and annular dilatation. Quadrangular, trapezoid or triangular resections are performed to reduce the amount of distortion. Artificial chords, e.g. Gore-Tex, are used to re-attach mitral leaflets to the papillary muscles. Shortening of excessively elongated anterior or posterior leaflets is achieved through resection or simple plication. Commissuroplasty is used for patients with flail segments adjacent to the commissures. The procedure is finished by annular remodeling usually with the one of the various annuloplasty rings commercially available (see figure 2.8(a)).

The therapy outcome is decisively influenced by a set of crucial decision addressed during planning and operation. Whether the valve can be repaired or needs replacement is still an area under investigation. Measuring neo-chords and defining the proper length to simultaneously avoid restriction and prolapse requires considerable judgment. The specific reconstructive approach presents difficulties especially in ischemic or functional mitral regurgitation cases. Advanced imaging in conjunction with patient-specific modeling and accurate quantification can provide substantial support to clinicians and potentially improve surgical success rates.

Robotic minimal invasive mitral repairs with port access, e.g. da Vinci system [117], offer a series of benefits: improved patient acceptance, improved cosmetic results, safety and effectiveness, shorter hospitalization and reduced postoperative disabilities. There is no doubt that image analysis will complement robotic improvements to overcome current limitation such as high rates of residual regurgitation and increased incidence of

perioperative stroke.

Right-Side Valve Repair: Tricuspid regurgitation is a predictor for advanced valve disease and is frequently found in patients with ventricular dysfunction. As tricuspid regurgitation may progress after mitral repair, concomitant tricuspid annuloplasty is advised. However, decision varies considerable across centers and strictly relies on expert's opinion rather than on quantitative facts. Reconstructive surgical techniques include suturing, repair with flexible rings and near complete remodeling rings.

Analogous to all other valves, whenever possible, the pulmonary valve is repaired to preserve the natural tissue and avoid infections as well as blood-thinning medication. Repair may include the separation of fused valve leaflets, sewing torn leaflets or reshaping parts of the valve.

Valve Replacement: For a large spectrum of valve dysfunctions such as rheumatic disease, endocarditis or calcification, repair methods including valvuloplasty, remodeling or calcium removal are not effective and were excluded from clinical treatment guidelines. Hence, valve replacement is imminent and a fundamental decision must be made about whether to implant a mechanical or tissue prosthesis.

Mechanical valves evolved from the first Starr-Edwards ball-in-cage to modern single, e.g. Medtronic Hall, or bi-leaflet, St. Jude Regent tilting disk prosthesis (see figure 2.8(b)). Randomized trial demonstrated equivalent performance of commercial mechanical valve. The average survival rate at 25 years lies at 24.9%, with significantly better results in patients under 18 years out of which 88% have survived 20 years past the replacement. Concomitant root and valve treatment, especially required in young patients with Marfan syndrome, can be performed with a mechanical valve implanted in a Dacron tube graft. Nevertheless, regardless of prosthesis and procedure type, the intrinsic mechanical durability is often outweighed by the associated side-effects of thromboembolic events, which requires life-long administration of anticoagulant.

A cumulative risk for hemorrhage and thrombosis of about 4% per year specific to mechanical valves motivated the development of bio-prostheses. Leaflets fabricated out of animal tissue are attached to a support frame that has a cloth sewing ring to allow surgical sutures (see figure 2.8(c)). Latest generations have an estimated durability of 15-20 years, which unfortunately decreases inverse proportionally to patient's age. Benefits include low rates of thromboembolism, lower complication rates, better survival, and easiness of implantation. Homografts, have also been used for aortic valve replacement, however with limited application due to lack of donors and cardiac surgeon experience.

2.4.2 Percutaneous Valve Therapy

Today, one third of the acute and symptomatic valve patients are not surgically operable. Percutaneous therapy has the potential to revolutionize the treatment of valve disease, offering a less invasive alternative to classic open-heart surgery. Prosthetic valves,

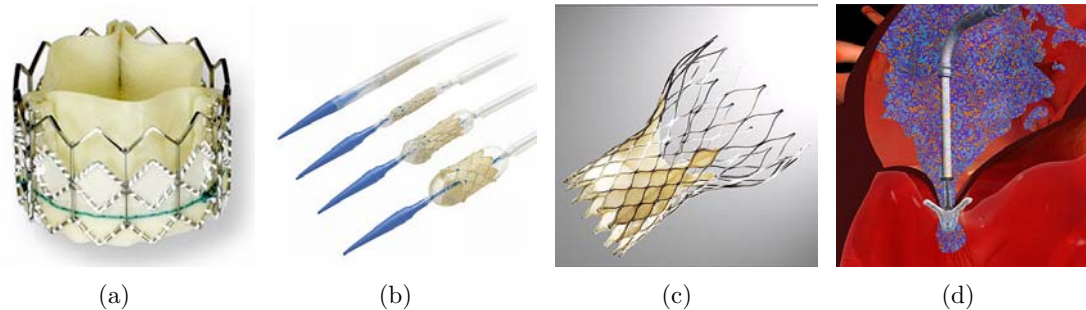


Figure 2.9: (a) SAPIEN, Edwards Lifescience, Irvine CA. (b) Melody Transcather Valve, Medtronic, Minneapolis MN. (c) CoreValve, Medtronic, Minneapolis MN. (d) MitraClip, Evalve, Menlo Park CA.

instruments and other devices are delivered through intravascular catheters using transvenous, transarterial or transapical entrance points. Interventions are performed in cardiac catheterization or hybrid operating rooms under general or local anesthesia and rapid phasing techniques. Without direct view and access to the affected valves, procedure guidance and critical decision are exclusively based on imaging techniques such as Fluoroscopy and Transesophageal Echocardiography.

Semilunar Valve Replacement: Aortic and pulmonary valves are replaced by pericardial implants mounted on balloon-expandable or self-expandable stents. Released in 2007 for commercialization in Europe, the SAPIEN, Edwards Lifescience, Irvine CA, is the most popular percutaneous aortic valve implant (see figure 2.9(a)). It is available in two sizes, 23 and 26mm, and has an in-vitro demonstrated durability of 200 million cycles or approximately 5 years. The Melody Transcather Valve, Medtronic, Minneapolis MN, received FDA approval in 2010 and is a similar device applicable in pulmonary valve pediatric and adult patients with RVOT conduit $\geq 16mm$ (see figure 2.9(b)).

CoreValve, Medtronic, Minneapolis MN, is a device with pericardial leaflets attached on a nitinol self-expandable frame, which exhibits three different radial forces at different parts of its peripheral circumference (see figure 2.9(c)). Deployment is achieved under rapid-pacing and fluoroscopic guidance after balloon valvuloplasty. The technique, which is usually performed in 1 ½ hours, received the European CE mark in 2007. Despite high success rates of over 95%, serious complications due to malpositioning occur in 3% of the cases.

Procedure planning is usually performed using CT, Magnetic Resonance Imaging (MRI) and Ultrasound images to assess annular and leaflet dimensions as well as vascular access anatomies. Navigation is assisted by a combination of fluoroscopic, angiographic and TEE imaging. Correct deployment coaxial to the native valve and at a specific annular height is imperative. Implants exhibit better hemodynamics but more residual regurgitation compared to surgically replaced valves, primarily due to paravalvular leakages.

Atrioventricular Valve Repair: Percutaneous therapies for atrioventricular valves mimic corresponding surgical strategies. The MitraClip, Evalve, Menlo Park CA, is based on the anterior-posterior surgical suturing, in which the mitral leaflets are clipped together into a double orifice valve (see figure 2.9(d)). Under TEE guidance, the clip is deployed via transseptal delivery catheters, where intra-operative assessment is performed using Doppler and fluoroscopic imaging.

Several percutaneous solutions reproduce the effect of annuloplasty rings to reduce the annular dimensions and consequently the regurgitation degree. The PTMA (Viacor, Wilmington, MA), Carillon Mitral Contour Device (Cardiac Dimensions, Kirkland, WA) and the MONARC device (Edwards Lifesciences, Irvine, CA) are examples of devices successfully demonstrated to reduce mitral insufficiency in animal and early clinical trials. These exploit the proximity of the coronary sinus relative to the posterior leaflet, which runs from the lateral LV wall medially to the RA. Inserted into the coronary sinus, these devices either cinch or compress the annulus to improve valve coaptation. Cardiac CT based planning is invaluable for these procedures.

Another technique worth mentioning is the QuantumCor device which uses a heat probe on the mitral annular collagen to short the strands and compress annular dimension. The iCoapsys device decreases the mitral annular septal-lateral dimensions, repositions and stabilizes the papillary muscles through two chord-connected pads placed on the epicardial surface and passing across the LV.

The current lack of standardized routines and the technological deficit determines the success of reconstructive surgery and percutaneous procedures to strongly rely on the experience and skills of the operator. To advance the clinical workflow, section 5.2 introduces an automated and robust approach for patient-selection and risk stratification. In Section 5.3 we propose a novel computation framework for preoperative planning, intraoperative guidance and post-operative assessment of percutaneous valve procedures. Our approach has the potential to advance replacement and repair operations as well as to fuel research on mixed valvular treatment.

2.5 Imaging Modalities

Modern medicine would be impracticable without the multitude of medical scanners available today. The entire clinical workflow targeted for treatment of cardiovascular disease, including assessment, planning, and therapy guidance, relies on qualitative and quantitative analysis of various types of images. Dictated by the underlining physical properties, each modality presents advantages as well as limitations in sensing specific morphological and functional aspects of the heart. In the following, imaging modalities relevant for the clinical management of valvular heart disease are briefly discussed.

2.5.1 X-Ray and Angiography

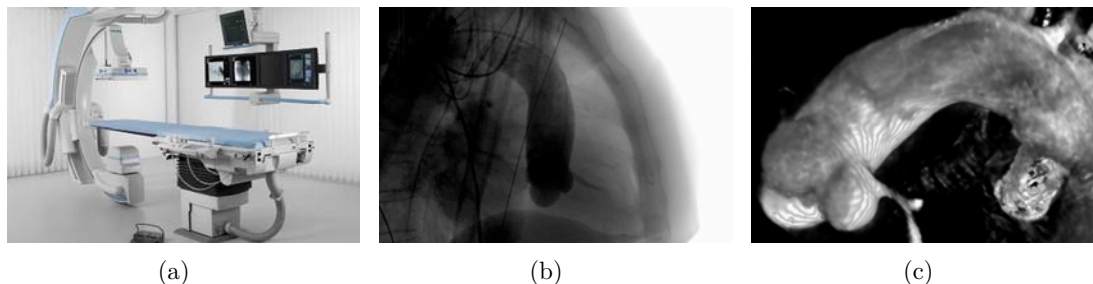


Figure 2.10: (a) C-arm X-ray - Artis zee Ceiling-mounted system, Siemens Healthcare, Forchheim, Germany. (b) Fluoroscopic image of the heart with contrast concentrated in the aorta. (c) Three-dimensional DynaCT reconstruction of the aorta.

X-ray photons of a specific energy are generated by a vacuum tube and emitted towards a flat panel detector, which is located on the other side of the patient (see figure 2.10(a)). The measured energy on the X-ray detector is attenuated by the material traversed along the beam, and its difference to the emitted radiation is used to produce grayscale images. Traditionally, X-ray has been applied to evaluate the skeleton and bony structures, as attenuation differences between soft tissue and bones results in high contrast images.

Angiographic techniques combine X-ray Imaging (X-ray) with a radiopaque contrast agent injected prior to the scanning, in order to visualize cardiovascular structures. These together with fluoroscopy, in which low-dose X-ray images are acquired in real-time, are essential imaging modalities in cardiac catheterization laboratories (see figure 2.10(b)). Under X-ray guidance, narrow tubes, called catheters, are inserted into the cardiovascular system to perform diagnostic and therapeutical procedures such as percutaneous valve repair or replacement. The most common indication for cardiac catheterization is the investigation and severity assessment of coronary artery disease [91]. In patients with VHD, cardiac catheterization provides complementary data with non-invasive studies and is recommended in patients with complex multi-valve disease, uncertain or discordant diagnosis or low-gradient aortic stenosis after dobutamine administration [122].

Modern C-arm X-ray methods, such as the syngo DynaCT, Siemens Healthcare, Forchheim, Germany, offer the capability to reconstruct 3D volumes from several hundred 2D projection images acquired by rotating the C-arm about 180 degrees around the patient (see figure 2.10(c)). Recently, DynaCT was demonstrated to acquire optimal intra-operative images of the aortic annulus under rapid biventricular pacing and aortic root injected contrast, during off-pump transapical aortic valve implantation [82].

The inherent limitation of X-ray imaging is the ionizing radiation applied to the patient and operating physician. Additional risk for kidney failure emerges from the injected contrast dye, while cardiac catheterization provokes serious complications in about 2% of the patients or even death in 0.08% of the cases.

2.5.2 Cardiac Computed Tomography

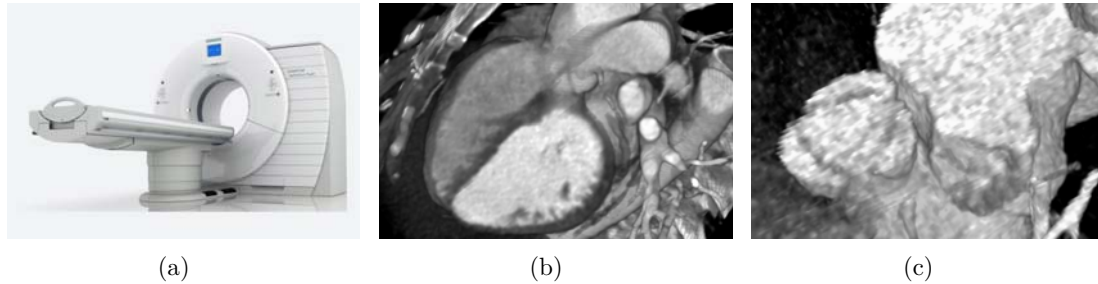


Figure 2.11: (a) CT - SOMATOM Definition Flash, Siemens Healthcare, Forchheim, Germany. (b) Complete heart scan with contrast on the left side. (c) Volumetric reconstruction of the aortic valve clipped at the valvular sinuses level.

Cardiac computed tomography (cardiac CT) is a procedure that uses a special X-ray machine to generate detailed images of the heart. During the cardiac CT scan the X-ray tube rotates around the body to acquire multiple images from different angles and combines them to reconstruct three-dimensional volumes of the heart (see figure 2.11(a)). A Computed Tomography Angiography (CTA) procedure uses Iodine-based contrast dye injected into veins while scanning to highlight blood vessels and soft tissue areas. Each portion of the heart can be imaged at several phases of the cardiac cycle. Retrospective Electrocardiography (ECG) gating is used to correlate the CT data with the corresponding phase and reconstruct a series of volumes which cover a complete cardiac cycle (Multiphase CT or CTA). New scanners, as the SOMATOM Definition Flash CT, Siemens Healthcare, Forchheim, Germany, achieve a temporal resolution of 75 milliseconds and require 0.6 seconds for a complete thorax scan at a radiation dose of 1 millisievert (mSv) (see figure 2.11(b)).

The main limitation of cardiac CT is the radiation caused by the X-ray machine, which is harmful to the human body. The radiation dose of a regular exam is comparable to the natural background radiation of 3-year period, 10 mSv. CT imaging of the heart is also prone to artifacts primarily due to cardiac and respiratory motion. The resulting blur contours or misalignments of adjacent slices reduce the diagnostic value of the images. Nevertheless, due to its relatively high spatial resolution cardiac CT provides accurate morphologic imaging of the heart, which is useful in various clinical scenarios such as: calcium assessment and scoring, and the visualization of the coronary arteries.

While visualization of the right-side valves is rather inconsistent, cardiac CT is reliable in depicting the aortic and mitral in contrast enhanced CTA procedures. It has been reported that CT can quantify the mitral regurgitant orifice as well as the mitral valve morphology [5]. Recent studies demonstrate the usage of CTA to measure the orifice area in normal and stenotic aortic valves in close correlation with TEE [59] (see figure 2.11(c)).

2.5.3 Cardiovascular Magnetic Resonance

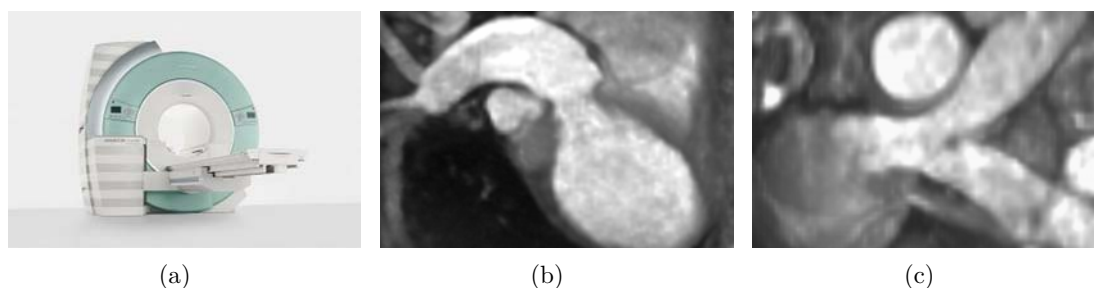


Figure 2.12: (a) MRI - Siemens Verio, Siemens Healthcare, Erlangen, Germany. (b) Heart image including the left ventricle and aorta. (c) Volumetric reconstruction of the right ventricular outflow tract and pulmonary arteries.

Cardiac magnetic resonance CMR imaging uses a high-strength magnetic field, most common 1.5 Tesla, to excite hydrogen nuclei within a body region by a pulse of radio waves, at a resonance frequency of 63MHz (see figure 2.12(a)). Images are built from wave echoes emitted during excitation decay, while contrast arises from different particle concentration of individual tissues. Discrimination between blood and myocardium tissue is possible in arbitrary planes without contrast medium.

After growing considerably over the past years, CMR is now firmly established in large centers and considered the most versatile non-invasive diagnostic modality. It enables high-resolution static and moving images of cardiac structures when combined with ECG synchronization (see figure 2.12(b)). Furthermore, phase-contrast protocols produce velocity-encoded images of the blood flow. The nonionizing technology offers CMR a fundamental advantage compared to X-ray and gamma ray modalities. Nevertheless, relative long examination times of 45-90min, compared to 15min for CT studies, obstruct CMR application for full 4D imaging.

CMR offers invaluable information about the valvular anatomy and function. It is the modality of choice for the analysis of dilated aorta with aortic regurgitation and most accurate to evaluate ventricular function [122]. CMR is ideally suited in pediatric cardiology to assess complex congenital heart disease of the valves and great vessels (see figure 2.12(c)). Especially in abnormalities of the right side, CMR assessment of the right ventricular outflow tract for RV - PV conduit insertion can be applied to define the timing of repair and decide between surgical or percutaneous PV treatment [153].

2.5.4 Echocardiography

Echocardiography is the principal imaging modality to evaluate all cardiovascular disease related to morphological, functional or hemodynamic dysfunctions [91]. Echocardiography is based on ultrasound technology, which uses a transducer loaded with an array or matrix of piezo-electric elements to generate ultrasound pulses, with a frequency between 1-

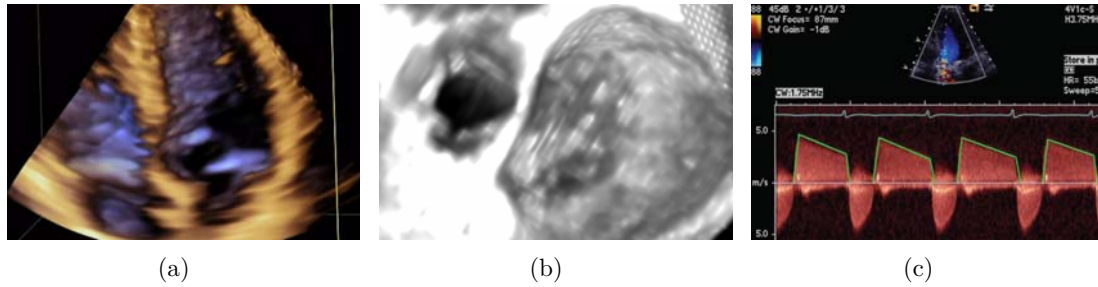


Figure 2.13: (a) TTE four chambers image of the heart. (b) TEE volumetric reconstruction of the mitral and aortic valves. (c) Doppler blood flow quantification.

15MHz. These traverse the human body and produce echoes captured by the device to assemble images. The result is a virtually risk-free, non-invasive imaging modality, which in comparison with other techniques, such as CT or MRI, is cost-effective and widely available in the majority of clinical units.

The downsides of ultrasound are low signal-to-noise ratio due to tissue frequency attenuation, artifacts caused by echo dropouts and speckle noise as well as suboptimal acoustic windows and insufficient depth penetration, which overall lead to limited image quality. Nevertheless, a wide range of techniques were developed to overcome these limitations and enable ultrasound technology not only for diagnosis, but also to guide interventional procedures, such as valve replacement or repair, or apply therapy for example in fragmentation of kidney and gall bladder stones .

Transthoracic Echocardiography In Transthoracic Echocardiography TTE the ultrasound transducer is coupled to the skin surface using a special gel and angulated to obtain images from four standard positions: parasternal, apical, subcostal and suprasternal (see figure 2.13(a)). TTE is the standard diagnostic method for patients with valvular heart disease, as it provides quantitative and qualitative information about the anatomy and function of the valves, as well as the etiology and severity of valvular stenosis and regurgitation [122]. Evaluation usually includes aortic and mitral valve area, LV volume, mass and ejection fraction, aortic root anatomy and right heart structure and function. Recent scanners such as the ACUSON SC2000, Siemens Healthcare, Mountain View, CA, USA, enable a real-time acquisition of up to 80 volumes per second of the full heart.

Transesophageal Echocardiography To obtain images from the proximity of the major cardiovascular structures, a special probe is introduced in the esophagus during Transesophageal Echocardiography TEE exams. TEE provides high-resolution images and is considered essential in a number of cases including studies in presence of prosthetic valves or evaluation of mitral valve and aortic lesions and regurgitant severity (see figure 2.13(b)). Recently introduced real-time 3D scanners enable unique perspective and time-resolved imaging of the valves, which advances visualization and quantification capabilities and improves severity assessment and treatment planning [91].

TEE is routinely used in operating rooms to assess the result of various valvular repair and replacement procedures. As a harmless alternative to fluoroscopy, TEE imaging is applied interventionally in minimal invasive procedures to guide placement and positioning of catheters, needles, and surgical instruments. Recent works investigate real-time cardiac 3D TEE image guidance to facilitate percutaneous cardiac surgical procedures such as transcatheter aortic valve replacement or mitral valve repairs [114, 93].

Doppler and Color Flow Imaging Doppler echocardiography quantifies blood flow velocity based on the shift in frequency of the reflected ultrasound waves, a phenomenon known as the Doppler Effect (see figure 2.13(c)). In color flow imaging, the measured blood velocities are color coded and displayed superimposed to the anatomical echo images. Doppler provides essential measurement in VHD assessment, including regurgitant volumes, valve areas and pressure gradients.

2.5.5 Nuclear Cardiology

Single Photon Emission Computed Tomography (SPECT) and Positron Emission Tomography (PET) scans are the most common nuclear imaging techniques applied in cardiology. Both modalities detect gamma rays emitted by injected radioactive tracers, which accumulate in functional active regions. Although PET offers an increased temporal resolution, both modalities are adequate for tomographic reconstruction and measurements of biological and physiological processes. However, their current spatial resolution does not permit for the evaluation or delineation of discrete anatomical structures. Given the passive nature of the heart valves, nuclear cardiology has no direct application in the context of valvular heart disease.

2.6 Overview of Medical Image Analysis

Over the last five decades, the domain of medical image analysis has rapidly expanded as countless non-invasive imaging methods have become largely available in clinical practice. Significant advancements in medical image acquisition, including image digitalization in the 1970's, adoption of MRI harmless imaging in the 1980's and movement from 2D scans to full 3D imaging in the 1990's have continuously fuelled the research and development of image processing algorithms. Although not in the focus of this thesis, acquisition related methods are a prerequisite and therefore briefly treated in section 2.6.1.

At the same time, a progressive adoption of sophisticated pattern recognition and computer vision techniques since the 1970's, has reshaped the focus of medical imaging analysis from image enhancement, reconstruction or storage problems towards image registration and segmentation tasks. As presented in section 2.6.2, these techniques support advanced quantitative and qualitative analysis essential for numerous clinical applications.

Machine learning in particular is regarded as one of the most promising research directions in medical image analysis. Learning from examples has been proved to be an effective approach in handling the inherent complexity and uncertainty encountered in

most clinical problems. Related methods and applications are briefly reviewed in section 2.6.3.

Section 2.6.4 reflects on future activities focused on the development and integration of computational models into physiological knowledge frameworks that enable prediction and personalization in the medical practice.

2.6.1 Image Reconstruction and Enhancement

To facilitate subsequent visualization and analysis, images are pushed through a processing pipeline immediately after acquisition. In general, images are reconstructed from raw data and enhanced to highlight relevant anatomical structures while the noise is suppressed.

Reconstruction: The image reconstruction process creates multidimensional raw images represented on rectilinear grids from measured signals provided by scanner detectors. Reconstruction can be performed from lower to higher dimensional image representation, as in 3D CT volumes reconstructed from 2D projection images [49], or 3D US volumes reconstructed from a series of 2D oriented slices [133], or vice-versa in the case of non-orthogonal 2D Multi Planar Reconstruction from 3D data sets. For temporal resolved studies the ECG signal is stored during the image acquisition and used to synchronize 2D slices to the cardiac cycle during reconstruction to produce 4D images.

Enhancement: Regardless of the modality, medical images are likely to be affected by noise or other artifacts due to multiple sources of interferences related to physical phenomena or acquisition systems. The traditional field of image acquisition is focused on distortion reduction and sensor development with improved signal-to-noise ratio from a hardware perspective. Image enhancement approaches apply mathematical techniques to improve the quality of raw images for the human observer or subsequent computer processing algorithms, mainly with respect to contrast, sharpness, noise or geometrical transforms. Basic approaches include Gaussian smoothing, histogram manipulation, median filtering and edge enhancement [80]. Advance techniques define hybrid nonlinear and adaptive filters to address noise suppression [12].

2.6.2 Computer Vision in Medical Imaging

Strong synergies between computer vision and medical imaging have significantly impacted the medical image analysis landscape over the past 30 years. Duncan and Ayache [45] divided the accelerated progress in this field into four stages: 2D image analysis era (1980-1984), MRI era (1985-1991), 3D image analysis era (1992-1999) and computing technologies, realistic visualization and procedure guidance for the future. To date major developments were in the areas of image registration and matching, image segmentation and shape modeling, and analysis of structure and motion, discussed in the reminder of this section.

Imager Registration and Matching: The integration of multiple forms of image-based information into a common visualization and analysis framework is referred to as registration. Fusion of structural and functional images often increases diagnosis potential by combining for instance complementary information obtained from radiological and nuclear exams. Surgical planning, radiation therapy and minimally invasive interventions, benefit from registration of pre-, intra- and post-operative imaging data to assist procedure navigation and guidance, as well as therapy assessment. The main challenges are due to structural dissimilarities in images as well as registration in multi-modal acquisition settings.

Various techniques proposed over the years can be classified in intensity vs. feature based, mono vs. multi modal, rigid vs. deformable registration [102, 202]. In early approaches to match 3D multi-modal images of the brain manually segmented cerebral boundaries obtained from CT, MRI and PET were used to compute the transformation [128]. Bookstein [20] proposed the thin-plate-splines to model non-linear deformations of biological and medical images. A further key contribution was the introduction of mutual information approaches for multi-modal registration [186]. Thirion, et al. [156] formulated registration as a diffusion process that directly utilizes superimposed intensities to enabled three-dimensional inter-patient registration of cardiac images.

Segmentation and Tracking: Segmentation algorithms originate in computer vision and are applied in medical image analysis to isolate structures of interest such as various organs, vessels, bones or tumors, from the original image. Tightly related, tracking addresses the extraction of information embedded in temporal sequences of images, especially necessary in cardiac areas. Together these techniques enable a variety of applications, including quantitative and qualitative evaluation of anatomies, lesion monitoring, therapy planning and preprocessing for registration or shape extraction.

Bottom-up approaches, such as thresholding, region growing or clustering, perform the separation based on image intensity without assuming knowledge about the object of interest. Due to the limited image quality and anatomical complexity, higher-level information usually leads to better results when applied to the medical field. Early techniques for cardiac image analysis [44] already incorporate knowledge about the left ventricle wall to segment it from echocardiography images. Shape priors became popular with the introduction of deformable models, which formulate the problem as the optimal deformation of elastic objects subject to internal and external forces [104, 81]. Subsequently, Cootes et al. proposed Active Shape Models (ASM) [36] and Active Appearance Models (AAM) [35] to effectively constrain the object delineation task by modeling domain specific variations from training sets of examples. Another model-based paradigm is given by the level-set formulation in which deformation is represented as a wave propagation subject to constraints [47].

2.6.3 Machine Learning in Medical Imaging

Machine learning plays an essential role in medical image analysis by successfully supporting numerous applications, including computer-aided diagnosis, case retrieval, organ

and lesion segmentation, and image analysis. In typical problems where accurate knowledge is absent and analytical formulation prohibited, algorithms that learn from examples are essential. Another strong argument for learning-based methods is the availability of large databases of medical images in the recent years, as a result of the proliferation of cost-effective non-invasive imaging techniques.

Computer-aided Diagnosis: Computer-aided diagnosis is a classic application, where rule based expert systems are often limited by the availability of formal knowledge to generate diagnostic hypothesis from patient data. For that reason, symbolic learning algorithms are applied to model expert knowledge from clinical cases that act as examples [22]. Neural networks are widely used to handle incomplete and noisy data and improve medical decision making [92]. Decision support system can be as well realized by integrating machine learning algorithms with knowledge provided by ontologies [163]. Furthermore, discriminative learning based distance functions were proposed in [161] for case retrieval and generation of neighborhood graphs for decision support.

Segmentation and Tracking: Image segmentation and tracking of organs or lesions involve the extraction of high dimensional parameters subject to substantial variations, which affects the robustness and efficiency of conventional techniques. Learning algorithms provide an adequate alternative, in which expert knowledge is emulated from sets of examples. In [57] the left ventricle endocardium is segmented from 2D echocardiography images by learning a discriminative classifier that separates target objects and background from expert annotations. The data-based guided paradigm is extended in [197] to automatically segment the four-chambers of the heart from 3D cardiac CT volumes. The use of probabilistic approaches was also demonstrated for the segmentation and measurement of follicles from 3D ultrasound data [31]. In order to perform fast and accurate tracking of the left ventricle from 4D echocardiography data, the algorithm in [191] learns a cardiac motion model using ISOMAP and K-means clustering. This is extended in [191] to automatically quantify the 3D myocardial motion from high frame rate instantaneous ultrasound images using learning-based information fusion.

Analysis and Quantification: Given the large amount of variations in shape and appearance of anatomical structures caused by diverse pathological conditions, image analysis is a tedious task mostly performed manually by expert physicians. Recent developments in machine learning algorithms have the potential to produce a paradigm shift by replacing user dependent processing with automatic quantification algorithms. An automatic tracing of Doppler spectra envelopes was proposed in [125]. By learning from a large database of expert annotated fetal anatomical structures, the algorithm in [28] demonstrated a comprehensive quantification package, which robustly handles appearance variation, speckle noise and signal drop-out specific to ultrasound imaging. In [187] automatic measurement of brain structures from 3D MRI data is performed through a combination of shape detection and shape inference.

The field of machine learning for medical image analysis is rapidly expanding with the abrupt advancement in imaging technology and continuous demand for complex clinical applications. This work fully exploits the advantages of machine learning techniques to extract patient-specific valvular models from multi-modal images. Chapter 4 exclusively addresses this topic, including an overview of discriminative learning algorithms, novel algorithms and corresponding results.

2.6.4 Computation Modeling and Simulation

There is a growing demand for detailed knowledge of physiological processes, which can advance medical practice through effective disease prediction and personalized treatment strategies. A tremendous worldwide scientific effort, including the Physiome Project by the International Union of Physiological Science (IUPS), the Virtual Physiological Human (VPH) by the European Commission (EC), and various related initiatives in the United States, Japan and Korea, is geared towards predictive multi-scale modeling and simulation, which will promote personalized, preventive and predictive healthcare [69].

In the last decade, computational modeling of the human body, and in particular of the cardio-vascular system has attracted increasing amounts of interest [11]. The models developed in [143] integrate anatomical, electrophysiological and biomechanics knowledge to represent the relation between measured kinematics and muscle contractility. Direct Numerical Simulation (DNS) is applied to solve the Navier-Stokes equations, modeling the dynamics of blood flow, in conjunction with deformable solid mechanics equations for viscoelastic non-isotropic deformable materials [136].

The primary objective in the future is the systematic knowledge integration multi-scale computational models into a unified and standardized framework. Personalized computational models, that leverage patient-specific measured data, will eventually enable comprehensive disease evolution and therapy outcome simulations that have the potential to revolutionize the current medical practice.

2.7 Conclusions

The heart is a fascinating pump that supplies the entire organism with oxygen and nutrition through rhythmic contractions. Its essential physiological function is facilitated by four valves located at the center of the cardiac fibrous skeleton. The aortic, mitral, tricuspid and pulmonary valve regulate the blood hemodynamics by enforcing unidirectional flow within the heart and towards the entire cardiovascular system. Valves guard the inlet and outlet of ventricles, and form a complex anatomical apparatus composed out of two to three leaflets and a supporting annulus. Their synchronized opening and closing activity during the cardiac cycle can be affected by two major dysfunctions: stenosis and regurgitation. Multiple etiologies can provoke valves to leak or block blood transfer inducing major physiological consequences and eventually heart failure and sudden death. No medication can cure or prevent the progression of valvular heart disease leaving the invasive repair or replacement procedures as the only treatment alternative. Despite continuous

advancements, surgical or interventional valve therapy remains the most expensive and riskiest among all cardiovascular operations.

To maximize the therapeutical outcome, modern medicine has heavily adopted medical imaging techniques to support the entire clinical management including assessment, planning and therapy guidance. Today, echocardiography followed by computed tomography and magnet resonance imaging are routinely employed to diagnose and evaluate the severity of valvular heart disease, and fluoroscopy is used to guide emerging percutaneous procedures. Nevertheless, the extraction of morphological and functional quantities, critical for clinical decision making, is often based on imperfect data and achieved using manual and potentially inaccurate methods leading to suboptimal results. The domain of medical imaging analysis has rapidly expanded over the last decades to provide solutions that effectively process raw medical images into relevant clinical information. The progressive adoption of pattern recognition and computer vision techniques, including image registration, segmentation and analysis, facilitates nowadays advanced clinical applications. Machine learning algorithms proved to be indispensable in dealing with the inherent complexity and uncertainty which characterizes the clinical environment. In this context, this thesis offers a novel modeling and analysis paradigm, which can potentially consolidate medical knowledge about the valvular apparatus and substantially benefit the entire clinical management of valvular heart disease patients.

The future challenges are focused on developing effective computational models and systematic integration into comprehensive physiological frameworks that permit preventive, predictive and personalized medicine.

Physiological Modeling and Parametrization

The term "Physiological Model" is defined by the neuroscience lexicon as "a mathematical description of the complex physical and temporal dependencies between a set of related biological entities and their immediate environment". Among the many fundamental perspectives and scales that characterize physiological systems, this dissertation addresses the modeling of morphological and functional aspects at the organ level. In particular the mathematical description of the heart valve geometry and dynamics is presented.

This chapter introduces our novel physiological model of the aortic, mitral, tricuspid and pulmonary valves, capturing complex morphological, dynamical and pathological variations. Following a condensed overview of existent cardiac models in section 3.1, and a brief overview on the proposed valvular model in section 3.2, we address two essential topics: the physiological modeling of individual valvular systems and the patient-population models of valvular parameters.

Section 3.3, 3.4, 3.5 and 3.6 present the proposed model and its different abstraction levels centered on the following objectives: accurate representation of morphology and dynamics, hierarchical description with incremental complexity, and spatio-temporal consistency through physiological constraints.

Section 3.7 describes statistical models of patient population with respect to relevant valvular parameters. Based on expert knowledge, these provide a compact representation for distributions of individuals to synthesize and explain the plausibility of domain instances.

3.1 Models of Cardiac Structures

This section presents an overview of existent cardiac models reported in the literature. Section 3.1.1 focuses on heart chambers models and other related cardiac structures, while section 3.1.2 reviews models of the heart valves.

3.1.1 Chamber and Related Models

Except for the past decade, cardiac modeling was almost exclusively focused on the left ventricle (LV), initially characterized by simplified ellipsoidal representation used in functional analysis [43]. However, as presented in the comprehensive review by Frangi *et al.* [51], the field rapidly developed to include various modeling approaches, which can be categorized in surface, volumetric and deformation models, parameterized by continuous, discrete or implicitly defined representations.

Based on the superquadrics representation [63] and subsequent extension to incorporate longitudinal and radial contraction, Metaxas and Axel [124] proposed a detailed model of the LV applied to motion analysis from tagged MRI images. Duncan *et al.* [149] introduced a LV model parameterized by sinusoidal basis functions, in which the smoothness of the geometries is controlled by the number of orthogonal harmonics in the Fourier expansion. Recently, a subject-specific dynamical model based on Multi-linear Principal Component Analysis (PCA) [201] was proposed, to simultaneously model variations in left ventricular shape and motion patterns using real-time three-dimensional echocardiography. Rueckert and Burger [135], achieved a combined model of the two ventricles, LV and RV, using geometrical deformable templates.

To enable clinical usage beyond the LV, the latest cardiac models evolved to include all ventricles, atria and elements of the great vessels. The model proposed by Lorenz and von Berg [99] comprises all four chambers, trunks of the connected vasculature, coronary arteries and cardiac landmarks. A total number of 20 different surface meshes are combined to construct the heart model from multi-slice computed tomography data. Zheng *et al.* [197] introduced a cardiac representation constructed from multiple model components, which considers the valve annuli, as well as the four chambers.

In a complementary research direction, geometrical information is enriched through physical components, including biomechanics, electrophysiology and hemodynamics, to construct computational cardiac models capable to predict physiological functions. To study the effect of electrical heterogeneity on myocardial mechanics, Nickerson *et al.* [116] used a strongly coupled electromechanical model mapped on a simplified LV geometry. Using a more realistic geometrical representation, Sermesant *et al.* [142, 143] built a volumetric biomechanical model of the two cardiac ventricles, which represents the myocardial contraction using by an electromechanical coupled constitutive law. The resulting deformable model is applied to extract functional parameters from SPECT volumetric sequences. The model is further personalized in [144] with measurements from CMR images and electrical parameters reported in the literature. A hemodynamic model of the LV applied for surgical ventricular reconstruction is proposed in [40]. The discrete geometrical and dynamical information of the four chambers, aorta, venae cavae and pulmonary artery are obtained from CMR acquisitions, and applied as boundary conditions for estimation of the blood flow dynamics.

Despite continuous progress, none of the previously discussed methods include an explicit model of the heart valves. If at all addressed, their geometric appearance and dynamic behavior are approximated through planar structures or other geometrical primitives.

3.1.2 Valve Models

When compared to the extraction of chambers and vessels from medical images, heart valve modeling is rather an uncharted territory. The majority of existent models presented in the literature are generic and rough approximations of the true valvular anatomy. Their primary application is the analysis of the blood-tissue interaction during the cardiac cycle as well as mechanical and functional behavior of the valvular apparatus.

The first cardiac model to include the heart valves was proposed by McQueen and Peskin [129]. Their approach is based on the anatomical and mechanical properties of heart muscle fibers used to solve the fiber-fluid problem of cardiac dynamics applying the immersed boundary method. Although geometrically simplified, the simulated blood flow pattern and myocardial motion correctly demonstrated the opening and closing motion of the valves.

De Hart *et al.* [39] introduced a refined computational model of the aortic valve, which assumes more realistic geometry and material properties based on dimensions reported in the literature. The fully coupled fluid-structure interaction is solved using Lagrange multipliers to represent the no-slip condition along the domain interface. Recently, Conti *et al.* [34] presented a realistic finite element model of the physiological aortic root from medical imaging data. The geometrical information of the root is adjusted based on quantitative observations from CMR images and combined with non-linear and anisotropic leaflet models. The results show the effect of root sinus dimensions on stress and strain patterns, which is notably higher in smaller anatomies.

Kunzelman *et al.* [86] introduced the first three-dimensional finite element model of the mitral valve, recently extended to include fluid flow. Normal and pathological function was assessed using the fluid-structure interaction model, with computed stress and strain properties in agreement with reported in vivo and in vitro measurements. Votta *et al.* [182] presented an extended mitral valve model based on in vivo data. The structural representation includes the major valvular components and real geometrical and dynamic information for the annuli and papillary muscles, reconstructed from four-dimensional ultrasound data. Experiments yield qualitatively correct mitral closure and measurements of annulus dynamics.

Black *et al.* [15] constructed a three-dimensional finite element model of a bicuspid bioprosthesis heart valve in order to study stress patterns of the leaflets. The geometry of the model is based on measurements from a real valve, which helped to conclude that the bending stress in the leaflets makes a significant contribution to their functional deformation. Motivated by the disappointing long-term performance of bioprosthesis valves, Kruncinski *et al.* [85] investigate design alternatives in order to reduce the risk of leaflets tearing at the points of their attachment. A finite element model demonstrated the effect of the aortic root expansion on the leaflet stress, during systole. A reduction of 40% in commissural stress was measured in bio-prosthetic valves mounted on expansible stents with respect to rigid stents. Following the same direction, Cacciola *et al.* [25] studied the leaflet stress for stentless prostheses with flexible leaflet attachment and aortic base. The geometry of their finite element model is based on a three-leaflet prototype. The leaflets have a uniform thickness of 0.2mm and show a cylindrical shape with a diameter of 22mm in the open position. The diameter of the basal ring and the sinutubular junction are

assumed to be equal to 24mm, while the distance between them is set to 16mm. The finite element analysis of the stress distribution shows a 75% reduction for the stentless models with respect to stented valves with the same type of reinforcement.

Watanabe *et al.* [184] introduced a geometrical model of the mitral valve, obtained from real-time three-dimensional TTE, to quantify mitral valve tenting in ischemic patients. By manually delineating the mitral annulus and leaflets in 18 radial planes from the mid-systole, they could demonstrate the deformity of the valve in ischemic regurgitation with the maximum tenting located in the anterior leaflet. The study by Veronesi and colleagues [173] also considers the aortic valve to investigate the functional dependency between the two left-side valves. A model of the aortic and mitral valve annuli is detected and tracked from TEE images to allow automated measurements of changes in aortic and mitral valve morphology. In conclusion, reciprocal changes in shape and position were observed, which underline the importance of joint evaluation and clinical management. Based on CMR data, Schievano *et al.* [140] proposed an analysis protocol of the pulmonary trunk based on rapid prototyping systems. The geometrical model is manually constructed and subsequently applied for qualitative patient selection for percutaneous pulmonary valve implantation.

The central conclusion drawn from the above presented literature review is that the majority of existing approaches focus on the construction of generic valve models, with high vertical complexity, primarily designed to reproduce and explain various physiological processes. To accommodate physical complexity, these models compromise on accurate anatomical information, are not patient-specific, and therefore of limited importance for the clinical practice.

Recent advances in medical equipment stimulated a new research direction that aims to extract precise patient-specific information from cardiac images. Despite the high clinical relevance, current methods are restricted to simplified representations of the aortic-mitral annuli and manual delineation of static mitral anatomies. In the remainder of this chapter we present our novel comprehensive model of the entire valvular apparatus, designed to accurately represent complex morphological, dynamical and pathological variations from non-invasive four-dimensional data.

3.2 Hierarchical Valvular Model

Technological innovations in cardiac imaging techniques have enabled acquisitions of 4D physiological data with continuously increasing spatial and temporal resolutions. Consequently, there has been a proportionally increasing demand for effective methods to process the large amount of data into clinically relevant information. The extraction of anatomical and functional parameters in the form of spatio-temporal geometrical models is invaluable for quantitative and qualitative cardiac analysis, and has generated significant scientific interest over the past four decades.

As far as the heart valves are concerned, there is still no consensus in the medical and clinical field on the best way to describe their anatomy. Valvular structures are complex and vary significantly in appearance across individuals and pathological conditions. Until

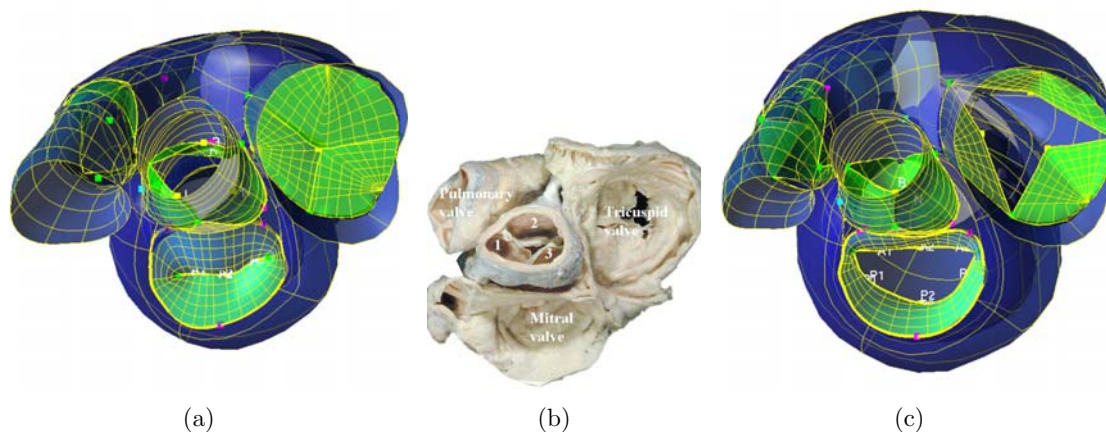


Figure 3.1: The proposed valvular model (including the ventricles from [197]) in systole (a) and diastole (c). (b) Explanted specimen of the heart valves - Reproduced with permission of the author and the European Association for Cardio-Thoracic Surgery from: Anderson RH. The surgical anatomy of the aortic root. Multimedia Man Cardiothorac Surg doi:10.1510/mmcts.2006.002527.

recently, non-invasive imaging of the heart valves was not practicable, and most data was obtained from animal studies or explanted specimens. Thus, none of the cardiac models described in the literature offers a comprehensive and physiologically accurate characterization of the valvular apparatus.

The scope of this chapter is to provide an explicit mathematical representation of the cardiac valves that parameterizes relevant clinical aspects observable through non-invasive imaging modalities. We proposed a novel physiological model of the aortic, mitral, tricuspid and pulmonary valve to precisely capture morphological, dynamical and pathological variations (see figure 3.1). To handle the inherent complexity, the representation is structured on three abstraction layers: global location and rigid motion, non-rigid landmark motion model, and comprehensive valvular model. Each model abstraction naturally links to anatomical and dynamical aspects at a specific level of detail, while the hierarchical interconnection of the individual parameterizations is driven by the physiology of the valves.

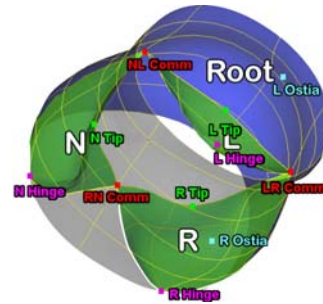
At first in section 3.3 we introduce a parameterization of the global location and rigid motion of individual valves. This explains the translation, rotation and scale of a specific valve as well as its temporal variation throughout the cardiac cycle with respect to a given cardiac image sequence. Section 3.4 extends the model through a parameterization of anatomical landmarks, which describe the rough valvular structure and motion. Besides the well-defined anatomical meaning, the chosen landmarks serve as anchor points for qualitative and quantitative clinical assessment, are robustly identifiable by doctors, and possess a particular visual pattern. The proposed model is concluded in section 3.5 with the complete four-dimensional representation of the valvular geometries and deformations. In the following we summarize the advantages of our method:

- **Hierarchical** - to handle the geometrical and dynamical complexity, the parameterization is defined hierarchically based on the natural level of detail of the underlying anatomies.
- **Complete** - the novel model includes all four cardiac valves and the associated comprehensive representations of their geometrical and dynamical variation.
- **Consistent** - anatomically-driven constraints and point-correspondence across time and individuals ensure a physiologically compliant and consistent parameterization.
- **Modular** - anatomical entities are loosely coupled to facilitate model extensions and individual integration of observations from various image modalities

Sections 3.2.1, 3.2.2, 3.2.3, and 3.2.4 briefly introduce the proposed model for the individual valves, while detailed description on parameterization and anatomical definition of each abstraction level is provided later in this chapter.

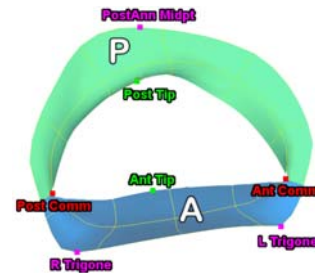
3.2.1 Aortic Valve

The aortic valve model consists of the aortic root and the attached L-Leaflet, R-Leaflet, and N-Leaflet, illustrated as the blue and green surfaces, respectively. The model also includes 11 landmarks, which denote key anatomical locations: 3 commissures - LR-Comm, NL-Comm, and RN-Comm, 3 hinges - L-Hinge, R-Hinge, and N-Hinge, 3 leaflet tips - L-Tip, R-Tip, and N-Tip, and 2 ostia - L-Ostium and R-Ostium.



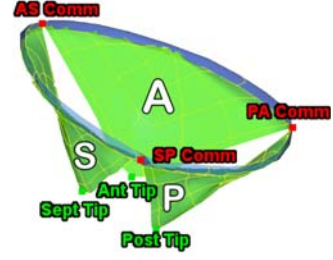
3.2.2 Mitral Valve

The mitral valve includes two leaflets attached to the mitral annulus: the posterior leaflet depicted in green and the anterior leaflet in blue. The considered anatomical landmarks are: 2 trigones - L-Trigone and R-Trigone, the posteroannular midpoint, 2 commissures - Post-Comm and Ant-Comm, and 2 leaflet tips - P-Tip and A-Tip.



3.2.3 Tricuspid Valve

The tricuspid valve comprises of three leaflets attached to the tricuspid annulus: A - anterior leaflet, P - posterior leaflet, and S - septal leaflet. Additionally, there are 6 tricuspid anatomical landmarks: 3 commissures - PA-Comm, SP-Comm, and AS-Comm, and 3 leaflet tips - S-Tip, P-Tip, and A-Tip.



3.2.4 Pulmonary Valve

The pulmonary valve is identically configured as the aortic valve and consists of the pulmonary trunk illustrated in blue, and the three leaflets in green. The model includes 12 landmarks: 3 commissures - LR-Comm, NL-Comm, and RN-Comm, 3 hinges - L-Hinge, R-Hinge, and N-Hinge, 3 leaflet tips - L-Tip, R-Tip, and N-Tip, the trigone, the bifurcation, and the RVOT landmark.



3.3 Global Location and Rigid Motion

In section 3.3.1 we present a parameterization of the global location and rigid motion of each valve. These explains the translation, rotation and scale along with temporal variation throughout the cardiac cycle. Section 3.3.2 presents the anatomical definition of the parameters for each individual valve.

3.3.1 Parameterization

The global location of the valves is parameterized through a similarity transformation in the Euclidean three-dimensional space, which includes nine parameters. A time variable t is augmenting the representation to capture the temporal variation during the cardiac cycle and model the rigid valve motion:

$$\theta(t)_i = \{(c_x, c_y, c_z)_i, (\vec{\alpha}_x, \vec{\alpha}_y, \vec{\alpha}_z)_i, (s_x, s_y, s_z)_i, t\}, i \in \{aortic, mitral, tricuspid, pulmonary\} \quad (3.1)$$

where (c_x, c_y, c_z) , $(\vec{\alpha}_x, \vec{\alpha}_y, \vec{\alpha}_z)$, (s_x, s_y, s_z) are the position, orientation and scale parameters. These define a bounding box around the corresponding anatomy as illustrated in figure 3.2, 3.3, 3.4 and 3.5. The location and rigid motion of each valve is modeled independently through its individual set of parameters $\theta(t)$, which results into a total of $36 \times T$ parameters for a given volume sequence $I(t)$ of length T .

3.3.2 Anatomical Definition

This section describes the anatomically-driven definition of the similarity parameters θ for all four valves. For a comprehensive anatomical description of the valvular apparatus the reader is referred to section 2.2.

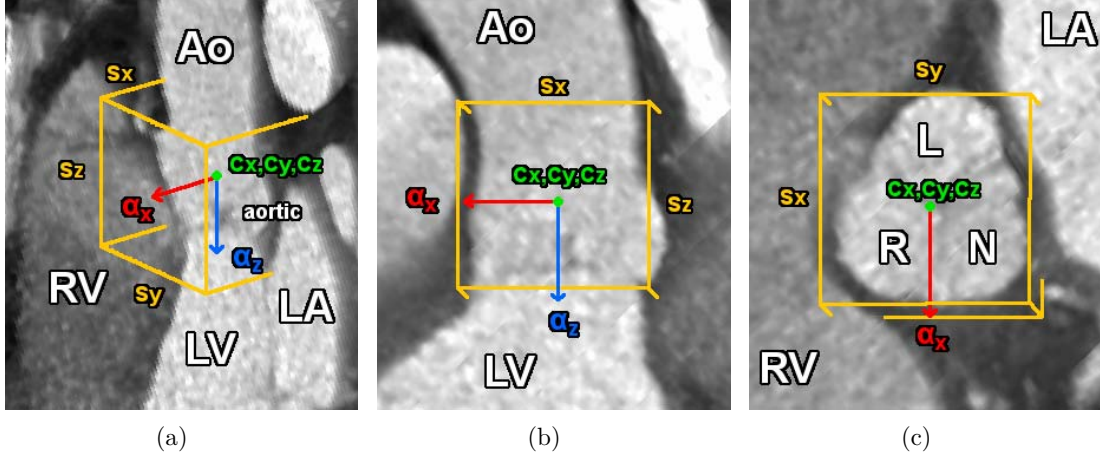


Figure 3.2: Similarity transform represented as a bounding box around the aortic valve from cardiac CT. (a) Perspective view; (b) Long Axis; (c) Short Axis.

Aortic Valve: The aortic valve AV connects the left ventricular outflow tract to the ascending aorta and includes the aortic root and three leaflets/cusps (left (L) aortic leaflet, right (R) aortic leaflet and none (N) aortic leaflet). The root extends from the basal ring to the sinotubular junction and builds the supporting structure for the leaflets. These are fixed to the root on a crown-like attachment and can be thought of as semi-lunar pockets. The position parameter $(c_x, c_y, c_z)_{aortic}$ is given by the valve's barycenter, while the corresponding scale $(s_x, s_y, s_z)_{aortic}$ is chosen to comprise the entire underlying anatomy (see figure 3.2(a)). The long axis $\vec{\alpha}_z$ is defined by the normal vectors to the aortic commissural plane, which is the main axis of the aortic root (see figure 3.2(b)). The short axis $\vec{\alpha}_x$ is given by the normalized vector pointing from the barycenter $(c_x, c_y, c_z)_{aortic}$ to the interconnection point of the left and right leaflets, the none/right-commissure point (see figure 3.2(c)). The $\vec{\alpha}_y$ direction is constructed from the cross-product of $\vec{\alpha}_x$ and $\vec{\alpha}_z$.

Mitral Valve: Located in between the LA and the LV, the mitral valve MV includes the posterior leaflet, anterior leaflet, annulus and the subvalvular apparatus. The latter consists of the chordae tendineae and papillary muscles, which are not explicitly treated in this work. Hence, we compute the barycentric position $(c_x, c_y, c_z)_{mitral}$ and scale parameters $(s_x, s_y, s_z)_{mitral}$ from the mitral leaflets (see figure 3.3(a)). $\vec{\alpha}_z$ is described by the normal vector to the mitral annulus (see figure 3.3(b)), while $\vec{\alpha}_x$ points from the barycenter $(c_x, c_y, c_z)_{mitral}$ toward the postero-annular midpoint (see figure 3.3(c)).

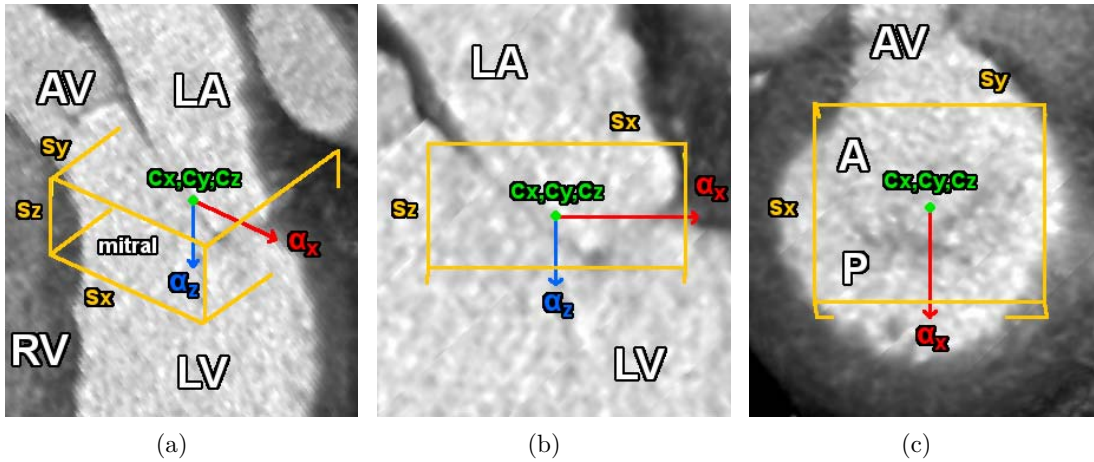


Figure 3.3: Similarity transform represented as a bounding box around the mitral valve from cardiac CT. (a) Perspective view; (b) Long Axis; (c) Short Axis.

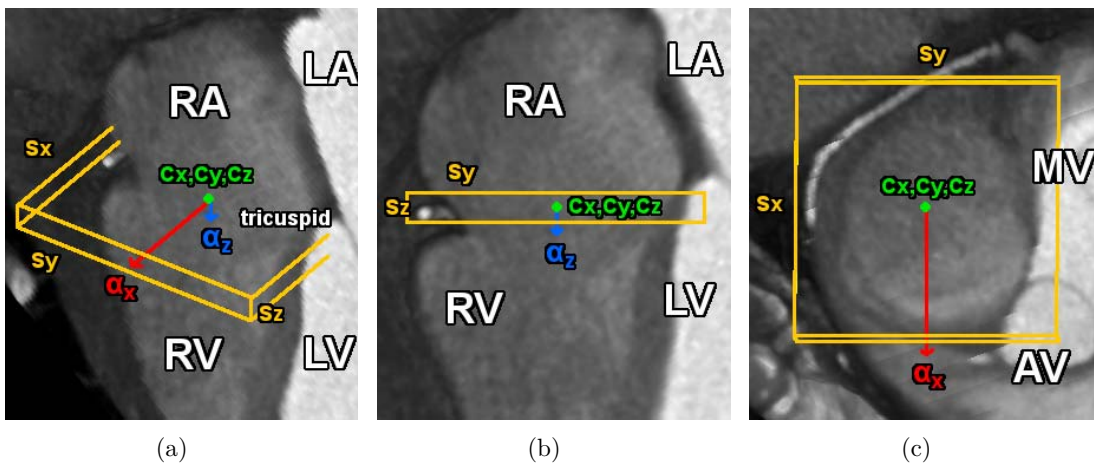


Figure 3.4: Similarity transform represented as a bounding box around the tricuspid valve from cardiac CT. (a) Perspective view; (b) Long Axis; (c) Short Axis.

Tricuspid Valve: The tricuspid valve TV, also called the right atrioventricular valve, separates the RA from the RV. It mainly consists of the annulus and subvalvular apparatus as well as three leaflets: septal, inferior and anterosuperior leaflet. As for the mitral, the position $(c_x, c_y, c_z)_{tricuspid}$ and scale $(s_x, s_y, s_z)_{tricuspid}$ parameters are defined from the three leaflets (see figure 3.4(a)). $\vec{\alpha}_z$ is perpendicular to the annular plane (see figure 3.4(b)), while $\vec{\alpha}_x$ points towards the interconnection of the septal-anterosuperior leaflets (see figure 3.4(c)).

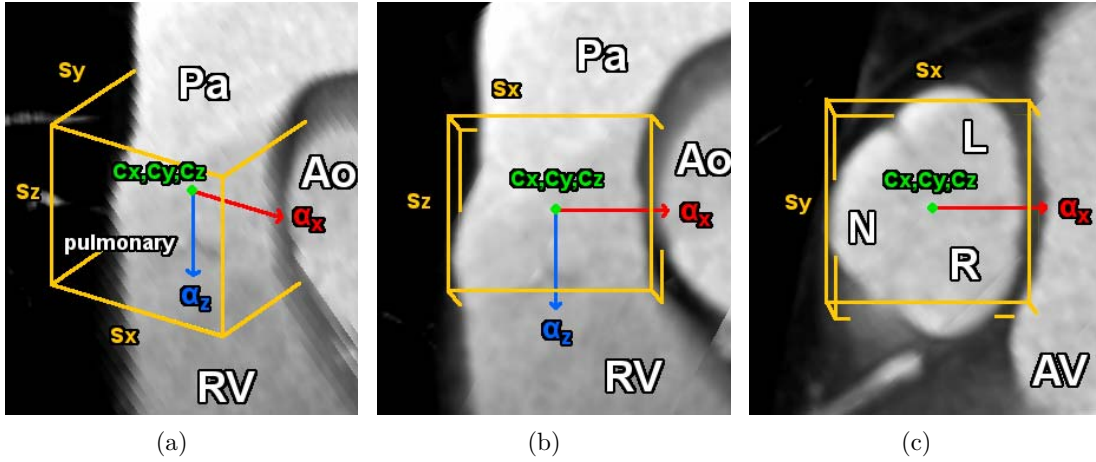


Figure 3.5: Similarity transform represented as a bounding box around the pulmonary valve from cardiac CT. (a) Perspective view; (b) Long Axis; (c) Short Axis.

Pulmonary Valve: The pulmonary trunk emerges out of the RV and branches into the left and right pulmonary arteries, which connect to the corresponding lung. It supports a semilunar valve, geometrically and topologically similar to the aortic valve. The three leaflets of the pulmonary valve PV are named according to their relationship with respect to the AV as left and right facing leaflet, and none facing leaflet. The position parameter $(c_x, c_y, c_z)_{pulmonary}$ is given by the valve's barycenter, while the corresponding scale $(s_x, s_y, s_z)_{pulmonary}$ comprises the pulmonary valve anatomy (see figure 3.5(a)). The long axis \vec{a}_z is perpendicular to the commissural plane, while the short axis \vec{a}_x points towards the interconnection of the left and right leaflets, the left/right-commissure point (see figure 3.5(b)). The \vec{a}_y direction is constructed from the cross-product of \vec{a}_x and \vec{a}_z (see figure 3.5(c)).

3.4 Non-Rigid Landmark Motion Model

The definition of the valvular global position and motion from given images was introduced in the previous section 3.3. This section extends the model by a parameterization of the complex and synchronized opening-closing movements of the valves through an anatomical landmark representation.

3.4.1 Parameterization

In this section, a model consisting of anatomically-defined landmarks, normalized by the time-dependent similarity transformation, is introduced. The chosen landmarks serve as anchor points for qualitative and quantitative clinical assessment, are robustly identifiable by doctors, and possess a particular visual pattern. The motion of each anatomical landmark j can be parameterized by its corresponding trajectory \vec{L}^j over a full cardiac cycle.

For a given volume sequence $I(t)$, one trajectory \vec{L}^j is composed by the concatenation of the spatial coordinates:

$$\vec{L}^j(\theta_i) = [\vec{L}^j(0), \vec{L}^j(1), \dots, \vec{L}^j(t), \dots, \vec{L}^j(T-1)], \quad j = 0, \dots, 35 \quad (3.2)$$

where \vec{L}^j are spatial coordinates with $\vec{L}^j(t) \in \mathbb{R}^3$ and t an equidistant discrete time variable $t = 0, \dots, T-1$. The total number of 36 landmarks includes 11 aortic, 7 mitral, 6 tricuspid and 12 pulmonary landmarks.

3.4.2 Anatomical Definition

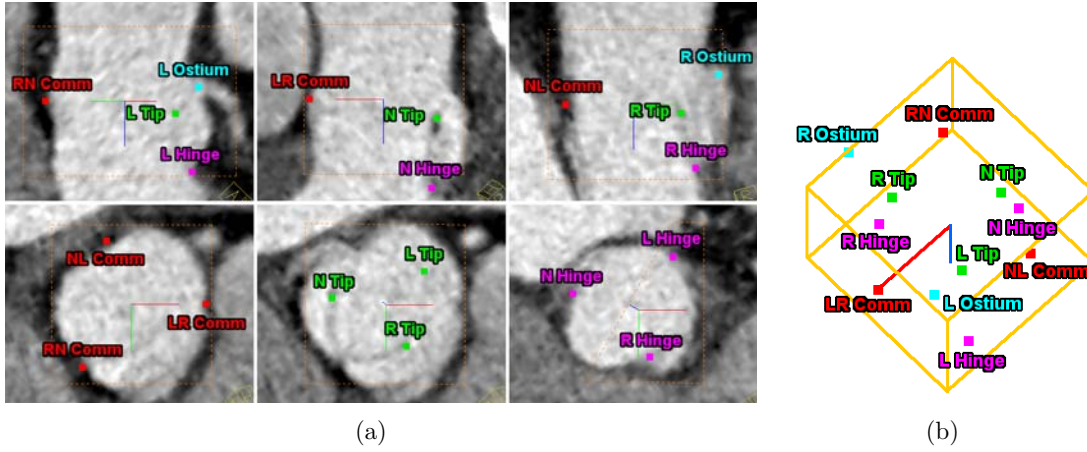


Figure 3.6: Anatomical landmark model of the aortic valve. (a) Landmarks relative to the anatomical location illustrated in long and short axis from an example CT study. (b) Perspective view including the bounding box.

Aortic Valve: Three aortic commissure points, LR-Comm, NL-Comm and RN-Comm, describe the interconnection locations of the aortic leaflets, while three hinges, L-Hinge, R-Hinge, and N-Hinge, are their lowest attachment points to the root. For each leaflet of the valve, the center of the corresponding free-edge is marked by the leaflet tip point: L/R/N-Tip. Finally, the interface between the aorta and coronary arteries is symbolized using the L/R-Ostium, the two coronary ostia (see figure 3.6(a)).

The anatomical landmarks are also used to describe the global location and rigid motion, defined in section 3.3, as follows (see figure 3.6(b)): $(c_x, c_y, c_z)_{aortic}$ equals to the gravity center of the aortic landmarks, except aortic leaflet tips. $\vec{\alpha}_z$ is the normal vector to the LR-Comm, NL-Comm, RN-Comm plane, $\vec{\alpha}_x$ is the unit vector orthogonal to $\vec{\alpha}_z$ which points from $(c_x, c_y, c_z)_{aortic}$ to LR-Comm, $\vec{\alpha}_y$ is the cross-product of $\vec{\alpha}_x$ and $\vec{\alpha}_z$. $(s_x, s_y, s_z)_{aortic}$ is given by the maximal distance between the center $(c_x, c_y, c_z)_{aortic}$ and the aortic landmarks, along each of the axes $(\vec{\alpha}_x, \vec{\alpha}_y, \vec{\alpha}_z)$.

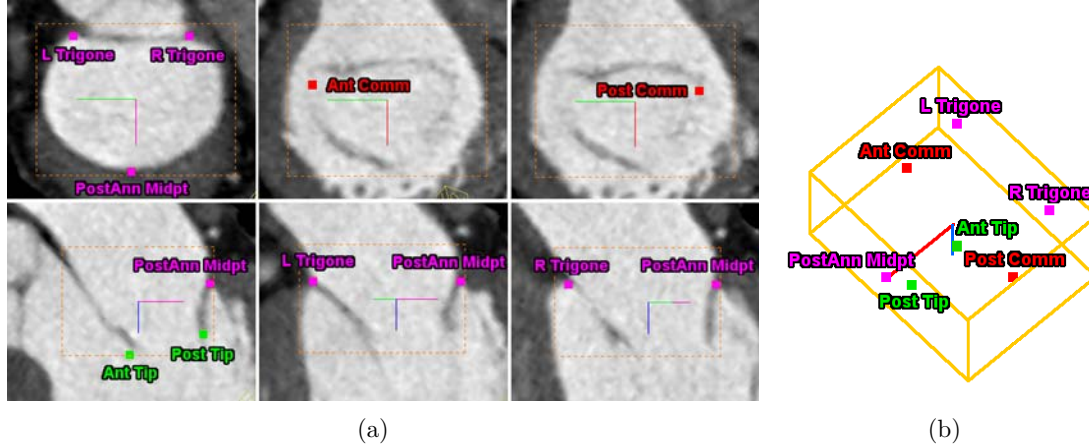


Figure 3.7: Anatomical landmark model of the mitral valve. (a) Landmarks relative to the anatomical location illustrated in long and short axis from an example CT study. (b) Perspective view including the bounding box.

Mitral Valve: The two interconnection points of the mitral leaflets at their free edges are defined by the mitral Ant/Post-Comm, while the mitral annulus is fixed by the L/R-Trigone and posteroannular midpoint (PostAnn MidPoint). The center of the two mitral leaflets' free-edge is marked by the leaflet point, the Ant and Post-Tip (anterior/posterior) leaflet tips (see figure 3.7(a))

The barycentric position $(c_x, c_y, c_z)_{mitral}$ is computed from the mitral landmarks, except mitral leaflet tips (see figure 3.7(b)). $\vec{\alpha}_z$ is the normal vector to the L/R-Trigone, PostAnn MidPoint plane, $\vec{\alpha}_x$ is orthogonal to $\vec{\alpha}_z$ and points from $(c_x, c_y, c_z)_{mitral}$ towards the PostAnn MidPoint. The scale parameters $(s_x, s_y, s_z)_{mitral}$ are defined as for the aortic valve, to comprise the entire mitral anatomy.

Tricuspid Valve: The three leaflets of the tricuspid valve, septal-, anterior- and posterior leaflet interconnect in three points marked by the AS Comm, PA Comm and SP Comm landmarks. The tricuspid landmark model is completed by the Sept Tip, Ant Tip and Post Tip landmarks, which mark the center of the leaflets' free edge (see figure 3.8(a)).

The barycentric position $(c_x, c_y, c_z)_{tricuspid}$ is computed from the tricuspid commissures, AS Comm, PA Comm and SP Comm (see figure 3.8(b)). $\vec{\alpha}_z$ is the normal vector to the commissural plane, $\vec{\alpha}_x$ is orthogonal to $\vec{\alpha}_z$ and points towards the AS Comm. The scale parameters $(s_x, s_y, s_z)_{tricuspid}$ are defined to comprise the entire tricuspid valve anatomy.

Pulmonary Valve: Identical as for the aortic valve, three commissure points, LR-Comm, NL-Comm and RN-Comm, describe the interconnection locations of the pulmonary leaflets, while three hinges, L-Hinge, R-Hinge, and N-Hinge, are their lowest attachment points to the pulmonary trunk. For each leaflet of the valve, the center of the corresponding free-edge is marked by the leaflet tip point: L/R/N-Tip. The pulmonary

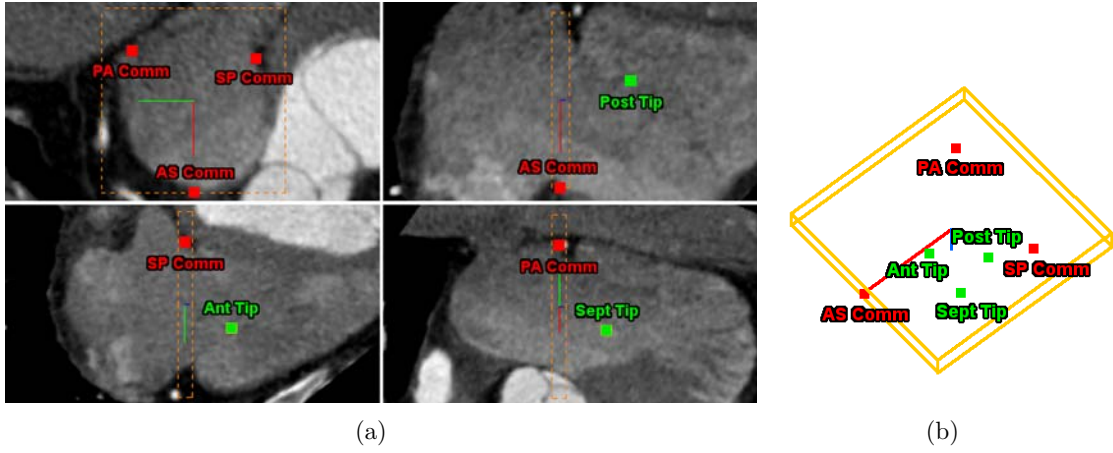


Figure 3.8: Anatomical landmark model of the tricuspid valve. (a) Landmarks relative to the anatomical location illustrated in long and short axis from an example CT study. (b) Perspective view including the bounding box.

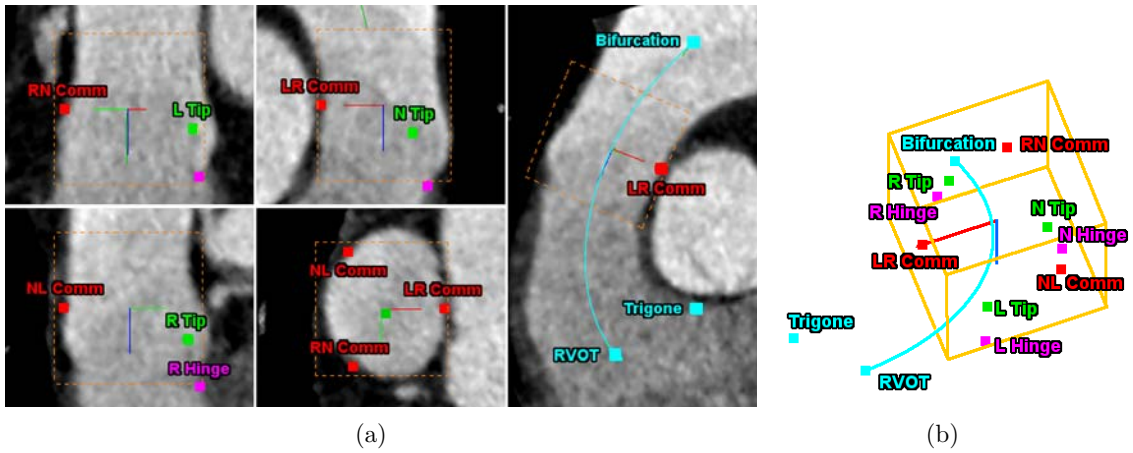


Figure 3.9: Anatomical landmark model of the pulmonary valve. (a) Landmarks relative to the anatomical location illustrated in long and short axis from an example CT study. (b) Perspective view including the bounding box.

trunk is bounded by two landmarks, the RVOT on the right ventricle sides and Bifurcation distal to the valve location. The model is completed by right ventricle Trigone landmark (see figure 3.9(a)).

The location $(c_x, c_y, c_z)_{pulmonary}$ equals to the gravity center of the commissures and hinges landmarks (see figure 3.9(b)). $\vec{\alpha}_z$ is the normal vector to the LR-Comm, NL-Comm, RN-Comm plane, $\vec{\alpha}_x$ is the unit vector orthogonal to $\vec{\alpha}_z$ which points from $(c_x, c_y, c_z)_{aortic}$ to LR-Comm, $\vec{\alpha}_y$ is the cross-product of $\vec{\alpha}_x$ and $\vec{\alpha}_z$. $(s_x, s_y, s_z)_{aortic}$ is given by the maximal distance between the center $(c_x, c_y, c_z)_{aortic}$ and the aortic landmarks, along each of the

axes $(\vec{\alpha}_x, \vec{\alpha}_y, \vec{\alpha}_z)$.

3.5 Comprehensive Valvular Model

The most complex abstraction level presented in the following section completes the models in section 3.3 and section 3.4 with the parameterization of valve surfaces and their temporal variation.

3.5.1 Parameterization

The full geometry of the valves is modeled using surface meshes constructed along rectangular grids of vertices. For each anatomic structure A_k , the underlying grid is spanned along two physiologically aligned parametric directions, \vec{u} and \vec{v} . Each vertex $\vec{p}^{A_k} \in \mathbb{R}^3$ has four neighbors, except the edge and corner points with three and two neighbors, respectively. Therefore, a rectangular grid with $n \times m$ vertices is represented by $(n - 1) \times (m - 1) \times 2$ triangular faces. The model M_i of a certain valve i at a particular time step t is uniquely defined by vertex collections of the anatomic structures A_k . The time parameter t extends the representation to capture valve dynamics:

$$M_i(\vec{L}^j, \theta_i) = \left[\overbrace{\{\vec{p}_0^{A_1}, \dots, \vec{p}_{N_1}^{A_1}\}_i}^{\text{first anatomy}}, \dots, \overbrace{\{\vec{p}_0^{A_n}, \dots, \vec{p}_{N_n}^{A_n}\}_i}^{\text{n-th anatomy}}, t \right], i \in \{\text{aortic, mitral, tricuspid, pulmonary}\} \quad (3.3)$$

where n is the number of represented anatomies equal to 4, 2, 3 and 4 for the aortic, mitral, tricuspid and pulmonary valve, respectively. $N_1 \dots N_n$ are the numbers of vertices for a particular anatomy given in the following section.

3.5.2 Anatomical Definition

Aortic Valve: Four surface structures represent the aortic valve: aortic root, left coronary leaflet, right coronary leaflet and non coronary leaflet. The aortic root connects the ascending aorta to the left ventricle outflow tract and is represented through a tubular grid (see figure 3.10(a)). This is aligned with the aortic circumferential u and ascending directions v and includes 36×20 vertices and 1368 faces. The root is constrained by six anatomical landmarks, i.e. three commissures and three hinges, with a fixed correspondence on the grid. The three aortic leaflets, the L-, R- and N-leaflet, are modeled as paraboloids on a grid of 11×7 vertices and 120 faces (see figure 3.10(b)). They are stitched to the root on a crown like attachment ring, which defines the parametric u direction at the borders. The vertex correspondence between the root and leaflets along the merging curve is symmetric and kept fixed. The leaflets are constrained by the corresponding hinges, commissures and tip landmarks, where the v direction is the ascending vector from the hinge to the tip (see figure 3.10(c)).

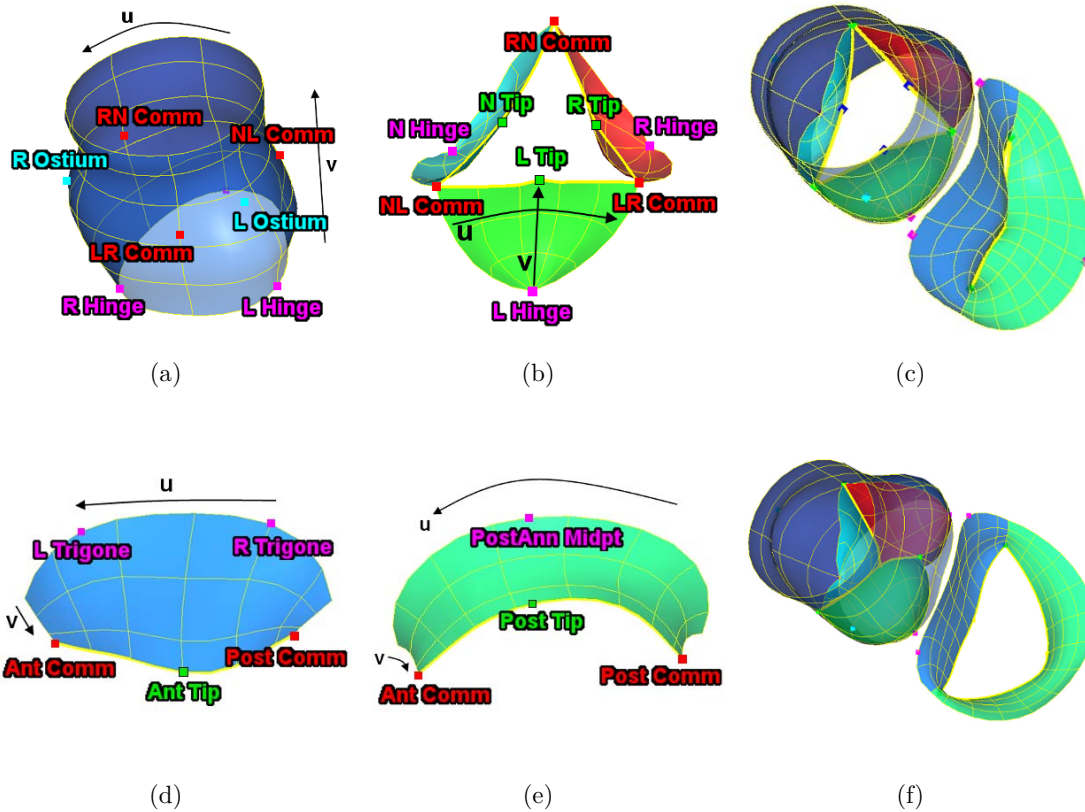


Figure 3.10: Isolated surface components of the aortic and mitral models with parametric directions and spatial relations to anatomical landmarks: (a) aortic root, (b) aortic leaflets, (c) aortic-mitral in end-systole, (d) anterior mitral leaflet, (e) posterior mitral leaflet and (f) aortic-mitral in end-diastole.

Mitral Valve: The mitral leaflets separate the LA and LV hemodynamically and are connected to the endocardial wall by the saddle shaped mitral annulus. Both are modeled as paraboloids and their upper margins implicitly define the annulus. Their grids are aligned with the circumferential annulus direction u and the orthogonal direction v pointing from the annulus towards leaflet tips and commissures (see figures 3.10(d) and 3.10(e)). The anterior leaflet is constructed from 18×9 vertices and 272 faces while the posterior leaflet is represented with 24×9 vertices and 368 faces. Both leaflets are fixed by the mitral commissures and their corresponding leaflet tips. The left / right trigones and the postero-annular midpoint further confine the anterior and posterior leaflets, respectively (see figure 3.10(f)).

Tricuspid Valve: The function of the tricuspid valve is to regulate the blood flow from the RA to the RV, staying closed during systole and open during diastole. The model is constrained by three surfaces: septal-, anterior- and posterior leaflet (see figure 3.11(a)).

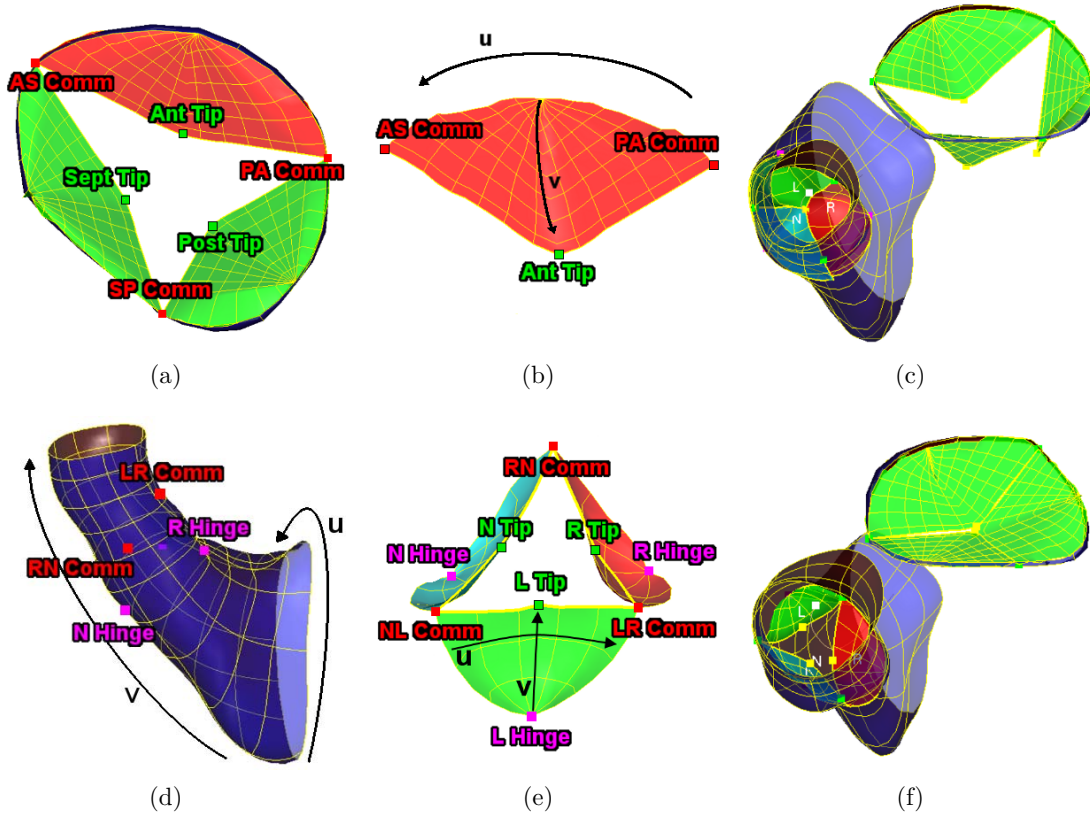


Figure 3.11: Isolated surface components of the tricuspid and pulmonary models with parametric directions and spatial relations to anatomical landmarks: (a) tricuspid leaflet, (b) tricuspid annulus and leaflets, (c) tricuspid-pulmonary in end-diastole, (d) pulmonary trunk, (e) pulmonary leaflets and (f) tricuspid-pulmonary in end-systole.

The tricuspid leaflets are modeled as hyperbolic paraboloids and implicitly describe the tricuspid annulus. Their grids are spanning along the annulus circumferential direction u and the perpendicular vector v pointing for the annulus towards the corresponding leaflet tip, and consist out of 22×14 vertices and 546 faces (see figure 3.11(b)). Each leaflet is constrained by the corresponding two commissures and one leaflet tip (see figure 3.11(c)).

Pulmonary Valve: The representation of the pulmonary valve is compounded out of four structures: pulmonary trunk, left facing leaflet, none facing leaflet and right facing leaflet. The pulmonary trunk emerges out of the right ventricular outflow tract, supports the pulmonary valves and its three leaflets, and ends at the level of the pulmonary artery bifurcation. The grid, which spans the pulmonary trunk surface, is aligned with the circumferential u and longitudinal direction v of the valve (see figure 3.11(d)). It includes 50×40 vertices and 3822 faces confined through the pulmonary commissures, hinges and the RV trigone. Additionally, the RVOT and Bifurcation landmarks determine its

longitudinal span. The attached L-, R- and N- leaflets, are modeled as paraboloids along the annulus circumferential direction u and vector v pointing from the corresponding hinge to the leaflet tip (see figure 3.11(e)). Each includes 11×7 vertices and 120 faces bounded by the associated two commissures, hinge and tip (see figure 3.11(f)).

3.6 Spatio-Temporal Consistency

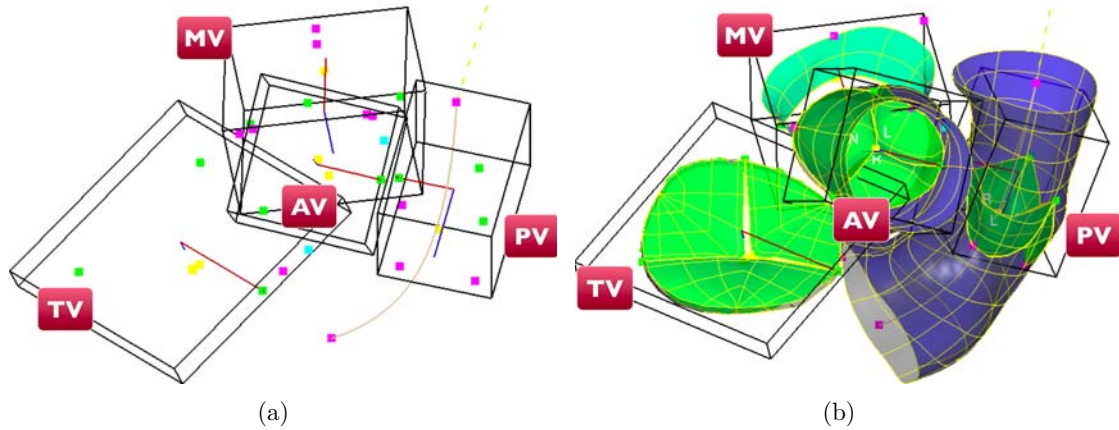


Figure 3.12: Complete heart valve model consisting of aortic valve (AV), mitral valve (MV), pulmonary valve (PV) and tricuspid valve (TV). (a) Similarity transform illustrated as a bounding box and anatomical landmarks. (b) Complete mesh surface model.

The complete model of the valvular system is shown in figure 3.12. An essential aspect addressed in this section is the point correspondence between models from different cardiac phases and across patients, which is required for building statistical shape models and, in general, for any kind of statistical processing over a population of individuals.

Few methods build a statistical shape model automatically using pair-wise or group-wise registration based approaches [52, 98], but these are complicated and time consuming. It is difficult to obtain and maintain a consistent parameterization for complex three-dimensional shapes. However, cutting planes can be applied to intersect surfaces and generate two-dimensional contours, which can be uniformly resampled using simple methods. Hence, by defining a set of physiological-based cutting planes for each model component, surfaces are consistently resampled to establish the desired point correspondence. We develop two resampling schemes, a pseudo parallel slicing for tubular structures and rotational slicing for parabola-like shapes.

For the aortic root and pulmonary trunk, a pseudo parallel slice-based method is used. Cutting planes are equidistantly distributed along the centerline following the v direction. To account for the bending of the arteries, at each location the plane normal is aligned with the centerline's tangent (see figure 3.13(b)). The two-dimensional contours, which result from the shape intersection with the described planes (see figure 3.13(a)), are independently and uniformly resampled to achieve point correspondence.

The rotational slicing method, applied for all the valve leaflets, is illustrated for the mitral valve. As mentioned, the mitral annulus is a saddle shaped curve and likewise the free edges are non-planar too. Thus a rotation axis based resampling method is applied for both mitral leaflets (see figure 3.13(c) and 3.13(d)). The intersection planes pass through the annular midpoints of the opposite leaflet. They are rotated around the normal of the plane spanned by the commissures and the respectively used annular midpoint.

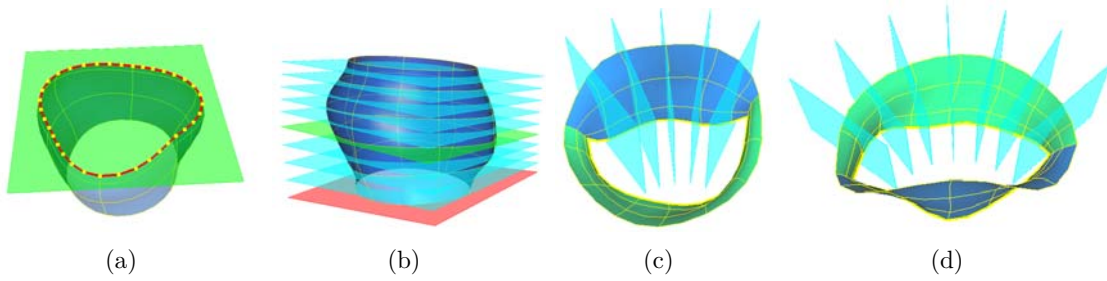


Figure 3.13: (a) Example of a two-dimensional contour and corresponding uniform samples, obtained from the intersection of a plane with the three-dimensional aortic root. Resampling planes for the mitral leaflets (b,c) and aortic root (d). The planes at the hinge and commissure levels of the aortic root in (d) are depicted in red and green respectively. Note that for the purpose of clarity only a subset of resampling planes is visualized in figs (b),(c) and (d).

The proposed method processes each shape independently and offers a fast and anatomical-oriented solution to establish point correspondence.

3.7 Patient-Population Models

The first part of this chapter presented a novel physiologically-driven and hierarchical parameterization of the heart valves, which specifies the exact mathematical representation and topological relations for a specific model instance. However, the shape of the valves changes considerably through time, among particular patients and pathologies.

In accordance with the model-based paradigm, it is prerequisite for the extraction of patient-specific model parameter from cardiac images, to confine the problem by incorporating prior knowledge. The following sections 3.7.1, 3.7.2, and 3.7.3 introduce methodologies to construct statistical shape models, which reduce the number of model parameters and constrain the variation to the specific domain.

3.7.1 Trajectory Models

A novel representation of landmark trajectory population is presented in this section. The temporal variation of each anatomical landmark described in section 3.4 is modeled using a clustering-based approach to satisfy the following properties:

- exploit statistics from a representative set of examples
- orthogonal parameterization of the spatio-temporal variation
- compact and clustered representation of periodic motion

Representation of Landmark Trajectories: Considering the parameterization in section 3.4, each anatomical landmark \vec{L}^j can be represented by the concatenation of its spatial coordinates $[\vec{L}^j(0), \vec{L}^j(1), \dots, \vec{L}^j(t), \dots, \vec{L}^j(T-1)]$, given a volume sequence $I(t)$ of length T . In the context of patient-specific estimation, the objective is to find the trajectory \vec{L}^j , with the maximum posterior probability given a sequence I :

$$\begin{aligned} \arg \max_{\vec{L}^j} p(\vec{L}^j|I) &= \arg \max_{\vec{L}^j} \\ p(\vec{L}^j(0), \dots, \vec{L}^j(T-1)|I(0), \dots, I(T-1)) \end{aligned} \quad (3.4)$$

Since it is difficult to solve Eq. 3.4 directly, various assumptions, such as the Markovian property of the motion [120, 191], have been introduced to model the distribution over \vec{L}^j . However, results are often not guaranteed to be smooth and may diverge over time, due to error accumulation. These fundamental issues can be addressed effectively if both, temporal and spatial appearance information is modeled over the whole sequence at once.

The original trajectory \vec{L}^j can be uniquely represented by the concatenation of its Discrete Fourier Transform (DFT) coefficients:

$$\vec{s}^j = [\vec{s}^j(0), \vec{s}^j(1), \dots, \vec{s}^j(T-1)] \quad (3.5)$$

obtained from the DFT equation [106]:

$$\vec{s}^j(f) = \sum_{t=0}^{T-1} \vec{L}^j(t) e^{-\frac{j2\pi tf}{T}} \quad (3.6)$$

where $\vec{s}^j(f) \in \mathbb{C}^3$ is the frequency spectrum of the x , y , and z components of the trajectory $\vec{L}^j(t)$, and $f = 0, 1, \dots, T-1$ (see figure 3.14). A trajectory \vec{L}^j can be reconstructed from the spectral coefficients \vec{s}^j applying the Inverse Discrete Fourier Transform (IDFT):

$$\vec{L}^j(t) = \sum_{f=0}^{T-1} \vec{s}^j(f) e^{\frac{j2\pi tf}{T}} \quad (3.7)$$

The estimated trajectory is obtained using the magnitude of the IDFT. From the DFT parameterization, the Eq.3.4 can be reformulated as finding the DFT spectrum \vec{s}^j , with maximal posterior probability:

$$\begin{aligned} \arg \max_{\vec{s}^j} p(\vec{s}^j|I, \theta) &= \arg \max_{\vec{s}^j} p(\vec{s}^j(0), \dots, \vec{s}^j(T-1)| \\ I(0), \dots, I(T-1), \theta(0), \dots, \theta(T-1)) \end{aligned} \quad (3.8)$$

Hence, a trajectory instance S of an anatomical landmark \vec{L}^j is represented by the concatenation of its DFT components:

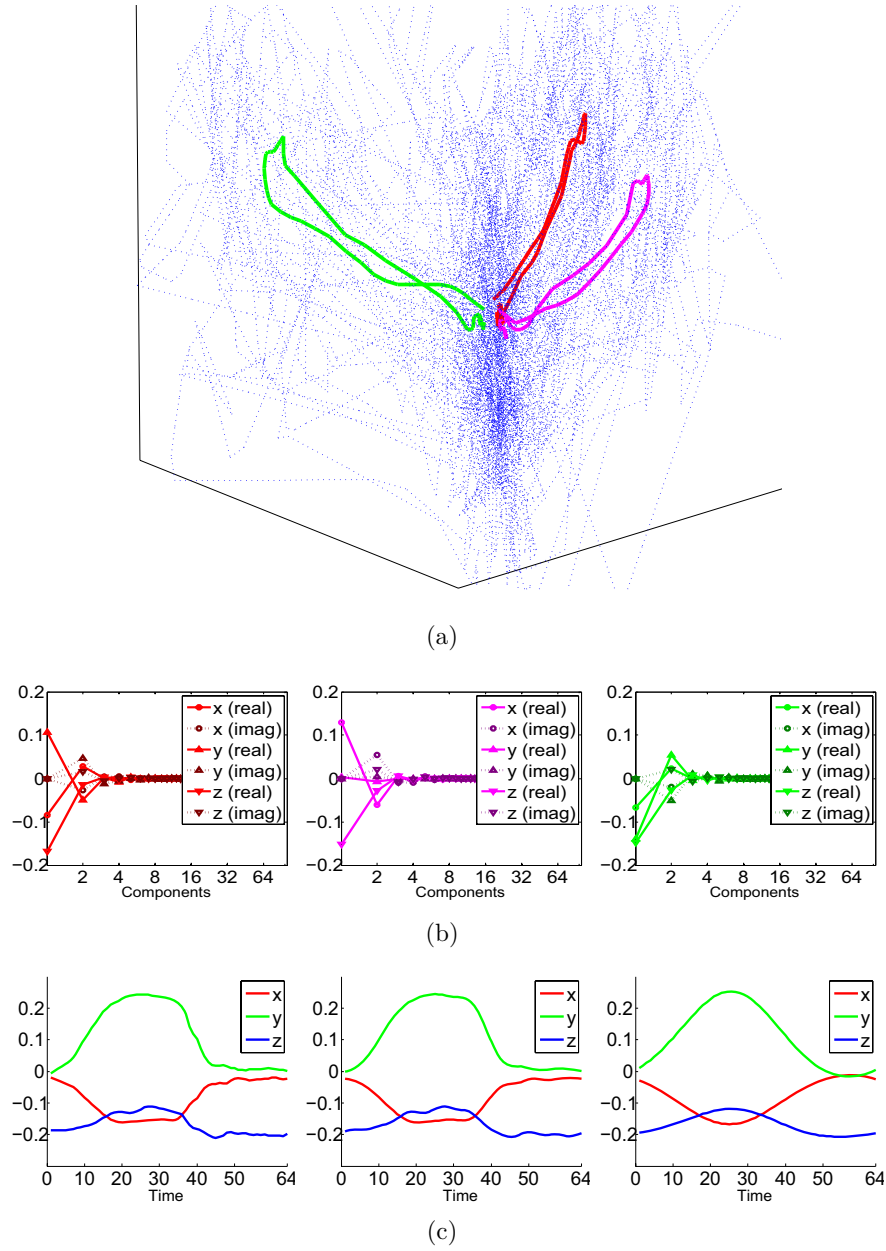


Figure 3.14: Example trajectories of aortic leaflet tips. (a) The aligned trajectories in the Cartesian space by removing the global similarity transformations. (b) Corresponding 3 trajectories highlighted in red, magenta and green, which demonstrates the compact spectrum representation. (c) Reconstructed trajectories of using 64, 10, and 3 components, respectively, showing that a small number of components can be used to reconstruct faithful motion trajectories.

$$S = [\vec{s}^j(0), \vec{s}^j(1), \dots, \vec{s}^j(N-1)] \quad (3.9)$$

where the fixed normalized length N of the orthogonal space is described in the following paragraph.

Temporal Alignment: To facilitate the frequency domain analysis, trajectories are normalized to a constant length. In our implementation, the Fast Fourier Transform (FFT) is used to achieve the speed performance, which requires the signal length to be a power of two. In order to faithfully reconstruct the training sequence, the number of discrete time instances in the normalized trajectory is chosen to satisfy the Nyquist theorem. Thus, each trajectory spectrum in the training set S_1, \dots, S_q is normalized in the Euclidean space to a fixed length $N = 64$.

Another important pre-processing step is the temporal alignment, which establishes temporal correspondences between different motion sequences. For the cardiac images used in our experiments, the alignment is typically based on the cardiac phase obtained from the ECG signal. In particular, the end-diastole and end-systole time instances are used as the anchor points for the piecewise linear interpolation of the time-series.

Trajectory Shape Space: As clearly illustrated in figure 3.14, the variation of the spectrum components decreases substantially as the frequency increases. Consequently, trajectories can be adequately approximated by a few dominant components $\zeta \subseteq \{0, \dots, N-1\}$, $|\zeta| \ll N$, identified during training.

The obtained compact trajectory space can be divided in a set of subspaces. We differentiate between two types of subspaces, individual component subspaces $\Sigma^{(k)}$ and marginalized subspaces Σ_k defined as:

$$\Sigma^{(k)} = \{S(k)\} \quad (3.10)$$

$$\Sigma_k = \Sigma_{k-1} \times \Sigma^{(k)} \quad (3.11)$$

$$\Sigma_0 \subset \Sigma_1 \subset \dots \subset \Sigma_{r-1}, r = |\zeta| \quad (3.12)$$

The subspaces $\Sigma^{(k)}$ are efficiently represented by a set of corresponding hypotheses $H^{(k)}$ learned from the training set. For each component k , the subspace $\Sigma^{(k)}$ is divided uniformly into a set of bins with a certain resolution. We iteratively increase the resolution until any two trajectories from the training set, S_a and S_b , fallen into the same bin satisfy: $d(IDFT(S_a), IDFT(S_b)) < d_{res}$, where

$$d(IDFT(S_a), IDFT(S_b)) = \max d(IDFT(S_a), IDFT(S_b), t) \quad (3.13)$$

$$d(IDFT(S_a), IDFT(S_b), t) = \|IDFT(S_a(t)) - IDFT(S_b(t))\| \quad (3.14)$$

We typically use $d_{res} = 0.5mm$, which reflects the image resolution. For each component k , the populated bins form the corresponding hypothesis set $\mathcal{H}^{(k)}$, which is at least one magnitude less than the original discretized search space. The pruned trajectory space is defined as:

$$\Sigma_{r-1} = \mathcal{H}^{(0)} \times \mathcal{H}^{(1)} \times \dots \times \mathcal{H}^{(r-1)}, r = |\zeta| \quad (3.15)$$

The obtained representation is used to marginalize the parameter space for the trajectory spectrum learning introduced in section 4.4.

3.7.2 Active Shape Models

In this section we construct a statistical shape model of the comprehensive valve model described in section 3.5, which models the variation of plausible instances from a training population. Although a substantial number of approaches have been proposed in the literature [148, 81, 104], the Active Shape Models ASM method by Cootes [36] is widely used in similar problems and is particularly suitable in our context for several reasons:

- captures knowledge from already available expert annotated examples
- provides a general formulation applicable for all valvular structures
- captures variation using a compact parameterization
- limits the model to shapes similar to the training set

Representation of Valve Population: The population of shapes used to learn the model consists of individual instance represented by a fixed number of points in an arbitrary dimension. It is also mandatory that the points are corresponding across the given population. The proposed comprehensive valve model fulfils both conditions, as each anatomy is represented by a fixed number of vertices (see section 3.5) and correspondence between vertices is maintained in time and between individual patients (see section 3.6). Additionally, a large training set, which covers a representative spectrum of normal and characteristic pathologies, is available as required for the discriminative learning framework introduced in the next chapter 4.

Due to the large changes introduced by cardiac and valvular motion, each anatomical structure A_k is processed separately since it incorporates less variation than the integrated model. This also facilitates the Gaussian assumption characteristic for the employed method. Hence, an instance of A_k , with N_k vertices $\vec{p}^{A_k} \in \mathbb{R}^3$ is represented as $3 \times N_k$ element vector X :

$$X = (p_x^1, \dots, p_x^{N_k}, p_y^1, \dots, p_y^{N_k}, p_z^1, \dots, p_z^{N_k})^T \quad (3.16)$$

Alignment of Valve Population: According to Kendall [83], shapes are defined as: "all the geometrical information that remains when location, scale and rotational effects are filtered out from the object". Thus, geometries need to be considered invariant to Euclidean similarity transformations within a reference coordinate system to which all shapes are aligned. Although analytical solutions exist [68], the most popular approach to shape alignment, also applied in our method, is the Generalized Procrustes Analysis (GPA) [60]. The task is defined as optimization problem of each shape, relative to the mean:

$$D = \sum |X_i - \bar{X}|^2 \quad (3.17)$$

where, X_i is a shape vector from a training set of S samples and \bar{X} the mean shape of this training set defined as:

$$\bar{X} = \frac{1}{S} \sum_{i=1}^S X_i \quad (3.18)$$

Two arbitrary shapes X_1 and X_2 , with their center of gravity at the origin, are aligned with respect to the scale s and rotation R parameters by minimizing the following equation:

$$\operatorname{argmin}_{s,R} D(s, R) = |T_{s,R}(X_1) - X_2|^2 \quad (3.19)$$

where the optimal solution is provided by the sum of squared differences between the points of X_2 and transformed points of X_1 . The iterative solution to the GPA includes four steps:

1. Choose an initial estimation of the mean shape, e.g. X_1
2. Align all shapes X_1, \dots, X_S with the current mean shape using Eq. 3.19
3. Re-estimate mean from aligned shapes with Eq. 3.18
4. If estimated mean has changed re-iterate from step 2.

Convergence is assumed if the current mean does not change significantly with respect to the previous estimation. Initially, all shapes X_1, \dots, X_S are translated into the origin and scaled such that $|X| = 1$, which will cause their alignment on a hypersphere after scale and rotation minimization. To avoid nonlinearities and simplify the shape distribution description, the minimization is performed on the tangent space to the mean. A simple approach to achieve this is to scale each shape with $\frac{1}{X_i \cdot \bar{X}}$ after step 2.

The initial shape space, which is the set of all shapes X_1, \dots, X_S , spans a space of dimensionality $k \times n = 3 \times N_k$. After adjusting for translation, scale and rotation, which removes k , 1 and $1/2k(k-1)$ dimensions respectively, the dimensionality of the aligned subspace is equal to $kn - k - 1 - \frac{k(k-1)}{2}$.

Shape Variation Model: Using the aligned training set of shapes X_1, \dots, X_S , a model of their distribution enables generation of new plausible shapes and, vice-versa, examination of new shapes for plausibility. The goal is to model $p(X)$ using a linear model $X = M(y)$, where the parameter vector y lies in a lower dimensional space. An effective approach to dimensionality reduction is the Principal Component Analysis PCA. Assuming a Gaussian distribution of the population with the variance equal to:

$$\Sigma_X = \frac{1}{S} \sum_{i=1}^S (X_i - \bar{X})(X_i - \bar{X})^T \quad (3.20)$$

each shape can be approximated using the mean shape \bar{X} and highest ranked eigenvectors ϕ_i , correspondent to largest eigenvalues λ_i of Σ_X :

$$X \approx \bar{X} + \Phi y, \quad y = \Phi^T (X - \bar{X}) \quad (3.21)$$

where the vector y contains the model parameters, Φ is the matrix formed by the first t column eigenvectors of the symmetric covariance matrix Σ_X . To enforce plausible shape generation with respect to the training set, y_i is bound by $\pm 3\sqrt{\lambda_i}$. The dimensionality of the model parameter vector y is equal to the number of eigenvectors retained.

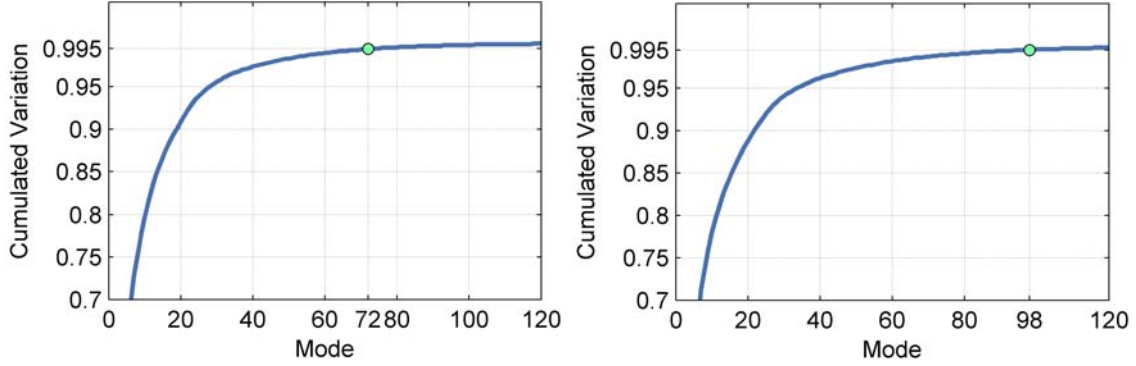


Figure 3.15: Cumulated shape variation for (a) aortic and (b) mitral valves. The green dot marks the threshold cumulated variance of 0.995.

According to Eq. 3.21, the number of retained modes t dictates the number of model parameters. Thus, the decision is problem specific and must consider the model complexity versus the desired specificity. The number of modes t can be determined by demanding that the model explains a certain percentage of the total domain variance. In order to define the dimensionality of the subspace, the cumulated variation $v(t)$ for the first t modes can be computed from the eigenvalues λ_i as follows:

$$v(t) = \frac{\sum_{i=1}^t \lambda_i}{\sum_{i=1}^S \lambda_i} \quad (3.22)$$

Figure 3.15 depicts the fraction $v(t)$ for the shapes of the aortic and mitral valve respectively. By demanding the subspace to cover 99.5% of the shape variation we determined the number of necessary modes as 72 and 98, respectively. The obtained statistical shape modal is applied in section 4.5 to constrain the estimation of the comprehensive valvular model.

3.7.3 Conditioned Multi-linear Principal Component Analysis

We described the ASM framework in section 3.7.2, which uses PCA to represent the shape variation of the valve model from a set of training shapes. However, ASM is a static approach and supplies a prior only for the shape, which does not explicitly include the motion variation. To address this problem, a subject specific dynamic model was proposed in [201], which captures statistics of the LV shape by decomposing subject and motion variability using multi-linear algebra. Multi-linear modeling enables the decomposition of a shape space into a temporal and spatial component in contrast to the ASM where both are coupled. Other approaches were proposed in [78, 150], however those describe generic

dynamical models and are not adequate to capture the complex motion of the valvular apparatus.

In this section we extend the Multi-linear Principal Component Analysis (MPCA) and Multi-linear Independent Component Analysis (MICA) shape models to incorporate conditions imposed by anatomical measurements. The obtained multi-linear model enables the generation of motion priors learned from a training set of shape sequences, subject to anatomical conditions.

Multi-linear Representation: Multi-linear algebra offers a generalization of matrices to higher-order tensors, which defines multi-linear operators over a set of vector spaces. A tensor, also known as multi-dimensional matrix, of order N is defined as $\mathbf{A} \in \mathbb{R}^{I_1 \times I_2 \times \dots \times I_N}$. A generalization of the product of two matrices is the product of a tensor and a matrix. The mode- n product of a tensor $\mathbf{A} \in \mathbb{R}^{I_1 \times I_2 \times \dots \times I_n \times \dots \times I_N}$ by a matrix $M \in \mathbb{R}^{J_n \times I_n}$, denoted by $\mathbf{A} \times_n M$, is a tensor $\mathbf{B} \in \mathbb{R}^{I_1 \times \dots \times I_{n-1} \times J_n \times I_{n+1} \times \dots \times I_N}$ with the entries:

$$(\mathbf{A} \times_n M)_{i_1 \dots i_{n-1} j_n i_{n+1} \dots i_N} = \sum_{i_n} a_{i_1 \dots i_{n-1} i_n i_{n+1} \dots i_N} m_{j_n i_n} \quad (3.23)$$

A matrix $M \in \mathbb{R}^{J_n \times I_n}$ has two associated vector spaces, which can be orthogonalized using Singular Value Decomposition (SVD). Thus, $M = U_1 \Sigma U_2^T$ is decomposed into the product of an orthogonal column space matrix $U_1 \in \mathbb{R}^{J_n \times K_n}$, a diagonal singular value matrix $\Sigma \in \mathbb{R}^{K_n \times K_m}$, and an orthogonal row space matrix $U_2 \in \mathbb{R}^{I_n \times K_m}$. The equivalent representation of the decomposition in mode- n product is $M = \Sigma \times_1 U_1 \times_2 U_2$. Following the generalization of SVD to N-mode SVD introduced in [170], the orthogonal vector spaces can be extended for tensors of order $N > 2$:

$$\mathbf{A} = \mathcal{Z} \times_1 U_1 \times_2 U_2 \dots \times_N U_N \quad (3.24)$$

where \mathcal{Z} is the core tensor, analogous to the diagonal singular value matrix in the classical SVD algorithm, which governs the interaction between the mode matrices U_i .

In case of order two tensors, PCA can be applied to reduce the dimensionality of a linear model. This is basically realized by truncating the SVD such that the eigenvectors associated with the smallest eigenvalues are discarded. A generalization for multi-linear analysis, MPCA, was proposed in [171], which allows for the selective dimensionality reduction of each mode matrix U_i . Analogous, a multi-linear version of the Independent Component Analysis (ICA), MICA, was proposed in [172].

Similar as in [201], we represent the training set as a third-order tensor $\mathbf{A} \in \mathbb{R}^{S \times N \times P}$, where S is the number of patients, N is the frame number inside a multi phase sequence of valve models and P represents the number of shape points. Beforehand, all sequences of shapes \vec{X} in the training set, which cover the motion variation over an entire cardiac cycle, were normalized to a temporal length N (see section 3.7.1) and aligned by utilizing the GPA (see section 3.7.2). Following the MPCA, we decompose the training tensor into:

$$\mathbf{A} = \mathcal{Z} \times_1 U_{patient} \times_2 U_{motion} \times_3 U_{points}$$

where $\mathcal{Z} \in \mathbb{R}^{S \times N \times P}$ is the core tensor, and $U_{patient}$, U_{motion} , and U_{points} the patient, motion and points subspaces, respectively. As the motion subspace is non-Gaussian, ICA is applied to obtain a set of independent modes C_{motion} in the motion subspace [201]:

$$\begin{aligned} \mathbf{A} &= \mathcal{Z} \times_1 U_{patient} \times_2 U_{motion} W^{-1} W \times_3 U_{points} \\ &= (\mathcal{Z} \times_2 W) \times_1 U_{patient} \times_2 U_{motion} W^{-1} \times_3 U_{points} \\ &= \mathcal{S} \times_1 U_{patient} \times_2 C_{motion} \times_3 U_{points} \end{aligned}$$

Conditioned Model Estimation: A set of anatomical measurements $\vec{M} = (m_1, m_2, \dots, m_R)$ extracted from the non-linear valve model is used to condition the static surface parameterization $X = (p_x^1, \dots, p_x^{N_k}, p_y^1, \dots, p_y^{N_k}, p_z^1, \dots, p_z^{N_k})$ [16]. Assuming the joint multivariate distribution $p(X|\vec{M})$ follows a Gaussian distribution, a conditioned shape $X^{\vec{M}}$ containing the anatomical measurements \vec{M} can be estimated as follows:

$$X^{\vec{M}} = \bar{X} + \Sigma_{X\vec{M}} \Sigma_{\vec{M}\vec{M}}^{-1} (\vec{M} - \bar{\vec{M}})$$

where \bar{X} is the mean surface parameterization from all training sets of the valve shapes X (see equation 3.18), $\bar{\vec{M}}$ the mean of the measurements \vec{M} in the training set, and $\Sigma_{X\vec{M}}$ the covariance matrix between X and \vec{M} .

By combing the static shape estimate $X^{\vec{M}}$ with the multi-linear model \mathbf{A} we can construct a dynamic motion prior, $\vec{X}^{\vec{M}}$, for the entire cardiac cycle. Therefore we first estimate the patient vector $\mathbf{u}_{patient}$ associated with the conditioned shape estimate $X^{\vec{M}}$:

$$\mathbf{u}_{patient} = X^{\vec{M}} \mathbf{T}_{(1)}^{-1} \quad \mathcal{T} = \mathcal{S} \times_2 C_{motion} \times_3 U_{points}$$

where $\mathbf{T}_{(1)}^{-1}$ is the pseudo-inverse of the tensor \mathcal{T} flattened along the first mode, and C_{motion} the one dimensional motion mode. The dynamic motion prior $\vec{X}^{\vec{M}}$ can be then reconstructed by a tensor multiplication:

$$\vec{X}^{\vec{M}} = \mathcal{S} \times_1 \mathbf{u}_{patient} \times_2 C_{motion} \times_3 U_{points}$$

The comprehensive surface model $\vec{X}^{\vec{M}}$ of each anatomical structure is estimated by adopting the conditioned multi-linear shape method using anatomical measurements \vec{M} defined between the landmarks $L^1 \dots L^{36}$. For instance, in case of the aortic root we use three measurements $\vec{M} = (m_1, m_2, m_3)$, where m_1 is the inter-commissure distance, m_2 the hinge-commissure plane distance, and m_3 the hinge-commissure plane angle. The obtained multi-linear model can be applied in section 4.5.2 to predict valvular dynamics and constrain the estimation of the comprehensive valvular model.

3.8 Conclusions

Newest medical imaging equipments produce large amounts of raw cardiac data that encode hidden information about the underlying physiological system. A multitude of

models, especially focused on the left ventricle, are proposed in the literature to extract anatomical and functional cardiac parameters from images. Following an opposing approach, some cardiac models enhance geometrical information with biomechanical components, to simulate physiological functions under various conditions. Regardless of the specific methodology, existent models of the heart valves are generic, simplified and not conceived to incorporate accurate morphological and functional information. Hence, their clinical applicability is limited to the study of common biological processes.

We proposed a novel physiological model of the heart valves, aortic, mitral, tricuspid and pulmonary valve to precisely capture morphological, dynamical and pathological variations. To handle the inherent complexity, the representation is structured on three abstraction layers: global location and rigid motion, non-rigid landmark motion model and comprehensive valve model. Each model abstraction naturally links to anatomical and dynamical aspects at a specific level of detail, while the hierarchical interconnection of the individual parameterizations is driven by the physiology of the valves.

In the last part of the chapter, we address models of patient population. The proposed physiological model provides implicit point correspondence across time and individuals, facilitating statistical modeling of relevant valvular parameters. Statistical representations of shapes and trajectories effectively incorporate prior variation knowledge to facilitate patient-specific parameter estimation.

Patient-specific Parameter Estimation

Data-driven healthcare is an unequivocal megatrend to which the plurality of medical images available today has contributed extensively. The large amount of images routinely produced has created an explicit demand for tools that efficiently process raw data into precise clinical knowledge. In particular, the extraction of morphological and functional parameters from cardiac images is a prerequisite for the management of cardiovascular disease. From a technological standpoint, model-based approaches have been traditionally applied in this context. A review of the most relevant methods is given in section 4.1.

In this chapter we introduce our novel methodology for patient-specific estimation of valvular models from multi-modal images. The entire algorithmic framework is based on robust discriminative learning approaches discussed in section 4.2. In concordance with the hierarchical model representation presented in chapter 3, the estimation of patient-specific valve parameters includes three stages: global location and rigid motion estimation, non-rigid landmark motion estimation, and comprehensive aortic-mitral estimation. Figure 4.1 illustrates the entire algorithm, which relies on novel techniques such as the Trajectory Spectrum Learning (TSL) with Local-Spatio-Temporal (LST) features, and extends recent machine learning methods. Initially we compute the location and rigid motion of the valves from volumetric sequences of cardiac images as described in section 4.3. The non-rigid and complex motion of the valves is estimated in section 4.4. In section 4.5, the obtained dynamic landmark model guides the fitting of the comprehensive valvular model. Extensive experiments on heterogenous data sets presented in section 4.6 demonstrate the performance of the proposed approach.

4.1 Model-based Paradigm

In the medical field, images are usually ambiguous and of limited quality, while the objects of interest, such as organs or lesions, are inherently complex and have large variations in shape and appearance. To guarantee robust solutions for the parameter estimation

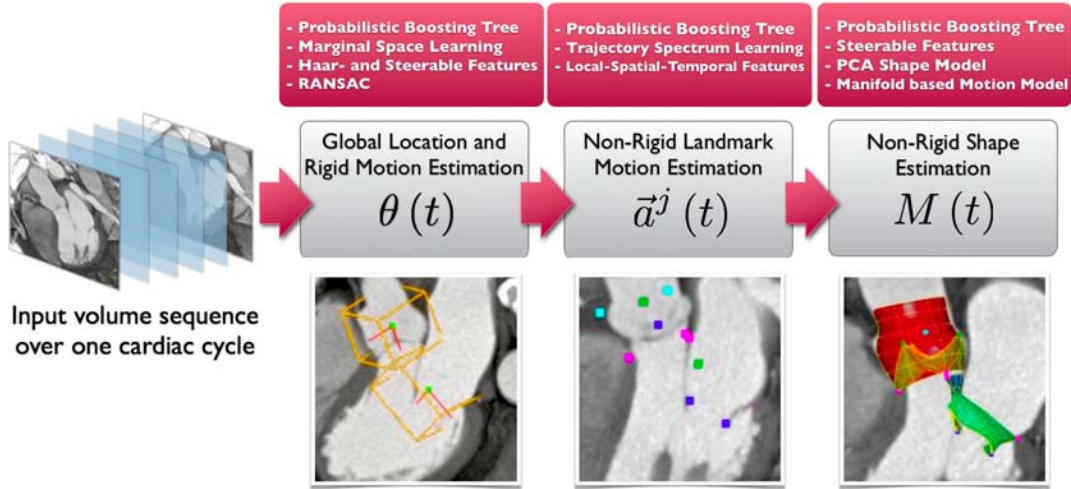


Figure 4.1: Diagram depicting the hierarchical model estimation algorithm. Each block describes the actual estimation stage, computed model parameters and underlying approach.

methods, prior knowledge about the expected results and image appearance must be incorporated in the solution.

The heart valves regulate the blood flow and generate some of the most complex and rapid motions in the human body. They open and close completely within 100ms, following a synchronized movement pattern repeated at each cardiac cycle. Valvular structures are small, present elaborate textures, and vary significantly in appearance across patients and pathological conditions. Thus, the spatio-temporal information about the valves, captured by cardiac images, is commonly limited and affected by noise and artifacts. Nevertheless, the estimation of anatomical and dynamical parameters of the valves from non-invasive images has a crucial importance for the clinical workflow.

Chapter 3 introduced our hierarchical representation of the valvular apparatus, which defines the target parameters and the model of their variation. The objective of the current chapter is to estimate patient-specific values for those parameters from a sequence of multi-modal images. To tackle the above mentioned challenges, we proposed a novel model-based framework illustrated in figure 4.1, which relies on discriminative learning techniques.

The input data is a temporal sequence of volumetric scans represented in Cartesian coordinates and acquired with one of the three modalities: CT, Ultrasound or MRI. The natural first task is to recover the pose and corresponding motion parameters of the valves from the input cardiac data. This problem is discussed in section 4.1.1, while our proposed solution, based on the Probabilistic Boosting Tree, Marginal Space Learning and RANSAC estimators is given in section 4.3. With the global parameters determined, the next task is to estimate the complex configuration and motion of the valvular anatomical landmarks. Section 4.1.2 addresses the motion estimation problem and section 4.4 intro-

duces our novel Trajectory Spectrum Learning algorithm to efficiently learn and estimate periodic motion in marginal trajectory spaces. The final stage tackles the boundary delineation of the complete valvular surfaces over the entire cardiac cycle. This is discussed in section 4.1.3 with our concrete method, based on motion manifold learning and robust boundary detectors, presented in section 4.5.

The output data of the proposed estimation framework are the patient-specific parameters of the valvular model presented in chapter 3, namely: the global location and rigid motion parameters, the location and motion parameters of the anatomical landmarks, and the parameters of the dynamic valvular surfaces. In the following we summarize the advantages of our method:

- **Hierarchical** - to handle the problem complexity, the estimation is following a coarse-to-fine strategy based on the natural level of detail of the underlining anatomies.
- **Robust** - learning-based approaches are ubiquitously applied to guarantee robustness against image artifacts and to handle the shape and appearance variations.
- **Fast** - search space marginalization methods are employed to efficiently perform optimization in multi-dimensional parameter domains.
- **Consistent** - the estimated motion is coherent and not affected by image discontinuities due to the usage of novel motion manifold learning and trajectory spectrum learning techniques.
- **Multimodal** - the same framework is applied to various image modalities without algorithm modifications, as only modality-specific detectors need to be trained.

For clarity, we divide the problem into three interrelated tasks and discuss each of them in the remainder of the section: object localization, motion estimation, and boundary delineation.

4.1.1 Object Localization

In general, the performance of model-based segmentation algorithms is highly reliant on adequate initialization, which is largely accomplished through manual or semi-automatic approaches. Recently, discriminative learning methods proved to be efficient in 2D object detection problems, offering an automatic and robust alternative to user-dependent initialization [175, 57]. Object detection is formulated as traditional classification, and solved by testing and ranking location hypotheses in an input image using a trained detector. Viola and Jones [175] introduced an effective image representation, which allows for efficient computation of Haar-like features used for classification. The detector is organized in a cascade of classifiers trained using AdaBoost to select critical visual features from a large pool, subsequently applied for face detection in 2D images. Georgescu *et al.* [57] applied discriminative learning algorithms to detect anatomical structures from medical

images. The proposed database-guided segmentation directly exploits expert annotations of the left ventricle from echocardiography.

Zheng *et al.* [197] extended the learning based approach to three-dimensional object localization by introducing an efficient search method referred to as Marginal Space Learning (MSL). To handle the large number of possible pose parameters of a 3D object, an exhaustive search of hypotheses is performed in sub-spaces with gradually increased dimensionality. Initially, MSL was successfully applied to localize the four-chamber of the heart in cardiac CT volumes. Subsequently, the framework was applied to detect the 3D location of various anatomical structures from multimodal images [31, 187, 191]. To further speedup the framework and handle the inherent drawback of Euler angles, Zheng *et al.* [198] proposed to exploit significant correlation among parameters in the same marginal space and apply quaternions to represent 3D object orientation.

We further advanced the learning-based approach by obtaining the location parameters of objects from four-dimensional images. In section 4.3 a novel approach is proposed, which combines space marginalization and RANdom SAmple Consensus (RANSAC) techniques to extract the time-coherent location of the four cardiac valves from 4D data.

4.1.2 Motion Estimation

The quantification of motion and deformation from images is an essential area of growth within the computer vision and medical image analysis community. Despite its difficulty, great progress has been made in the last couple of decades [193]. However, the direct application of traditional tracking algorithms to medical images produces unsatisfactory results due to inherent pathophysiological complexity and image quality limitations.

To achieve robust motion estimation and minimize error accumulation, numerous approaches proposed to integrate the key frame detection into the tracking [50, 94]. In most tracking-by-detection approaches, the detector is often loosely coupled with the tracker, i.e., the trajectory is recovered by connecting the object detection result on each individual frame. To achieve a more effective search, sophisticated statistical techniques are introduced in the estimation process [145, 190]. Strong dynamical motion models are also adopted in many approaches to improve the estimation robustness [2, 152].

Recently, trajectory-based features have also attracted more and more attentions in motion analysis and recognition [115, 183]. It has been shown that the inherent representative power of both shape and trajectory projections of non-rigid motion are equal, but the representation in the trajectory space can significantly reduce the number of parameters to be optimized [4]. This duality has been exploited in motion reconstruction and segmentation [10, 195] and structure from motion [4]. In particular, for periodic motions, such as the movement of a vehicle [132] and a human body [131], frequency domain analysis shows promising results in motion estimation and recognition [95, 120, 113, 24].

In section 4.4, we propose a novel algorithm, Trajectory Spectrum Learning (TSL), to simultaneously estimate location and motion of non-rigid objects using trajectory-based features and strong trajectory spectrum classifiers. By decomposing the full trajectory space into orthogonal subspaces defined by generic bases, such as the Discrete Fourier Transform (DFT), the obtained representation is shown to be compact [4]. Consequently,

this compact representation allows for efficient learning and optimization in its marginal spectrum space.

4.1.3 Boundary Delineation

Given the complexity of anatomical structures and typical erroneous data sources, the capacity of traditional bottom-up segmentation approaches to extract consistent object boundaries is limited. Over the past two decades, numerous methods have been designed to incorporate a priori domain knowledge and constrain the boundary delineation problem.

A prominent family of algorithms, reviewed in detail by McInerney and Terzopoulos [104] are Deformable Models. Inspired from the physical theory of elasticity within a Lagrangian formulation, object boundaries are modeled as elastic bodies subject to applied forces and constraints. The segmentation is typically performed by optimizing an objective function composed out of an internal energy term, which controls the smoothness or symmetry of the model, and an external energy, which deforms the model to fit the underlying data. While first introduced in computer vision by Terzopoulos [155], one of the most popular forms, are the two-dimensional deformable contours, or snakes, proposed by Kass *et al.* [81]. Following the same principle, Amini *et al.* [6] proposes a dynamic programming framework to optimize the objective function by searching all possible solutions. To speed up the algorithm, Geiger [56] applied multi-scale images within a non-iterative method. Staib and Duncan [148] used Fourier parameterizations of 3D surfaces to extract geometrical models controlled by a reduced number of variables. Their gradient ascent optimization algorithm deforms the surfaces towards strong image gradients. Gerard *et al.* [58] combined 3D deformable surface with statistical heart motion model to represent the left ventricular function from 3D echocardiography. Using Boolean operations from solid representations for the deformable model, Park *et al.* [126] extracted patient specific heart shapes of the left and right ventricle from tagged MRI images.

Another research direction proposed by Cootes *et al.* [36] advocates the usage of point distribution models to represent domain specific variability. Within the popular Active Shape Models (ASM) framework, the variation of deformation is enforced to be consistent with a representative training set, thereby increasing robustness during boundary delineation. Duta and Sonka [46] applied the ASM method to segment MRI brain images. Von Assen *et al.* [166] extended the framework to segment volumetric left ventricle models from sparse CMR datasets, consisting of multiple planes with arbitrary orientation and sampling rates. To address the specific lack of tolerance to grayscale variation, Cootes *et al.* [35] introduced Active Appearance Models (AAM), which simultaneously consider shape and texture information. Mitchell *et al.* [110] demonstrated the clinical potential of 3D AAM in three-dimensional cardiac segmentation from short-axis CMR images and Echo images. Andreopoulos and Tsotsos [9] proposed the integration temporal and structural constraints to enhance AAM and analyze short axis CMR data.

Among other notorious approaches to model-based segmentation, level-sets were successfully applied in various medical imaging problems. Level-set methods, which can be thought of as Eulerian formulations of deformable models, represent deformation as wave front propagation of an evolving function subject to intrinsic constraints [47].

Section 4.5 introduces our model-based approach to delineate the boundary of the valvular apparatus from 4D images. In the first step, the boundary is determined in the end-diastole and end-systole phase, using robust learning-based boundary detectors within a ASM framework. Subsequently, the estimation is performed in the entire cardiac cycle using manifold based motion models and collaborative trackers.

4.2 Discriminative Learning Methods

The task of estimating the valvular model parameters θ , L and M from an image I is extremely challenging due to the large number of model parameters, the complex shape and motion variation, the different image aspects and the limited image quality. In conclusion to section 2.6.3 and 4.1 we argue that machine learning techniques offer a robust and efficient alternative to solve our estimation problems. They allow for the implicit incorporation of prior knowledge through data annotation, avoiding elaborate and rigid mathematical formulations. Thereby complex statistical models can be learned in a robust and straightforward manner. Furthermore, an incremental estimation approach can be addressed under a unified and consistent framework leveraging the same dataset of expert annotations.

A common approach is to use a generative model with likelihood probability $p(I|\theta, L, M)$. However, these models are often based on too simple assumptions of data distributions to describe the true underlying complexity. Furthermore, generative approaches are exclusively focused on learning the target objects, rather than the discrimination between foreground and background. On the contrary, discriminative models have a superior predictive performance in finding separation boundaries between classes than generative models do[169]. Therefore, we formulate the estimation as a discriminative problem and focus on learning the posteriori distribution $p(\theta, L, M|I)$ directly.

The classic approach to supervised learning includes two stages: training and testing. In the first stage, a function D is learned from training data to model $p(\theta, L, M|I)$. An established approach for the training of discriminative models, used throughout the thesis is boosting. Section 4.2.1 presents the general idea and two prominent algorithms: AdaBoost and Probabilistic Boosting Tree (PBT). To facilitate effective learning, statistically rich information is usually captured through image features. We use three different classes of features introduced in section 4.2.2: Haar-like Features, Steerable Features and Local-Spatio-Temporal (LST) Features. In the second stage, the learned function D is applied to predict θ, L and M given an image I . The entire pipeline for training, testing, as well as space marginalization relevant for all subsequent algorithms is discussed in section 4.2.3.

4.2.1 Boosting Algorithms

According to machine learning approaches, parameter estimation is formulated as a classification problem. A trained classifier scans the search space and computes the probability of the target parameters.

However, it is very difficult to define a single robust predictor. It is much more appropriate to find a set of weak predictors, which combined provide a strong classification rule. In machine learning, this approach is referred to as boosting. According to Freund & Schapire [53], boosting is a supervised machine learning method for improving the accuracy of any given learning algorithm. The basic idea is to combine many rough rules of thumb into a single classifier that will be much more accurate than any one of the weak rules.

The input of boosting algorithms is a training set $\{(x_1, y_1), \dots, (x_N, y_N)\}$, where x_i belongs to a certain domain X , and y_i is in a certain label set Y (we assume $Y = \{-1, 1\}$, as multi-class is not relevant in our work). Given a set of weak learners $\{h_1, \dots, h_l\}$, with $h_i : X \rightarrow Y$, the boosting algorithm generates a strong classifier $D(x)$.

There are two fundamental problems to be solved by a boosting algorithm: how to choose a certain weak classifier h_i (in each iteration) from a given set and how to combine the weak classifiers into a strong predictor $D(x)$?

Two established algorithms, AdaBoost and Probabilistic Boosting Tree, presented in the remainder of this section provide a concrete solution for the two fundamental questions. The former boosting method is used throughout the model estimation algorithms presented in this chapter.

AdaBoost: Although there are many methods presented in the literature [105], the most studied and perhaps the most popular boosting algorithm is AdaBoost, introduced in 1995 by Freund and Schapire [53]. This algorithm presented in figure 4.2 provides very attractive properties regarding training error and generalization performance.

The algorithm is called AdaBoost due to its capability to adjust adaptively to the errors of the weak hypotheses. In each step t of its main loop it selects a weak hypothesis h_t from a given set, which outputs the smallest error e_t given the current sample distribution W . The weight vector \bar{w}^t , which defines the sample distribution is updated each step according to the current selected weak hypothesis h_t . The update rule reduces the weight of the correctly predicted samples and increases the weight of the examples on which the prediction is poor. This explains the adaptive property of AdaBoost, which during the learning process concentrates on harder samples by increasing their weights.

The final hypothesis $D(x)$ is generated by the weighted average of the selected weak hypotheses. The weight of each hypothesis is determined by its error. Obviously, more accurate hypotheses have more influence on the outcome of the final classifier.

AdaBoost provides very strong guarantees for the learning performance. It was proved that the training error of the final classifier approaches zero exponentially with the number of rounds T . More importantly, strong bounds on generalization performance were later proved in [137]. Based on observations that AdaBoost often does not overfit the data, the generalization error was proven to be bounded by the margins of the training set, which are reduce with each boosting round.

Probabilistic Boosting Tree: The Probabilistic Boosting Tree (PBT) learns a composite strong classifier by exploiting a divide-and-conquer strategy. Thereby it aims to overcome an essential problem of AdaBoost where ϵ_t approaches $\frac{1}{2}$ quickly, which slows

Input

- set of N labeled samples $\{(x_1, y_1), \dots, (x_N, y_N)\}$
- distribution W over the examples
- weak learning algorithm **WeakLearn**
- number of iterations T

Initialization

- set the weight vector $w_i^1 = W(i)$ for $i = 1, \dots, N$

Main Loop, for $t=1, \dots, T$

- set $\vec{p}^t = \frac{\vec{w}^t}{\sum_{i=1}^N w_i^t}$ (update the samples' probability distribution)
- get $h_t = \mathbf{WeakLearn}(\vec{p}^t)$ (get back a hypothesis h_t from **WeakLearn** by providing it with the distribution \vec{p}^t)
- set $\epsilon_t = \sum_{i=1}^N p_i^t |h_t(x_i) - y_i|$
- set $\beta_t = \frac{\epsilonpsilon_t}{1 - \epsilonpsilon_t}$
- set $w_i^{t+1} = w_i^t \beta_t^{1 - |h_t(x_i) - y_i|}$ (update the samples' weight)

Output:

- $D(i) = \begin{cases} 1 & : \sum_{t=1}^T (\log \frac{1}{\beta_t}) h_t(i) \geq \frac{1}{2} \sum_{t=1}^T \log \frac{1}{\beta_t} \\ 0 & : \textit{otherwise} \end{cases}$

Figure 4.2: The adaptive boosting (AdaBoost) algorithm introduced by Freund and Schapire in [53].

down convergence. Instead of learning one strong classifier from a pool of weak learners, PBT constructs multiple strong classifiers connected through a binary tree.

The algorithm summarized in figure 4.3 recursively learns a tree illustrated in figure 4.4. At each node, a standard boosting algorithm is applied to learn a strong classifier with a relaxed exit condition, e.g. $\epsilon_t < 0.45$. The training set is recursively divided into two subsets by the trained strong classifier, and used to train the subsequent left and right tree branches. This allows for a natural division of the positive and negative samples until a given tree depth L is reached. A variable ϵ controls the subset division and allows hard to classify samples to get passed in both sub-trees. In PBT, the tree depth L and ϵ , which defines confusing samples, are the main parameters to control overfitting.

Figure 4.5 illustrates the computation of $p(y|x)$ from a learned binary tree. Any tree node aggregates information from its descendents, while the posteriori approximation at

Input

- A training set $S = \{(x_1, y_1, w_1), \dots, (x_N, y_N, w_N)\}$; $x_i \in \mathcal{X}, y_i \in \{-1, +1\}, \sum_1 w_i = 1$
- Tree maximum depth L and confusion tolerance ϵ , e.g. $\epsilon = 0.1$
- compute empirical distribution $\hat{q}(y) = \sum_i w_i \delta(y_i = y)$

Main Loop

- Exit if current tree depth is L
 - From the training set S learn a strong classifier using a boosting algorithm with T weak classifiers and early exit $\epsilon_t > \theta$, e.g. $\theta = 0.45$
 - Initialize empty sets S_{left} and S_{right}
 - For each (x_i, y_i) compute the probability $q(+1|x_i)$ and $q(-1|x_i)$ from the learned strong classifier
 - if $q(+1|x_i) - \frac{1}{2} > \epsilon$ then $(x_i, y_i, 1) \rightarrow S_{right}$
 - else if $q(-1|x_i) - \frac{1}{2} > \epsilon$ then $(x_i, y_i, 1) \rightarrow S_{left}$
 - else $(x_i, y_i, q(+1|x_i)) \rightarrow S_{right}$ and $(x_i, y_i, q(-1|x_i)) \rightarrow S_{left}$
 - Normalize all the sample weights in S_{right} and repeat procedure recursively
 - Normalize all the sample weights in S_{left} and repeat procedure recursively
-

Figure 4.3: The probabilistic boosting-tree training as introduced by Zhuowen Tu in [164]

the top node constitutes the final result.

4.2.2 Image Features

PBT is a powerful learning algorithm and very well suited to solve the parameter estimation problem within our framework. Nevertheless, as any other boosting algorithm, it does not make any statements about the weak rules, which are boosted during the learning process. Thus, an appropriate set of weak predictors has to be defined, in order to achieve a robust classifier.

In our context the weak predictors are constructed from a pool of image features, which form an overcomplete representation of the original image. Depending on the estimation problem, a specific class of features is chosen, considering both discriminative power and computation efficiency. Three types of image features relevant to our algorithms are introduced in the following: Haar-like features, Steerable features and Local-Spatio-Temporal features.

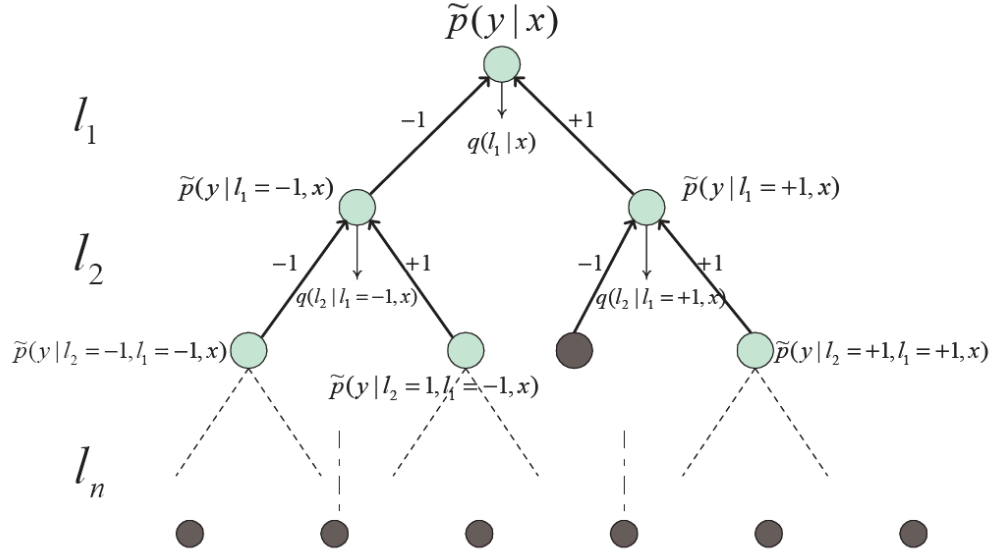


Figure 4.4: Illustration of the probabilistic model of the tree. The dark nodes are the leaf nodes. Each level of the tree corresponds to an augmented variable. Each tree node is a strong classifier. Figure from Tu *et al.* [164].

Compute $p_N(y|x)$ the posterior distribution at a tree node N

- Compute $q_N(+1|x)$ and $q_N(-1|x)$ at level N from corresponding strong classifier
 - $p_N(y|x) = q(+1|x)p_{right}(y) + q(-1|x)p_{left}(y)$
 - If $q(+1|x) - \frac{1}{2} > \epsilon$ then $p_{right}(y) = p_{right(N)}(x, y)$ and $p_{left}(y) = q_{left(N)}(y)$
 - Else if $q(+1|x) - \frac{1}{2} < -\epsilon$ then $p_{right}(y) = q_{right(N)}(y)$ and $p_{left}(y) = p_{left(N)}(x, y)$
 - Else $p_{right}(y) = p_{right(N)}(x, y)$ and $p_{left}(y) = p_{left(N)}(x, y)$
-

Figure 4.5: The probabilistic boosting-tree testing as introduced by Zhuowen Tu in [164]

Haar-like Features: Haar wavelet features have been proven to be very efficient for object detection problems. These have been first introduced by Papageorgiou *et al.* in [123]. Similar rectangle-based features have been used by Viola for object detection in 2D [176]. Zheng *et al.* used Haar wavelet features for object detection in 3D images [197].

The idea is to define a set of rectangular image regions and perform simple Haar-based transformations over the selected pixels. For instance, in case of a two-rectangle feature, the difference between the sums of the pixels within the two regions is computed. The two rectangular regions are adjacent and have the same size. In the same way, features with a larger number of rectangles can be defined. In concordance with the Haar wavelet

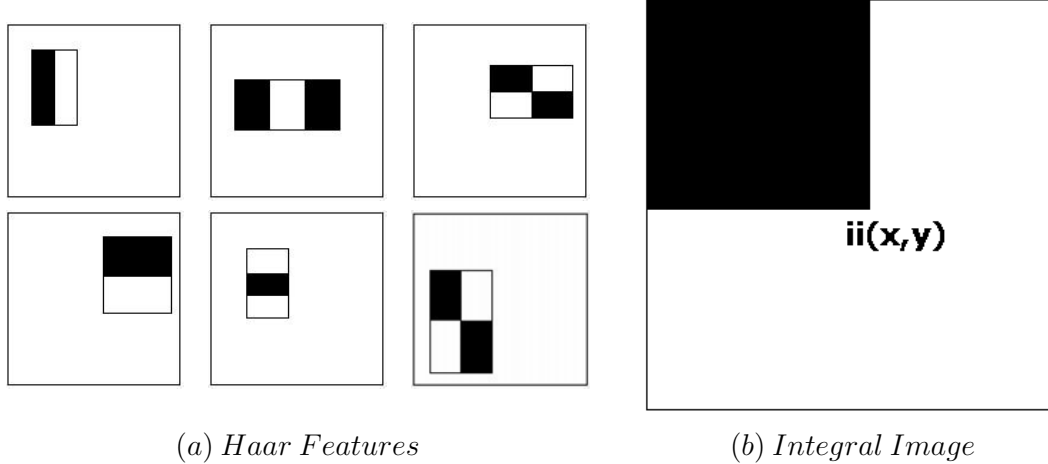


Figure 4.6: (a) Examples of rectangle (Haar) features. The sum of the pixels which lie within the white rectangles are subtracted from the sum of pixels in the grey rectangles. From left to right are shown: two-rectangle features, three-rectangle feature and four-rectangle feature. (b) The integral image at point (x, y) is the sum of the pixels marked by the black rectangle.

transformation, the regions are always adjacent and have the same size, while summation and subtraction of the rectangles is alternating (see figure 4.6 (a)).

The scale of the features' mask can vary. Also features may be applied vertically or horizontally at any sampled location. Hence, a large set of features can be generated, which provide an overcomplete representation of the original image. Empirically it was shown that this rich representation supports an effective learning [176].

The integral image representation provides an elegant and efficient method to compute rectangle features. The integral image is an intermediate representation defined as follows:

$$ii(x, y) = \sum_{x' \leq x, y' \leq y} i(x', y') \quad (4.1)$$

where ii is the integral image and i is the original image. At location (x, y) the integral image contains the sum of the pixel above and to the left of (x, y) (see figure 4.6 (b)). The following recurrence rule allows the computation of the integral image in one pass over the original image:

$$\begin{aligned} s(x, y) &= s(x, y - 1) + i(x, y) \\ ii(x, y) &= ii(x - 1, y) + s(x, y) \end{aligned} \quad (4.2)$$

The pre-computed integral image allows for the computation of any rectangular feature in constant time. One rectangle can be computed by subtracting the bottom left and top right corners from the sum of the remaining two. As the features defined above include adjacent rectangles their computation is very efficient.

Rectangle features are less complex when compared with alternatives such as steerable filters. Although sensitive to edges, corners and other structures, they are quite imprecise. However, the extreme computational efficiency of rectangular features outweighs their limitations. It is important to note that it is straightforward to extend the rectangle features, as well as the integral image representation of three-dimensional images. Although the computation time increases with the dimensionality, Haar features are very efficient for 3D images as well.

Steerable Features: Haar wavelet features are effective to capture statistics of global model parameters from images. However, to capture orientation and scale information either the feature template or the volume has to be rotated and scaled according to each hypothesis in the search space. As the integral image technique, presented in the previous paragraph, is not efficient under volume rotation or resampling, different features must be defined to facilitate learning of orientation parameters.

Zheng *et al.* [197] proposed steerable features, which can capture orientation and scale information in a computationally efficient fashion. The idea is to compute local features from the original images at specific locations determined by a steerable sampling pattern. Instead of aligning the input image with different hypotheses, which is computational expensive, orientation or scale information can be embedded into the distribution of sampling points.

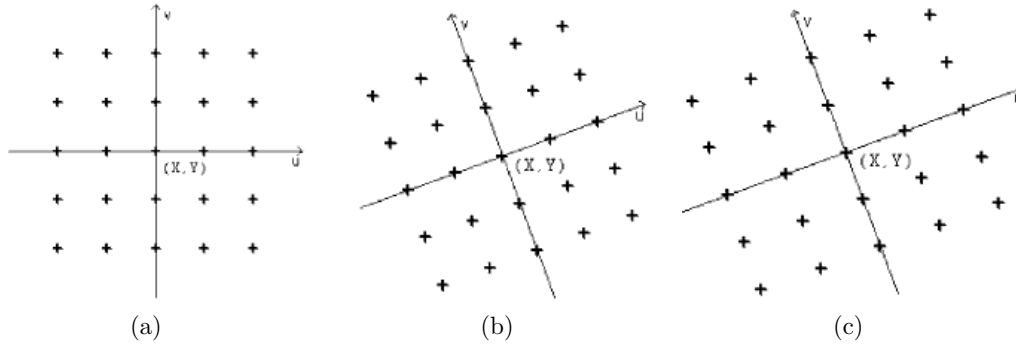


Figure 4.7: Steerable sampling pattern aligned with an example hypothesis $(x, y, \vec{\alpha}_x, s_x, s_y)$ for a two-dimensional problem. Sampling locations are defined as '+'. (a) Pattern centered at (x, y) . (b) Pattern oriented with $\vec{\alpha}_x$. (c) Pattern scaled along the axes proportional to (s_x, s_y) .

Figure 4.7 illustrates an example of the steerable sampling pattern for two-dimensional images. For a specific hypothesis $\{(c_x, c_y, c_z), (\vec{\alpha}_x, \vec{\alpha}_y, \vec{\alpha}_z), (s_x, s_y, s_z), t\}$ of a possible valve location (see section 3.3), the steerable pattern is centered in (c_x, c_y, c_z) . Also, its axes are aligned with the orientation $(\vec{\alpha}_x, \vec{\alpha}_y, \vec{\alpha}_z)$ and the distance along a specific axis is proportional to the corresponding scale parameter (s_x, s_y, s_z) . Fast local features are computed from sampling points selected with the resulting pattern.

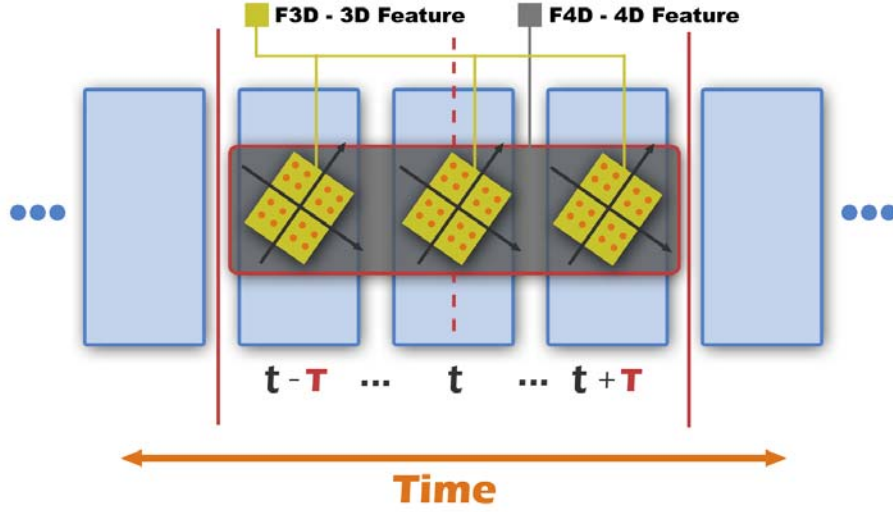


Figure 4.8: An example of a local-spatio-temporal feature, aligned with a certain position, orientation and scale, at time t . The temporal context length of the illustrated LST feature is T , spanned symmetrically relative to t .

A total of 24 distinct features based on image intensities and gradients are proposed in [197] and also used in our algorithms: $I, \sqrt{I}, \sqrt[3]{I}, I^2, I^3, \log I, \|g\|, \sqrt{\|g\|}, \sqrt[3]{\|g\|}, \|g\|^2, \|g\|^3, \log \|g\|, \alpha, \sqrt{\alpha}, \sqrt[3]{\alpha}, \alpha^2, \alpha^3, \log \alpha, g_x, g_y, g_z, n_x \cdot g, n_y \cdot g, n_z \cdot g$. I is the image intensity at location (x, y, z) and $g = (g_x, g_y, g_z)$ the corresponding gradient. n_x, n_y, n_z are the three axis of the local coordinate system and $\alpha = \arccos(n_z \cdot g)$ the angle between the gradient and the n_z axis. The pool of features is given by computing each local feature at each sampling location according to the aligned sampling pattern.

Local-Spatio-Temporal Features: Both classes of features introduced above are defined for two- and three-dimensional images. To maximize both the robustness and accuracy of motion estimation from noisy data, statistics obtained in a spatial context should be enhanced with temporal information. We introduce a novel over-complete image representation defined by the Local-Spatial-Temporal (LST) features, which extends the steerable features to four-dimensional images and facilitates learning of motion parameters.

It has been shown that local orientation and scaling of image features reduce ambiguity and significantly improve learning performance [165]. We extend the image representation by aligning contextual spatial features in time, to capture four-dimensional information and support motion learning from noisy data. The 4D location of the proposed $f^{4D}()$ features is parameterized by the similarity parameters $\theta = (x, y, z, \vec{\alpha}_x, \vec{\alpha}_y, \vec{\alpha}_z, s_x, s_y, s_z)$ plus time t :

$$f^{4D}(\theta(t), T|I, s) = \tau(f^{3D}(I, \theta(t + i * s)), i = -T, \dots, T) \quad (4.3)$$

As presented in the previous paragraph, three-dimensional $f^{3D}()$ features can be constructed to extract simple gradient and intensity information from steerable pattern spatially align with $\theta(t)$. Please note that in our context, the similarity parameters θ are defined separately for the four heart valves (see section 3.3). Knowing that the motion is locally coherent in time, $f^{3D}()$ is applied in a temporal neighborhood $t - T$ to $t + T$ at discrete locations evenly distributed with respect to the current time t (see figure 4.8). The final value of a Local-Spatial-Temporal (LST) feature is the result of time integration using a set of linear kernels τ , which weight spatial features $f^{3D}()$ according to their distance from the current frame t . A simple example of τ , also used in our implementation, is the uniform kernel over the interval $[-T, T]$:

$$\tau = \frac{1}{2T + 1} \sum_{i=-T}^T (f^{3D}(I, \theta(t + i * s))) \quad (4.4)$$

For this choice of τ , each f^{3D} contributes equally to the f^{4D} . The parameter T steers the size of the temporal context, while s is a time normalization factor derived from the training set and the number of time steps of the volume sequence I . Values for T can be selected by the probabilistic boosting tree (PBT) [164] in the training stage. Since the time window size has an inverse relationship with the motion locality, the introduced 4D local features are in consensus with a coarse-to-fine search. Our experimental results support this property by showing that the features with larger T values are selected to capture the lower frequency motion, and the value of T decreases for higher frequency motion components.

4.2.3 Training, Testing and Space Marginalization

The classic discriminative learning approach to parameter estimation involves searching a domain Σ for the highest probable values using a learned detector D . Assuming an abstract model parameterization x and an input image I , the task can be formulated as:

$$\operatorname{argmax}_x p(x|I) = \operatorname{argmax}_x D(x, I), x \in \Sigma \quad (4.5)$$

The entire process involves two phase: training and testing. Firstly, the detector D is constructed during an offline training phase. Subsequently, this is used to scan the parameter search space and find the optimal solution in the online testing phase.

Training: The objective of the training stage is to learn a detector D from a given training set. This comprises out of pairs of labeled parameter instances (x, y) , $y \in \{+1, -1\}$ and includes positive $(x, +1)$ and negative $(x, -1)$ samples. Positive and negative examples are obtained from a set of images associated with a ground truth annotation (I, \bar{x}) . In general, positives are considered in a close vicinity to the ground truth, with respect to a distance measure d and threshold value δ_s :

$$y = \begin{cases} 1 & \text{if } d(x, \bar{x}) < \delta_s \\ -1 & \text{otherwise} \end{cases} \quad (4.6)$$

Weak learners h are employed to model the target distribution. Those are constructed from a pool of image features parameterized by the model:

$$h(x, f, p, \delta_f) = \begin{cases} 1 & \text{if } pf(x) < p\delta_f \\ 0 & \text{otherwise} \end{cases} \quad (4.7)$$

Examples of feature f relevant for our work were presented in section 4.2.2. The threshold δ_f and polarity p are chosen during learning such that the minimum number of training samples are misclassified. In practice, single weak learners h cannot perform the estimation task with low error. Therefore, as illustrated in section 4.2.1, boosting algorithms are employed to select key weak learners and aggregate them to build a strong classifier D .

Testing: The objective of the testing stage is to identify the highest probable parameter values in a predefined search domain Σ . The search domain is usually discretized by a set of hypotheses \mathcal{H} . The learned detector D exhaustively tests and ranks each parameter hypothesis, while the highest ranked is generally considered the final result. Exhaustive search provides robustness against local minima and assuming that the true solution is captured in \mathcal{H} , it also provides the optimal parameter estimation.

However, the exhaustive search strategy can become computationally expensive as its complexity increases exponentially with the number of target parameters, which prohibits estimation of high-dimensional models. For instance, consider the problem of estimating the similarity transformation of an object in a three-dimensional Euclidean space. The model has nine parameters $\dim(x) = 9$ and if each dimension of the search domain Σ is discretized by only 10 values, the number of hypotheses to be tested is $|\mathcal{H}| = 10^9$, which is beyond the computation power of current computers.

To overcome this limitation, the next paragraph presents a space marginalization framework, which drastically reduces the search domain.

Marginal Space Learning: In general, it is unnecessary to search the entire domain Σ , as the target a posteriori is clustered in a small region of the high-dimensional space spanned by the parameters in x . This observation is exploited within the Marginal Space Learning (MSL) framework [197], which breaks the original domain Σ into subsets of marginal spaces with increased dimensionality:

$$\Sigma_1 \subset \Sigma_2 \subset \dots \subset \Sigma_n = \Sigma \quad (4.8)$$

where $\dim(\Sigma_1) \ll \dim(\Sigma)$ and $\dim(\Sigma_k) - \dim(\Sigma_{k-1})$ is small. A search in Σ_1 with a detector D_1 learned in this marginal space finds a subspace $\mathcal{C}_1 \subset \Sigma_1$, which contains only the most probable parameter values and discards the rest of the space, such that $|\mathcal{C}_1| \ll |\mathcal{H}_1|$. Another stage of training and testing is performed in the extended $\mathcal{C}_1^e = \mathcal{C}_1 \times \mathcal{H}_2 \subset \Sigma_2$ to obtain a restricted marginal space $\mathcal{C}_2 \subset \Sigma_2$. The procedure ends when the final dimensionality of Σ is reached.

In practice, the optimal arrangement for MSL sorts the marginal spaces in a descending order based on their variance. Learning parameters with low variance first will decrease the overall precision of the detection.

4.3 Object Localization and Rigid Motion Estimation

The goal of object localization or detection is to identify regions in images which contain a predefined object of interest. This is a natural first step when extracting high level information from images. The majority of existent methods focus on specific objects such as faces [192], pedestrians [146], or vehicles [151].

The task in our context is to determine the location of each specific valve from multimodal cardiac images. In contrast to classic detection problems focused on the identification of multiple instances of the target object from input images, we assume the singleton existence of the target valve, and we are rather interested in its location parameters. Thus, the location and motion parameters θ of each valve, defined in section 3.3, are estimated from a sequence of volumes I :

$$\begin{aligned} \arg \max_{\theta} p(\theta|I) &= \arg \max_{\theta} \\ p(\theta(0), \dots, \theta(n-1)|I(0), \dots, I(n-1)) \end{aligned} \quad (4.9)$$

4.3.1 Location Estimation

To solve equation 4.9, we formulate the object localization as a classification problem and estimate $\theta(t)$ for each time step t independently from the corresponding volumes $I(t)$. The probability $p(\theta(t)|I(t))$ can be modeled by a learned detector D , which evaluates and scores a large number of hypotheses for $\theta(t)$. However, we recall that $\theta = ((c_x, c_y, c_z), (\vec{\alpha}_x, \vec{\alpha}_y, \vec{\alpha}_z), (s_x, s_y, s_z))$, and the exhaustive search along a nine-dimensional space is computationally prohibited even for a sparse discretization.

To overcome this limitation, we apply the MSL framework and break the original parameter space into a subset of increasing marginal spaces:

$$\Sigma_1 \subset \Sigma_2 \subset \dots \subset \Sigma_n = \Sigma$$

The nine-dimensional space described by the similarity transform in a three-dimensional Euclidean space is decomposed as follows:

$$\begin{aligned} \Sigma_1 &= (c_x, c_y, c_z) \\ \Sigma_2 &= (c_x, c_y, c_z, \vec{\alpha}_x, \vec{\alpha}_y, \vec{\alpha}_z) \\ \Sigma_3 &= (c_x, c_y, c_z, \vec{\alpha}_x, \vec{\alpha}_y, \vec{\alpha}_z, s_x, s_y, s_z) \end{aligned}$$

where Σ_1 represents the position marginal space, Σ_2 the position + orientation marginal space and Σ_3 the position + orientation + scale marginal space, which coincides with the original domain. In practice, the optimal arrangement for MSL sorts the marginal spaces in a descending order based on their variance. In our case, due to the CT, MRI and TEE acquisition protocols and physiological variations of the heart, the highest variance comes from translation followed by orientation and scale. This order is confirmed by our experiments to output the best results.

From the marginalization of the search domain, the target posterior probability can be expressed as:

$$\begin{aligned} p(\theta(t)|I(t)) &= p(c_x, c_y, c_z|I(t)) \\ p(\vec{\alpha}_x, \vec{\alpha}_y, \vec{\alpha}_z|c_x, c_y, c_z, I(t)) \\ p(s_x, s_y, s_z|\vec{\alpha}_x, \vec{\alpha}_y, \vec{\alpha}_z, c_x, c_y, c_z, I(t)) \end{aligned}$$

Instead of using a single detector D , we train detectors for each marginal spaces D_1 , D_2 and D_3 , and estimate $\theta(t)$ by gradually increasing the dimensionality. After each stage only a limited number of high-probability candidates are kept to significantly reduce the search space. Initially, D_1 is trained to model the position posteriori $p(c_x, c_y, c_z|I(t))$ using the Probabilistic Boosting Tree and 3D Haar wavelet image features as discussed in section 4.2. During testing, D_1 exhaustively searches the three-dimensional marginal space Σ_1 to rank all position hypotheses $\mathcal{H}_1 = (c_x, c_y, c_z)$ and preserve the most probable candidates in \mathcal{C}_1 . The second detector D_2 models $p(\vec{\alpha}_x, \vec{\alpha}_y, \vec{\alpha}_z|c_x, c_y, c_z, I(t))$ to jointly estimate the position and orientation. The training samples are obtained by augmenting the position candidates with orientation hypotheses $(\vec{\alpha}_x, \vec{\alpha}_y, \vec{\alpha}_z)$, while the Probabilistic Boosting Tree and 3D steerable features are applied to learn the posteriori. Analogous, D_2 evaluates all position + orientation hypotheses $\mathcal{H}_2 = (c_x, c_y, c_z, \vec{\alpha}_x, \vec{\alpha}_y, \vec{\alpha}_z)$ and retains the best candidates in \mathcal{C}_2 . The final detector D_3 learns the actual similarity transformation $p(s_x, s_y, s_z|\vec{\alpha}_x, \vec{\alpha}_y, \vec{\alpha}_z, c_x, c_y, c_z, I(t))$ by adding scale parameters to the search domain. D_3 it is trained only on the pruned search space built by $\mathcal{C}_2 \times (s_x, s_y, s_z)$ using the PBT and steerable features. Experimentally determined as in [197], 100 highest score candidates are retained in Σ_1 , 50 in Σ_2 and 25 in Σ_3 , such that the smallest subgroup which is likely to include the optimal solution is preserved.

For an unseen volume $I(t)$, all position hypotheses \mathcal{H}_1 for a subject valve are tested by D_1 and the top 100 candidates are stored in \mathcal{C}_1 . Each candidate is augmented with the orientation hypotheses and D_2 is used to estimate the most probable position + orientation candidates \mathcal{C}_2 . In the last stage D_3 determines the most likely 25 candidates of similarity transformer parameters. The procedure is repeated for each of the four valves and each volume $I(t)$ in the input series $I(0), \dots, I(n-1)$.

4.3.2 Robust Motion Aggregation

For a target valve, we obtained the candidates with the highest score estimated at each time step t , $t = 0, \dots, n-1$: $[\theta_0(0) \dots \theta_{25}(0)] \dots [\theta_0(n-1) \dots \theta_{25}(n-1)]$. A straightforward approach to the final solution can be the frame-wise averaging of the candidates. However, to obtain a temporally consistent global location and motion $\theta(t)$, a RANSAC estimator is employed.

To suppress temporally inconsistencies, we assume a constant model for the cardiac motion, which drives the global movement of the entire valvular apparatus. From randomly sampled candidates, the one yielding the maximum number of inliers is picked as the final motion. Inliers are considered within a distance of $\sigma = 7mm$ from the current candidate and extracted at each time step t . The distance measure $d(\theta(t)_1, \theta(t)_2)$ is given by the maximum L1 norm of the standard unit axis deformed by the parameters $\theta(t)_1$ and $\theta(t)_2$, respectively:

$$\begin{aligned}
L1(\vec{a}_1, \vec{a}_2) &= \max \{|x1 - x2|, |y1 - y2|, |z1 - z2|\} \\
d(\theta(t)_1, \theta(t)_2) &= \frac{1}{4}(L1(\vec{c}_1, \vec{c}_2) + L1(\vec{X}_1 s_{x1}, \vec{X}_2 s_{x2}) + L1(\vec{Y}_1 s_{y1}, \vec{Y}_2 s_{y2}) \\
&\quad + L1(\vec{Z}_1 s_{z1}, \vec{Z}_2 s_{z2}))
\end{aligned} \tag{4.10}$$

where X, Y and Z are the unit axes obtained from the Euler angles $(\vec{\alpha}_x, \vec{\alpha}_y, \vec{\alpha}_z)$, \vec{c} the position vectors, and s_x, s_y, s_z scale parameters. The procedure is applied for each valve separately, in order to obtain the resulting time-coherent similarity transform $\theta(t)_{aortic}$, $\theta(t)_{mitral}$, $\theta(t)_{tricuspid}$ and $\theta(t)_{pulmonary}$, which describes the corresponding global location and rigid motion over the entire cardiac cycle.

4.4 Trajectory Spectrum Learning for Non-Rigid Motion Estimation

In this section we propose a novel Trajectory Spectrum Learning (TSL) algorithm to localize and estimate the non-rigid motion of the anatomical landmarks defined in section 3.4. Most existing methods compute trajectories by evolving the object positions along the time direction. To exploit the temporal information, a dynamic model of the object motion is incorporated in many algorithms, such as condensation [77] and particle filtering [41]. Other methods are based on iterative optimization such as mean shift [33] and Kanade-Lucas-Tomasi tracking [159]. Limited by the assumption of the local temporal constraint, detecting the motion directly in the Euclidean space is often found difficult to guarantee a smooth result and might be affected by drifting. These issues, however, can be addressed effectively by considering the global characteristics of the motion.

We formulate the motion estimation problem as spectrum learning and detection in the trajectory space. The object localization and motion estimation, referred traditionally as detection and tracking, are solved simultaneously. Consequently, a robust and efficient approach is proposed to estimate the motion of non-rigid objects with the following advantages:

- By decomposing the full trajectory space into orthogonal subspaces defined by generic bases, such as the Discrete Fourier Transform (DFT), the obtained representation is shown to be compact especially for the periodic motions, such as the movements of the heart valves. This resulting compact representation allows efficient learning and optimization in its marginal spaces.
- In the training stage, local features are extended in the temporal domain to integrate the time coherence constraint. The Local-Spatial-Temporal (LST) features are selected via boosting to form strong classifiers.
- In the testing stage, an incremental optimization is performed in sparse marginal spaces learned from the training data. To maximize efficiency and robustness we constrain the search based on clusters of hypotheses defined in each subspace.

Please note that our proposed approach is not limited to any particular type of generic bases. The Discrete Cosine Transform (DCT) or the Discrete Wavelet Transform (DWCT) can be used without any major changes.

4.4.1 Problem Formulation

Based on the determined global location and rigid motion, in this section we introduce a novel trajectory spectrum learning algorithm to estimate the non-linear valve movements from volumetric sequences. Considering the representation in section 3.4 equation 3.2, the objective is to find for each landmark j its trajectory \vec{L}^j , with the maximum posterior probability from a series of volumes $I(t)$, given the rigid motion $\theta(t)$:

$$\arg \max_{\vec{L}^j} p(\vec{L}^j | I, \theta) = \arg \max_{\vec{L}^j} p(\vec{L}^j(0), \dots, \vec{L}^j(n-1) | I(0), \dots, I(n-1), \theta(0), \dots, \theta(n-1)) \quad (4.11)$$

Note that Eq. 4.11 only models the non-rigid landmark motion, as the global location and motion is removed from the trajectories by aligning $L^j(t)$, $j = 0 \dots 10$ with the aortic similarity parameters $\theta(t)_{aortic}$, $j = 11 \dots 17$ with the mitral similarity parameters $\theta(t)_{mitral}$, $j = 18 \dots 22$ with the tricuspid similarity parameters $\theta(t)_{tricuspid}$, and $j = 23 \dots 35$ with the pulmonary similarity parameters $\theta(t)_{pulmonary}$ estimated as described in section 4.3.

While it is difficult to solve Eq. 4.11 directly, various assumptions, such as the Markovian property of the motion [191], have been proposed to the posterior distribution over $L^j(t)$ given images up to time t . However, results are often not guaranteed to be smooth and may diverge over time, due to error accumulation. These fundamental issues can be addressed effectively if both, temporal and spatial appearance information is considered over the whole sequence at once.

In section 3.7.1 we showed that the trajectory can be uniquely represented by the concatenation of its Discrete Fourier Transform (DFT) coefficients,

$$\vec{s}^j = [\vec{s}^j(0), \vec{s}^j(1), \dots, \vec{s}^j(n-1)] \quad (4.12)$$

where $\vec{s}^j(f) \in \mathcal{C}^3$ is the frequency spectrum of the x , y , and z components of the trajectory $\vec{L}^j(t)$, and $f = 0, 1, \dots, n-1$. The magnitude of $\vec{s}^j(f)$ is used to describe the shift-invariant motion according to the shift theorem of DFT, while the phase information is used to handle temporal misalignment. From the DFT parameterization the equation 4.11 can be reformulated as finding the DFT spectrum \vec{s}^j , with the maximal posterior probability:

$$\arg \max_{\vec{s}^j} p(\vec{s}^j | I, \theta) = \arg \max_{\vec{s}^j} p(\vec{s}^j(0), \dots, \vec{s}^j(n-1) | I(0), \dots, I(n-1), \theta(0), \dots, \theta(n-1)) \quad (4.13)$$

Instead of estimating the motion trajectory directly, we apply discriminative learning to detect the spectrum \vec{s}^j in the frequency domain by optimizing equation 4.13. The proposed formulation benefits from three qualities:

- the DFT decomposes the trajectory space in **orthogonal subspaces**, which enables the estimation of each component $\vec{s}^j(f)$ separately.

- the DFT spectrum **representation is compact**, especially for periodic motion allowing for efficient learning and optimization.
- the **posterior distribution is clustered** in small regions facilitating marginalization and pruning of the higher dimensional parameter spaces.

We observed that in many real applications especially for the periodic motions, such as the movements of heart valves, the posterior distribution is clustered in a small region in the high dimensional trajectory space. Therefore, for each component $\vec{s}^j(f)$, we can select a limited number of candidates from the previous components, $\vec{s}^j(0), \dots, \vec{s}^j(f-1)$, to reduce the search space. To prevent overfitting to the training image sequences, we use a small set of local image features in the training stage and use cross-validation to select the stable features.

4.4.2 Search Space Marginalization

Inspired by the MSL reviewed in section 4.2.3, we efficiently perform trajectory spectrum learning and detection in DFT subspaces with gradually increased dimensionality. The intuition is to perform a spectral coarse-to-fine motion estimation, where the detection of coarse level motion (low frequency) is incrementally refined with high frequency components representing fine deformations.

As described earlier, the motion trajectory is parameterized by the DFT spectrum components $\vec{s}^j(f), f = 0, \dots, n-1$. In section 3.7.1 we introduced the search space marginalization used for the learning 4.4.3 and estimation 4.4.4 of the trajectories. We differentiate between two types of subspaces, individual component subspaces $\Sigma^{(k)}$ and marginalized subspaces Σ_k defined as:

$$\Sigma^{(k)} = \{\vec{s}(k)\} \quad (4.14)$$

$$\Sigma_k = \Sigma_{k-1} \times \Sigma^{(k)} \quad (4.15)$$

$$\Sigma_0 \subset \Sigma_1 \subset \dots \subset \Sigma_{r-1}, r = |\zeta| \quad (4.16)$$

The subspaces $\Sigma^{(k)}$ are efficiently represented by a set of corresponding hypotheses $\mathcal{H}^{(k)}$ obtained from the training set. The pruned search space enables efficient learning and optimization:

$$\Sigma_{r-1} = \mathcal{H}^{(0)} \times \mathcal{H}^{(1)} \times \dots \times \mathcal{H}^{(r-1)}, r = |\zeta|$$

4.4.3 Learning in Marginal Trajectory Spaces

The trajectory learning is performed in marginal spaces with increasing dimensionality using the local-spatial-temporal features (see section 4.2.2). The training algorithm starts by learning the posterior probability distribution in the DC marginal space Σ_0 . Subsequently, the learned detector D_0 is applied to identify high probable candidates \mathcal{C}_0 from the hypotheses $\mathcal{H}^{(0)}$. In the following step, the dimensionality of the space is increased by adding the next spectrum component (in this case the fundamental frequency, $\Sigma^{(1)}$). Learning is performed in the restricted space defined by the extracted high probability

for each joint $j \in 1, \dots, m - 1$ in model
 for each frequency $k \in 1, \dots, r - 1$ in spectrum

Generate positive and negative positions

Input: Detectors D_0, \dots, D_{k-1} and ground-truth spectrum S and clustered hypotheses \mathcal{H} from the training data

Output: Positive positions Pos_k and negative positions Neg_k

- compute the trimmed ground truth \vec{s}_k spectrum:

$$\vec{s}_k = [s(0), \dots, s(k), 0, \dots, 0]$$

- construct samples from the permutation of the candidates from \mathcal{C}_{k-1} with hypotheses $\mathcal{H}^{(k)}$, i.e., $\mathcal{C}_{k-1} \times \mathcal{H}^{(k)}$
- positive positions are in a certain range $dist_{pos}$ from the trimmed trajectory $\vec{L}_k = IFFT(\vec{s}_k)$ for the whole trajectory: $\forall \vec{C}_k \in \mathcal{C}_{k-1} \times \mathcal{H}^{(k)}$, insert \vec{C}_k in Pos_k if $d(IFFT(\vec{S}_k), IFFT(\vec{C}_k)) < dist_{pos}$, where $d()$ is the distance function defined in Eqn. 4.17. e.g. $dist_{pos} = 1.5$
- negative positions are further away than $dist_{neg}$ from X_k : $\forall \vec{C}_k \in \mathcal{C}_{k-1} \times \mathcal{H}^{(k)}$, insert \vec{C}_k in Neg_k if $d(IFFT(\vec{s}_k), IFFT(\vec{C}_k)) > dist_{neg}$, e.g. $dist_{neg} = 3.5$

Learn detector D_k for each component k

Input: Positive positions Pos_k and negative positions Neg_k

Output: Posterior distribution D_k

- extract 4D local-spatial-temporal features F^{4D} as described in section 4.2.2, based on the positive positions Pos_k and negative positions Neg_k
- train the detector D_k using the probabilistic boosting tree based on the local-spatial-temporal features

Figure 4.9: The outline of our marginal trajectory space learning algorithm.

regions and hypotheses set $\mathcal{C}_0 \times \mathcal{H}^{(1)}$. The same operation is repeated until reaching the genuine search space Σ_{r-1} .

For each marginal space Σ_k , corresponding discriminative classifiers D_k are trained on sets of positives Pos_k and negatives Neg_k . We analyze samples constructed from high probability candidates \mathcal{C}_{k-1} and hypotheses $\mathcal{H}^{(k)}$. The sample set $\mathcal{C}_{k-1} \times \mathcal{H}^{(k)}$ is separated into positive and negative examples by comparing the corresponding trajectories to the ground truth in the spatial domain using the following distance measure:

$$d(\vec{L}_1^j, \vec{L}_2^j) = \max_t \|\vec{L}_1^j(t) - \vec{L}_2^j(t)\| \quad (4.17)$$

where \vec{L}_1^j and \vec{L}_2^j denote two trajectories for the j -th landmark. It is important

for each joint $j \in 1, \dots, m - 1$ in model
 for each frequency $k \in 1, \dots, r - 1$ in spectrum

Find candidates \mathcal{C}_k for marginal spaces $0, \dots, k$

Input: Candidates \mathcal{C}_{k-1} , detector D_k , augmented hypothesis set $\mathcal{H}^{(k)}$, and testing image sequence I

Output: Candidates \mathcal{C}_k

- construct samples from the permutation of the candidates from \mathcal{C}_{k-1} with hypotheses $\mathcal{H}^{(k)}$, i.e., $\mathcal{C}_{k-1} \times \mathcal{H}^{(k)}$
 - evaluate the posterior probability on the testing image sequence I : $\forall C_k \in \mathcal{C}_{k-1} \times \mathcal{H}^{(k)}$, insert C_k in \mathcal{C}_k if a high value is returned by the cost function defined in Eqn. 4.18
-

Figure 4.10: The outline of our parameter search algorithm.

to note that the ground truth spectrum is trimmed to the $k - th$ component to match the dimensionality of the current marginal space Σ_k . Positives are in a certain distance $dist_{pos}$ (e.g. 1.5mm) to the ground-truth over the whole trajectories. Negatives, however, are selected individually for each time step, if the tested position in space and time is larger than $dist_{neg}$ (e.g. 3.5mm). Given the local-spatio-temporal features extracted from positive and negative positions, the probabilistic boosting tree (PBT) is applied to train a strong classifier D_k . The above procedure is illustrated in figure 4.9 and repeated by increasing the search space dimensionality in each step, until detectors are trained for all marginal spaces $\Sigma_0, \dots, \Sigma_{r-1}$.

4.4.4 Motion Trajectory Estimation

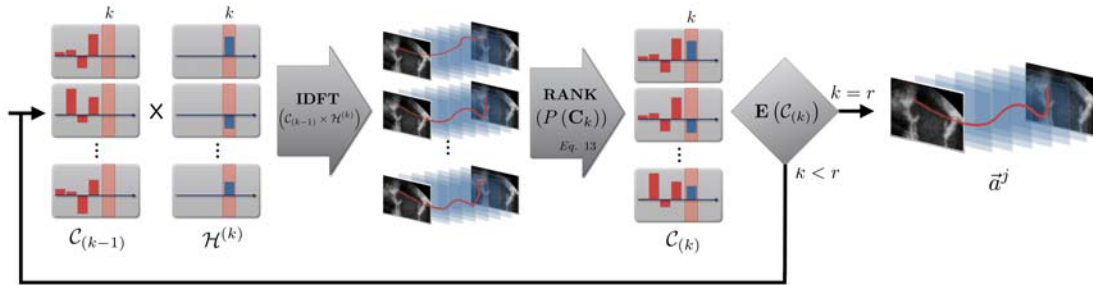


Figure 4.11: Diagram depicting the estimation of non-rigid landmark motion using trajectory spectrum learning.

In this section we describe the detection procedure for object localization and motion estimation of valve landmarks from unseen volumetric sequences. As discussed in sec-

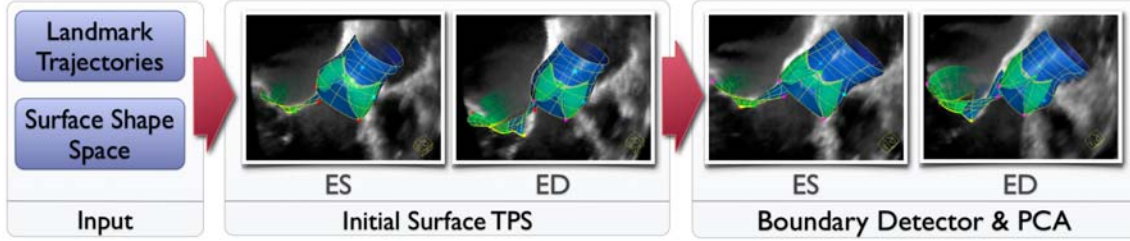


Figure 4.12: Diagram depicting the estimation of the comprehensive valve model. Estimation in cardiac key phases, end-diastole and end-systole.

tion 4.4.1, the local non-rigid motion is parameterized by both magnitude and phase of the trajectory spectrum $\vec{s}^j(f)$. The parameter estimation is conducted in the marginalized search spaces $\Sigma_0, \dots, \Sigma_{r-1}$ using the trained spectrum detectors D_0, \dots, D_{r-1} as illustrated in figure 4.11. Starting from an initial zero-spectrum, we incrementally estimate the magnitude and phase of each frequency component $\vec{s}(k)$. At the stage k , the corresponding robust classifier D_k is exhaustively scanned over the potential candidates $\mathcal{C}_{k-1} \times \mathcal{H}^{(k)}$. The probability of a candidate $\vec{C}_k \in \mathcal{C}_{k-1} \times \mathcal{H}^{(k)}$ is computed by the following objective function:

$$p(\vec{C}_k) = \prod_{t=0}^{n-1} D_k(IDFT(\vec{C}_k), I, t) \quad (4.18)$$

where $t = 0, \dots, n-1$ is the time instance (frame index). After each step k , the top 50 trajectory candidates \mathcal{C}_k with high probability values are preserved for the next step $k+1$. The set of potential candidates \mathcal{C}_{k+1} is constructed from the permutation of the candidates $\mathcal{C}_k \times \mathcal{H}^{(k+1)}$ (see figure 4.10). The procedure is repeated until a final set of trajectory candidates \mathcal{C}_{r-1} , defined in the full space Σ_{r-1} , is computed. The final trajectory is reported as the average of all elements in \mathcal{C}_{r-1} (see figure 4.10).

The procedure is applied for each anatomical landmark separately, to obtain its corresponding location and non-rigid motion $\vec{L}^j(t)$, $j = 0, \dots, 35$ from an unseen sequence of cardiac volumes $I(t)$.

4.5 Comprehensive Model Estimation

The final stage in our hierarchical model estimation algorithm is the delineation of the full morphology and dynamics of the heart valves:

$$\arg \max_M p(M|I, \theta, \vec{L}) = \arg \max_M p(M(0), \dots, M(n-1) | I(0), \dots, I(n-1), \theta(0), \dots, \theta(n-1), \vec{L}(0), \dots, \vec{L}(n-1)) \quad (4.19)$$

The shape model is first estimated in the End-Diastole (ED) and End-Systole (ES) phases of the cardiac cycle as presented in section 4.5.1. Then, in section 4.5.2 the non-rigid deformation is propagated to the remaining phases using a learned motion prior.

4.5.1 Estimation in Cardiac Key Phases

Using the previously estimated model parameters, a pre-computed mean shape of the comprehensive valvular model is placed into the volumes $I(t_{ED})$ and $I(t_{ES})$ through a thin-plate-spline (TPS) transform [20]. The initial estimate is then deformed to fit the true valvular anatomy using learned object boundary detectors, regularized by statistical shape models (see figure 4.12).

In section 3.7.2 we showed how a mean shape model \bar{X} can be obtained from a training set of valvular models. The obtained mean shape is mapped into the image by a TPS transformation estimated from the pair of corresponding landmarks. Given the set $\{(\vec{L}^j, \bar{L}^j), j = 0, \dots, 35\}$, where \vec{L}^j are the landmarks estimated in section 4.4 and \bar{L}^j the corresponding anatomical location in the mean shape, the TPS transformation is defined as follows:

$$T_{TPS}(\bar{L}^i) := \begin{bmatrix} A & \vec{b} \\ 0 & 1 \end{bmatrix} \begin{bmatrix} \bar{L}^i \\ 1 \end{bmatrix} + \begin{bmatrix} \sum_{i=1}^n \vec{w}_i U(|\vec{L}^i - \bar{L}^i|) \\ 0 \end{bmatrix} \quad (4.20)$$

where A and b are the affine parameters, w_i the non-affine parameters, and U the TPS radial basis functions: $U(r) = r^2 \log r^2$. The coefficients are chosen to minimize the energy of a thin metal plate:

$$\int \int_{\mathbb{R}^2} \left(\frac{\partial^2 T_{TPS}}{\partial x^2} \right)^2 + 2 \left(\frac{\partial^2 T_{TPS}}{\partial x \partial y} \right)^2 + \left(\frac{\partial^2 T_{TPS}}{\partial y^2} \right)^2 dx dy \quad (4.21)$$

Thus, the comprehensive model of each valve is initialized with the corresponding mean shape transform $T_{TPS}(\bar{X})$.

The ASM framework [36] is commonly applied to shift boundary points of an initial estimate towards locations with abrupt intensity variations under statistical shape constraints. Solely gradient-based detectors perform poorly in our case due to weak and noisy edges, signal dropouts and low signal-to-noise ratio characteristic to cardiac images.

We have shown that learning based methods provide robust results [197, 191] when utilizing both gradients and image intensities at different image resolutions and by incorporating the local context. Hence, the non-rigid deformation is guided by a boundary detector D_b learned using the probabilistic boosting-tree and steerable features. After initialization, D_b evaluates hypotheses for each discrete boundary point along its corresponding normal direction. The new boundary points are set to the hypotheses with maximal probability. To guarantee physiologically compliant results, the final model is obtained after projecting the estimated points to the statistical shape space described in section 4.4.

The above procedure is applied separately for the four valves in the end-diastolic (ED) and end-systolic (ES) frames, $I(t_{ED})$ and $I(t_{ES})$, to estimate the comprehensive valvular models $M_{aortic}(t_{ED})$, $M_{mitral}(t_{ED})$, $M_{tricuspid}(t_{ED})$, $M_{pulmonary}(t_{ED})$, $M_{aortic}(t_{ES})$, $M_{mitral}(t_{ES})$, $M_{tricuspid}(t_{ES})$ and $M_{pulmonary}(t_{ES})$.

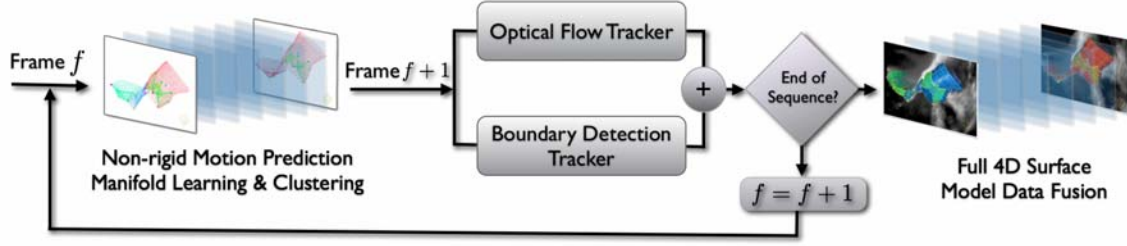


Figure 4.13: Diagram depicting the estimation of the comprehensive valve model. Estimation in the full cardiac cycle.

4.5.2 Motion Estimation

Starting from the detection results in the ED and ES phases, the model deformations are propagated in both forward and backward directions using learned motion priors similar as in [191] (see figure 4.13). The motion prior is estimated at the training stage using motion manifold learning and hierarchical K-means clustering, from a pre-annotated database of sequences containing one cardiac cycle each. First the temporal deformations are aligned by 4D generalized procrustes analysis. Next a low-dimensional embedding is computed from the aligned training sequences using the ISOMAP algorithm [154], to represent the highly nonlinear motion of the heart valves. Finally, in order to extract the modes of motion \bar{X}_m , the motion sequences are clustered with hierarchical K-means based on the Euclidean distance in the lower dimensional manifold.

One-step forward prediction is used to select the correct motion mode for predicting time step T . Therefore the previous shapes $M(t)$ from time steps $t = 1 \dots T - 1$ and the corresponding time steps in each of the motion modes \bar{X}_m are sub-sampled by a constant factor k and the TPS transform T_{TPS} computed. The mean error between the warped shape and the corresponding shape on each motion mode is computed, and the motion mode with minimum distance is selected for prediction:

$$E_{TPS}(\bar{X}_m(t), M(t)) = \frac{k}{N} \sum_{j=1}^{N/k} \|\bar{X}_m^j(t) - T_{TPS}(M^j(t))\| \quad (4.22)$$

$$\bar{X}(T) = \arg \min_m \frac{1}{T-1} \sum_{t=1}^{T-1} E_{TPS}(\bar{X}_m(t), M(t)) \quad (4.23)$$

where N denotes the number of points in $M(t)$, \bar{X}_m^j and M^j are shape vertices, and $\bar{X}(T)$ the selected motion mode. The shape prediction $M(T)'$ for the following frame T is then computed by inverse TPS mapping $M(T)' = T_{TPS}^{-1}(\bar{X}(T))$ and the boundary detector D_b deforms the initialization to make it fit the data in the update step.

To ensure temporal consistency and smooth motion and to avoid drifting and outliers, two collaborative trackers, an optical flow tracker and a boundary detection tracker D_b , are used in our method. The optical flow tracker directly computes the temporal displacement

for each point from one frame to the next. Initialized by one-step forward prediction, the detection tracker obtains the deformations in each frame with maximal probability. The results are then fused into a single estimate by averaging the computed deformations and the procedure is repeated until the full 4D model is estimated for the complete sequence. In this way the collaborative trackers complement each other, as the optical flow tracker provides temporally consistent results and its major issue of drifting is addressed by the boundary detection along with the one-step forward prediction.

Thus, the entire patient-specific estimation of valvular models is concluded with the determination of M_{aortic} , M_{mitral} , $M_{tricuspid}$ and $M_{pulmonary}$.

4.6 Results

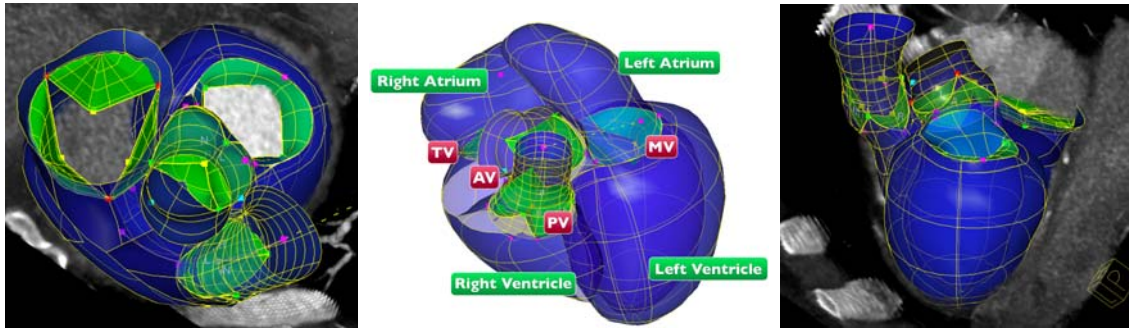


Figure 4.14: Examples of the full heart estimation from cardiac CT.

In this section we demonstrate the performance of the proposed patient-specific parameter estimation framework of the cardiac valvular apparatus from multi-modal images. Experiments are performed on a large and heterogeneous data set described in section 4.6.1. Ground-truth parameters are obtained by following a standardized process discussed in section 4.6.2. The performance of the object localization and rigid motion estimation is presented in section 4.6.3. Subsequently, results of the trajectory spectrum learning algorithm and comprehensive model estimation are given in section 4.6.4 and 4.6.5, respectively. Section 4.6.6 demonstrates the estimation robustness with respect to multiple image modalities and inter-user variability. The overall performance is summarized in section 4.6.7, while preliminary results for the full heart estimation (chamber modeling from [197]) are illustrated in figure 4.14.

4.6.1 Data Set

Cardiac studies were acquired using CT, Ultrasound and MRI scanners from 476 patients affected by a large spectrum of cardiovascular and valvular heart diseases. Among the included pathologies are: regurgitation, stenosis, prolapse, aortic root dilation, bicuspid aortic valve and Tetralogy of Fallot. The imaging data set includes 1330 cardiac CT, 5061 TEE and 83 CMR volumes, which were collected from medical centers around the world

over a period of three years. Using heterogeneous imaging protocols, cardiac CT exams were performed with Siemens Somatom Sensation or Definition scanners, TEE images were acquired with Siemens Acuson Sequoia, Mountain View CA, USA and Philips IE33 ultrasound machines, and CMR data was captured with Siemens MAGNETOM Avanto devices.

The ECG gated cardiac CT sequences include 10 volumes per cardiac cycle, where each volume contains 80-350 slices with 153×153 to 512×512 pixels. The in-slice resolution is isotropic and varies between 0.28 to 1.00mm with a slice thickness from 0.4 to 2.0mm. TEE data includes an equal amount of rotational (3 to 5 degrees) and matrix array acquisitions. A complete cardiac cycle is captured in a series of 7 to 39 volumes, depending on the patient's heart beat rate and scanning protocol. Image resolution and size varies for the TEE data set from 0.60 to 1.00mm and $136 \times 128 \times 112$ to $160 \times 160 \times 120$ voxels, respectively. CMR studies include isotropic, end-diastolic volumetric acquisitions, with contrast agent in the right side of the heart. Capture ranges vary between $144 \times 256 \times 80$ to $176 \times 256 \times 122$ and resolution from 1.20 to 1.56mm. Figure 4.15 illustrates examples of input cardiac data.

Please note that while cardiac CT acquisitions cover all valves, it is not the case for the TEE exams, which usually focus either on the aortic or mitral valve. Similarly, the CMR data is specifically acquired for the Right Ventricular Outflow Tract (RVOT) and pulmonary valve analysis. Due to lack of annotation, results for the tricuspid valve estimation are not reported.

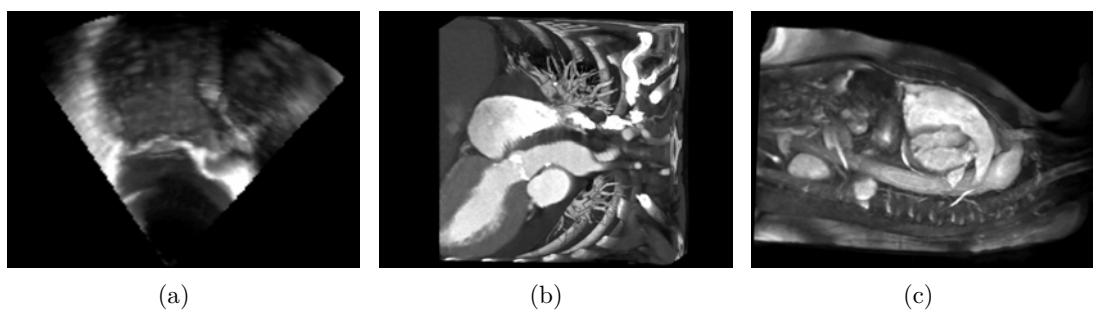


Figure 4.15: Examples of cardiac data: (a) TEE study, (b) cardiac CT study. and (c) CMR study.

4.6.2 Ground Truth

Considering the machine learning approaches adopted throughout this thesis, the ground truth is a crucial component for our framework, equally important for the training and testing of the proposed algorithms. Therefore, each volume in our data set is associated with an annotation obtained through an expert-guided process that includes the following steps:

- the non-rigid landmark motion model is manually determined by placing each

anatomical landmark (see section 3.4) at the correct location in the entire cardiac cycle of a given study.

- the comprehensive valve model is initialized through its mean model placed at the correct image location, expressed by the thin-plate-spline transform estimated from the previously annotated non-rigid landmark motion model (see section 4.5).
- the annotation of the comprehensive valve model is manually adjusted to delineate the true valves boundaries over the entire cardiac cycle (see section 3.5).
- from the annotated non-rigid landmark motion model, the global location and rigid motion model is determined as described in section 3.4.

The model parameters θ , L and M obtained from the annotation are considered the ground truth values. Independent of the acquisition modality, the process is equally performed for each valve contained in a given cardiac study. Three-fold cross validation was performed for all experiments and reported results reflect performance on unseen, test data.

Ten TEE cases were annotated by four distinct users for the purpose of conducting inter-user variability study. Further, for a group of ten patients we obtained both, cardiac CT and CMR studies and used that for an inter-modality study. The same experiment was performed on four patients, which underwent both TEE and cardiac CT imaging.

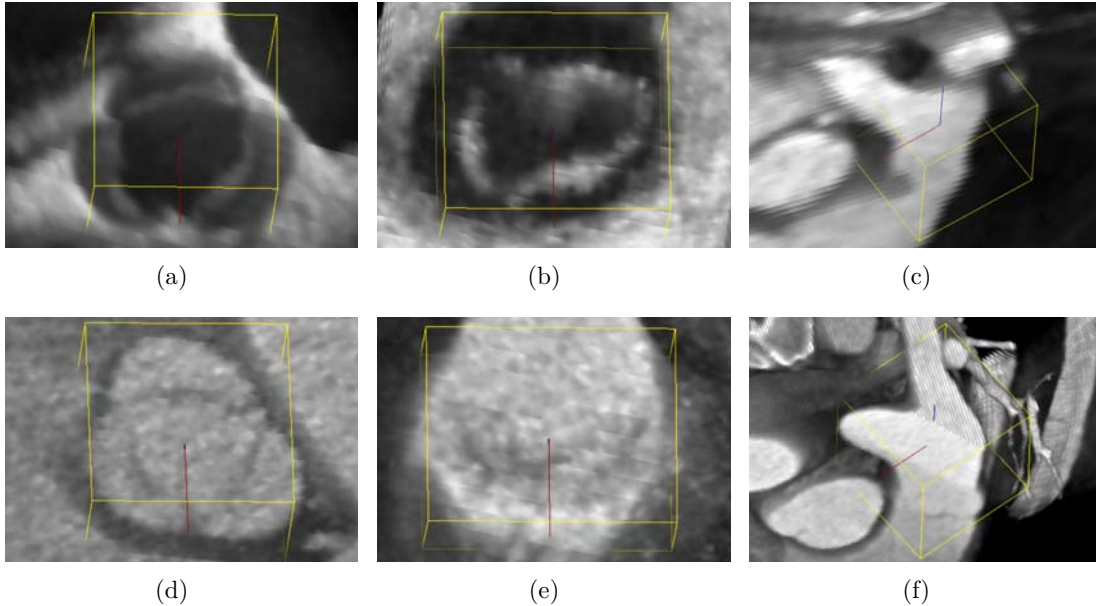


Figure 4.16: Examples of global location and rigid motion estimation: (a) aortic valve in TEE, (b) mitral valve in TEE, (c) pulmonary valve in CMR, (d) aortic valve in cardiac CT, (e) mitral valve in cardiac CT, and (f) pulmonary valve in cardiac CT.

4.6.3 Performance of the Object Localization and Rigid Motion Estimation

The performance of the global location and rigid motion estimation, θ , described in section 4.3, is evaluated in three distinct experiments. First, the overall detection precision is quantified at the box corners of the detected time-dependent similarity transformation. The average Euclidean distance between the eight bounding box points, defined by the similarity transform parameters $\{(c_x, c_y, c_z)_i, (\vec{\alpha}_x, \vec{\alpha}_y, \vec{\alpha}_z)_i, (s_x, s_y, s_z)_i, t\}$ and the ground-truth box is reported. Table 4.1 illustrates the mean errors and corresponding standard deviations distributed over the four valves and employed image modalities. Examples of estimation results are given in figure 4.16.

Mean / STD (mm)	Aortic Valve	Mitral Valve	Pulmonary Valve	Tricuspid Valve
TEE	4.78±3.26	5.00±2.02	-	-
Cardiac CT	4.40±1.98	6.94±2.19	7.72±10.03	-
CMR	-	-	7.19±3.50	-

Table 4.1: Accuracy of the global location and rigid motion estimation, quantified from the box corners and reported using the mean error and standard deviation distribution over each valve and employed modality.

In a second experiment, the accuracy of the individual detection stages is investigated. Absolute differences between estimated and ground truth parameters of the position, orientation, and scale are reported in table 4.2. The 80% column represents the 80th percentile of the error values. Please note that in order to speed up the algorithm, estimation of global location and rigid motion is always performed on downsampled data with an isotropic resolution of 3mm.

	Mean / STD	Median	80%	t-Var
Position (mm)	3.09±3.02	2.33	3.23	0.016
Orientation (deg)	9.72±5.98	7.93	10.73	2e-05
Scale (mm)	6.50±4.19	5.09	7.81	0.02

Table 4.2: Accuracy of the global location and rigid motion estimation reported separately for position, orientation and scale.

Finally, performance is analyzed with respect to the time-consistency of the similarity transform parameters over the entire cardiac cycle. The robust clustering is demonstrated by measuring the variation of the error in time, $t - Var$, the last column in table 4.2. Overall, the conclusion is that the global location and rigid motion detection is robust and accurate enough to be performed prior to the non-rigid trajectory estimation.

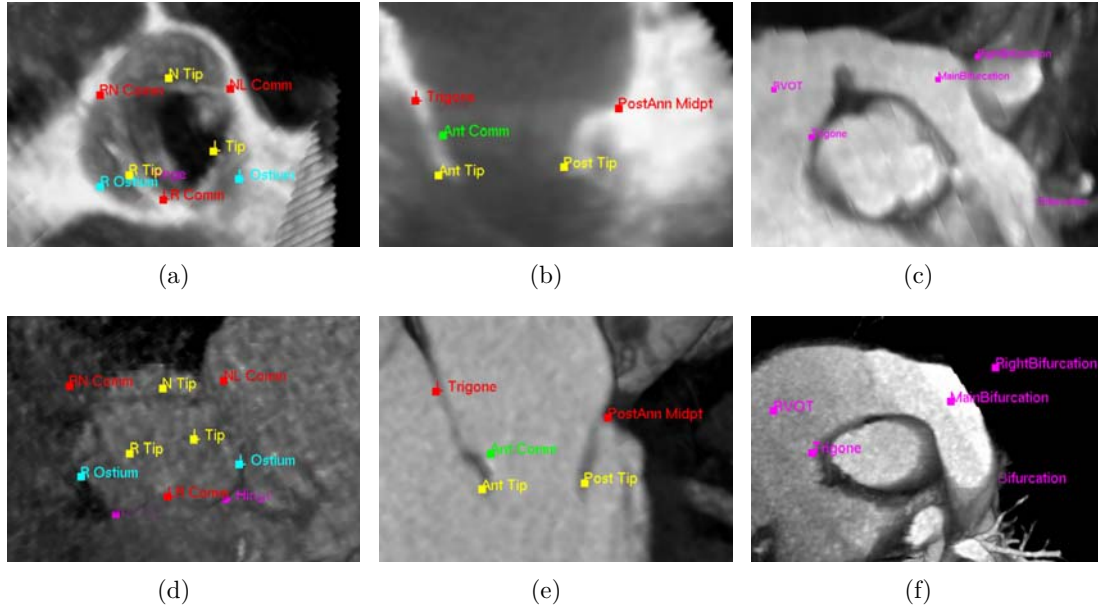


Figure 4.17: Examples of non-rigid landmark motion estimation: (a) aortic valve in TEE, (b) mitral valve in TEE, (c) pulmonary valve in CMR, (d) aortic valve in cardiac CT, (e) mitral valve in cardiac CT, and (f) pulmonary valve in cardiac CT.

4.6.4 Performance of the Non-Rigid-Landmark Motion Estimation

This section evaluates the performance of the proposed Trajectory Spectrum Learning algorithm (see section 4.4), which estimate the non-rigid landmark motion model, L , presented in section 3.4. The accuracy is measured using the Euclidean distance between detected and corresponding ground truth landmark trajectories. Table 4.3 demonstrates the precision expressed in mean errors and standard deviations, distributed over the four valves and three data sources. Note that reported values are obtained by averaging the performance of individual landmarks with respect to the corresponding valve. Examples of estimation results are given in figure 4.17.

Mean / STD (mm)	Aortic Valve	Mitral Valve	Pulmonary Valve	Tricuspid Valve
TEE	2.79 ± 1.26	3.60 ± 1.56	-	-
Cardiac CT	2.72 ± 1.52	2.79 ± 1.20	3.50 ± 2.70	-
CMR	-	-	4.30 ± 3.00	-

Table 4.3: Accuracy of the non-rigid landmark motion estimation, quantified by the Euclidean distance and reported using the mean error and standard deviation distribution over each valve and employed modality.

(mm)	Mean / STD	Median	80%	Max
Optical Flow	4.06±1.2	3.89	5.09	8.19
Track by Detection	2.93±0.9	2.83	3.73	6.40
Trajectory Spectrum	1.81±0.7	1.73	2.91	5.31

Table 4.4: Performance comparison of three algorithms for the aortic and mitral valve model from TEE.

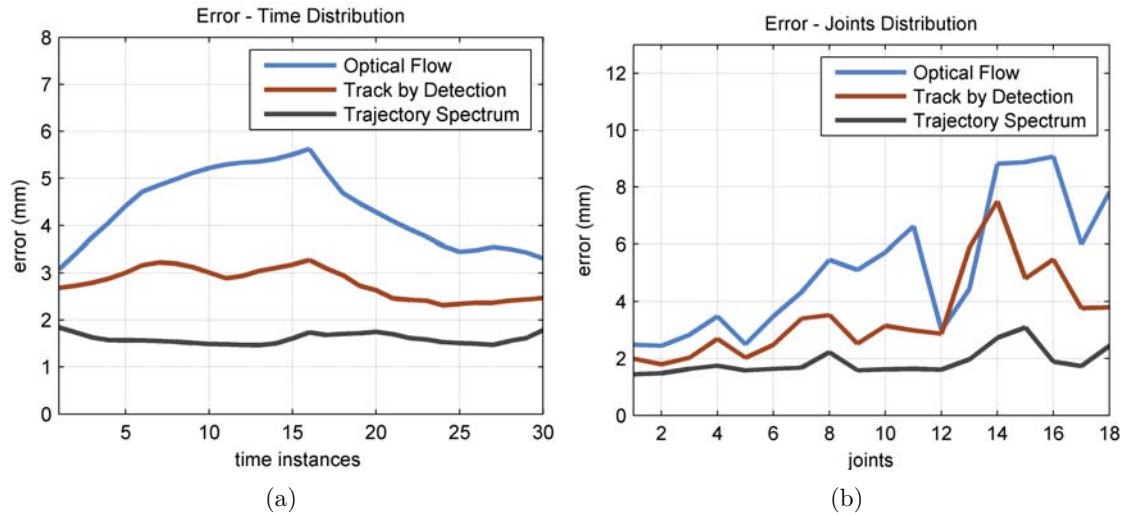


Figure 4.18: Error comparison between the optical flow, tracking-by-detection and our trajectory-spectrum approach distributed over (a) time and (b) detected anatomical landmarks. The curve in black shows the performance of our approach, which has the lowest error among all three methods.

Quantitative values are compared to tracking by optical flow [42] and tracking by detection [196]. For this experiments only aortic and mitral landmarks are considered, which are estimated from a subset of 65 TEE studies. As presented in table 4.4 our method yields the best results. We also analyzed the error distribution of our approach and compared it to optical flow and tracking by detection. Figure 4.18(a) presents the error distribution over the entire cardiac cycle, where the end-diastolic phase is at $t = 0$. It can be seen that, although performed forward and backward, the optical flow approach is affected by drifting. At the same time, the tracking-by-detection error is unevenly distributed, which reflects in temporal inconsistent and noisy results. Figure 4.18(b) shows the error distribution over the 18 landmarks of the aortic and mitral valves. Both tracking-by-detection and optical flow perform significantly worse on highly mobile landmarks as the aortic leaflet tips (landmarks 9, 10 and 11) and mitral leaflet tips (landmarks 15 and 16). The proposed trajectory spectrum learning demonstrates a time consistent and model-independent precision, superior in both cases to the reference methods.

Mean / STD (mm)	Aortic Valve	Mitral Valve	Pulmonary Valve	Tricuspid Valve
TEE	1.35 ± 0.54	2.29 ± 0.64	-	-
Cardiac CT	1.22 ± 0.38	2.02 ± 0.57	1.60 ± 0.20	-
CMR	-	-	1.90 ± 0.20	-

Table 4.5: Accuracy of the comprehensive valve model estimation, quantified by the Point-to-Mesh distance and reported using the mean error and standard deviation distribution over each valve and employed modality.

4.6.5 Performance of the Comprehensive Valve Model Estimation

The accuracy of the algorithm in section 4.5 to estimate the comprehensive valvular model, M , (see section 3.5) is evaluated by utilizing the point-to-mesh distance. For each point on a surface \vec{p} , we search for the closest point (not necessarily one of the vertices) on the other surface to calculate the Euclidean distance. To guarantee a symmetric measurement, the point-to-mesh distance is calculated in two directions, from detected to ground truth surfaces and vice versa. Table 4.5 contains the mean error and standard deviation distributed over the four valves and image types. Examples of estimation results are given in figure 4.19

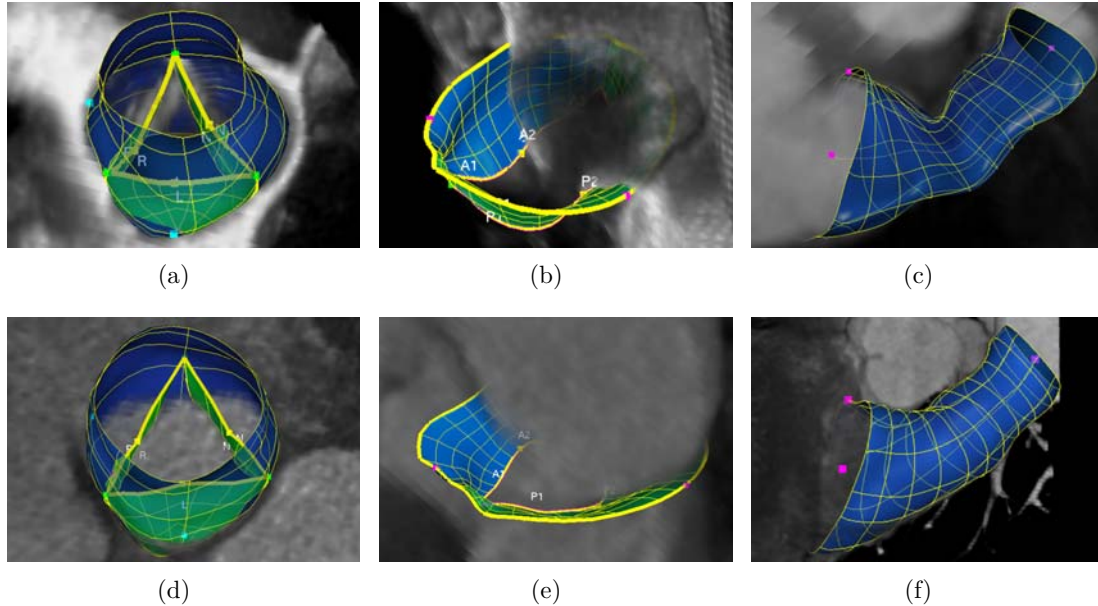


Figure 4.19: Examples of comprehensive valves model estimation: (a) aortic valve in TEE, (b) mitral valve in TEE, (c) pulmonary valve in CMR, (d) aortic valve in cardiac CT, (e) mitral valve in cardiac CT, and (f) pulmonary valve in cardiac CT.

4.6.6 Inter-modality and Inter-user Variability Analysis

The inter-modality consistency of the model is demonstrated in two experiments. The first experiment is based on a subgroup of four patients, which underwent both cardiac CT and TEE. To demonstrate the inter-modal consistency of the proposed approach, we estimated the aortic valve model and selected clinical measurements from both CT and TEE scans, and compared the results. The included measurements are: aortic valve area, inter-commissural distances, ventriculoarterial junction, valsava sinuses and sinotubular junction diameters (see section 5.1). The experiment demonstrated a strong correlation $r = 0.98$, $p < 0.0001$ and $0.97 - 0.99$ confidence interval.

The second experiment is based on a subset of ten patients, which underwent both, cardiac CT and CMR. Ground-truth and detected pulmonary trunk models from each modality were compared using the abstract point-to-mesh measurement and clinical relevant diameter measurements: RVOT, hinges and commissures. Results are summarized in table 4.6 and illustrated in figure 4.20. A strong inter-modality correlation, $r = 0.992$, $p < 0.0001$ and confidence of 98% was obtained for CT and CMR based on the pulmonary trunk model.

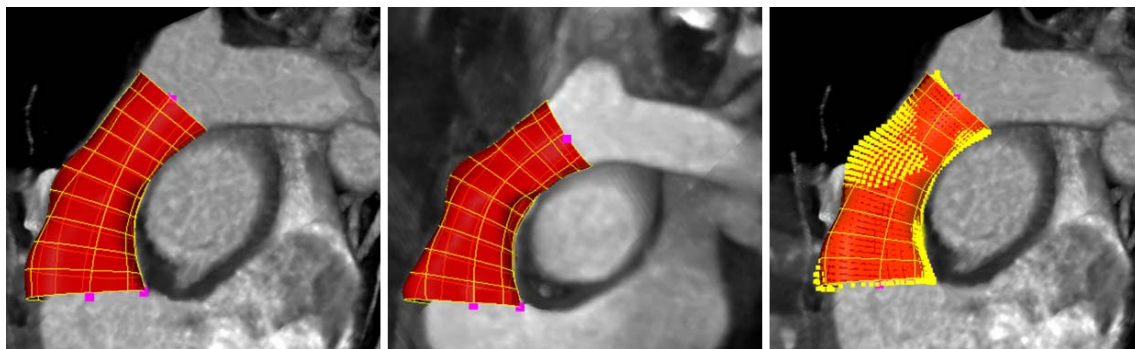


Figure 4.20: Illustration of the inter-modality consistency; from left to right, pulmonary trunk model in end-diastole from cardiac CT, CMR and CMR model projection (yellow points) into the corresponding CT image.

Table 4.6: Model based intra-modality comparison between CT and MRI

(mm)	Ground truth	Estimation
RVOT	0.7 ± 0.5	3.8 ± 1.5
Hinges	1.2 ± 1.4	2.6 ± 4.7
Commissures	1.5 ± 1.2	3.2 ± 1.7
Point-to-mesh	1.4 ± 0.1	2.5 ± 0.7

Furthermore, an inter-user experiment was conducted on a randomly selected subset of ten studies, which had their corresponding patient-specific valve models manually fitted by four experienced users. The inter-user variability and automated model-based estimation was computed on four measurements derived from the aortic and mitral valve models.

These are the interannular angle and interannular centroid distance performed in end-diastolic (ED) and end-systolic (ES) phases. The inter-user variability was determined by computing the standard deviation for each of the four different user measurements and subsequently averaging those to obtain the total variability. To quantify the error of the model-based estimation, we compare the automatic measurement result to the mean of the different users. Figure 4.21 shows the system error for the selected sequences with respect to the inter-user variability. Note that except for 3% of the cases, the estimation error lies within 90% of the inter-user confidence interval. Thus the variability of measurements obtained by different users on the same data reveals feasible confidence intervals and desired precision of the automated patient-specific modeling algorithm.

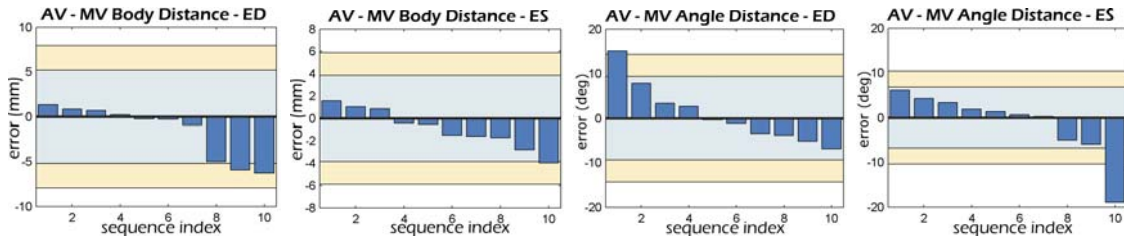


Figure 4.21: System error compared to the inter-user variability. The sorted automated estimation error (blue bars) and the 80% (light blue area) and 90% (yellow) confidence intervals of the user variability determined from the standard deviation.

4.6.7 Overall Performance Results

The performance evaluation experiments presented above were conducted using three-fold cross-validation by dividing the entire dataset into three equally sized subsets, and sequentially using two sets for training and one for testing. Overall, the estimation accuracy of the patient-specific valvular parameters from multi-modal images is 1.73mm. On a standard PC with a quad-core 3.2GHz processor and 2.0GB memory, the total computation time for the all three estimation stages is 4.8 seconds per volume (approx 120sec for average length volume sequences), from which the global location and rigid motion estimation requires 15% of the computation time (approx 0.7sec), non-rigid landmark motion 54% (approx 2.6sec), and comprehensive valvular estimation 31% (approx 1.5sec).

Figure 4.22 shows estimation results at different phases of the cardiac cycle and on various aortic and mitral valve pathologies from different image modalities.

4.7 Conclusions

Decisions in the current healthcare practice rely to a large extent on data coming from a multitude of non-invasive investigation techniques. In particular, morphological and functional parameters captured from cardiac images are prerequisite for the management of complex cardiovascular pathologies, such as diseases of the heart valves. From an image analysis perspective, algorithms that incorporate domain specific prior knowledge have

proven to be most adequate in dealing with the inherent complexity and limited image quality specific to the medical image field.

We proposed a novel estimation framework, based on discriminative learning algorithms, to extract patient-specific parameters of the valvular apparatus from multi-modal cardiac images. In agreement with the hierarchical valvular modeling, introduced in chapter 3, the parameter estimation includes three stages: object localization and rigid motion estimation, trajectory spectrum learning for non-rigid motion estimation, and comprehensive model estimation. Initially, the location and time-coherent rigid motion of each valve is robustly determined from a series of cardiac volumes by a novel algorithm, which combines efficient subspace searching with a RANSAC approach. The non-rigid landmark model is estimated using another new method: Trajectory Spectrum Learning (TSL) in combination with Local-Spatial-Temporal (LST) features. This algorithm estimates location and motion simultaneously through a spectrum learning and detection formulation, which operates in marginal trajectory spaces. In the final stage, the margins of the complete valvular model are delineated by applying robust boundary detectors and motion manifold learning.

The performance of the proposed approach was demonstrated on a large and heterogeneous database, which contains 476 patients affected by various cardiovascular and valvular diseases. Overall, the precision of the patient-specific estimation is 1.73mm at a speed of 4.8 seconds per volume. Furthermore, the method was demonstrated to be robust with respect to the three image modalities investigated (CT, Ultrasound and MRI), and to inter-user variability computed from clinical parameters.

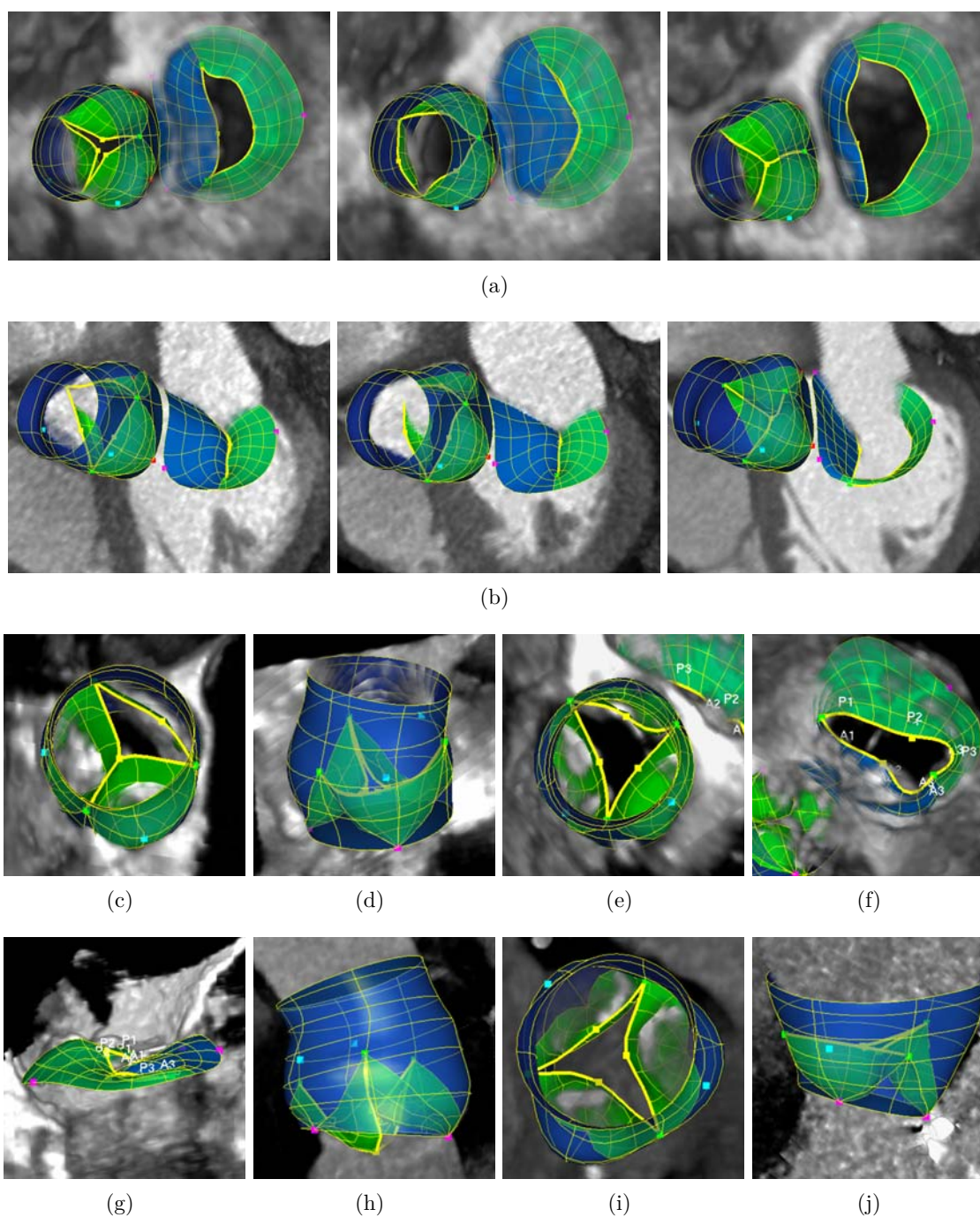


Figure 4.22: Examples of estimated patient-specific models from TEE and CT data: healthy valves from three different cardiac phases in (a) TEE from atrial aspect and (b) CT data in four chamber view. Pathologic valves with (c) bicuspid aortic valve, (d) aortic root dilation and regurgitation, (e) moderate aortic stenosis, (f) mitral stenosis, (g) mitral prolapse, (h) bicuspid aortic valve with prolapsing leaflets, (i) aortic stenosis with severe calcification and (j) dilated aortic root.

The methodology proposed in the previous chapters lies at the cornerstone of advanced clinical applications for treatment support of patient with valvular heart disease. The patient-specific model obtained from multiple image modalities enables a variety of non-invasive analysis procedures, which can lead to reduced therapeutical costs and complication risks, as well as improved treatment outcome. To demonstrate the practical benefit of the proposed technology, this chapter introduces three novel applications in the context of valvular heart disease management.

Initially, a new paradigm for the clinical quantitative and qualitative evaluation of the valvular apparatus is proposed in section 5.1, which intends to replace manual analysis from 2D images with automated model-based quantification from 4D data. Subsequently, a novel approach to learn discriminative distance functions from anatomical geometrical data is presented in section 5.2. This is applied to provide robust and automated shape-based diagnosis of valvular diseases and patient selection for percutaneous valve implantations. Finally, a computational decision support framework for percutaneous valve procedures is introduced in section 5.3. By combining patient-specific models with physical models of devices, we demonstrate and validate in-silicio valve implantation with the scope of predicting the success of percutaneous treatments under various conditions.

5.1 Quantitative and Qualitative Analysis

It is axiomatic that precise quantification of the anatomy and function is fundamental in the medical management of valvular heart disease. Both, the American College of Cardiology (ACC) and European Society of Cardiology (ESC) have published guidelines for the management of patients with valvular heart disease, which describe in detail decision schemes and key parameters. Anatomical, functional and hemodynamical valve measurements are important throughout the clinical workflow for diagnosis, severity assessment, patient and treatment selection, surgery planning and risk stratification.

Valvular dimensions, such as the aortic valve area, mitral valve area and mitral annulus area are routinely used to evaluate the overall structural and functional condition. Further, advanced analysis through independent aortic sinus volumes or mitral prolapse distribution is required for the patients that are candidates for surgical treatment. Dimensions of the aortic root at the ventriculoarterial junction, valsalva sinuses and sinotubular junction as well as the inter-commissural distance and inter-ostia angle are crucial in planning for aortic valve replacement and repair surgery [38]. Analogous, mitral valve repair procedures require measurements of the mitral annulus and leaflets, such as the mitral annular circumference and anterolateral-posteromedial diameter.

Due to the strong anatomical, functional and hemodynamic inter-dependency of the heart valves, VHD does not affect only one valve, but rather several valves are impaired. Recent studies demonstrate strong influence of pulmonary artery systolic pressure on the tricuspid regurgitation severity [112]. In [88, 158] the simultaneous evaluation of aortic and mitral valves is encouraged, given the fibrous aortic-mitral continuity, which anchors the left side valves and facilitates the reciprocal opening and closing motion during the cardiac cycle. Thus, measurements such as the centroid distances and angles between the aortic-mitral and pulmonary-tricuspid valves can provide additional pathophysiological information.

Emerging percutaneous and minimally invasive valve interventions require extensive non-invasive assessment, as clinicians have restricted direct access to the sensitive anatomies [3, 130]. For instance, precise knowledge of the coronary ostia position prevents hazardous ischemic complications by avoiding the potential misplacement of aortic valve implants. Data about the integral three-dimensional configuration of critical structures (ostia, commissures, hinges, etc.) and their relative location over the entire cardiac cycle is mandatory.

5.1.1 Model-based Valvular Quantification

We proposed a paradigm shift in the clinical evaluation of the valvular apparatus, which aims to replace manual analysis based on 2D images with automated model-based quantification from 4D data. At the center of the proposed approach is the dynamic valvular model introduced in chapter 3, which captures comprehensive patient specific information of the morphology and functions from multi-modal images following the methods described in chapter 4. The explicit mathematical model is exploited to express a wide-ranging collection of quantitative parameters that support the overall clinical decision making process. In comparison with the gold standard, which processes 2D images and performs manual measurements, the benefits of the proposed model-based analysis are:

- **Precision** - increased by robust modeling and measuring the natural three-dimensional valve anatomy.
- **Efficiency** - by automated quantification that outperforms manual measuring in terms of required analysis time.
- **Reproducibility** - through robust learning-based technology and avoidance of user-dependent manipulation.

Table 5.1: Valvular Measurements automatically computed from the patient-specific model over the entire cardiac cycle

Aortic Root

Ventriculoarterial Junct. \odot, f, \vee [174]
 Valsava Sinuses \odot, f, \vee [174]
 Sinotubular Junct. \odot, f, \vee [174]
 Commissure-Hinge Plane \angle
 Sinus Volumes

Aortic Landmarks

Commissure-Hinge Distance [174]
 Hinge-Ostium Distance [3]
 Ostium-Commissure Distance
 Inter-Commissural \vee, \angle [174]
 Inter-Ostia \angle

Aortic Leaflets

Aortic Valve f [3]
 Coaptation Height [174]
 Leaflet Height [3]
 Effective Cusp Height [3]
 Leaflet Free Edge \vee [3]
 Leaflet-Ostium Distance

Mitral Annulus

Annular f, \vee [19, 174]
 Annular Deviation Ratio[90]
 Annular Non-Planarity \angle [101]
 Sphericity Index

Mitral Landmarks

Inter-Commissural Distance[19]
 Inter-Trigonal Distance[19]
 Annular-Posterior \odot [19]
 Anterolateral-Posteromedial \odot [19]
 Annular-Commissural Ratio[157]

Mitral Leaflets

Anterior/Posterior Surface f, \vee
 Valve Opening f [19]
 Valve to Area Ratio
 Tenting Height and Volume[19, 147]

Aortic-Mitral

Centroid Distances [174]
 Inter-Annular \angle [174]

Pulmonary Valve

RVOT \odot [139]
 Min/Max Trunk \odot [139]
 Bifurcation \odot [139]

Tricuspid Valve

Valve f

Pulmonary-Tricuspid

Centroid Distances

\odot - diameter, f - area, \vee - circumferential length, \angle - angle.

- **Functional** - assessment from dynamic measurements performed over the entire cardiac-cycle.
- **Comprehensive** - analysis including complex parameters such as shape curvatures, deformation fields and volumetric variations.
- **Integrated** - evaluation of inter-valvular morphological and functional coupling from the complete valvular model.

A compilation of measurements rendered together with collaborating cardiologists, cardiac surgeons radiologists and anesthesiologists is presented in table 5.1. The integrated

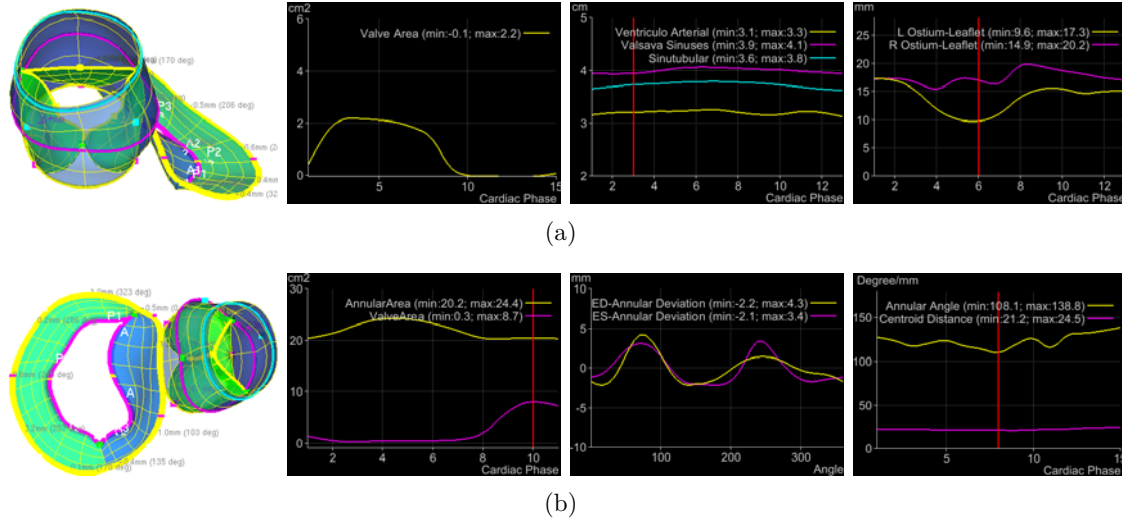


Figure 5.1: Examples of aortic-mitral morphological and functional measurements. (a) From left to right: aortic valve model with measurement traces, aortic valve area, aortic root diameters and ostia to leaflets distances. (b) Mitral valve with measurement traces, mitral valve and annulus area, mitral annular deviation in ED and ES and aortic-mitral angle and centroid distance.

analysis capabilities simultaneously serve for diagnosis, severity assessment, patient selection, surgery planning for valve replacement or repair and planning for percutaneous interventions. Figure 5.1 illustrates model-based quantification examples for the aortic-mitral complex.

It is important to notice that the quantification potential of the proposed method is not limited to the above mentioned measurements. Through the consistent and comprehensive spatial and temporal representation, the introduced system offers unique analysis features, which facilitate decisions during the whole clinical workflow. For the first time, functional and morphological measurements can be efficiently performed for individual valve patients and potentially improve their clinical management in terms of procedure costs, complication risks and treatment outcome.

In the following we present a series of clinical validation experiments performed jointly with various clinical collaborators and published in several medical articles [26, 55, 71, 32]. Currently, prototype systems based on the technology presented in this thesis are installed in multiple leading cardiac centers around the world for clinical evaluation purposes.

5.1.2 Results on Left-Side Valve Measurements

Aortic Valve Opening Area Analysis from cardiac CT: The usefulness of cardiac CT to assess the aortic valve opening area (AVA) has been exhaustively documented [66]. However, manual valve planimetry is cumbersome and time-consuming. In the following experiment we evaluated the accuracy and time-effectiveness of automated model-based AVA computation compared to manual planimetry. Retrospectively ECG-gated cardiac

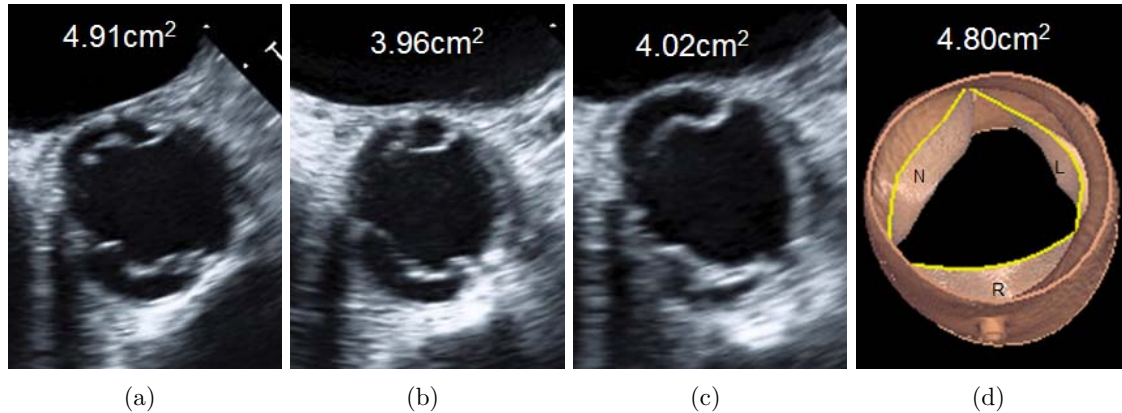


Figure 5.2: Aortic Valve Area measured manually from 2D images versus the automatic 3D model-based quantification: (a), (b) and (c) show the manual measurement from three different 2D TEE images of the same patient, which demonstrate the sensitivity of the current gold standard approach to the position of the 2D-dimensional section. (d) shows the proposed precise and reproducible 3D model-based measurement.

CT data of 32 patients scanned with dual-source CT ($n=21$) or 64-slice CT ($n=11$) were included. Data were reconstructed at 10% increments across the cardiac cycle with 1.5mm section thickness and 1mm increment. Two independent observers performed manual planimetric measurements by tracing the maximal systolic orifice on double oblique short axis multiplanar reconstructions. The same data were then analyzed using an automatic model-based method. The leaflets' geometries during maximal opening define the course of the free margins. The encompassed AVA can be computed as a surface integral.

Data was analyzed using linear regression and Bland Altman plots. Interobserver and intermethod variances were calculated. Analysis times for both methods were recorded. Mean AVA by CT planimetry was $3.62 \pm 1.21 \text{ cm}^2$. Mean AVA derived from the model was $3.74 \pm 1.34 \text{ cm}^2$. Excellent correlation was found between planimetric and automated quantification ($r=0.963$, $p<0.0001$). Bland Altman plots revealed a systematic bias of $0.12 \pm 0.38 \text{ cm}^2$. Intermethod variance did not differ significantly from interobserver variance (0.28 vs 0.25 cm^2 , $p>0.05$), placing 82% of model measurements between user measurements. Mean analysis time was significantly ($p<0.05$) reduced for model-based measurements (mean 125sec), compared with manual planimetry (mean 230sec). The proposed model-based method allows automated, patient specific morphologic and dynamic quantification of AVA. Measurement results are within the interobserver variance of manual planimetry. Quantification of AVA derived from an aortic valve model enables fast, accurate assessment in excellent agreement with manual planimetry and has the potential to improve cardiac imaging workflow.

Aortic Valve and Root Analysis from cardiac CT and 3D TEE: Accurate anatomical and functional assessment of AV and aortic root is crucial for understanding the pathophysiology of abnormalities and for management decision-making in patient

with aortic valve disease and aortic aneurysm. The aim of this study was to evaluate the feasibility of the modal-based method to assess the aortic valve and aortic root from volumetric 3-D Echo compared to CT. Volume-rendered 3-D TEE data were obtained using V5M transducer, Siemens Sequoia. Volumetric CT images were acquired using 64-Slice CT(Avanto, Siemens). We dynamically measured the AVA(cm^2), diameter of sinotubular junction(d-STJ, mm), sinus of Valsalva(d-SV, mm) and basal ring(d-BR, mm). 364 CT volumes from 41 patients and 23, 3-D TEE volumes from 15 patients with normal to mild AR were acquired. 3-D TEE data about AV and root showed strong correlation with CT data, as illustrated in table 5.2. This novel automated model-based approach provides accurate dimensions of the AV and the aortic root and may aid in valve and root repair procedures (see figure 5.2).

Table 5.2: Comparison of AVA and aortic diameter between cardiac CT and 3D TEE

	3D TEE	cardiac CT	r-value	p-value
AVA (cm^2)	3.09 ± 0.85	4.33 ± 1.36	0.707	0.013
Max. Ventriculoarterial Junct. \varnothing (mm)	2.42 ± 0.27	2.74 ± 0.36	0.982	0.018
Max. Valsava Sinuses \varnothing (mm)	3.16 ± 0.32	3.92 ± 0.46	0.993	0.007
Max.Sinotubular Junct. \varnothing (mm)	2.69 ± 0.26	3.19 ± 0.21	0.775	0.042

Aortic Valve and Root in Aortic Regurgitation from 3D TEE: In this study we applied the model-based analysis approach to automatically quantify the aortic valve and the root from 3-D TEE data in patients with aortic regurgitation (AR). Volumetric 3-D TEE of the AV and proximal root from 15 patients with AR was analyzed. The conventional measures were compared to 2-D, and the non-conventional measures were compared to known normal database. Conventional measures- 2-D and the model-based measures of AV area ($r=0.98$), STJ diameter ($r=0.73$) and SV diameter ($r=0.79$) showed good correlation; annular diameter was discordant ($r=0.58$) consistent with its complex geometry in AR. Nonconventional measures (abnormal vs. normal, mm) by the model-based method - Inter-commissural distance (mm) was increased (Left: $25.9+3$ Vs. 25 , Right: $27.1+3$ Vs. 25.9 and Non: $27.2+3$ Vs. 25.5), Annulus to coronary ostia distance (mm) was increased (Right: $19.3+3$ Vs. $17.2+3$ and Left $16.9+3$ Vs. $14.4+3$); also, leaflet tip to ostia minimum distance was $5+1.6$ (R) and $8+1.2$ (L). The directly measured 3-D ERO in mild AR was $10 - 20mm^2$ and moderate AR was $30mm^2$. Automated quantification of the aortic and the root yields vital and incremental measures which may be valuable to guide surgical and percutaneous interventions to improve outcomes.

Left Valve Analysis: Table 5.3 shows the accuracy for the Ventriculoarterial Junction, Valsava Sinuses and Sinotubular Junction aortic root diameters as well as for Annular Circumference, Annular-Posterior Diameter and Anterolateral-Posteromedial Diameter of the mitral valve. The Bland-Altman plots [17] in figure 5.3 demonstrate a strong agreement between manual and model-based measurements for aortic valve areas and mitral annular areas.

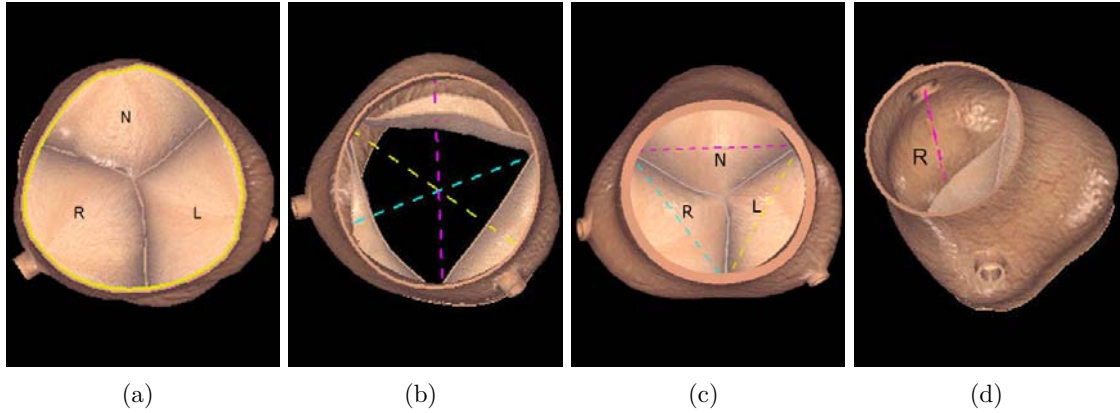


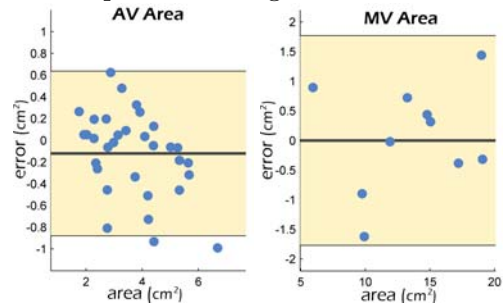
Figure 5.3: Examples of model-based aortic valve measurements: (a) aortic annular diameter (ventriculoarterial junction), (b) sinus width, (c) inter-commissural distances, and (d) coronary ostia to leaflet tip distances.

Moreover, from a subset of 19 TEE patients, we computed measurements of the aortic-mitral complex and compared those to literature reported values [174]. Distances between the centroids of the aortic and mitral annulae as well as interannular angles were computed. The latter is the angle between the vectors, which point from the highest point of the anterior mitral annulus to the aortic and mitral annular centroids respectively. The mean interannular angle and interannular centroid distance were 137.0 ± 12.2 and 26.5 ± 4.2 , respectively compared to 136.2 ± 12.6 and 25.0 ± 3.2 reported in the literature [174].

Table 5.3: Precision for various dimensions of the aortic-mitral coupling along with Bland-Altman plots for the aortic valve area and mitral annular area. The aortic valve experiments were performed on CT data from 36 patients, while the mitral valve was evaluated on TEE data from 10 patients, based on the input of a expert cardiologists.

	<i>cm</i>	Mean	STD
Ventriculoarterial Junct. \oslash		0.137	0.017
Valsava Sinuses \oslash		0.166	0.043
Sinotubular Junct. \oslash		0.098	0.029
Annular \vee		0.846	0.3
Annular-Posterior \oslash		0.325	0.219
Anterolateral-Posteromedial \oslash		0.509	0.37

\oslash - diameter, \vee - circumferential length.



Case Study: We studied our quantification performance on a patient who underwent a mitral annuloplasty procedure, intended to reduce mitral regurgitation. Pre- and post-TEE exams were performed before and after the successful mitral valve repair. The

measurements of the mitral valve area in figure 5.4(a) demonstrates the regurgitant mitral valve to be cured after procedure. Although not explicitly targeted, the intervention had an indirect effect on the aortic valve, also illustrated in figure 5.4(b) by the annular and valvular areas. The observation concurs with clinical findings reported in [88, 158, 174] and shows the converse effect to the one reported by [168], where an intervention on the aortic affected the mitral valve.

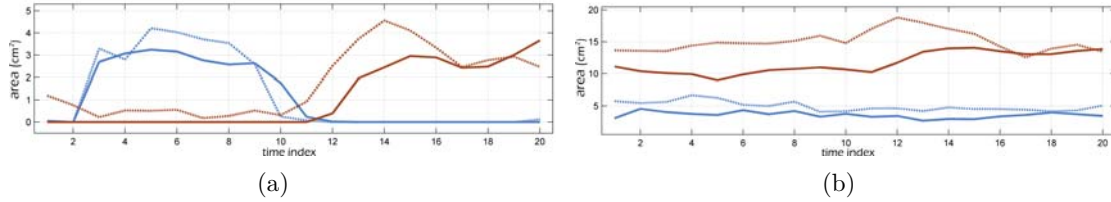


Figure 5.4: Measurements obtained before (dotted lines) and after (solid lines) mitral annuloplasty: (a) Aortic (blue) and Mitral (red) valvular area, (b) Aortic (blue) and Mitral (red) annular area.

5.1.3 Results on Right-Side Valve Measurements

Percutaneous Pulmonary Valve Implantation: The reliable assessment of the three-dimensional geometry of the right ventricular outflow tract and pulmonary trunk is essential for preprocedural assessment and patient selection in potential PPVI patients [140]. Thus, Schievano *et al.* [139] proposed a set of measurements to characterize the safe anchoring location, size and shape of the valve implant [18]. These include diameters at the RVOT and bifurcation levels as well as MIN/MAX values of the pulmonary trunk. PPVI intervention is avoided for patients with RVOT diameter $> 22\text{mm}$ due to device limitations [21, 140, 139, 84].

To demonstrate the applicability and precision of the proposed quantification for the management of PPVI patients, in table 5.4 we compared measurements derived from the modal to expert measurements and literature reported values [119].

(mm)	Observed	Literature
Bifu. Diam.	30.2 ± 1.6	30.7 ± 3.6

(mm)	Mean Err.	Std. Dev.
Min Diam.	1.99	0.64
Max Diam.	4.06	2.09
Bifu. Diam.	1.04	0.65

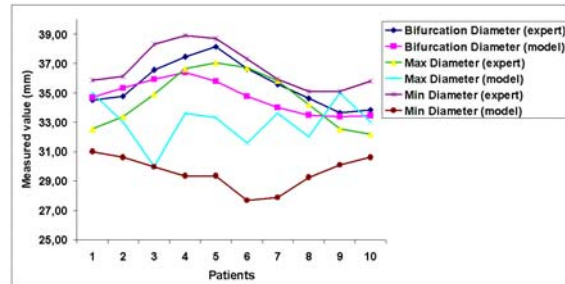


Table 5.4: Model-based quantification error with respect to literature(upper table) and expert measurements(lower table).

Right Valves Analysis: Important clinical parameters are extracted from the personalized model in the right heart. These include the evaluation of the tricuspid function quantified by the valve opening area and pulmonary-tricuspid coupling through the distance of the valvular centers. Quantitative comparison is shown in figure 5.5 by comparing ground truth and model-based measurements, demonstrating a strong correlation.

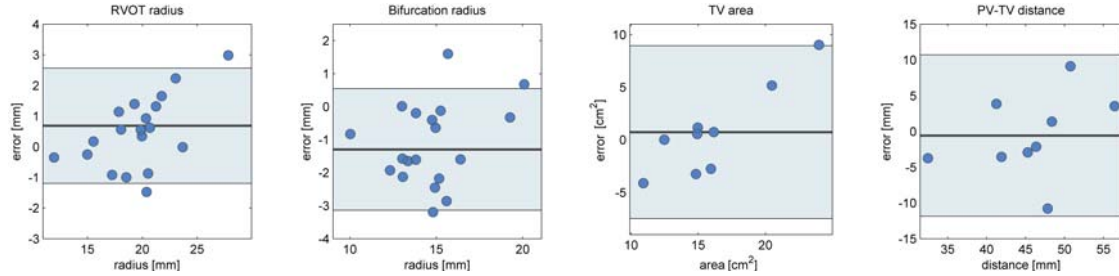


Figure 5.5: Bland altman plots for a) right ventricle output tract diameter, b) pulmonary valve bifurcation diameter, c) tricuspid valve area and d) distance between pulmonary and tricuspid valve

Case Study: We show quantitative comparison between a healthy patient and a post-operative patient who underwent a Ross operation. Several clinical measurements extracted from the personalized aortic and pulmonary valve model, demonstrated in figure 5.6), confirm a successful outcome since no regurgitation is observed at the aortic valve.

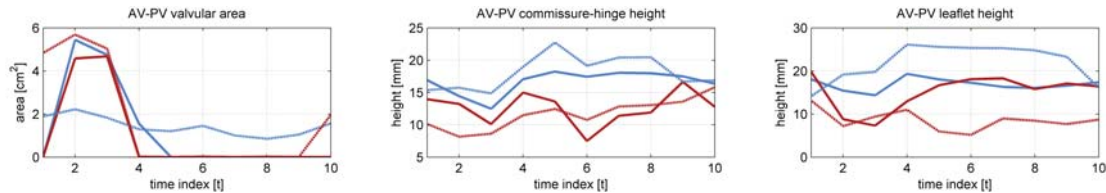


Figure 5.6: Aortic (AV) and pulmonary valve (PV) area, mean commissure-hinge plane height and mean leaflet height obtained from a normal patient (solid lines) and a post Ross operation patient (dotted line). The red graph is representing the aortic valve and the blue the pulmonary.

5.1.4 Discussion

We proposed a novel paradigm for the clinical analysis of the valvular apparatus, which replaces manual measurements from 2D images with model-based quantification from 4D data. The approach is based on patient-specific parameters extracted from multi-modal cardiac images. In comparison with the gold standard, our method provides, fast, precise, reproducible, functional and comprehensive measurements of the heart valves. The modal-based morphological and functional quantification can potentially reduce costs

and complication risks as well as improved therapeutical outcome in the context of valvular heart disease management.

5.2 Computer Aided Diagnosis, Patient Selection and Case Retrieval

Valvular heart diseases (VHD) represent an important public-health problem notably common in elderly population [118]. Among all cardiovascular diseases, treatment of VHD is most expensive and has the highest in-hospital death rate [134] due to elaborate, time consuming and potentially inaccurate diagnostic procedures and complex interventions into one of the most essential physiological systems of the human body. Furthermore, information on the morphology of the heart valves has been mainly obtained from explanted specimens or animal models [37] and reported standard dimensions vary considerably. To date, quantitative and qualitative assessment of the valves is mainly based on manually processed 2D imaging and aggregation of isolated measurements subject to potential inaccuracies [167]. Inconclusive or discordant clinical finding enforce invasive investigation methods, significantly increasing procedures' risks and costs.

Recent advances in scanner technology enable for 4D imaging of the heart with CT, MRI and Ultrasound equipment. These modalities are well suited for the non-invasive assessment of valve morphology and dynamics. However, due to the lack of efficient and convenient tools, clinical decisions still rely on manual measurements in 2D image planes, derived from volumetric acquisitions, which is error prone and time consuming. These significantly influence the quality of diagnosis and treatment as well as interventional planning and follow up evaluation.

We propose a generic method on how to automatically derive high-level clinical information from geometric valve models using learning based discriminative distance functions. The inference is performed in a comprehensive feature space, which incorporates the complex morphologic and functional information of the valves by applying robust statistical methods. The method described in section 5.2.1 is generic and flexible and enables for arbitrarily learning of similarities among shapes based on any meaningful concept. In our context the patient-specific valve models extracted from 4D cardiac CT, 4D trans-esophageal Ultrasound and 3D isotropic MRI are leveraged to provide advanced clinical decision support. Shape-based diagnosis and treatment guidance are demonstrated in section 5.2.2 for the aortic valve. Section 5.2.3 introduces shape-based patient selection for percutaneous pulmonary valve implantation (PPVI). Results and discussions are given in section 5.2.4 and section 5.2.5, respectively.

5.2.1 Learning Discriminative Distance Functions

Generally we address two tasks: retrieval of similar cases using a learned distance function, which measures the similarity of two particular shapes, and a binary classification problem, based on geometric valve models and derived features. The second task can actually be formulated using the first [162, 160]. Therefore, instead of learning a classifier directly,

we choose to divide the learning process into two sequential steps, i.e. distance learning followed by classification or clustering.

Given the geometric information provided by the valvular models introduced in chapter 3 and estimate from patient-specific cardiac images in chapter 4, the problem can be formulated as follows:

$$\hat{y} = \underset{y \in \{-1, +1\}}{\operatorname{argmax}}(p(y|C)) \quad C = (\vec{p}_0, \dots, \vec{p}_N, F_0, \dots, F_Q) \quad (5.1)$$

where $y \in \{-1, +1\}$ are the application specific labels and each model instance is represented by a parameter vector C , composed out of N surface vertices $\vec{p}_i \in M$ (see Section 3.5) and Q application dependent features F_i derived from the model.

Instead of learning directly the posterior probability, a distance learning followed by the actual classification is performed, where each step requires search in a less complex functional space than in the immediate learning [160]. Learning a distance function helps to combine the power of strong learners with the transparency of nearest neighbor classification [13]. Moreover, learning a proper distance function was shown to be especially helpful for high dimensional data with many correlated, weakly relevant and irrelevant features, where most traditional techniques would fail. Also, it is easy to show that choosing an optimal distance function makes classifier learning redundant.

Currently, in distance based classification, canonical distance functions are used most commonly. Today in many areas including computer vision the Euclidean distance is one of the most widely used, though it is well known that its use is justified only when the data distribution is Gaussian. During the last three decades, the importance of learning a proper distance function in machine learning has been gradually acknowledged [13]. Different imaging applications have been considered, including image retrieval, object detection [100], motion estimation and image registration [199].

Equivalence constraints: Historically, the research on distance function learning has started from supervised learning of distance functions for k-nearest neighbor learning in the original feature space C representation. Today the most commonly used representation, especially in computer vision, is the one based on equivalence constraints [67]. Interestingly, the distance learnt from labels is almost always metric, while learning from weak representations such as equivalence constraints usually provides more flexibility for learning arbitrary functions.

Equivalence constraints are represented using triplets (C^1, C^2, y) , where C^1 and C^2 are feature vectors (see Equation. 5.1) and $y \in \{+1, -1\}$ is a label indicating whether the two instances are similar or dissimilar [67].

Learning from these triplets is often called learning in the product space [67, 13, 199]. Another common alternative is to learn in the difference space, the space of feature vector differences [194]. While both representations demonstrate promising empirical results in different contexts, there is no understanding which representation is better and when.

Commonly a binary distance function is the output from learning from equivalence constraints, predicting only whether the two instances are similar or dissimilar. However, this can be combined with the signed margin of margin-based classifiers such as SVM

and boosting as the required distance function. The most popular learning algorithm in the area of distance function learning from weak representations is boosting [53]. Random Forests also demonstrated promising results on public benchmark datasets and are normally faster than boosting. Both product and difference spaces were implemented in our framework. The signed margin of models constructed using AdaBoost and Random Forests is used as the required distance function for our experiments with equivalence constraints.

The intrinsic Random Forest distance function: For a Random Forest (RF) learned for a certain classification problem, the proportion of the trees where two instances appear together in the same leaves can be used as a measure of similarity between them [23, 160]. For a given forest f the similarity between two instances C^1 and C^2 is calculated as follows: 1) the instances are propagated down all K trees within f and their terminal positions z in each of the trees ($z_1 = (z_{11}, \dots, z_{1K})$ for C^1 , similarly z_2 for C^2) are recorded, and 2) the similarity between the two instances then equals to (I is the indicator function):

$$S(C^1, C^2) = \frac{1}{K} \sum_{i=1}^K I(z_{1i} = z_{2i}) \quad (5.2)$$

Neighborhood graphs for patient similarity visualization: Neighborhood graphs provide an intuitive way of patient similarity visualization with an entity-relationship representation [162]. In a relative neighborhood graph (RNG), two vertices corresponding to two instances C^1 and C^2 in a data set are connected with an edge, if there is no other instance C^3 which is closer to both C^1 and C^2 with respect to a certain distance function d [79]:

$$\forall C^3 : d(C^1, C^2) \leq \max\{d(C^1, C^3), d(C^2, C^3)\} \quad (5.3)$$

An important advantage of the RNG visualization is that graphs are always planar or close to planar and connected, while nodes have a reasonable small degree in contrast to related concepts like directed nearest neighbor or distance threshold graphs. In comparison to the well known heatmaps, they are easier to read with the more intuitive node-link representation, they allow visualizing additional features or even image thumbnails at nodes, and they have a flexible layout allowing to naturally visualize clusters, enlarge nodes, and filter out a set of nodes and edges [162].

5.2.2 Diagnosis and Severity Assessment of Aortic Valves

The accurate assessment of the disease severity is crucial for clinical decision making in patients with aortic valve disease. Several indices have been used for this purpose, mostly based on echocardiography imaging, including aortic valve area, transvalvular velocity and gradient, left ventricular ejection fraction, vena contract width and regurgitant orifice area. Unfortunately, these indices are all potentially affected by the haemodynamic state of the patient and other inaccuracies, which makes assessment especially for difficult cases as severe asymptomatic or moderate symptomatic patients, difficult [167].

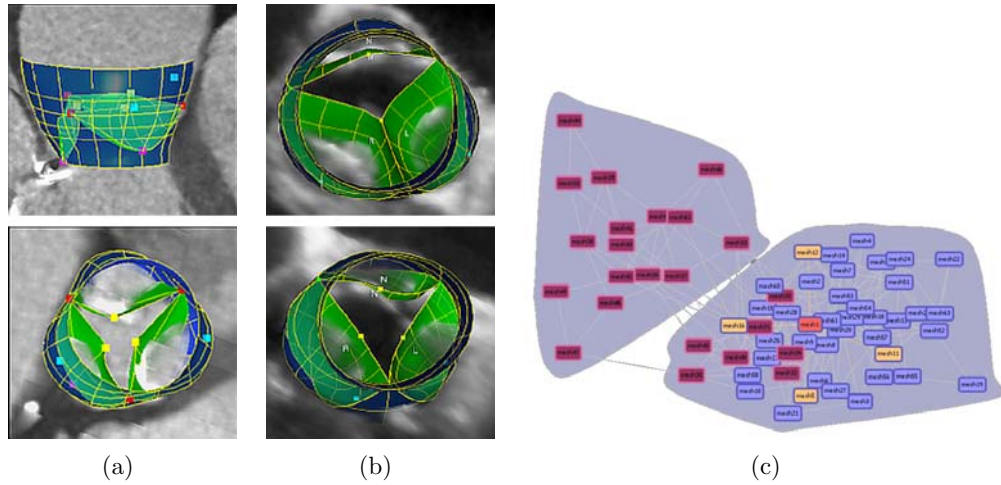


Figure 5.7: (a) Pathological aortic valves in CT: dilated aortic root and stenotic and calcified aortic valve. (b) Pathological aortic valves in TEE: bicuspid aortic valve and moderate stenotic valve. (c) Relative neighborhood graph with health (blue) and diseased (red) entries.

Using the method presented in section 5.2.1, we formulate a robust and reproducible shape-based diagnosis solution, which aggregates the complete morphological information of patient-specific aortic valves. From the model parameters M_{aortic} (see section 3.5), we learn a distance based function and apply in conjunction with a clustered RNG to discriminate between two groups of patients: 1) normal - mild and 2) moderate - severe aortic valve dysfunction. A severity score can be inferred from the similarity score between the subject case and the available training population. Figure 5.7 illustrates representative aortic valve pathology along with the obtained shape-based classification.

Furthermore, the coupling of the aortic and mitral valvular annuli through fibrous tissue is evident and leads to strong functional and morphological interdependency. Recent studies emphasize their correlation given by the anatomy [88, 158]. We propose to exploit this mutual morphological correlation among the different valves, for retrieval of similar healthy valves for a diseased case, in order to define precise and personalized targets of an intervention.

The following example illustrates the proposed use case: in case of a patient with a diseased mitral valve (MV), affected by annular dilation, and a healthy aortic valve (AV), we retrieve a case with a similar healthy AV and a healthy MV. The latter can then be used to determine the annular dimensions of the formerly healthy MV for mitral annuloplasty, i.e. the system provides a suggestion to the surgeon, which dimension of the prosthesis would actually be the best fit, such that the surgeon has an additional statistically based decision support, rather than having to rely on generic indication from clinical guidelines, publications and personal experience only. Moreover another interesting use case would be the design of personalized prostheses instead of selecting an optimal generic one, which would fit and reflect the formerly healthy valve's morphology and performance

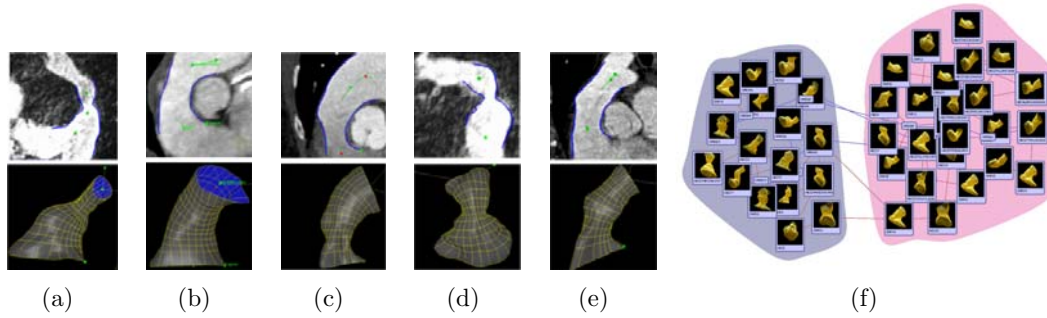


Figure 5.8: Types of pulmonary trunk morphologies: (a) pyramidal shape, (b) constant diameter, (c) inverted pyramidal shape, (d) narrowed centrally but wide proximally and distally, (e) wide centrally but narrowed proximally and distally [139]. (f) Relative neighborhood graph with unsuitable (blue cluster) and suitable (red cluster) individuals.

even better.

5.2.3 Patient Selection in PPVI

Until recently, pulmonary valve replacement has been exclusively performed through open heart surgery [21], with all associated risks: high morbidity, incidence of neurological damage, stroke and repeated valve replacement [127]. Novel percutaneous pulmonary valve implantation (PPVI) techniques [140], offer a less traumatic and safer treatment of the pulmonary valve [27].

The selection of patient for PPVI treatment is largely based on the morphology of the pulmonary trunk [18]. Intervention in unsuitable anatomies exposes patients to unnecessary invasive catheterization, for which the implanted device has a high probability of proximal device dislodgment. In an effort to standardize the selection process, Schievano *et al.* [139] proposed a classification of various morphologies, based on geometric measures and appearance of the right-ventricular outflow tract and the pulmonary trunk, into five groups: pyramidal shape (type I), constant diameter (type II), inverted pyramidal shape (type III), wide centrally but narrowed proximally and distally (type IV), and narrowed centrally but wide proximally and distally (type V) (see figure 5.8). Patients from type I are considered to be unsuitable for PPVI due to the narrow artery and high probability of device migration. Therefore the main challenge lies in discriminating anatomies of type I from other four classes.

The methodology from section 5.2.1 is applied to shape features extracted from the pulmonary trunk model $M_{pulmonary}$ (see section 3.5), estimated for specific individuals from cardiac images. To provide automated patient selection, a discriminative distance function learned using Random Forest in the product space is applied to classify subjects into two classes: PPVI suitable and PPVI unsuitable (see figure 5.8(f)).

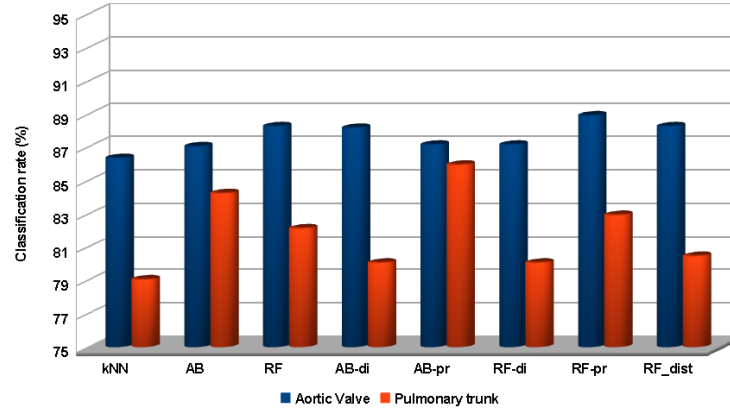


Figure 5.9: Classification accuracy for the different learning techniques applied to Aortic Valve Disease classification and PPVI suitability selection.

5.2.4 Results

The performance of the proposed method was evaluated on 4D cardiac CT and trans-esophageal echocardiographic data from 288 patients for the aortic valve diagnosis application (section 5.2.2) and 4D cardiac CT and 3D isotropic MRI data from 102 patients for the pulmonary trunk suitability selection for PPVI (section 5.2.3), with significant variation in image resolution and capture ranges.

For the aortic valve diagnosis experiment the evaluation set includes 234 healthy and 54 diseased valves, where one or multiple attributes of the following could be observed: regurgitation, stenosis, bicuspid malformation, dilation. In total 288 volumes associated with manual annotations were processed. For the PPVI suitability selection experiment the evaluation set includes 50 patients with pulmonary trunk geometry of type I (i.e. unsuitable for PPVI) and 52 patients with suitable geometries, totaling in 102 volumes and associated manual annotations. The population in both datasets covers a great range of ages, many different disease and appearance patterns, such as calcified aortic valves (typically a condition in elderly patients), but also bicuspid aortic valves, which is a congenital malformation (see figure 5.7). Each type of pulmonary trunk geometry (see figure 5.8) is represented, where many diseased cases are children, while a large portion of healthy valves was modeled from mature patients. Therefore besides pathology and individual variation yet another important factor, which increases the data heterogeneity is patient's age, influencing the valve morphology and complicating the task of learning from such data.

The accuracy of the model based classification presented in figure 5.9 is validated by 10-fold cross-validation. The figure demonstrates the classification accuracy of k-Nearest Neighbors (kNN), AdaBoost (AB) and Random Forests (RF) in the canonical space, as well as AdaBoost and Random Forests[23] in the product and difference spaces (AB-pr, RF-pr, AB-di and RF-di) and intrinsic RF distance (RF-dist). Prior to learning the valve shapes were normalized by their individual size and aligned with procrustes analysis,

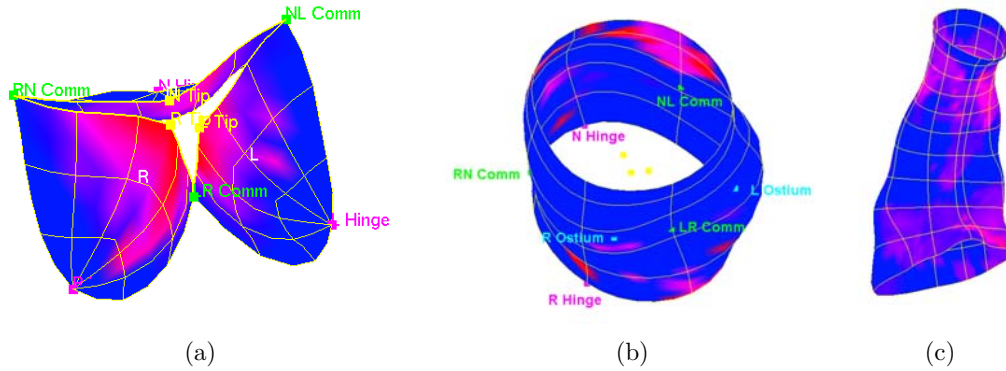


Figure 5.10: Discriminant anatomical regions for (a,b) aortic valve disease and (c) pulmonary trunk morphology: blue - less discriminate, red - more discriminate.

to cancel out translation, orientation and scale and minimize the effects of age. Each cross-validation run was performed on 200 (aortic) and 600 (PPVI) pre-selected features respectively, which were determined using the Gain-Ratio feature filter.

Learning from equivalence constraints improves the accuracy in comparison with learning in the canonical space. For this task the product space leads to the best accuracy in both experiments. While for the aortic valve experiment RF showed best performance in the product space with a classification rate of 88.9%, AdaBoost in the product space showed higher performance for the PPVI suitability selection with 85.9%. Learning distance functions from equivalence constraints helps to combine the power of boosting and random forests with the transparency of case retrieval.

For our experiments in the setting of the aortic valve disease classification we investigated the computed Gain-Ratio values for each coordinate of the geometrical model, in order to better understand the correlation between morphology and pathology. The most relevant regions for diseased valves are the free parts of the leaflets (see figure 5.10(a)), around the tips, as well as the right coronary ostium region and the upper part of the aortic valve towards the aorta (see figure 5.10(b)). This demonstrates, in concordance with the current pathological knowledge, the significantly higher sensibility of the aortic leaflets and ascending aorta.

A similar investigation conducted on the pulmonary trunk data set (see figure 5.10(c)) showed that the discriminant regions are around pulmonary valve sinuses and at the right ventricular outflow tract. This clearly reflects the morphologic differences between the types of pulmonary trunks. Moreover this shows, that the relevant regions are much larger compared to the aortic valve, which also necessitates the use of larger numbers of features compared to the experiments with the aortic valves. Therefore the use of shape models and manifolds as subspace representations will be part of our future work, in order to find more representative local shape descriptors as features.

5.2.5 Discussion

We propose a framework for retrieval and decision support in the management of VHD, which uses learning based discriminative distance functions. Various learning distance functions were evaluated including learning from equivalence constraints and the intrinsic Random forest distance. The generality and accuracy was shown by applying the method to different problems and large datasets from the domain of cardiology. Our method integrates the entire 3D geometrical expression of subject patient in an automatic classification framework offering a reliable and reproducible solution for diagnosis and decision support, which has the potential to advance the clinical management of valvular heart diseases.

5.3 Computational Decision Support for Percutaneous Valve Procedures

Valve replacement is the most common therapy for diseased aortic valves. Percutaneous approaches are becoming increasingly popular, due to reduced procedural complications and lower follow-up rates. Still there is a lack of efficient tools for valve quantification and preoperative simulation of replacement and repair procedures. Thus, the success of the intervention relies to a large portion on experience and skills of the operating surgeon or interventional cardiologist. We propose a novel computational framework for percutaneous aortic valve replacement procedures with stent mounted devices, which aims to provide advanced decision support for preoperative planning, intraoperative guidance and post-operative assessment.

5.3.1 Clinical Scope

Percutaneous aortic valve implantation (PAVI) has the potential to revolutionize the treatment of aortic valve disease, offering a less invasive alternative to open heart surgery. PAVI is already emerging as a feasible treatment for patients with high-surgical risk [65], over 30% of the symptomatic cases, and will account for 41.1% of the procedures by 2012 (Millennium Research Group 2008). The prosthetic implants are delivered through catheters using transvenous, transarterial or transapical techniques, while clinicians do not have direct view and access to the affected valve and surrounding anatomies.

Hence, critical decisions such as, type of procedure, implant type and sizing, deployment location and timing, and treatment assessment, are exclusively based on imaging techniques [122]. A misplaced implant can block the coronary ostia inducing a life threatening ischemic condition. Suboptimal deployment location can result in poor hemodynamic performance with severe paravalvular leakages and/or high gradients and suboptimal effective orifice. Wrong implant sizing may require re-operation or can damage the vessel tissue and cause catastrophic events as arterial dissection or rupture. Therefore advanced image analysis and computational models for precise planning, procedure guidance, and outcome assessment, may significantly improve percutaneous valve implantation techniques.

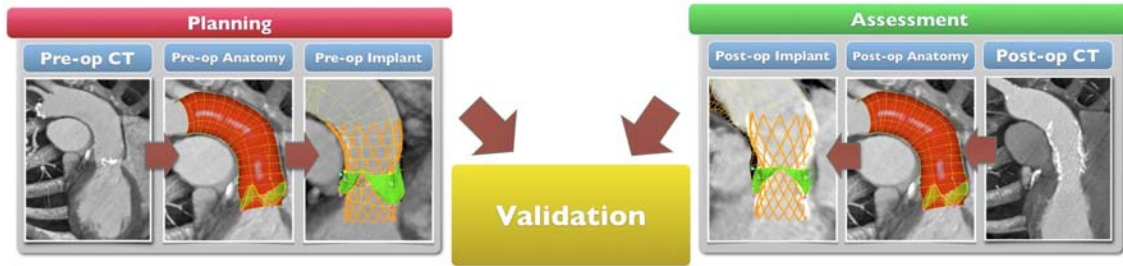


Figure 5.11: Schematic description of the proposed PAVI computational decision support workflow.

We propose a computational framework for percutaneous aortic valve implantation, which supports decisions throughout the clinical workflow, which is summarized in section 5.3.2. Modeling of the aortic valve and ascending aorta and patient-specific estimation from pre- and post-operative cardiac CT images is described in section 5.3.3. Section 5.3.4 presents the computational environment, which allows for in-silico valve implantation for evaluation and prediction of procedure success under various treatment scenarios. Comprehensive validation and performance evaluation is given in section 5.3.5 by comparing the simulation results from preoperative data with the real device imaged in the postoperative data.

5.3.2 Workflow Overview

The proposed PAVI computational decision support workflow is illustrated in figure 5.11:

Pre-operative workflow: 1) Pre-operative cardiac CT volume acquisition for procedure planning purposes 2) Patient-Specific anatomical model estimation and automatic quantification for valve assessment and patient selection 3) In-silico valve implantation under various interventional procedure conditions for identification of optimal device type, size and deployment location as well as treatment outcome prediction until optimal predicted performance is observed.

Post-operative workflow: 4) Post-operative cardiac CT volume acquisition for treatment evaluation 5) Patient-Specific anatomical model estimation for quantitative anatomical assessment 6) Patient-Specific deployed device estimation for quantitative implant assessment.

5.3.3 Patient-Specific Anatomical Modeling and Estimation

This section reviews the anatomical model of the aortic valve and ascending aorta as well as the patient-specific estimation of its parameters from imaging data as in presented in chapter 3 and 4 (see figure 5.12).

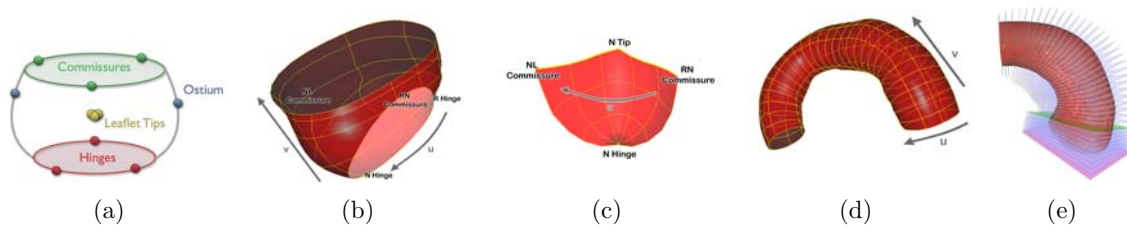


Figure 5.12: Aortic valve and ascending aortic root model. (a) generic model of the aortic valve including nine anatomical landmarks. (b) point distribution model of the aortic root. (c) aorta leaflet model - the N leaflet is depicted. (d) ascending aortic root model. (e) full model with the corresponding anatomical parameterization.

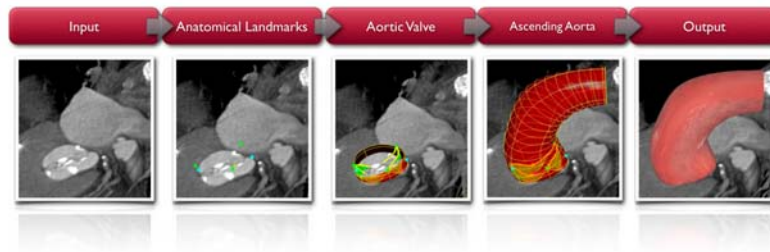


Figure 5.13: A survey of our hierarchical model estimation schema.

Anatomical Landmarks: Represented by three-dimensional points in the Euclidean space; the considered anatomical landmarks are: L / R / N Hinges, LR / RN / NL commissures, L / R / N leaflet tips, and L / R coronary ostia.

Aortic valve root and leaflets: The aortic valve root is constrained by the commissures, hinges and ostia and represented as a tubular surface mesh. The mesh is aligned with the aortic circumferential u and ascending directions v and includes 36×10 vertices. The left / right / none aortic leaflets, are modeled as hyperbolic paraboloids on a grid of 11×7 vertices. Each leaflet is defined by one hinge, two commissures and one leaflet tip.

Ascending aortic root: The ascending aorta emerges from the aortic root and incorporates a variable length. The anatomy is composed of a fixed number of circumferential coordinates $u = 36$ and a variable number of coordinates along the ascending direction v . The first ring starts at from the commissures.

Patient-Specific Model Estimation The patient-specific parameters of the aortic valve and ascending aorta model are estimated from volumetric images using a robust learning-based algorithm as in chapter 4. The a posteriori probability $p(M|I)$ of the model M given the image data I , is hierarchically estimated within the Marginal Space Learning (MSL) framework. Detectors are successively trained using the Probabilistic Boosting Tree (PBT) [164] with Haar and Steerable features, and consequently applied to

estimate the anatomical landmarks and structures from cardiac CT volumes as illustrated in figure 5.13.

5.3.4 Device Modeling and In-Silico Deployment

Stent Model: A library of virtual devices/implants was created based on manufacturers' description to incorporate realistic geometrical properties. In this work two models of the CoreValve Revalving System by Medtronic (Minneapolis, MN, USA) are treated, namely the models CRS-P3-640 and CRS-P3-943 (see figure 5.14(a)). The implant consists of 165 cells formed by the struts. The two models have length of 53 and 55 mm and diameters at the inflow, middle and outflow levels of 26, 22, 40 and 29, 24, 43 mm respectively. The Xenograft artificial valve consist of porcine pericardial tissue, out of which the leaflets are manufactured and mounted to the implant's stent. The library can be easily extended with future devices using the methods described in the following. The device is modeled out of two parts: a geometric representation, which precisely mimics the exact geometry of the device, the so-called *stent mesh*, and a second superimposed 2-simplex mesh, named in the following *computational mesh*, which is used for computation and to guide the expanding deformation [89, 111]. Figure 5.14(b) depicts the topological relationship between the computational mesh and the stent mesh, which is composed of struts connecting a subset of points of the computational mesh. In order to infer the geometrical properties of the stent model various dimension were measured from stereolithographic scans of the modeled implants. These are the strut lengths, the characteristic angles in each cell and the device's circumferences at each level, where each level is defined by the strut joints.

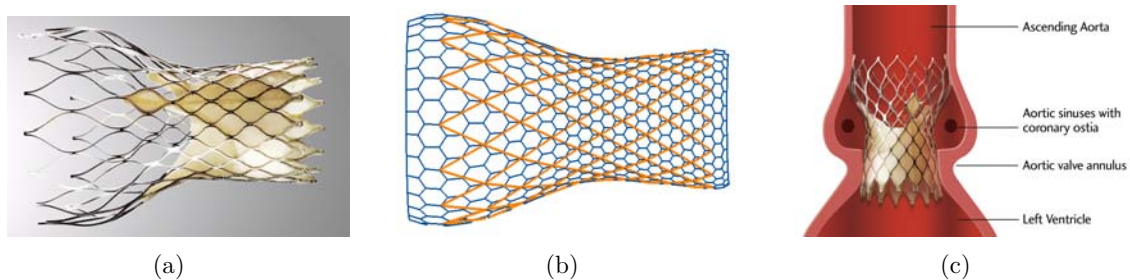


Figure 5.14: (a) CoreValve implant, (b) long axis cross section of stent mesh (orange) with superimposed computational mesh (blue) and (c) CoreValve implant with sketch of target anatomy (Sources a & c: <http://www.medtronic.com>).

Virtual Stent Deployment: To simulate valve replacement under various conditions, different devices are chosen from the library and virtually deployed under different parameters, into the previously extracted patient-specific model of the affected valve. The expansion of the device is modeled by balancing external and internal forces as encountered in the actual procedure, using iterative optimization methods. Following the works

of Larrabide et. al. and Montagnat et. al. [89, 111], the expansion is described by a finite difference discretization of a second order differential equation:

$$p_i^{\vec{n}+1} = p_i^{\vec{n}} + (1 - \gamma)(p_i^{\vec{n}} + p_i^{\vec{n}-1}) + f_{int}(p_i^{\vec{n}}) + f_{ext}(p_i^{\vec{n}}) + f_{reg}(p_i^{\vec{n}}) \quad (5.4)$$

where p_i is a point on the computational mesh, n is the iteration number, f_{ext} , f_{int} and f_{reg} external, internal and regularizing forces and the weighting parameter γ . Figure 5.15 shows a visual description of each of the forces. An outline of the algorithm is given in figure 5.16. The internal forces $f_{int}(p_i^{\vec{n}}) = f_{length}(p_i^{\vec{n}}) + f_{angle}(p_i^{\vec{n}}) + f_{circ}(p_i^{\vec{n}})$ model the intrinsic properties of the stent and enforce deformation along it's surface normals and long axis as the device is self-expandable. Hence they are parameterized by strut lengths, characteristic angles and device circumferences, which were measured from the expanded template. Accordingly, these forces are adapted, such that the implant attempts to achieve the targeted dimensions, and they induce different expanding pressures at different levels. Particularly $f_{circ}(p_i^{\vec{n}}) = \vec{n}_i(c_k - \sum_{\forall j \in \mathcal{N}_k} \|p_j^{\vec{n}} - p_{j+1}^{\vec{n}}\|)/2\pi$ pushes the points $p_i^{\vec{n}} \in \mathcal{N}_k$ along the surface normal \vec{n}_i to satisfy the reference circumference c_k of the stent shape, where \mathcal{N}_k is the set of strut joints at a level k . It is important to note, that f_{circ} does not enforce the stent diameter directly but the stent circumference instead to account for expansion into arbitrary shaped vessel geometries, which have typically non-circular cross sections. f_{length} and f_{angle} enforce the strut lengths and characteristic angles observed in the expanded shape [89]. The external forces $f_{ext}(p_i^{\vec{n}})$ model the interaction of stent and aortic valve and aorta tissue, and guide the implant deformation by balancing the internal device forces: $f_{ext}(p_i^{\vec{n}}) = -\vec{n}_i(\vec{n}_i \cdot f_{int}(p_i^{\vec{n}}))(\|p_i^{\vec{n}} - \vec{c}_k\|/\|\vec{v} - \vec{c}_k\|)$ with stent centroid \vec{c}_k at level k and the intersection point \vec{v} of normal and vessel surface. The regularizing forces f_{reg} are solely defined on the computational mesh to provide smoothness as described in [111]. As mentioned above the method focusses on self-expanding implants, which inherently exercise forces of minor amplitudes onto the surrounding vessel tissue. Therefore we argue, that the resulting minor deformations can be neglected.

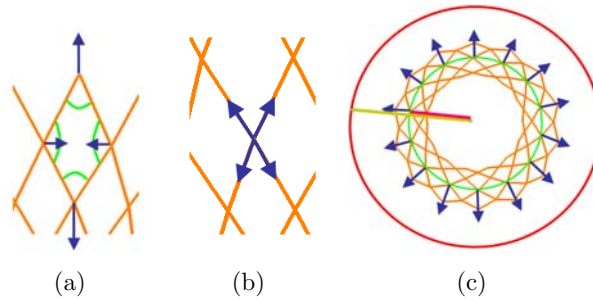


Figure 5.15: Forces acting on the model on deployment to converge to the observed geometric properties: (a) f_{angle} enforces the charateristic angles at the strut joints (green), (b) f_{length} maintains the strut lengths. (c) f_{circ} enforces the circumference (green), while f_{ext} dampens and eliminates the all forces acting along the stent mesh normal wheighted by the fraction of distances of strut joint and vessel wall (red) to the stent centroid (magenta/yellow). Please note that (c) shows a short axis cross section of the stent mesh.

Input:

- Patient-specific model of aortic valve and aorta ascendens
- implant placement position and orientation

Output: Deployed Implant**Execute:**

- create computational mesh and stent mesh with constant radius of 1 mm at manually selected placement position, oriented along the aortic root centerline
 - **repeat:**
 - for each point $p_i^{\vec{n}}$ on the *computational mesh*, calculate $f_{reg}(p_i^{\vec{n}})$, $f_{angle}(p_i^{\vec{n}})$, $f_{length}(p_i^{\vec{n}})$, $f_{circ}(p_i^{\vec{n}})$ and $f_{ext}(p_i^{\vec{n}})$
 - for each $p_i^{\vec{n}}$, compute $p_i^{\vec{n}+1}$ according to Eq. 5.4
 - if mean point displacement on the *stent mesh* $< \epsilon$, convergence achieved; stop execution
-

Figure 5.16: The outline of our virtual stent deployment algorithm.

5.3.5 Experimental Results

The validation of the proposed framework is divided in two experiments. First we present results on the performance of the automatic patient-specific model estimation from pre- and post- cardiac CT data, as well as the quantitative variation between pre and post anatomies. Second we validate the proposed in-silico implantation, by comparing predicted valve deployment, using pre-operative data, with real deployment from post-operative data.

Validation of Patient-Specific Model Estimation: The data set used for patient-specific model estimation consists of 63 multi-phase (10 frames per cycle) cardiac CT and 21 single-phase cardiac CT acquisitions, which sums up to 651 CT volumes. Scans are acquired from different patients with various cardiovascular diseases (including ascending aortic root aneurysm, regurgitation, calcific stenosis and bicuspid aortic valves), using different protocols, resulting in volumes with 80 to 350 slices and 153x153 up to 512x512 voxel grid resolution and 0.28mm to 2.0mm spatial resolution. Each data set is associated with an expert annotation used as ground-truth.

A combined accuracy for the patient-specific model estimation of 1.45mm is obtained in 30sec on a standard desktop machine (Intel Xeon 2.66Ghz, 2GB RAM) for both pre- and post-operative volumes. Performance is reported on test data, which represents randomized 20% of the complete dataset, while the remaining 80% were used for training.

Due to different factors, a bias between the pre- and post-operative anatomical models can be expected. These are cardiac phase shifts and image noise but also deformation of the aortic vessel wall due to stent deployment, where the latter was assumed to be sufficiently small to be neglected in the deployment algorithm (see section 5.3.4). There-

fore we quantified the differences for a subset for each pair of corresponding anatomical models obtained from a subset of 20 patients with pre- and postoperative image data. Quantitative results in table 5.5 support the validity of our assumption, showing a mean relative deviation of up to 6.46% between pre- and post-operative anatomies.

Table 5.5: Deviation of pre- and postoperative anatomies: Differences in diameter at sinutublar junction, valsava sinuses and aortic annulus are given in absolute values as well as relative to the postoperative measurement. Values of Mean and standard deviation are provided as well as 80-percentile and maximum.

measurement	absolute (mm)			relative (%)		
	mean (std)	80%	max	mean (std)	80%	max
<i>sinutublar junction</i>	2.3 (1.7)	3.7	5.7	6.46 (4.6)	10.5	14.9
<i>valsava sinuses</i>	1.1 (0.9)	1.7	4.1	3.49 (2.6)	5.2	9.98
<i>annulus</i>	1.5 (1.2)	2.5	5.2	5.06 (3.2)	7.7	14.3
<i>point-to-mesh distance</i>	1.6 (0.98)	2.4	2.8	-	-	-

Validation of In-Silico Valve Deployment: The validation of the in-silico valve deployment is performed on 20 patients with pre- and post-operative cardiac CT images. It is important to note, that for this purpose the preoperative prediction result is compared with the real device imaged in the postoperative data.

From the pre-operative volume, we automatically estimated the aortic valve and ascending aorta model, and virtually deploy the implant using the proposed computational method and constraints from the patient-specific anatomical model. Please note that in order to perform a fair comparison, only the deployment location and orientation is inferred from the post-operative data. From the post-operative volume, we automatically estimated the aortic valve and ascending aorta model. The real implant is manually placed and fit to the imaged stent, which is well visible in the post-operative volume, using a semi-automatic method based on the thin-plate-spline transformation. A selection of deployed and corresponding manually placed stents is depicted in figure 5.17. The performance is reported in table 5.6 in terms of internal precision, by comparing only the virtual and real implants shape in isolation via symmetric point-to-point distance, and external precision. The latter means to compare the virtual and real implants position relative to clinically relevant locations, in order to account for the potentially critical conditions due to wrong implant sizing and placement such as blockage of coronary ostia and more importantly paravalvular leakages at the annular level as mentioned in section 5.3.1. This is done by computing the differences of the pre- and postoperatively measured distances from annulus ring and coronary ostia to the closest stent point respectively.

In the clinical context, the required accuracy is proportional to the tolerance between therapeutical alternatives. Considering the diameter differences of 3mm (at the annular level) of the Medtronic CoreValve implants (see Section 5.3.4), the system provides a sufficient approximation in at least 80% of the cases for prevention of paravalvular leakages, with an external accuracy of up to 1.4mm at the annular level. The algorithm performed at an average speed of 55sec on a standard desktop machine (Intel Xeon 2.66Ghz, 2GB

Table 5.6: Accuracy of in-silico valve deployment measured in mm: besides point-to-point distance between pre- and postop stent, accuracy relative to the anatomies was estimated from the differences in distances between aortic valve annulus and coronary ostia and implant. Values of mean and standard deviation are provided as well as 80-percentile and maximum.

	mean (std)	80%	max
<i>stent point-to-point</i>	2.18 (1.77)	2.4	8.45
<i>annulus</i>	0.7 (0.73)	1.4	2.14
<i>L coronary ostium</i>	1.42 (1.51)	2.16	4.75
<i>R coronary ostium</i>	1.55 (1.24)	2.02	4.27

RAM). Thus our framework enables for fast and efficient preoperative planning and risk minimization by finding the best implant type, size and deployment location and orientation via varying these parameters until optimal predicted performance is observed.

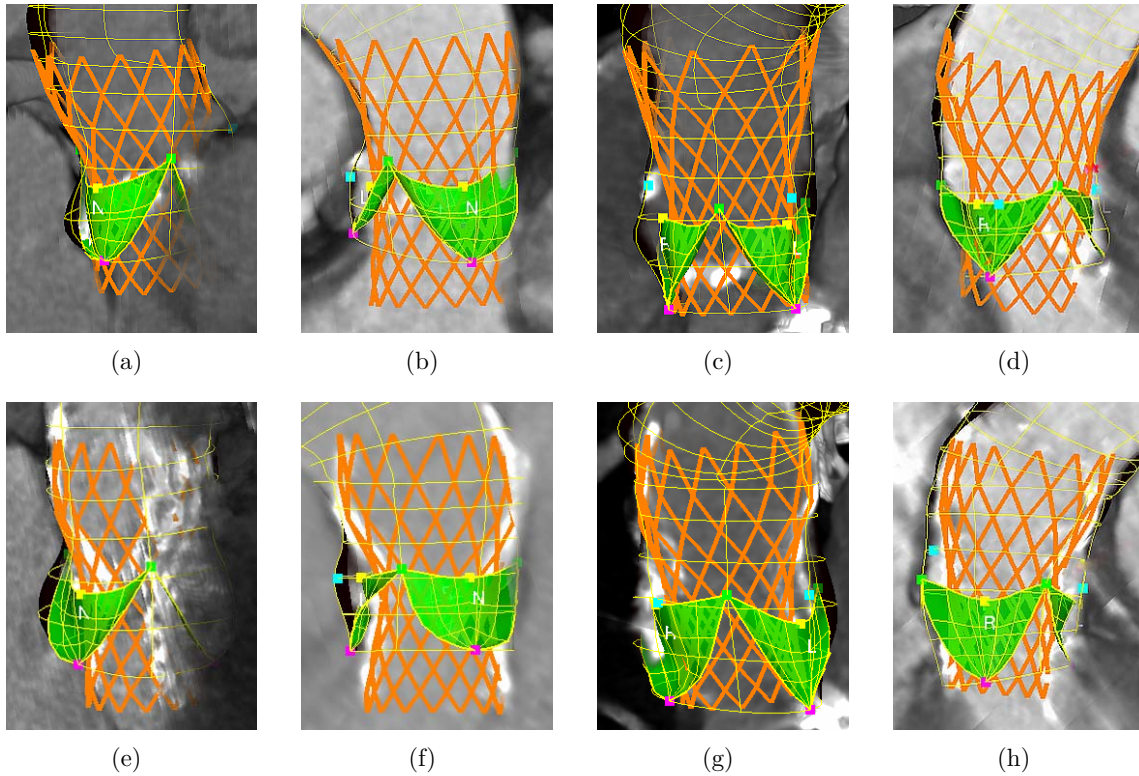


Figure 5.17: Example results of preoperative virtual stent deployment (a-d) vs. post-operative stent models (e-h) overlaid with with the anatomical models. Note the deviation of the virtually deployed stent around the sinutubular junction (upper end) in contrast to the close approximation at sinus and annular level, which is due to the fact, that internal stiffness of the stent configuration is not modeled yet.

5.3.6 Discussion

A novel framework for computational decision support for percutaneous aortic valve implantation was presented. A fast and robust estimation of an anatomical model enables for precise modeling of the patient-specific morphology and is consequently used for in-silico implant deployment. The approach was validated with pre- and post-operative data sets from 20 patients and shows reasonable accuracy within the variation in appearance given by image and motion artifacts. To the best of our knowledge, this is the first time a computational framework is validated using real pre- and postoperative patient data. The framework is targeted for fast and efficient preoperative planning with a library of different implants, intraoperative guidance and postoperative assessment of interventional outcome. It may have impact on the cardiology of the future and improve the OR towards increased transparency.

6.1 Summary

The main subject addressed in this thesis is the patient-specific estimation of physiological valvular models from multi-modal cardiac images. Based on the extracted explicit mathematical representation of real morphological and functional parameters, a series of clinical applications are proposed, which may advance the treatment of patients suffering from valvular heart disease.

Dysfunctions of the heart valves affect 2.5% of the global population and require yearly over 100,000 surgeries in the United States alone. Despite continuous progress in surgical and interventional therapy, with an average cost of \$141,200 and 4.9% in-hospital death rate, valve treatment remains the most expensive and also the most precarious among all cardiovascular procedures. Chapter 2 discussed relevant clinical and medical aspects as well as the role of non-invasive imaging and medical imaging analysis technologies in upgrading the contemporary healthcare delivery. In section 2.6.3 we advocated for the essential role of machine learning in future clinical applications, given the ability of this approach to deal with the inherent complexity and uncertainty of the medical field. Another strong argument for algorithms that learn from examples is the availability of large databases of medical images in the recent years, as a result of the proliferation of cost-effective non-invasive imaging techniques.

The first contribution of this thesis is introduced in chapter 3, where we proposed a novel physiological model of the heart valves to precisely capture their anatomical, dynamical and pathological variations. Previous cardiac models were proposed in the literature and proven to be beneficial in the clinical setting, however none of those explicitly treat the valvular apparatus. Our model is hierarchically defined and comprehensively represents the location and rigid motion, anatomical landmarks and the comprehensive shape and dynamics of all four cardiac valves: aortic, mitral, tricuspid and pulmonary valves. Based on the proposed mathematical formulation, we as well addressed statistical

models of patient populations in section 3.7. Those effectively describe parameter variation across the cardiac cycle and individuals, and incorporate prior knowledge critical for the patient-specific estimation from cardiac images.

Our next core contribution is the development of discriminative learning-based algorithms that permit the estimation of patient-specific model parameters from cardiac images. Chapter 4 presented a course-to-fine methodology, which is aligned with the three abstraction levels of the valvular model. In the first step we combine two established algorithms, Marginal Space Learning (MSL) and RANdom SAmple Consensus (RANSAC) to build a new approach for the time-coherent detection of the valvular location and motion from an arbitrary four-dimensional cardiac scan. Subsequently, in section 4.4 we introduced a novel learning algorithm, Trajectory Spectrum Learning (TSL), which coupled with Local-Spatial-Temporal (LST) features facilitates the estimation of periodic motion. TSL handles location and motion simultaneously, through a spectrum learning and optimization formulation that operates in marginal trajectory spaces. In our context, it is used to robustly estimate the parameters of the anatomical landmarks from four-dimensional image sequences. The last method described in section 4.5 is applied for the object delineation of dynamic models, using boundary detectors and motion manifold learning techniques. In section 4.6 the performance of the proposed estimation framework is demonstrated through extensive experiments on 476 patients, which results into an average precisions of 1.73mm and speed of 4.8 seconds per volume.

Chapter 5 introduced three-clinical applications based on the modeling and estimation techniques described in this thesis. A novel paradigm for the clinical analysis of the valvular apparatus is presented in section 5.1. This has the potential to replace current manually performed measurements on 2D images with automated model-based quantification from 4D data, which offer an accurate, efficient and comprehensive valvular evaluation solution. In section 5.2 we proposed a novel methodology to automatically derive high-level clinical information from anatomical models using learning-based discriminative distance functions. The feasibility of the introduced concept is exemplified in the context of automated shape-based diagnosis and patient selection for percutaneous treatment. Finally, a computational decision support framework is presented in section 5.3, which combines models of devices with patient-specific anatomical information to simulate and predict the outcome of percutaneous procedures under various treatment scenarios.

The technology described in this thesis can potentially advance the management of patients affected by valvular heart disease by reducing clinical investigation costs, risks for complications during procedures, and ultimately by improving the overall outcome of valvular treatment.

6.2 Discussion and Future Work

Valvular Modeling and Estimation: Future work will continue to focus on the advancement of the parameter estimation framework and the direct extensions of the valvular model. With the scope of constraining the estimation problem, multilinear statistical modeling was demonstrated to decompose shape spaces in temporal and spatial com-

ponents, in contrast to Active Shape Models in which both are coupled [201]. Section 3.7.3 presented a model of complex spatio-temporal variation that can be exploited in learning-based approaches to parameter estimation. In fact, our tensor formulation advances the state-of-the-art by conditioning the shape parameterization with additional physiologically-driven measurements. Such surrogate variables were proven to increase performance for PCA models of anatomical structures [16]. Other promising directions that may lead to improved estimation results include manifold learning techniques [191] and simultaneous detection of multiple objects [189].

On the modeling side, one important extension for the future will be the inclusion of the subvalvular apparatus of the mitral and tricuspid valves [122]. Although critical in the clinical context, these structures are not included in standard TEE scans and difficult to distinguish in cardiac CT or CMR. Thus, patient-specific parameters must be inferred from statistical models or by fusing additional imaging information. The extension to a volumetric representation, which models the tissue thickness of the valves is also of high clinical importance. Such parameters could be estimated within the same discriminative-learning framework, while the ground-truth for training and validation could come from in-vivo measurements of resected tissue, post repair or replacement procedures.

Integration and Computation: One pivotal direction for future developments is the horizontal and vertical integration of the valvular model into a comprehensive, multi-physics, multi-scale model of the full heart. While realistic patient-specific computational modeling of the cardiac system is unfeasible without a precise model of the valvular apparatus, existent approaches [138] are lacking this essential component. Initial integration efforts presented in appendix A, demonstrated the capabilities of joint chamber-valve models to simulate hemodynamics within a computational fluid dynamic formulation. Future horizontal extension actions will include the addition of right-side chambers and valves, pulmonary veins, superior and inferior vena cava as well as the right and left pulmonary arteries.

Biomechanical models, which have attracted increasing amounts of interest over the last decade [11], are indispensable for the development of advanced treatments of cardiovascular disease. Ayache and collaborators demonstrated a electromechanical model of the left and right ventricles capable to simulate propagation of the electrical front and myocardial contraction [143, 142]. Additionally, their recent work focuses on the personalization of simulations in various cardiovascular contexts [144, 141, 14]. Future horizontal and vertical integration of cardiac models is in perfect agreement with the worldwide scientific effort under the Virtual Human Physiome projects and will promote a more personalized, preventive and predictive healthcare.

Treatment Simulation and Prediction: From an application stand point, simulation of surgical and interventional procedures would advance valvular treatment to become safer and with improved post-operative results. In section 5.3, we proposed a novel computation framework to simulate percutaneous aortic valve implantations. An important extension to be considered in the future research is the modeling of material properties of the valvular and cardiac tissue. Fully coupled fluid-structure interaction formulations

were proven to be affective for the computation of material properties [39, 182]. In contrast to existent solutions, our approach will be based on patient-specific geometrical and dynamical constraints obtained from multi-modal cardiac images. The collateral benefit of adding material properties is the enrichment of the valve analysis capabilities to include quantification of stress and strain parameters. Recently, models were proposed to predict the outcome of cardiac remodeling procedures [103]. Such techniques can be directly adopted to simulate valvular repair procedures and potentially mainstream reconstructive treatment beyond specialized cardiac centers.

Model-based Information Fusion: Parameters contained by the estimated patient-specific model are also beneficial in the context of image registration and reconstruction. In the appendix B, we demonstrated a model-based approach to recover full dynamic information of the pulmonary trunk within and cross-modality CT-CMR formulation. A novel regression based reconstruction method is proposed, which learns the anatomical and dynamical correlation from 4D cardiac CT estimated models and infers the incomplete temporal information based on sparse CMR images. Following the same principle, model parameters estimated from multi-modal images of the same patient can be directly used to compute a focused deformation field and perform image registration. This will enable the combination of complementary information acquired with various techniques into a comprehensive patient-specific physiological model. A practical example would be the model-based fusion of highly resolved anatomical information from cardiac CT, with Doppler velocity data from Ultrasound and highly resolved dynamic parameters from CMR. Among other advantages, future progress in model-based information fusion will enable the augmentation of real-time intra-operative (fluoroscopy, TEE and intravascular ultrasound) images with detailed preoperative data, to guide complicated cardiovascular interventions [185].

Appendix

Patient-Specific Modeling of Left Heart Anatomy, Dynamics and Hemodynamics from High Resolution 4D CT

Abstract - There is a growing need for patient-specific cardiac models for intervention planning, outcome prediction or assessment of cardiac disease progression. However, most of the recent work in cardiovascular simulation relies on generic heart models built from at most one cardiac phase with simplified motion, driven by fluid dynamics equations. We propose to advance the state-of-the-art by exploiting a comprehensive, patient-specific left heart model extracted from 4D Computed Tomography (CT) data. Explicit physiological constraints are captured in the modeling of the left ventricle (including outflow tract), left atrium (including pulmonary veins), mitral valve, and aortic valve (including ascending aorta). By using this patient-specific model as an input to a 3D Navier-Stokes solver we derive realistic hemodynamics, constrained by the local anatomy, along the entire heart cycle. We present a differential assessment of the flow dynamics corresponding to specific heart conditions. The simulation results shed light upon the functional differences between one normal and two diseased hearts - one with a dilated aortic root and one with a bicuspid aortic valve.

Introduction

Patient-specific cardiac models are a longstanding medical goal that is close to becoming reality. Advances in cardiovascular imaging, automatic data parsing and model extraction, and computational fluid dynamics contribute to more and more refined models of a patient's heart. Such models will allow in the near future to assess cardiac disease progression or predict intervention and treatment outcome [48].

Machine learning methods recently demonstrated robust performance in recovering the anatomy and dynamics of the heart chambers and heart valves from 4D CT data.

This work was presented at ISBI in 2010, Rotterdam, The Netherlands.

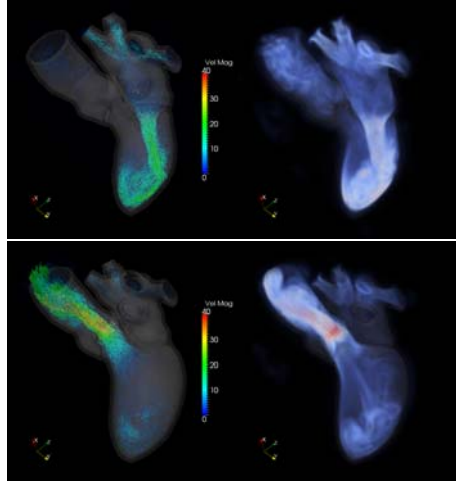


Figure A.1: Visualizations of patient-specific truncated velocity (left) and vorticity fields (right). Normal heart in early diastolic stage (top) and early systolic stage (bottom).

The parametric models of the left atrium, left ventricle, right atrium and right ventricle are estimated in [197] for the entire the heart cycle. The physiological modeling of the aortic and mitral valves along with estimation methods of patient-specific geometry and dynamics are presented in [74]. As the heart valves regulate the blood flow inside the heart and towards the human body, morphological and functional parameters are essential for accurate hemodynamic simulations of the cardiac system. However, valves alone cannot explain the complex variation in flow patterns, thus these must be considered in connection with the heart chambers, main arteries and veins for a truthful and comprehensive cardiac flow analysis.

Earlier work in blood flow simulation simplified computations by using generic cardiac models or reduced dynamics assumptions for the blood flow. Generic cardiac flow models (e.g. [64]) were important pioneering steps in blood flow simulation. The usual criticism of this work that it does not rely on patient-specific data. Models of the left side of the heart, with smooth ventricular walls, and imposed boundary conditions in the valve regions are used in [97] and [136]. Blood flow simulations based on a hybrid model of the left side of the heart have been recently presented in [109], with the geometry derived from the Visible Human Project and dynamics transferred to the chamber models from MRI data.

This work advances the state-of-the-art by exploiting for the first time full 4D CT data sets to compute patient-specific anatomy, dynamics and hemodynamics (see figure A.1). We derive explicit dynamic physiological models for the left ventricle, left atrium and pulmonary veins, aortic valve, aortic root, ascending aorta, and mitral valve. We use the recovered motion of the chambers and valves to provide geometric and velocity boundary conditions to the blood flow at every step in the cardiac cycle. Namely, we use normal and diseased left heart models, imposed as boundary conditions in a 3D Navier-Stokes simulator. In the results we show that the computed blood flow is quite different for each of the patients involved in this study and we analyze the hemodynamic differences.

In the following we make a presentation of the cardiac geometry and dynamics recovery (section A) and of the fluid simulation system used in this work (section A), and go at length into the blood flow computational results in section A. We end with a conclusion and plans for future work.

Patient-specific cardiac geometry and dynamics

The four-dimensional left heart model applied is physiologically defined to capture complex morphological, dynamical and pathological variations [197], [74]. The model includes the following anatomic structures (see figure A.2): left atrium (LA), left ventricle (LV), right atrium (RA), right ventricle (RV), aortic valve (AV), mitral valve (MV), ascending aorta (Ao), and pulmonary veins (Pv). Each of the structures is parameterized along an anatomical defined regular grid of vertices, which implicitly guarantees point-correspondences of the geometric meshes, mandatory in patient-specific computational modeling. Anatomical landmarks govern the interconnection of the cardiac components, which result into a comprehensive model of the heart. In addition, we enhanced the model introduced in [197] to include the ascending aorta and a more detailed left atrium structure that includes the pulmonary veins (see figure A.2). Note that the hemodynamic simulations are performed on the left components of the heart.

From 4D cardiac CT images, we automatically estimate patient-specific left heart models by applying a hierarchical learning-based framework. Robust anatomy detectors D are trained using the Probabilistic Boosting Tree based on over-complete image representations given by Harr-like, steerable and local-spatial-temporal image features. The detectors estimate the posterior probability of the model fitting given the input images $p(M|I)$ and are applied in effective optimization algorithms to determine the patient-specific parameters.

Detectors D_{pos} , D_{ori} and D_{siz} , for position, orientation and size, are used within the Marginal Space Learning (MSL) algorithm [197] to solve for the object localization of each anatomy. The complex opening and closing motion of the aortic and mitral valves is estimated by trajectory detectors D_{traj} within the Trajectory Spectrum Learning (TSL) framework [74]. A statistical model of the left heart, learned from the training data is projected with the estimated location and motion parameters to initialize the patient-specific geometry and dynamics. The estimation is concluded with a local non-rigid deformation, guided by boundary detectors D_{bou} , to accurately delineate the true object boundary from images. Complete details of the learning framework for automatic model fitting can be found in [197], [74].

Training and verification of the patient-specific estimation is performed on a large database of expert annotated 4D cardiac CT images that includes 69 valve patients and 137 studies for the two chambers, aorta and pulmonary veins. Included data was collected in multiple medical centers around the world, from patients affected by various cardiac diseases with images aquired using heterogeneous scanning protocols. Each study is ECG gated and includes 10 volumes per cardiac cycle, with 80-350 image slices per volume, 512x512 pixels per slices, 0.28 to 0.74mm isotropic in plane resolution and slice tickness of 0.4 to 2mm.

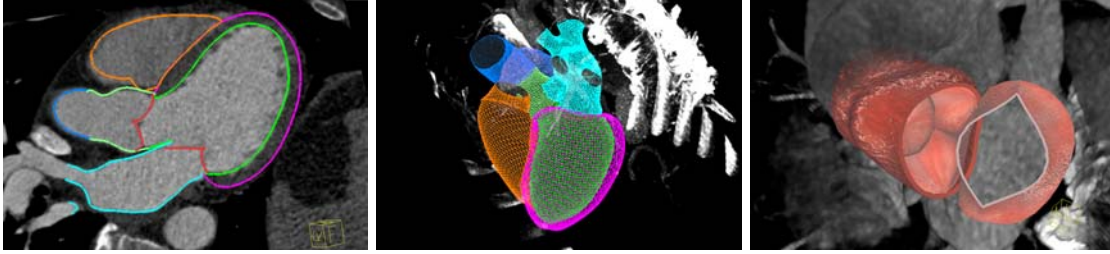


Figure A.2: Patient specific cardiac model fitted to 4D CT data with chambers and valve details.

The performance for the recovery of cardiac geometry and dynamics from 4D CT images was evaluated using cross-validation. Comparison of the automatic estimation with ground-truth annotation using the point to mesh error function resulted in the following average accuracy values: left atrium and pulmonary veins 1.32mm, left ventricle 1.13mm, ascending aorta, aortic and mitral valves 1.36mm. Inter-user variability experiments were conducted with five experts which compared the estimation precision of the proposed method to the variation of manual modeling between different users, demonstrated the system-error to lie within 90% of the inter-user confidence interval.

Cardiac Hemodynamics Simulation Given the Heart Geometry and Dynamics

The framework used for simulating blood flow in the left heart follows the setting introduced in [109]. Namely, the heart mesh is immersed in a computational box fitted with a regular grid, and the Navier-Stokes equations are solved inside the box using finite differences. The liquid inside the box and "outside" the left heart plays the role of the body circulatory system connected to the left heart, and imposing slip or no slip boundary conditions on the sides of the box simulates the flow resistance of the circulatory system.

The heart mesh is allowed to have small gaps that are not recognized by the grid (namely the width of the gap should be less than the grid spacing dx), which makes the code quite robust to initial mesh quality. This is achieved by using in the simulation a level set corresponding to the heart mesh, defined as $\psi(x) = \text{dist}(x, \text{mesh}) - dx$. All the visualizations presented show the zero level isosurface of this level set function.

Inside the computational box we solve the 3D Navier-Stokes equation for incompressible flow with viscous terms which are described for example in [109]. The physical parameters are set to the blood density $\rho_{\text{liquid}} = 1050 \text{kg/m}^3$ and dynamic viscosity $\mu = 4 \text{mPa}\cdot\text{s}$. The velocity of the mesh walls is extrapolated in space (and interpolated in time between two consecutive mesh positions) to the grid nodes, and used to enforce no-slip conditions to the Navier-Stokes solver during the computation. One difference between our solver and the one presented in [109] is the treatment of the isovolumic stages. In [109], the closed regions (e.g. the ventricular chamber) that possibly may have a variable volume during isovolumic stages, were treated robustly by relaxing the incompressibility condi-

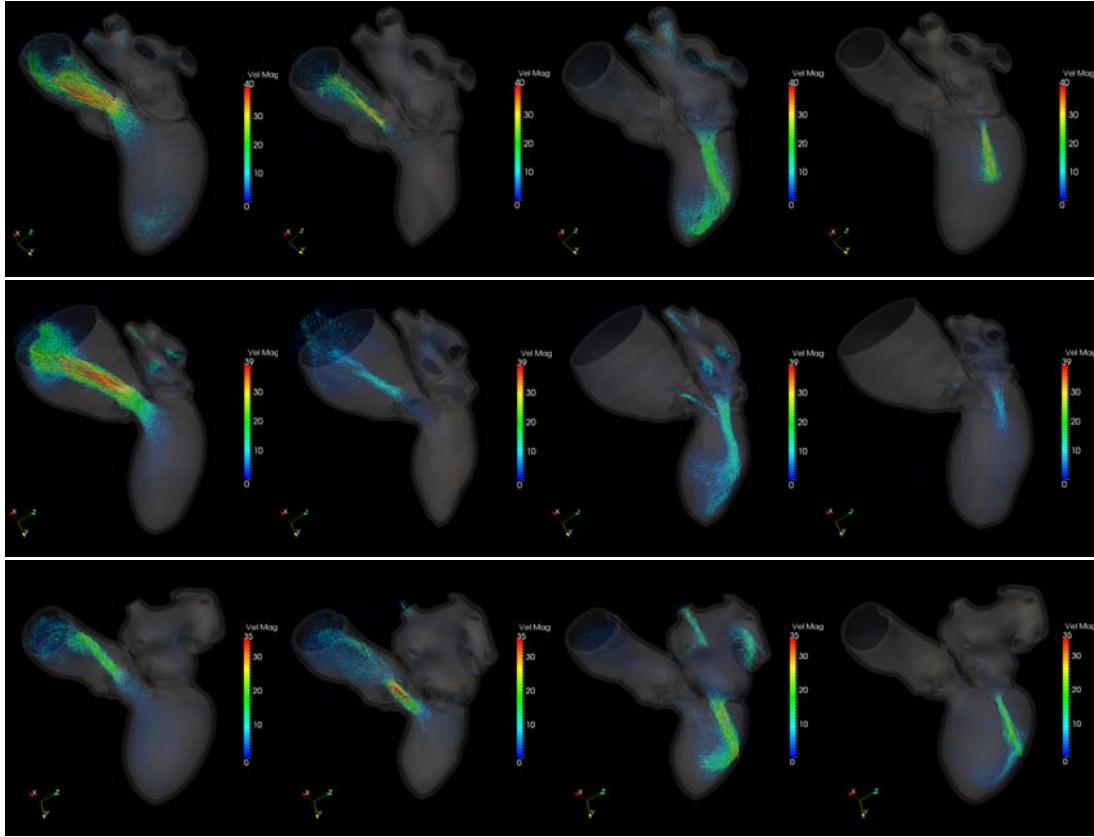


Figure A.3: Comparison of diseased hearts. Top: normal heart; Middle: heart with dilated aorta; Bottom: heart with bicuspid valve. First column: early systole; Second column: late systole; Third column: early diastole; Fourth column: late diastolic filling.

tion. We use a more physically meaningful approach by enforcing the incompressibility requirement in each connected component.

The flow parameter visualizations are done in Paraview. We visualize in 3D the heart walls, as they are used in the simulations, the truncated velocity, its magnitude, and also the associated vorticity magnitude. Typical visualizations of these fields are presented in figure A.1.

Comparison of Diseased Hearts

In our experiments we include 4D cardiac CT studies acquired from three patients: healthy subject, dilated aortic root and bicuspid aortic valve. The patient-specific geometry and kinematics of their left heart was obtained applying the method in section A. Hemodynamic parameters were obtained using the simulation framework in section A. The obtained results confirmed the validity of the proposed approach producing flow patterns and values similar to the ones reported in the literature. It also revealed flow irregularities for the two pathology cases (dilated root and bicuspid aortic valve).

General comparison

The first two datasets had heart cycles of 65 bpm, while the bicuspid one of 60bpm. The diseased hearts featured reflux phenomena in both the valves and the pulmonary vein regions. The only reflux for the normal one was the small pulmonary venous flow reflux during the late mitral filling, which is a normal phenomenon. We should underline that the magnitudes of the reflux flows (and actually all the flows) presented, are likely to be somewhat larger than the reality, due to the framework which models the walls as "hard", rather than soft tissue. In future work this will be addressed, by including more realistic geometry recovery for the walls (papillary muscles and trabeculae carnae), soft tissue models for the walls and also elastic properties for the valves.

The systole was almost twice shorter for the normal heart compared to the diseased ones. This is a well known phenomenon in which diseased hearts developed longer systolic cycles in order to counteract the anatomic faults, which led to regurgitations and inefficient blood pumping.

Normal heart

The normal heart (see figure A.3, top row) had a fairly short systole (190ms) in a cardiac cycle of 923ms. During the systole the aortic flux was strong, as was the flow into the LA. The diastole started with a strong flow through the mitral valve, during which a main rotating vortex formed in the center of the LV, and a smaller vortex formed at the entrance of the aortic valve. The late mitral filling happened concurrently with a small pulmonary vein reflux, which is normal.

Heart with dilated aorta

This heart (figure A.3, middle row) featured a heavily enlarged aorta. As a consequence, the aortic valve never closed completely for this particular heart, leading to massive aortic regurgitation during diastole. There was some small but abnormal regurgitation also at the level of the pulmonary veins and mitral region. One interesting fact was that, during systole, the flow was directed straight toward the abnormally enlarged region of the aorta, which raises the question which one contributed to the creation of the other? Was it weak aortic valves that directed the flow obliquely, enlarging the aorta, or was it the aortic weakening that pulled the aortic valves and redirected the flow?

Heart with bicuspid aortic valve

For the bicuspid subject (see figure A.3, bottom row) we can observe the deflection of the output jet towards the aortic wall which can explain the fact that the patients with bi-leaflet aortic valve develop aortic root dilation. In addition, the bicuspid aortic valve is also insufficient, which results into a regurgitant jet towards the left ventricle, observed at the beginning of the diastole (see figure A.3 second column). Simulation results indicated that the aortic and mitral valves were not synchronously opening and closing, which contributes to atrial regurgitation from the ventricle.

Conclusion

We presented a novel framework for patient-specific hemodynamics analysis of the left heart. Geometric and kinematic parameters of the left ventricle, left atrium, pulmonary veins, mitral valve, aortic valve and ascending aorta are automatically estimated from 4D cardiac CT scans using a robust learning-based algorithm. A 3D Navier-Stokes solver, constrained by the patient-specific dynamic model, is applied to simulate the blood flow in the left heart over the whole cardiac cycle. We demonstrate the results of the proposed method on a group of three subjects, which includes one healthy heart, a dilated aortic root and a bicuspid aortic valve patient. To the best of our knowledge, this is the first framework which allows for simultaneous and integrated analysis of morphology, dynamics and hemodynamics of patient-specific left hearts.

Cross-modality Assessment and Planning for Pulmonary Trunk Treatment using CT and MRI imaging

Abstract - Congenital heart defect (CHD) is the primary cause of death in newborns, due to typical complex malformation of the cardiac system. The pulmonary valve and trunk are often affected and require complex clinical management and in most of the cases surgical or interventional treatment. While minimal invasive methods are emerging, non-invasive imaging-based assessment tools become crucial components in clinical settings. For advanced evaluation and therapy planning purposes, cardiac computed tomography (CT) and cardiac magnetic resonance (CMR) are important non-invasive investigation technique with complementary properties. Although, characterized by high-temporal resolution, CMR does not cover the full motion of the pulmonary trunk. The sparse CMR data acquired in this context include only one 3D scan of the whole heart in the end-diastolic phase and two 2D planes (long and short axes) over the whole cardiac cycle. We present a cross-modality framework for the evaluation of the pulmonary trunk, which combines the advantages of both, cardiac CT and CMR. A patient-specific model is estimated from both modalities using hierarchical learning-based techniques. The pulmonary trunk model is exploited within a novel dynamic regression-based reconstruction to infer the incomplete CMR temporal information. Extensive experiments performed on 72 cardiac CT and 74 MR sequences demonstrated the average speed of 110 seconds and accuracy of 1.4mm for the proposed approach. To the best of our knowledge this is the first dynamic model of the pulmonary trunk and right ventricle outflow track estimated from sparse 4D MRI data.

Introduction

Congenital heart defect (CHD) is the primary cause of death in newborns characterized by complex malformations of the heart and great vessels. Often, the right side of the heart is affected and especially the pulmonary trunk, as in Tertalogy of Fallot (TOF) and pulmonary artesia or stenosis. The clinical management of such conditions is confronted with complex treatment decisions, which include pulmonary valve procedures in the majority of the cases.

Percutaneous interventions for pulmonary valve replacement are emerging as feasible treatment alternatives to classic cardiac surgery with important benefits: less invasive, reduced risks associated with cardiopulmonary bypass, bleeding, infections and reduced expenses for postoperative intensive care [18]. Nevertheless, comprehensive investigation, based on non-invasive imagine techniques, is mandatory for clinical decision making and treatment success.

For therapy planning purposes, the pulmonary trunk is increasingly imaged using either cardiac computer tomography (CT) or cardiac magnetic resonance (CMR) [153]. While CT has a high spatial resolution, fast acquisition times without anesthesia, it has the disadvantages of poor temporal resolution and ionizing radiation. Contrary, MRI has high temporal resolution without X-ray radiation, but long acquisition times and usually does not cover the full 4D information. The regular protocol, so called sparse 4D CMR, involves an end-diastolic (ED) 3D heart image and two orthogonal cine projections 2D+t, short axis (SA) and long axis (LA). LA passes through the main pulmonary artery and the descending aorta, while SA is aligned with pulmonary valve, perpendicular to the LA (see figure B). Ideally, clinicians would be provided with accurate morphological and functional quantification of the pulmonary trunk, independent of the employed imaging technique.

We present a cross-modality framework for the evaluation of the pulmonary trunk, which combines the advantages of both, cardiac CT and CMR, non-invasive imaging techniques. A physiological model, which captures complex morphological, dynamical and pathologic variations of the pulmonary trunk is presented in Sec. B. In Sec. B, the patient-specific model parameters are estimated from both modalities within hierarchical learning-based framework, which involves three-stages: landmark detection, center line detection and dynamics estimation. A novel dynamic regression-based reconstruction is proposed to infer the incomplete temporal information characteristic to the sparse MRI protocols.

Extensive experiments are performed on 72 cardiac 4D CT (720 volumes) and 74 sparse MRI (74 3D ED volumes associated with 4736 2D slides over the cardiac cycle) data, from which 10 patients underwent both imaging interventions, CT and sparse MRI. Mean reconstruction error of 1.44 mm within 110 seconds demonstrates the strength of our proposed regression based reconstruction method.

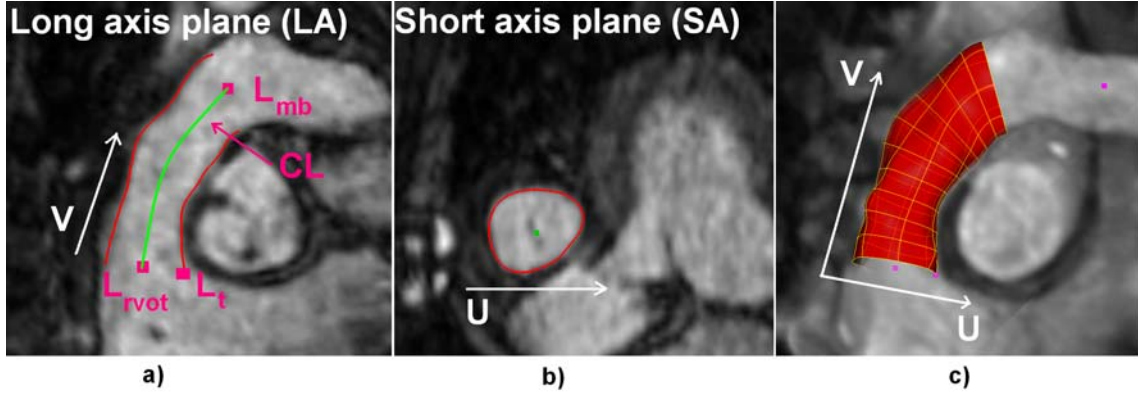


Figure B.1: 3D MRI scan of the whole heart in the ED phase (a). 2D long axis (LA) plane (b) and short axis (SA) plane (c) of the pulmonary artery over the cardiac cycle

Physiological Pulmonary Trunk Modelling

In this section we introduce our physiological model of the RVOT and pulmonary trunk, which represents both morphological and dynamical variations. Similar as in [178], the anatomical complexity is reduced by employing a coarse to fine parameterization which includes: anatomical landmarks, pulmonary artery center line and full surface model of the pulmonary trunk. As illustrated in figure B(a), the considered anatomical landmarks include, Trigone (L_t), RVOT (L_{rvot}) and Main-Bifucation (L_{mb}), each represented in the Euclidean 3D space, $L_x \in R^3$. The centre line CL passes through the pulmonary artery center and is parameterized by 12 points, $CL = CL_0 \dots CL_{11}$. The surface model S is represented by a structured grid, spanned along two anatomical directions, u -circumferential and v -longitudinal, using 50×40 vertices (see figure B(c)). Point correspondence in time and across patients is enforced by intrinsic re-sampling of S , using a set of anatomical-driven cutting-planes, described by center line points CL_x and corresponding tangential directions. Given the different modalities supported and characteristic imaging protocols, we differentiate among two dynamic extensions of the proposed physiological model. The definition of a full 4D model, which can be directly estimated from 4D cardiac CT data, is rather straightforward and realized by concatenating a time variable t :

$$Model_{full4D} = \{L_t, L_{rvot}, L_{mb}, CL, S\}_t \quad (B.1)$$

However, given the sparse 4D acquisition, common to MRI exams, the extension to a temporal model includes two additional representations: LA and SA . LA - describes the contour of S intersected with the plane with the origin in L_{rvot} and the normal obtained from the cross-product between the $L_{trigone}$ and L_{rvot} , and the center line tangent at CL_0 - these represents a specific 2D+time long axis acquisition (see figure B(a)). SA - describes the contour of S intersected with the plane center in CL_{middle} and the corresponding tangent as normal (see figure B(b)). Hence, the sparse dynamic model is parameterized as follows:

$$Model_{sparse4D} = \{L_t, L_{rvot}, L_{mb}, CL, S\}_{ED} + \{LA, SA\}_t \quad (B.2)$$

Dynamic Regression Based 4D Model Reconstruction

As describe above, the dynamic information in case of MRI 4D is incomplete but rather available only in two orthogonal projections, as opposed to 4D cardiac CT, which provides full dynamics over the cardiac cycle. In this section we propose a novel dynamic regression method to learn the pulmonary trunk spatial-temporal variation from a heterogonous training population and apply it to predict a full dynamic model from partial 4D usually provide by MRI.

In *regression* a solution to the following optimization problem is normally sought [200]:

$$\hat{\mathcal{R}}(\mathbf{x}) = \underset{\mathcal{R} \in \mathfrak{S}}{\operatorname{argmin}} \sum_{n=1}^N L(y(\mathbf{x}_n), \mathcal{R}(\mathbf{x}_n)) / N \quad (B.3)$$

where \mathfrak{S} is the set of possible regression functions, $L(\circ, \circ)$ is a loss function that penalizes the deviation of the regressor output $\mathcal{R}(\mathbf{x}_n)$ from the true output, and N is the number of available training examples. In our case the reconstruction task is defined as a regression problem between the full dynamic model of the pulmonary trunk extracted from 4D CT data and the sparse one extracted from the sparse MRI data:

$$Y(Model_{full4D}) = \hat{\mathcal{R}}(X(Model_{sparse4D})) + \epsilon \quad (B.4)$$

In our regression problem we focus on shape information and completely neglect volume data. As descriptors both for the input $X(Model_{sparse4D})$ and output elements $Y(Model_{full4D})$ of the models we choose *coordinates* of mesh vertices normalized with the generalized procrustes analysis. This representation has been already used before, with the purpose of model classification into diseased and healthy, and has a uniform representation of the input and the output data. The training set T used to generate the regression model includes feature vectors T_i as follows:

$$T_i = \langle (S_i^{ED}, LA_i^t, SA_i^t)_{MRI}, (S_i^t)_{CT} \rangle, \quad (B.5)$$

where t is the time step within the cardiac cycle, S_i^{ED} is a set of 3D coordinates representing each point of the end-diastolic model (2000 3D points), LA_i^t and SA_i^t are point sets (80 and 50 3D points respectively) representing the model curves extracted from the MRI's long axis stack and short axis stack respectively, for the current time step t , and $(S_i^t)_{CT}$ are the corresponding point coordinates for the point set to be reconstructed (238 3D points). Due to the dense representation of our model (2000 3D points) we reconstruct only the most significant 238 3D points from the associated CT model. The rest of the points are interpolated and projected onto the PCA shape space from which the complete final model is then obtained.

The formulated regression problem is solved by learning the regression function \mathcal{R} with two different methods: *boosting-based additive regression* [54] and *random forest* [23]. Two main reasons motivate our choice. First, these techniques were shown to

be robust to high-dimensional data with many irrelevant, redundant and noisy features, without the need for additional data pre-processing and feature selection. This was shown both for classification [175],[164] and regression [200] tasks. Second, both boosting-based and random forest-based models are relatively fast to train and to evaluate comparing for example with Support Vector Regression. In the spirit of [175],[200], we use *simple 1D linear regression* as the base learner for boosting-based regression. At each boosting iteration, a feature which results in the smallest squared loss with linear regression is added to the pool of already selected features. Each weak learner is thus a simple linear regressor of the form:

$$y = \beta_0 x + \beta_1 \tag{B.6}$$

where x is the selected scalar input coordinate and y is a scalar output coordinate. Using more sophisticated weak learners such as CART decision trees and multiple linear regression with greedy forward feature inclusion, has proven to always result in a worse or no better performance while the resulting model gets significantly more complicated. Using simple 1D binary decision stumps as in [200] has also proven to lead to suboptimal accuracy; the reason for this is perhaps the nature of the data, as it is rather impossible to generate as many candidate decision stumps with the coordinate - based features as it is possible with the Haar-like features. For each boosting-based model, we generate 200 weak learners. The accuracy plateaus with this number of component models, and the further accuracy increase is always insignificant with this data.

For random forests, we always generate 25 component trees. The accuracy usually remains same or even decreases with the addition of more trees to the model. The minimum leaf size is set to 1; the trees are thus generated to the full with no pruning. The number of features considered at each node is set to the value recommended by Breiman [23], which is one third of the total number of features for regression. Using other parameter settings was shown to lead to worse or no better accuracy in our preliminary experiments.

In boosting-based regression the output function is assumed to take a linear form as follows [200]:

$$\hat{\mathcal{R}}(\mathbf{x}) = \sum_{t=1}^T \alpha_t h_t(x) \in H \tag{B.7}$$

where $h_t(x)$ is a base (weak) learner and T is the number of boosting iterations. Having a *linear* base learner (simple linear regression), a *linear* final solution is thus also found. In contrast to this, random forests seek for a non-linear function approximation, recursively splitting the feature space in the nodes of component decision trees.

In contrast to [200], we use *naive decoupling* of the regression problem into a number of single output problems. While multi-output regression solutions do exist both for boosting [200], for our task multi-output optimization was not shown to lead to error decrease and time savings were rather insignificant.

Estimating Patient-Specific Model Parameters

The patient-specific model parameters described in Section B are estimated from cardiac acquisition using a learning-based algorithm. Detectors are learned separately for both modalities, CT and MRI, and applied to estimate model parameters in a hierarchical three-stage approach: Anatomical Landmarks Estimation, Center Line Estimation and Full Surface Model Estimation.

Anatomical Landmarks Estimation By defining the localization as a classification problem, the anatomical landmarks, L_t, L_{rvot}, L_{mb} , are estimated within the Marginal Space Learning (MSL) framework [197]. Separate detectors $D_t^L, D_{rvot}^L, D_{mb}^L$, are learned using the Probabilistic Boosting Tree (PBT) [164] in combination with Haar-like feature from a training dataset annotated by experts.

$$p(L_x|x, y, z) = D_x^L(x, y, z), (x, y, z) \in \sigma^x \quad (\text{B.8})$$

the trained detectors D_x^L models the target posteriori distribution $p(L_x|x, y, z)$ for a specific search space σ^x given by the training set. MSL is applied to exhaustively search the parameter space using the learned detectors and obtained the location of the anatomical landmarks. Note that in case of 4D cardiac CT anatomical landmark are detected in each volume to obtain the dynamic parameters $\{L_t, L_{rvot}, L_{mb}\}_t$, while in sparse cardiac MR only a static detection in the end-diastolic volume is performed $\{L_t, L_{rvot}, L_{mb}\}_{ED}$,

Center Line Estimation CL passes through the centre of the pulmonary trunk and is initialized by the previously detected landmarks L_t and L_{rvot} . A robust detector D^{CL} is learned using the same MSL framework to detect circular structures, parameterized by center line points CL_x , corresponding tangent and fixed radius $r = 20mm$ obtained from the average value in the training set. An incremental approach is used to search circles on a series of successively updating planes. Please note, as for the Anatomical Landmarks Estimation, a temporal center-line model CL_t is detected in CT and a static CL in MR.

Full Surface Model Estimation The full model of the pulmonary trunk S is initialized in the end-diastolic frame using the estimated landmarks and centerlines, using a piecewise affine transformation along the center line [178]. Robust boundary detectors D^s , trained using the PBT and steerable feature [197] are applied to locally refine the surface by moving it along normal directions towards the position with highest boundary probability. To obtain spatially smooth delineation, the final results is obtained by projecting S to a previously learned shape space model.

In case of CT, the above describe algorithm is applied in each time step to obtain the full temporal model $\{L_t, L_{rvot}, L_{mb}, CL, S\}_t$. In case of MR, the estimated surface in the end-diastolic frame S_{ED} is used to initialize the contours LA and SA . These are refined using a trained D^c contour detector as described above. A full dynamic 4D model is then estimated by using a learned regression model (see Eq. B.4) to predict the missing temporal information.

Results

Results on Patient-Specific Model Parameters Estimation

The proposed framework for detecting a personalized pulmonary trunk model in 4D CT and sparse MRI data was evaluated on 50 4D CT(500 volumes) and 74 sparse MRI (74 ED Volumes associated with 4736 LA/SA planes) studies from patients with different CHD. Each volume in the data set is associated with annotation, manually generated by experts, which is considered as ground truth. Three-fold cross validation was used to divide the data set into training and test data.

Table B.1 summarizes the detection performance on both modalities (CT and sparse MRI), from the test data. Point-to-mesh measurement error was used to evaluate the detection accuracy between the ground-truth and detected model for both modalities. Average speed of 10sec per frame was achieved for both modalities on a standard 2.0GHz Dual Core PC.

Table B.1: Detection accuracy

CT/MRI	Mean Error(mm)	Median(mm)	Std.Dev(mm)
Landmarks	3.5/4.3	5.1/6.4	2.7/3.0
Center Line	3.0/3.3	2.3/2.3	1.7/2.0
Full Surface	1.6/1.9	1.2/1.3	0.2/0.2

Intra-modality comparison between CT and MRI

The inter-modality consistency of the model was demonstrated on a subset of 10 patients which underwent both imaging investigations, 4D CT and sparse MRI (see figure B.2). Ground-truth and detected pulmonary trunk models from both modalities were compared using the abstract point-to-mesh measurement and clinical relevant diameter measurements: RVOT, hinges and commissures. Results are summarized in Table B.2. A strong inter-modality correlation, $r = 0.992$, $p < 0.0001$ and confidence of 98%, was obtained for CT and CMR based on the pulmonary trunk model.

Table B.2: Model based intra-modality comparison between CT and MRI

(mm)	Ground truth	Estimation
RVOT	0.7 ± 0.5	3.8 ± 1.5
Hinges	1.2 ± 1.4	2.6 ± 4.7
Commissures	1.5 ± 1.2	3.2 ± 1.7
Point-to-mesh	1.4 ± 0.1	2.5 ± 0.7

Results on Regression Based Dynamic Model Reconstruction

As described in Section B the sparse MRI protocol is able to capture the full anatomy of the pulmonary trunk only in the ED phase (3D volume) of the heart and parts of

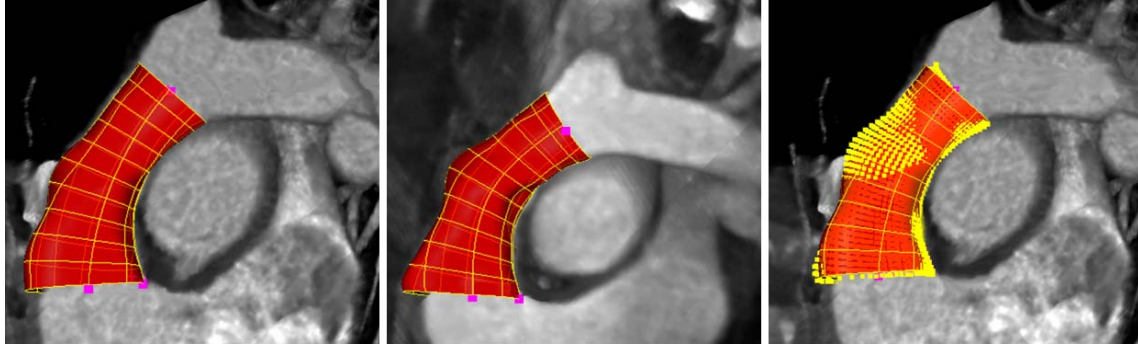
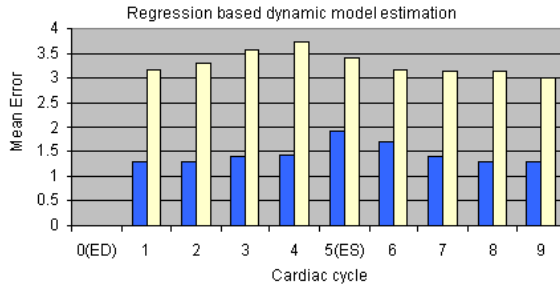


Figure B.2: Pulmonary trunk model in CT (**left**) and MRI (**middle**) data for the ED phase. Inter-modality consistency by projecting the MRI model(yellow points) into the CT data (**right**).

the pulmonary trunk in 2D planes (LA and SA) over the cardiac cycle. However, a full 4D model of the pulmonary trunk can be still computed from the available sparse data by learning the full motion from 4D CT data. For this purpose we learned a regression model as presented in Section B on a training data set of 72 4D CT (720 Volumes) studies. Two different machine-learning techniques (boosting and random forest) are used to train the regression model and to evaluate the reconstruction error. Table B.3 presents values obtained by applying the regression method on sparse CMR images and evaluate it on full 4D CT, for a set of 10 patients, which underwent both imaging modalities. Figure B.3 illustrates the reconstruction error distributed over the cardiac cycle.

Table B.3: Reconstruction error for Random Forest and Boosting

	Boosting	Random Forest
Mean Err.	1.44(mm)	3.2(mm)
Std. Dev	0.21(mm)	0.23(mm)
Speed	3.07 (ms)	6.21 ms



Conclusion

We proposed a cross-modality detection framework for estimating a dynamic personalized model of the pulmonary trunk from the available data, 4D CT and sparse MRI. A novel regression based reconstruction method is presented and used to infer the incomplete temporal information characteristic to the sparse MRI protocols. The estimated model from both modalities can be utilized to extract morphological and functional information of the pulmonary trunk and dynamics over the cardiac cycle. Extensive experiments

performed on a large heterogeneous data set demonstrated a precision of 1.44mm data at a speed of 11 seconds per volume. The proposed method has the potential to significantly advance the pulmonary trunk treatment.

List of Authored Publications and Patents

- i. R. IONASEC, I. VOIGT, B. GEORGESCU, Y. WANG, H. HOULE, N. NAVAB, D. COMANICIU, *Patient-Specific Modeling and Quantification of the Aortic and Mitral Valves from 4D Cardiac CT and TEE*, IEEE Transactions on Medical Imaging - TMI 2010, in press 2010.
- ii. S. GRBIC, R. IONASEC, D. VITANOVSKI, I. VOIGT, B. GEORGESCU, , N. NAVAB, D. COMANICIU, *Complete Valvular Heart Apparatus Model from 4D Cardiac CT*, Medical Image Computing and Computer Assisted Intervention - MICCAI 2010, Beijing, China, September 20-24 2010.
- iii. D. VITANOVSKI, R. IONASEC, A. TSYMBAL, B. GEORGESCU, M. HUBER, J. HORNEGGER, D. COMANICIU, *Cross-modality Assessment and Planning for Pulmonary Trunk Treatment using CT and MRI imaging*, Medical Image Computing and Computer Assisted Intervention - MICCAI 2010, Beijing, China, September 20-24 2010
- iv. I. VOIGT, R. IONASEC, B. GEORGESCU, J. BOSE, J. HORNEGGER, D. COMANICIU, *Computational Decision Support and Intraoperative Guidance for Percutaneous Aortic Valve Implantation*, Medical Image Computing and Computer Assisted Intervention Workshop - MIAR 2010, Beijing, China, September 20-24 2010
- v. V. MIHALEF, R. IONASEC, Y. WANG, Y. ZHENG, B. GEORGESCU, D. COMANICIU, *Patient-specific Modeling of Left Heart Anatomy, Dynamics and Hemodynamics from High Resolution 4D CT*, IEEE International Symposium on Biomedical Imaging - ISBI 2010, Rotterdam, Netherlands, April 2010.
- vi. A. CALLEJA, R. IONASEC, H. HOULE, S. LIU, J. DICKERSON, P. THAVENDIRANATHAN, C. SAI-SUDHAKAR, J. CRESTANELLO, T. RYAN, M. VANNAN, *Automated Quantitative Modeling of the Aortic Valve and Root in Aortic Regurgitation*

- Using Volume 3-D Transesophageal Echocardiography*, American College of Cardiology Annual Meeting - ACC 2010, Atlanta, USA, March 2010.
- vii. V. MIHALEF, R. IONASEC, P. SHARMA, B. GEORGESCU, M. HUBER, D. COMANICIU, *Patient-Specific Modeling of Whole Heart Anatomy, Dynamics and Hemodynamics from 4D cardiac CT Images*, VPH Virtual Physiological Human - Annual Conference 2010, Brussels, Belgium, October 2010.
- viii. R. IONASEC, V. MIHALEF, B. GEORGESCU, N. NAVAB, D. COMANICIU, *Patient-Specific Modelling of Left-Heart Anatomy, Dynamics and Hemodynamics from 4D cardiac CT Images*, BMT Biomedizinische Technik 2010, Rostock, Germany, October 2010.
- ix. I. VOIGT, D. VITANOVSKI, R. IONASEC, A. TSYMBAL, B. GEORGESCU, K. ZHOU, M. HUBER, N. NAVAB, J. HORNEGGER, D. COMANICIU, *Learning discriminative distance functions for valve retrieval and improved decision support in valvular heart disease*, SPIE Medical Imaging, 2010, San Diego, USA, February 2010.
- x. S. GRBIC, R. IONASEC, Y. ZHENG, D. ZAEUNER, B. GEORGESCU, D. COMANICIU, *Aortic Valve and Ascending Aortic Root Modeling from 3D and 3D+t CT*, SPIE Medical Imaging, 2010, San Diego, USA, February 2010.
- xi. R. IONASEC, Y. WANG, B. GEORGESCU, I. VOIGT, N. NAVAB, D. COMANICIU, *O. Kutter, W. Wein, N. Navab*, Robust Motion Estimation Using Trajectory Spectrum Learning: Application to Aortic and Mitral Valve Modeling from 4D TEE International Conference on Computer Vision (ICCV), Kyoto, Japan, 2009.
- xii. R. IONASEC, B. HEIGL, J. HORNEGGER, *Acquisition-related motion compensation for digital subtraction angiography*, Computerized Medical Imaging and Graphics, Volume 33, Issue 4, Pages 247-332 (June 2009).
- xiii. A. BARBU, R. IONASEC, *Boosting Cross-Modality Image Registration*, Joint Urban Remote Sensing, Shanghai 2009.
- xiv. I. VOIGT, R. IONASEC, B. GEORGESCU, H. HOULE, M. HUBER, J. HORNEGGER, D. COMANICIU, *Model-driven physiological assessment of the mitral valve from 4D TEE*, SPIE Medical Imaging, 2009, Orlando, USA, February 2009.
- xv. R. IONASEC, A. TSYMBAL, D. VITANOVSKI, B. GEORGESCU, K. ZHOU, N. NAVAB, D. COMANICIU, *Shape-based diagnosis of the aortic valve*, SPIE Medical Imaging, 2009, Orlando, USA, February 2009.
- xvi. D. VITANOVSKI, R. IONASEC, B. GEORGESCU, M. HUBER, R. TAYLOR, J. HORNEGGER, D. COMANICIU, *Personalized pulmonary trunk modeling for intervention planning and valve assessment estimated from CT data*, Medical Image Computing and Computer Assisted Intervention (MICCAI), London, UK, September 20-24 2009.

-
- xvii. R. IONASEC, I. VOIGT, B. GEORGESCU, H. HOULE, J. HORNEGGER, N. NAVAB, D. COMANICIU , *Modeling and assessment of the Aortic-Mitral valve coupling from 4D TEE and CT* , Medical Image Computing and Computer Assisted Intervention (MICCAI), London, UK, September 20-24 2009.
- xviii. E. GASSNER, R. IONASEC, B. GEORGESCU, S. VOGT, U. J. SCHOEPF, D. COMANICIU , *Performance of a Dynamic Aortic Valve Model for Quantification of the Opening Area at Cardiac MDCT . Comparison to Manual Planimetry*, Radiological Society of North America, RSNA, 2008, Chicago, USA, November 2008.
- xix. R. IONASEC, B. GEORGESCU, D. COMANICIU, S. VOGT, U. J. SCHOEPF, E. GASSNER , *Patient Specific 4D Aortic Root Models Derived from Volumetric Image Data Sets* , Radiological Society of North America, RSNA, 2008, Chicago, USA, November 2008.
- xx. R. IONASEC, B. GEORGESCU, E. GASSNER, S. VOGT, O. KUTTER, M. SCHEUERING, N. NAVAB, D. COMANICIU , *Dynamic model-driven quantification and visual evaluation of the aortic valve from 4D CT* , Medical Image Computing and Computer-Assisted Intervention, MICCAI, 2008, New York, USA, September 6-10 2008.
- xxi. J. CHOI, B. GEORGESCU, R. IONASEC, S. RAMAN, G. HONG, S. LIU, H. HOULE, M. A. VANNAN , *Novel Semi-Automatic Quantitative Assessment of The Aortic Valve and Aortic Root from Volumetric 3D Echocardiography: Comparison to Volumetric Cardiac Computed Tomography (CT)* , AHA, New Orleans, USA, November 2008.



US 20090123050A1

(19) **United States**
 (12) **Patent Application Publication** (10) **Pub. No.: US 2009/0123050 A1**
Ionasec et al. (43) **Pub. Date: May 14, 2009**

(54) **METHOD AND SYSTEM FOR AUTOMATIC QUANTIFICATION OF AORTIC VALVE FUNCTION FROM 4D COMPUTED TOMOGRAPHY DATA USING A PHYSIOLOGICAL MODEL**

Related U.S. Application Data

(60) Provisional application No. 60/984,749, filed on Nov. 2, 2007, provisional application No. 61/012,120, filed on Dec. 7, 2007, provisional application No. 61/020,513, filed on Jan. 11, 2008.

(76) Inventors: **Razvan Ionasec**, Princeton, NJ (US); **Bogdan Georgescu**, Plainsboro, NJ (US); **Helene C. Houle**, Sunnyvale, CA (US); **Sebastian Vogt**, Lawrenceville, NJ (US); **Michael Scheuering**, Nurnberg (DE); **Estelle Camus**, Mountain View, CA (US); **Dorin Comaniciu**, Princeton Junction, NJ (US)

Publication Classification

(51) **Int. Cl.**
G06K 9/00 (2006.01)
 (52) **U.S. Cl.** **382/131**
 (57) **ABSTRACT**

Correspondence Address:
SIEMENS CORPORATION
INTELLECTUAL PROPERTY DEPARTMENT
170 WOOD AVENUE SOUTH
ISELIN, NJ 08830 (US)

A method and system for modeling the aortic valve in 4D image data, such as 4D CT and echocardiography, is disclosed. An initial estimate of a physiological aortic valve model is determined for at least one reference frame of a 4D image sequence based on anatomic features in the reference frame. The initial estimate is refined to generate a final estimate in the reference frame. A dynamic model of the aortic valve is then generated by estimating the physiological aortic valve model for each remaining frame of the 4D image sequence based on the final estimate in the reference frame. The aortic valve can be quantitatively evaluated using the dynamic model.

(21) Appl. No.: **12/288,215**

(22) Filed: **Oct. 17, 2008**

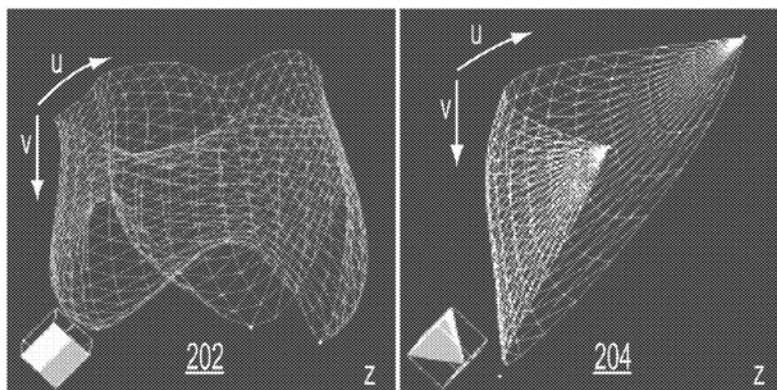


Figure C.1: Patent US 2009/0123050, <http://www.freepatentsonline.com/20090123050.pdf>



US 20090154785A1

(19) **United States**
 (12) **Patent Application Publication** (10) **Pub. No.: US 2009/0154785 A1**
 Lynch et al. (43) **Pub. Date: Jun. 18, 2009**

(54) **METHOD AND SYSTEM FOR DYNAMIC PULMONARY TRUNK MODELING IN COMPUTED TOMOGRAPHY AND MAGNETIC RESONANCE IMAGING**

Related U.S. Application Data

(60) Provisional application No. 61/013,018, filed on Dec. 12, 2007.

Publication Classification

(51) **Int. Cl.**
G06T 7/00 (2006.01)
 (52) **U.S. Cl.** **382/131**
 (57) **ABSTRACT**

(76) Inventors: **Michael Lynch**, Toronto (CA); **Razvan Ionasec**, Erlangen (DE); **Bogdan Georgescu**, Plainsboro, NJ (US); **Dorin Comaniciu**, Princeton Junction, NJ (US); **Dime Vitanovski**, Erlangen (DE)

Correspondence Address:
SIEMENS CORPORATION
INTELLECTUAL PROPERTY DEPARTMENT
170 WOOD AVENUE SOUTH
ISELIN, NJ 08830 (US)

(21) Appl. No.: **12/315,343**
 (22) Filed: **Dec. 1, 2008**

A method and system for modeling the pulmonary trunk in 4D image data, such as 4D CT and MRI data, is disclosed. Bounding boxes are detected in frames of the 4D image data. Anatomic landmarks are detected in the frames of the 4D image data based on the bounding boxes. Ribs or centerlines of the pulmonary artery are detected in the frames of the 4D image data based on the anatomic landmarks, and a physiological pulmonary trunk model is fit the frames of the 4D image data based on the detected ribs and anatomic landmarks. The boundary of the pulmonary trunk is detected in order to refine the boundary of the pulmonary trunk model in the frames of the 4D image data, resulting in a dynamic model of the pulmonary trunk. The pulmonary trunk can be quantitatively evaluated using the dynamic model.

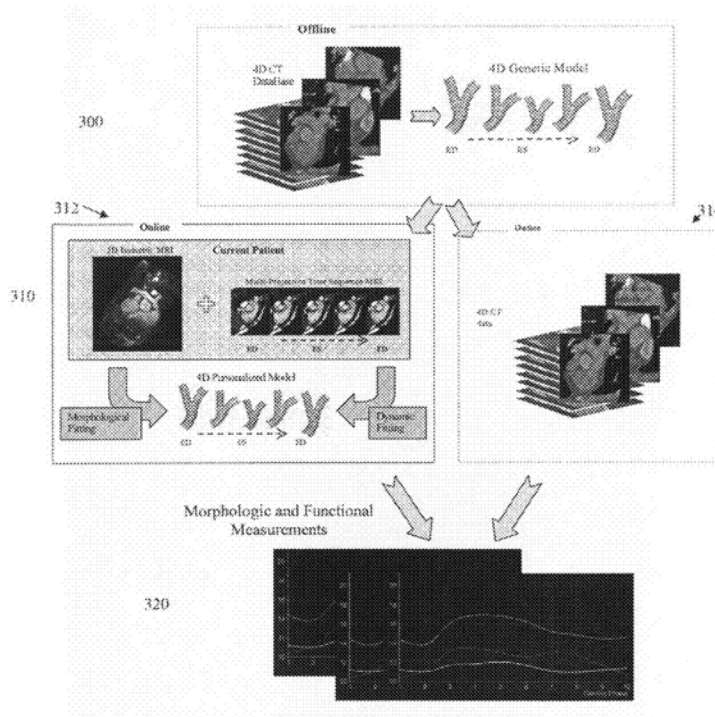


Figure C.2: Patent US 2009/0154785, <http://www.freepatentsonline.com/20090154785.pdf>



US 20100070249A1

(19) **United States**
 (12) **Patent Application Publication** (10) **Pub. No.: US 2010/0070249 A1**
Ionasec et al. (43) **Pub. Date: Mar. 18, 2010**

(54) **METHOD AND SYSTEM FOR GENERATING A PERSONALIZED ANATOMICAL HEART MODEL**

Related U.S. Application Data

(60) Provisional application No. 61/097,966, filed on Sep. 18, 2008.

(75) Inventors: **Razvan Ionasec**, Lawrenceville, NJ (US); **Bogdan Georgescu**, Plainsboro, NJ (US); **Yefeng Zheng**, Dayton, NJ (US); **Dorin Comaniciu**, Princeton Junction, NJ (US)

Publication Classification

(51) **Int. Cl.**
G06G 7/60 (2006.01)
G06F 7/60 (2006.01)
G06F 17/10 (2006.01)
 (52) **U.S. Cl.** 703/2; 703/11
 (57) **ABSTRACT**

Correspondence Address:
SIEMENS CORPORATION
INTELLECTUAL PROPERTY DEPARTMENT
170 WOOD AVENUE SOUTH
ISELIN, NJ 08830 (US)

A method and system for generating a patient specific anatomical heart model is disclosed. Volumetric image data, such as computed tomography (CT) or echocardiography image data, of a patient's cardiac region is received. Individual models for multiple heart components, such as the left ventricle (LV) endocardium, LV epicardium, right ventricle (RV), left atrium (LA), right atrium (RA), mitral valve, aortic valve, aorta, and pulmonary trunk, are estimated in said volumetric cardiac image data. A patient specific anatomical heart model is generated by integrating the individual models for each of the heart components.

(73) Assignee: **Siemens Corporate Research, Inc.**, Princeton, NJ (US)

(21) Appl. No.: **12/562,454**

(22) Filed: **Sep. 18, 2009**

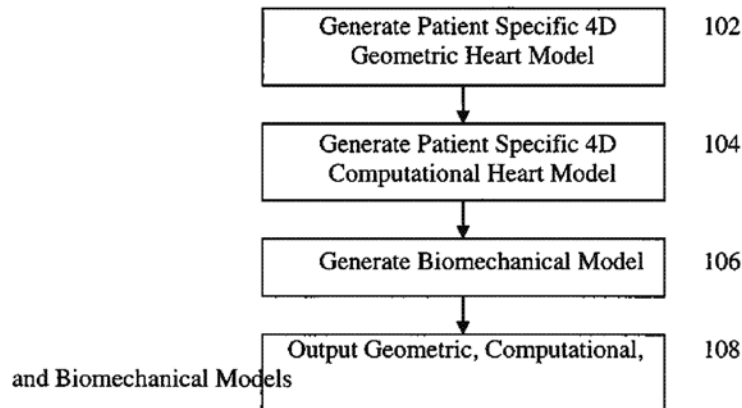


Figure C.3: Patent US 2010/0070249, <http://www.freepatentsonline.com/20100070249.pdf>



US 20100067768A1

(19) **United States**
 (12) **Patent Application Publication** (10) **Pub. No.: US 2010/0067768 A1**
Ionasec et al. (43) **Pub. Date: Mar. 18, 2010**

(54) **METHOD AND SYSTEM FOR PHYSIOLOGICAL IMAGE REGISTRATION AND FUSION** (22) Filed: **Sep. 18, 2009**
Related U.S. Application Data
 (60) Provisional application No. 61/097,969, filed on Sep. 18, 2008.
Publication Classification
 (51) **Int. Cl.** **G06K 9/00** (2006.01)
 (52) **U.S. Cl.** **382/131; 382/128**
 (57) **ABSTRACT**
 A method and system for physiological image registration and fusion is disclosed. A physiological model of a target anatomical structure is estimated each of a first image and a second image. The physiological model is estimated using database-guided discriminative machine learning-based estimation. A fused image is then generated by registering the first and second images based on correspondences between the physiological model estimated in each of the first and second images.

(75) Inventors: **Razvan Ionasec**, Lawrenceville, NJ (US); **Bogdan Georgescu**, Plainsboro, NJ (US); **Yefeng Zheng**, Dayton, NJ (US); **Dorin Comaniciu**, Princeton Junction, NJ (US)

Correspondence Address:
SIEMENS CORPORATION
INTELLECTUAL PROPERTY DEPARTMENT
170 WOOD AVENUE SOUTH
ISELIN, NJ 08830 (US)

(73) Assignee: **Siemens Corporate Research, Inc.**, Princeton, NJ (US)

(21) Appl. No.: **12/562,483**

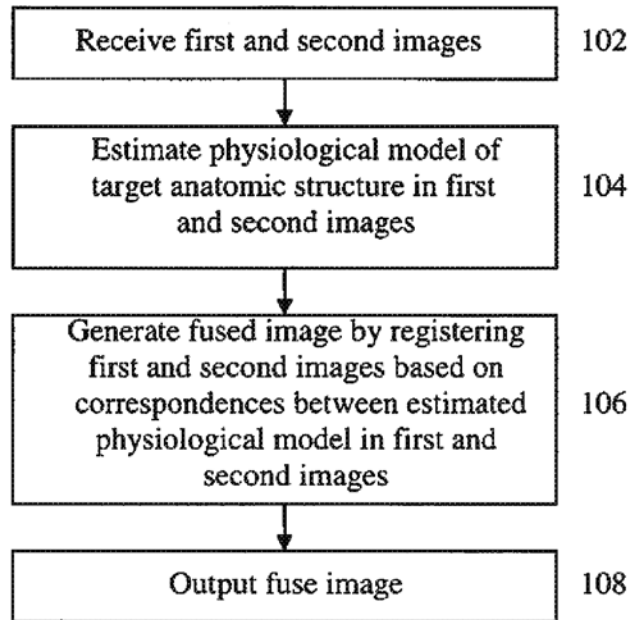


Figure C.4: Patent US 2010/0067768, <http://www.freepatentsonline.com/20100067768.pdf>

Acronyms

- AAM** Active Appearance Models. 29, 65
- ACC** American College of Cardiology. 97
- ASM** Active Shape Models. 29, 54, 56, 65, 66, 84
- AV** Aortic Valve. 10, 11, 13, 40, 42
- CMR** Cardiovascular Magnetic Resonance. 2, 3, 15, 17, 25, 34–36, 65, 86–88, 93, 125, 126
- CT** Computed Tomography. 2, 3, 17, 21, 24–26, 28, 29, 64, 86–88, 93, 95, 125, 126
- CTA** Computed Tomography Angiography. 24
- CVD** Cardiovascular Disease. 1, 2
- DCT** Discrete Cosine Transform. 79
- DFT** Discrete Fourier Transform. 51, 64, 78–80
- DWCT** Discrete Wavelet Transform. 79
- ECG** Electrocardiography. 24, 25, 28, 53, 87
- ED** End-Diastole. 83–85
- ES** End-Systole. 83–85
- ESC** European Society of Cardiology. 97
- FFT** Fast Fourier Transform. 53

- GPA** Generalized Procrustes Analysis. 54, 57
- ICA** Independent Component Analysis. 57, 58
- IDFT** Inverse Discrete Fourier Transform. 51
- LA** Left Atrium. 7, 11, 12, 16, 17, 40, 47
- LST** Local-Spatio-Temporal. 61, 66, 73, 74, 78, 95
- LV** Left Ventricle. 8, 11, 12, 16, 17, 22, 26, 34, 40, 47
- MICA** Multi-linear Independent Component Analysis. 57
- MPCA** Multi-linear Principal Component Analysis. 57
- MRI** Magnetic Resonance Imaging. 21, 26, 27, 29, 34, 65, 86, 95
- MSL** Marginal Space Learning. 64, 75, 76, 80
- MV** Mitral Valve. 10, 40
- PBT** Probabilistic Boosting Tree. 66–69, 74, 82
- PCA** Principal Component Analysis. 34, 55–57
- PET** Positron Emission Tomography. 27, 29
- PV** Pulmonary Valve. 10, 25, 42
- RA** Right Atrium. 8, 22, 41, 47
- RANSAC** RANdom SAmple Consensus. 64
- RV** Right Ventricle. 8, 13, 25, 34, 41, 42, 47, 48
- RVOT** Right Ventricular Outflow Tract. 87
- SPECT** Single Photon Emission Computed Tomography. 27, 34
- SVD** Singular Value Decomposition. 57
- TEE** Transesophageal Echocardiography. 2, 3, 17, 21, 22, 24, 26, 27, 36, 86–88, 91, 93, 125, 126
- TPS** thin-plate-spline. 84, 85
- TSL** Trajectory Spectrum Learning. 61, 64, 78, 95
- TTE** Transthoracic Echocardiography. 17, 26, 36

TV Tricuspid Valve. 10, 41

VHD Valvular Heart Disease. 1, 2, 13, 14, 17, 23, 27, 98

X-ray X-ray Imaging. 23

List of Figures

2.1	(a) Diagram of the human heart showing the chambers, valves and great vessels - by Wapcaplet in Sodipodi. (b) Diagram of the systole and diastole showing the opening and closing of the heart valves - by A.D.A.M. inc. . . .	8
2.2	Diagram of events in the left-side heart during the cardiac cycle - by DestinyQx in Wikipedia	9
2.3	The four cardiac valves centered on the aortic valve, which builds the cornerstone of the fibrous extension. Reproduced with permission of the author and the European Association for Cardio-Thoracic Surgery from: Anderson RH. The surgical anatomy of the aortic root. Multimedia Man Cardiothorac Surg doi:10.1510/mmcts.2006.002527.	10
2.4	(a) Parasternal long axis section through the heart showing the aortic root at the centerpiece of the heart. (b) Cartoon of a bisected aortic root illustrating its cylindrical shape and the leaflets attachments. (c) Cartoon of an idealized aortic root presenting the commissures and hinges as well as the semilunar attachments. Reproduced with permission of the author and the European Association for Cardio-Thoracic Surgery from: Anderson RH. The surgical anatomy of the aortic root. Multimedia Man Cardiothorac Surg doi:10.1510/mmcts.2006.002527.	11
2.5	(a) Parasternal long axis section through the heart showing the complex mitral valve structure. (b) Cartoon depicting the anterior and posterior leaflets viewed from the left atrium. (c) Cartoon illustrating the mitral valve scallops. Reproduced with permission of the author and the European Association for Cardio-Thoracic Surgery from: Anderson RH. The surgical anatomy of the aortic root. Multimedia Man Cardiothorac Surg doi:10.1510/mmcts.2006.002147 and [30]	12
2.6	Examples of aortic valve disease: bicuspid aortic valve from TEE (a) and CT (d), stenotic aortic valve with calcification from TEE (b) and CT (e), and dilated aortic root with valve regurgitation from TEE (c) and CT (f).	15

2.7	Examples of mitral valve disease: stenotic mitral valve from TEE (a) and CT (d), mitral valve prolapse from TEE (b) and CT (e), and mitral valve regurgitation from TEE (c) and CT (f).	16
2.8	(a) GeoForm Annuloplasty Ring, Edwards Lifescience, Irvine CA. (b) Hall Easy-Fit Mechanical Prosthesis, Medtronic, Minneapolis MN. (c) Carpentier-Edwards PERIMOUNT Pericardial Bioprosthesis, Edwards Lifescience, Irvine CA.	18
2.9	(a) SAPIEN, Edwards Lifescience, Irvine CA. (b) Melody Transcatheter Valve, Medtronic, Minneapolis MN. (c) CoreValve, Medtronic, Minneapolis MN. (d) MitraClip, Evalve, Menlo Park CA.	21
2.10	(a) C-arm X-ray - Artis zee Ceiling-mounted system, Siemens Healthcare, Forchheim, Germany. (b) Fluoroscopic image of the heart with contrast concentrated in the aorta. (c) Three-dimensional DynaCT reconstruction of the aorta.	23
2.11	(a) CT - SOMATOM Definition Flash, Siemens Healthcare, Forchheim, Germany. (b) Complete heart scan with contrast on the left side. (c) Volumetric reconstruction of the aortic valve clipped at the valvular sinuses level.	24
2.12	(a) MRI - Siemens Verio, Siemens Healthcare, Erlangen, Germany. (b) Heart image including the left ventricle and aorta. (c) Volumetric reconstruction of the right ventricular outflow tract and pulmonary arteries.	25
2.13	(a) TTE four chambers image of the heart. (b) TEE volumetric reconstruction of the mitral and aortic valves. (c) Doppler blood flow quantification.	26
3.1	The proposed valvular model (including the ventricles from [197]) in systole (a) and diastole (c). (b) Explanted specimen of the heart valves - Reproduced with permission of the author and the European Association for Cardio-Thoracic Surgery from: Anderson RH. The surgical anatomy of the aortic root. Multimedia Man Cardiothorac Surg doi:10.1510/mmcts.2006.002527.	37
3.2	Similarity transform represented as a bounding box around the aortic valve from cardiac CT. (a) Perspective view; (b) Long Axis; (c) Short Axis.	40
3.3	Similarity transform represented as a bounding box around the mitral valve from cardiac CT. (a) Perspective view; (b) Long Axis; (c) Short Axis.	41
3.4	Similarity transform represented as a bounding box around the tricuspid valve from cardiac CT. (a) Perspective view; (b) Long Axis; (c) Short Axis.	41
3.5	Similarity transform represented as a bounding box around the pulmonary valve from cardiac CT. (a) Perspective view; (b) Long Axis; (c) Short Axis.	42
3.6	Anatomical landmark model of the aortic valve. (a) Landmarks relative to the anatomical location illustrated in long and short axis from an example CT study. (b) Perspective view including the bounding box.	43
3.7	Anatomical landmark model of the mitral valve. (a) Landmarks relative to the anatomical location illustrated in long and short axis from an example CT study. (b) Perspective view including the bounding box.	44

3.8	Anatomical landmark model of the tricuspid valve. (a) Landmarks relative to the anatomical location illustrated in long and short axis from an example CT study. (b) Perspective view including the bounding box. . . .	45
3.9	Anatomical landmark model of the pulmonary valve. (a) Landmarks relative to the anatomical location illustrated in long and short axis from an example CT study. (b) Perspective view including the bounding box. . . .	45
3.10	Isolated surface components of the aortic and mitral models with parametric directions and spatial relations to anatomical landmarks: (a) aortic root, (b) aortic leaflets, (c) aortic-mitral in end-systole, (d) anterior mitral leaflet, (e) posterior mitral leaflet and (f) aortic-mitral in end-diastole. . . .	47
3.11	Isolated surface components of the tricuspid and pulmonary models with parametric directions and spatial relations to anatomical landmarks: (a) tricuspid leaflet, (b) tricuspid annulus and leaflets, (c) tricuspid-pulmonary in end-diastole, (d) pulmonary trunk, (e) pulmonary leaflets and (f) tricuspid-pulmonary in end-systole.	48
3.12	Complete heart valve model consisting of aortic valve (AV), mitral valve (MV), pulmonary valve (PV) and tricuspid valve (TV). (a) Similarity transform illustrated as a bounding box and anatomical landmarks. (b) Complete mesh surface model.	49
3.13	(a) Example of a two-dimensional contour and corresponding uniform samples, obtained from the intersection of a plane with the three-dimensional aortic root. Resampling planes for the mitral leaflets (b,c) and aortic root (d). The planes at the hinge and commissure levels of the aortic root in (d) are depicted in red and green respectively. Note that for the purpose of clarity only a subset of resampling planes is visualized in figs (b),(c) and (d).	50
3.14	Example trajectories of aortic leaflet tips. (a) The aligned trajectories in the Cartesian space by removing the global similarity transformations. (b) Corresponding 3 trajectories highlighted in red, magenta and green, which demonstrates the compact spectrum representation. (c) Reconstructed trajectories of using 64, 10, and 3 components, respectively, showing that a small number of components can be used to reconstruct faithful motion trajectories.	52
3.15	Cumulated shape variation for (a) aortic and (b) mitral valves. The green dot marks the threshold cumulated variance of 0.995.	56
4.1	Diagram depicting the hierarchical model estimation algorithm. Each block describes the actual estimation stage, computed model parameters and underlying approach.	62
4.2	The adaptive boosting (AdaBoost) algorithm introduced by Freund and Schapire in [53].	68
4.3	The probabilistic boosting-tree training as introduced by Zhuowen Tu in [164]	69
4.4	Illustration of the probabilistic model of the tree. The dark nodes are the leaf nodes. Each level of the tree corresponds to an augmented variable. Each tree node is a strong classifier. Figure from Tu <i>et al.</i> [164].	70

4.5	The probabilistic boosting-tree testing as introduced by Zhuowen Tu in [164]	70
4.6	(a) Examples of rectangle (Haar) features. The sum of the pixels which lie within the white rectangles are subtracted from the sum of pixels in the grey rectangles. From left to right are shown: two-rectangle features, three-rectangle feature and four-rectangle feature. (b) The integral image at point (x, y) is the sum of the pixels marked by the black rectangle. . . .	71
4.7	Steerable sampling pattern aligned with an example hypothesis $(x, y, \vec{\alpha}_x, s_x, s_y)$ for a two-dimensional problem. Sampling location are defined as '+'. (a) Pattern centered at (x, y) . (b) Pattern oriented with $\vec{\alpha}_x$. (c) Pattern scaled along the axes proportional to (s_x, s_y)	72
4.8	An example of a local-spatio-temporal feature, aligned with a certain position, orientation and scale, at time t . The temporal context length of the illustrated LST feature is T , spanned symmetrically relative to t	73
4.9	The outline of our marginal trajectory space learning algorithm.	81
4.10	The outline of our parameter search algorithm.	82
4.11	Diagram depicting the estimation of non-rigid landmark motion using trajectory spectrum learning.	82
4.12	Diagram depicting the estimation of the comprehensive valve model. Estimation in cardiac key phases, end-diastole and end-systole.	83
4.13	Diagram depicting the estimation of the comprehensive valve model. Estimation in the full cardiac cycle.	85
4.14	Examples of the full heart estimation from cardiac CT.	86
4.15	Examples of cardiac data: (a) TEE study, (b) cardiac CT study. and (c) CMR study.	87
4.16	Examples of global location and rigid motion estimation: (a) aortic valve in TEE, (b) mitral valve in TEE, (c) pulmonary valve in CMR, (d) aortic valve in cardiac CT, (e) mitral valve in cardiac CT, and (f) pulmonary valve in cardiac CT.	88
4.17	Examples of non-rigid landmark motion estimation: (a) aortic valve in TEE, (b) mitral valve in TEE, (c) pulmonary valve in CMR, (d) aortic valve in cardiac CT, (e) mitral valve in cardiac CT, and (f) pulmonary valve in cardiac CT.	90
4.18	Error comparison between the optical flow, tracking-by-detection and our trajectory-spectrum approach distributed over (a) time and (b) detected anatomical landmarks. The curve in black shows the performance of our approach, which has the lowest error among all three methods.	91
4.19	Examples of comprehensive valves model estimation: (a) aortic valve in TEE, (b) mitral valve in TEE, (c) pulmonary valve in CMR, (d) aortic valve in cardiac CT, (e) mitral valve in cardiac CT, and (f) pulmonary valve in cardiac CT.	92
4.20	Illustration of the inter-modality consistency; from left to right, pulmonary trunk model in end-diastole from cardiac CT, CMR and CMR model projection (yellow points) into the corresponding CT image.	93

4.21	System error compared to the inter-user variability. The sorted automated estimation error (blue bars) and the 80% (light blue area) and 90% (yellow) confidence intervals of the user variability determined from the standard deviation.	94
4.22	Examples of estimated patient-specific models from TEE and CT data: healthy valves from three different cardiac phases in (a) TEE from atrial aspect and (b) CT data in four chamber view. Pathologic valves with (c) bicuspid aortic valve, (d) aortic root dilation and regurgitation, (e) moderate aortic stenosis, (f) mitral stenosis, (g) mitral prolapse, (h) bicuspid aortic valve with prolapsing leaflets, (i) aortic stenosis with severe calcification and (j) dilated aortic root.	96
5.1	Examples of aortic-mitral morphological and functional measurements. (a) From left to right: aortic valve model with measurement traces, aortic valve area, aortic root diameters and ostia to leaflets distances. (b) Mitral valve with measurement traces, mitral valve and annulus area, mitral annular deviation in ED and ES and aortic-mitral angle and centroid distance.	100
5.2	Aortic Valve Area measured manually from 2D images versus the automatic 3D model-based quantification: (a), (b) and (c) show the manual measurement from three different 2D TEE images of the same patient, which demonstrate the sensitivity of the current gold standard approach to the position of the 2D-dimensional section. (d) shows the proposed precise and reproducible 3D model-based measurement.	101
5.3	Examples of model-based aortic valve measurements: (a) aortic annular diameter (ventriculoarterial junction), (b) sinus width, (c) inter-commissural distances, and (d) coronary ostia to leaflet tip distances.	103
5.4	Measurements obtained before (dotted lines) and after (solid lines) mitral annuloplasty: (a) Aortic (blue) and Mitral (red) valvular area, (b) Aortic (blue) and Mitral (red) annular area.	104
5.5	Bland altman plots for a) right ventricle output tract diameter, b) pulmonary valve bifurcation diameter, c) tricuspid valve area and d) distance between pulmonary and tricuspid valve	105
5.6	Aortic (AV) and pulmonary valve (PV) area, mean commissure-hinge plane height and mean leaflet height obtained from a normal patient (solid lines) and a post Ross operation patient (dotted line). The red graph is representing the aortic valve and the blue the pulmonary.	105
5.7	(a) Pathological aortic valves in CT: dilated aortic root and stenotic and calcified aortic valve. (b) Pathological aortic valves in TEE: bicuspid aortic valve and moderate stenotic valve. (c) Relative neighborhood graph with health (blue) and diseased (red) entries.	109
5.8	Types of pulmonary trunk morphologies: (a) pyramidal shape, (b) constant diameter, (c) inverted pyramidal shape, (d) narrowed centrally but wide proximally and distally, (e) wide centrally but narrowed proximally and distally [139]. (f) Relative neighborhood graph with unsuitable (blue cluster) and suitable (red cluster) individuals.	110

5.9	Classification accuracy for the different learning techniques applied to Aortic Valve Disease classification and PPVI suitability selection.	111
5.10	Discriminant anatomical regions for (a,b) aortic valve disease and (c) pulmonary trunk morphology: blue - less discriminate, red - more discriminate.	112
5.11	Schematic description of the proposed PAVI computational decision support workflow.	114
5.12	Aortic valve and ascending aortic root model. (a) generic model of the aortic valve including nine anatomical landmarks. (b) point distribution model of the aortic root. (c) aorta leaflet model - the N leaflet is depicted. (d) ascending aortic root model. (e) full model with the corresponding anatomical parameterization.	115
5.13	A survey of our hierarchical model estimation schema.	115
5.14	(a) CoreValve implant, (b) long axis cross section of stent mesh (orange) with superimposed computational mesh (blue) and (c) CoreValve implant with sketch of target anatomy (Sources a & c: http://www.medtronic.com).	116
5.15	Forces acting on the model on deployment to converge to the observed geometric properties: (a) f_{angle} enforces the characteristic angles at the strut joints (green), (b) f_{length} maintains the strut lengths. (c) f_{circ} enforces the circumference (green), while f_{ext} dampens and eliminates the all forces acting along the stent mesh normal weighted by the fraction of distances of strut joint and vessel wall (red) to the stent centroid (magenta/yellow). Please note that (c) shows a short axis cross section of the stent mesh.	117
5.16	The outline of our virtual stent deployment algorithm.	118
5.17	Example results of preoperative virtual stent deployment (a-d) vs. post operative stent models (e-h) overlaid with with the anatomical models. Note the deviation of the virtually deployed stent around the sinutubular junction (upper end) in contrast to the close approximation at sinus and annular level, which is to due to the fact, that internal stiffness of the stent configuration is not modeled yet.	120
A.1	Visualizations of patient-specific truncated velocity (left) and vorticity fields (right). Normal heart in early diastolic stage (top) and early systolic stage (bottom).	130
A.2	Patient specific cardiac model fitted to 4D CT data with chambers and valve details.	132
A.3	Comparison of diseased hearts. Top: normal heart; Middle: heart with dilated aorta; Bottom: heart with bicuspid valve. First column: early systole; Second column: late systole; Third column: early diastole; Fourth column: late diastolic filling.	133
B.1	3D MRI scan of the whole heart in the ED phase (a). 2D long axis (LA) plane (b) and short axis (SA) plane (c) of the pulmonary artery over the cardiac cycle	139

B.2	Pulmonary trunk model in CT (left) and MRI (middle) data for the ED phase. Inter-modality consistency by projecting the MRI model(yellow points) into the CT data (right).	144
C.1	Patent US 2009/0123050, http://www.freepatentsonline.com/20090123050.pdf	150
C.2	Patent US 2009/0154785, http://www.freepatentsonline.com/20090154785.pdf	151
C.3	Patent US 2010/0070249, http://www.freepatentsonline.com/20100070249.pdf	152
C.4	Patent US 2010/0067768, http://www.freepatentsonline.com/20100067768.pdf	153

References

- [1] *National center for health statistics: National hospital discharge survey: Annual summaries with detailed diagnosis and procedure data; series 13.*
- [2] A. AGARWAL AND B. TRIGGS, *Tracking articulated motion using a mixture of autoregressive models*, in Proc. European Conf. Computer Vision, 2004, pp. III 54–65.
- [3] M. AKHTAR, E. M. TUZCU, S. R. KAPADIA, L. G. SVENSSON, R. K. GREENBERG, E. E. ROSELLI, S. HALLIBURTON, V. KURRA, P. SCHOENHAGEN, AND S. SOLA, *Aortic root morphology in patients undergoing percutaneous aortic valve replacement: Evidence of aortic root remodeling*, The Journal of Thoracic and Cardiovascular Surgery, 137 (2009), pp. 950 – 956.
- [4] I. AKHTER, Y. SHEIKH, S. KHAN, AND T. KANADE, *Nonrigid structure from motion in trajectory space*, in Advances in Neural Information Processing Systems, 2008, pp. 41–48.
- [5] H. ALKADHI, S. WILDERMUTH, D. BETTEX, A. PLASS, B. BAUMERT, S. LESCHKA, L. DESBIOLLES, B. MARINCEK, AND T. BOEHM, *Mitral regurgitation: quantification with 16-detector row ct-initial experience*, Radiology, 238 (2006), pp. 454–463.
- [6] A. A. AMINI, T. E. WEYMOUTH, AND R. C. JAIN, *Using dynamic programming for solving variational problems in vision*, IEEE Trans. Pattern Anal. Mach. Intell., 12 (1990), pp. 855–867.
- [7] R. H. ANDERSON, *The surgical anatomy of the aortic root*, Multimedia Manual of Cardiothoracic Surgery (MMCTS), (2006). doi:10.1510/mmcts.2006.002527.
- [8] R. H. ANDERSON AND M. KANANI, *Mitral valve repair: critical analysis of the anatomy discussed*, Multimedia Manual of Cardiothoracic Surgery (MMCTS), (2006). doi:10.1510/mmcts.2006.002147.

- [9] A. ANDREOPOULOS AND J. K. TSOTSOS, *A novel algorithm for fitting 3-D active appearance models: Application to cardiac MRI segmentation*, in Proc. Scandinavian Conf. Image Analysis, 2005, pp. 729–739.
- [10] S. AVIDAN AND A. SHASHUA, *Trajectory triangulation: 3D reconstruction of moving points from a monocular image sequence*, IEEE Trans. Pattern Anal. Machine Intell., 22 (2000), pp. 348–357.
- [11] N. AYACHE, *Computational Models for the Human Body*, ser. *Handbook of Numerical Analysis*, P.G. Ciarlet, Ed., Elsevier, Amsterdam, Netherlands, 2004.
- [12] I. N. BANKMAN, *Handbook of Medical Imaging: Processing and Analysis Management*, Academic Press, San Diego, CA, USA, 2000.
- [13] A. BAR-HILLEL AND D. WEINSHALL, *Learning distance functions by coding similarity*, vol. 227, 2007, pp. 1031–1038.
- [14] F. BILLET, M. SERMESANT, H. DELINGETTE, AND N. AYACHE, *Cardiac motion recovery and boundary conditions estimation by coupling an electromechanical model and cine-mri data*, In Proceedings of Functional Imaging and Modeling of the Heart 2009 (FIMH'09), 5528 (2009), pp. 376–385.
- [15] M. M. BLACK, I. C. HOWARD, X. HUANG, AND E. A. PATTERSON, *A three-dimensional analysis of a bioprosthetic heart valve*, Journal of Biomechanics, 24 (1991), pp. 793–801.
- [16] R. BLANC, M. REYES, C. SEILER, AND G. SZEKELY, *Conditional variability of statistical shape models based on surrogate variables*, in Medical Image Computing and Computer-Assisted Intervention MICCAI 2009, vol. Volume 5761 2009 of Lecture Notes in Computer Science, October 2009, pp. 124–131.
- [17] J. BLAND AND D. ALTMAN, *Statistical methods for assessing agreement between two methods of clinical measurement*, Lancet, (1986).
- [18] P. BONHOEFFER, S. A. BOUDJEMLINE, Y. QURESHI, J. L. BIDOIS, L. ISERIN, P. ACAR, J. MERCKX, J. KACHANER, AND D. SIDI, *Percutaneous insertion of the pulmonary valve*, Journal of the American College of Cardiology, 39 (2002), pp. 1664–1669.
- [19] R. O. BONOW, B. A. CARABELLO, K. CHATTERJEE, A. C. J. DE LEON, D. P. FAXON, M. D. FREED, W. H. GAASCH, B. W. LYTLE, R. A. NISHIMURA, P. T. O'GARA, R. A. O'ROURKE, C. M. OTTO, P. M. SHAH, AND J. S. SHANEWISE, *Acc/aha 2006 guidelines for the management of patients with valvular heart disease: a report of the american college of cardiology/american heart association task force on practice guidelines (writing committee to develop guidelines for the management of patients with valvular heart disease)*, Circulation, 114 (2006), pp. 84–231.

-
- [20] F. L. BOOKSTEIN, *Principal warps: thin-plate splines and the decomposition of deformations*, Pattern Analysis and Machine Intelligence, IEEE Transactions on, 11 (1989), pp. 567–585.
- [21] Y. BOUDJEMLINE MD, G. AGNOLETTI MD, D. BONNET MD, D. SIDI MD, AND P. BONHOEFFER MD, *Percutaneous pulmonary valve replacement in a large right ventricular outflow tract: An experimental study*, American College of Cardiology, 43 (2004), pp. 1082–1087.
- [22] P. BOURLAS, E. GIAKOUMAKIS, AND G. PAPAKONSTANTINOY, *A knowledge acquisition and management system for ecg diagnosis*, in Proceedings of Workshop on Machine Learning in Medical Applications, Advance Course in Artificial Intelligence-ACAI99, 1999, pp. 30–36.
- [23] L. BREIMAN, *Random forests*, in Machine Learning, 2001, pp. 5–32.
- [24] A. BRIASSOULI AND N. AHUJA, *Extraction and analysis of multiple periodic motions in video sequences*, IEEE Trans. Pattern Anal. Machine Intell., 29 (2007), pp. 1244–1261.
- [25] G. CACCIOLA, G. PETERS, AND P. SCHREURS, *A three-dimensional mechanical analysis of a stentless fibre-reinforced aortic valve prosthesis*, Journal of Biomechanics, 33 (2000), pp. 521–530.
- [26] A. CALLEJA, I. RAZVAN, H. HOULE, S. LIU, J. DICKERSON, P. THAVENDIRANATHAN, C. SAI-SUDHAKAR, J. CRESTANELLO, T. RYAN, AND M. VANNAN, *Automated quantitative modeling of the aortic valve and root in aortic regurgitation using volume 3-d transesophageal echocardiography*, in American College of Cardiology Annual Meeting - ACC 2010, Atlanta, USA, March 2010.
- [27] H. CARNAGHAN, *Percutaneous pulmonary valve implantation and the future of replacement*, Science and Technology, 20 (2006), pp. 319–322.
- [28] G. CARNEIRO, B. GEORGESCU, S. GOOD, AND D. COMANICIU, *Automatic fetal measurements in ultrasound using constrained probabilistic boosting tree*, IEEE Trans. Medical Imaging, (2008).
- [29] A. CARPENTIER, *Cardiac valve surgery – the french correction*, The Journal of thoracic and cardiovascular surgery, 86 (1983), pp. 323–337.
- [30] A. CARPENTIER, D. H. ADAMS, AND F. FILSOUFI, *Carpentier’s Reconstructive Valve Surgery*, Saunders Elsevier, Maryland Heights MO, USA, 2010.
- [31] T. CHEN, W. ZHANG, S. GOOD, K. ZHOU, AND D. COMANICIU, *Automatic ovarian follicle quantification from 3d ultrasound data using global/local context with database guided segmentation*, in Proc. Int’l Conf. Computer Vision, 2009.

- [32] J. H. CHOI, B. GEORGESCU, R. I. IONASEC, S. RAMAN, G.-R. HONG, S. LIU, H. HOULE, AND M. A. VANNAN, *Novel semi-automatic quantitative assessment of the aortic valve and aortic root from volumetric 3d echocardiography: Comparison to volumetric cardiac computed tomography (ct)*, in AHA, New Orleans, USA, November 2008.
- [33] D. COMANICIU, V. RAMESH, AND P. MEER, *Real-time tracking of non-rigid objects using mean shift*, in Proc. IEEE Conf. Computer Vision and Pattern Recognition, 2000, pp. II: 142–149.
- [34] C. A. CONTI, E. VOTTA, A. D. CORTE, L. D. VISCOVO, C. BANCONE, M. COTRUFO, AND A. REDAELLI, *Dynamic finite element analysis of the aortic root from mri-derived parameters*, Medical Engineering and Physics, 32 (2010), pp. 212 – 221.
- [35] T. F. COOTES, G. J. EDWARDS, AND C. J. TAYLOR, *Active appearance models*, IEEE Trans. Pattern Anal. Machine Intell., 23 (2001), pp. 681–685.
- [36] T. F. COOTES, C. J. TAYLOR, D. H. COOPER, AND J. GRAHAM, *Active shape models—their training and application*, Computer Vision and Image Understanding, 61 (1995), pp. 38–59.
- [37] P. DAGUM, G. GREEN, F. NISTAL, G. DAUGHTERS, T. TIMEK, L. FOPPIANO, A. BOLGER, N. INGELS, AND D. MILLER, *Deformational dynamics of the aortic root: modes and physiologic determinants.*, Circulation, 100 (1999), pp. II54–II62.
- [38] T. E. DAVID, *Cardiac Surgery in the Adult : Aortic Valve Repair and Aortic Valve Sparing Operations*, McGraw-Hill, New York, NY, USA, 2008.
- [39] J. DE HART, G. PETERS, P. SCHREURS, AND F. BAAIJENS, *A three dimensional computational analysis of fluid structure interaction in the aortic valve*, Journal of Biomechanics, 36 (2002), pp. 103–110.
- [40] T. DOENST, K. SPIEGEL, M. REIK, M. MARKL, J. HENNIG, S. NITZSCHE, F. BEYERSDORF, AND H. OERTEL, *Fluid-dynamic modeling of the human left ventricle: Methodology and application to surgical ventricular reconstruction*, The Annals of Thoracic Surgery, 87 (2009), pp. 1187 – 1195.
- [41] A. DOUCET, N. D. FREITAS, AND N. GORDON, *Sequential Monte Carlo Methods in Practice*, NY:Springer-Verlag, 2001.
- [42] Q. DUAN, E. ANGELINI, S. HOMMA, AND A. LAINE, *Validation of optical-flow for quantification of myocardial deformations on simulated RT3D ultrasound*, in ISBI, 2007.
- [43] M. DULCE, G. MOSTBECK, K. FRIESE, G. CAPUTO, AND C. HIGGINS, *Quantification of the left ventricular volumes and function with cine mr imaging: comparison of geometric models with three-dimensional data*, Radiology, 188 (1993), pp. 371–376.

-
- [44] J. S. DUNCAN, *Knowledge directed left ventricular boundary detection in equilibrium radionuclide angiocardigraphy*, IEEE Trans. Medical Imaging, 6 (1987), pp. 325–336.
- [45] J. S. DUNCAN AND N. AYACHE, *Medical image analysis: Progress over two decades and the challenges ahead*, IEEE Transactions on Pattern Analysis and Machine Intelligence, 22 (2000), pp. 85–106.
- [46] N. DUTA AND M. SONKA, *Segmentation and interpretation of mr brain images: An improved active shape model*, IEEE Trans. Medical Imaging, 17 (1998), pp. 1049–1062.
- [47] Y. J. E. D. ANGELINI AND A. F. LAINE, *Handbook of Medical Image Analysis : Advanced Segmentation and Registration Models, chapter State-of-the-Art of Levelset Methods in Segmentation and Registration of Medical Imaging Modalities*, Kluwer Academic Publishers, 2004.
- [48] K. S. ET AL, *Correction of pulmonary arteriovenous malformation using image-based surgical planning*, J Am Coll Cardiol Img, (2009), pp. 1024–1030.
- [49] L. A. FELDKAMP, L. C. DAVIS, AND J. W. KRESS, *Practical cone-beam algorithm*, Journal of the Optical Society of America, 1 (1984), pp. 612–619.
- [50] A. FOSSATI, M. DIMITRIJEVIC, V. LEPETIT, AND P. FUA, *Bridging the gap between detection and tracking for 3D monocular video-based motion capture*, in Proc. IEEE Conf. Computer Vision and Pattern Recognition, 2007.
- [51] A. F. FRANGI, W. J. NIESSEN, AND M. A. VIERGEVER, *Three-dimensional modeling for functional analysis of cardiac images: A review*, IEEE Trans. Medical Imaging, 20 (2001), pp. 2–25.
- [52] A. F. FRANGI, D. RUECKERT, AND J. S. DUNCAN, *Three-dimensional cardiovascular image analysis*, IEEE Trans. Medical Imaging, 21 (2002), pp. 1005–1010.
- [53] Y. FREUND AND R. E. SCHAPIRE, *A decision-theoretic generalization of on-line learning and an application to boosting*, J. Computer and System Sciences, 55 (1997), pp. 119–139.
- [54] J. H. FRIEDMAN, *Greedy function approximation: A gradient boosting machine*, Annals of Statistics, 29 (2000), pp. 1189–1232.
- [55] E. GASSNER, R. I. IONASEC, B. GEORGESCU, S. VOGT, U. SCHOEPF, AND D. COMANICIU, *Performance of a dynamic aortic valve model for quantification of the opening area at cardiac mdct . comparison to manual planimetry*, in Radiological Society of North American (RSNA), Chicago, USA, November 2008.
- [56] D. GEIGER, A. GUPTA, L. A. COSTA, AND J. VLONTZOS, *Dynamic programming for detecting, tracking, and matching deformable contours*, IEEE Trans. Pattern Anal. Mach. Intell., 17 (1995), pp. 294–302.

- [57] B. GEORGESCU, X. S. ZHOU, D. COMANICIU, AND A. GUPTA, *Database-guided segmentation of anatomical structures with complex appearance*, in IEEE Conf. Computer Vision and Pattern Recognition (CVPR 05, 2005).
- [58] O. GERARD, A. C. BILLON, J.-M. ROUET, M. JACOB, M. FRADKIN, AND C. ALLOUCHE, *Efficient model-based quantification of left ventricular function in 3-D echocardiography*, IEEE Trans. Medical Imaging, 21 (2002), pp. 1059–1068.
- [59] R. GILKESON, A. MARKOWITZ, A. BALGUDE, AND P. SACHS, *Mdct evaluation of aortic valvular disease*, AJR. American journal of roentgenology, 186 (2006), pp. 350–360.
- [60] C. GOODALL, *Procrustes methods in the statistical analysis of shape*, Journal of the Royal Statistical Society. Series B (Methodological), 53 (1991), pp. 285–339.
- [61] S. GRBIC, R. IONASEC, D. VITANOVSKI, I. VOIGT, B. GEORGESCU, N. NAVAB, AND D. COMANICIU, *Complete valvular heart apparatus model from 4d cardiac ct*, in International Conference on Medical Image Computing and Computer-Assisted Intervention (MICCAI), Beijing, China, September 20-24 2010.
- [62] S. GRBIC, R. I. IONASEC, Y. ZHENG, D. ZAEUNER, B. GEORGESCU, AND D. COMANICIU, *Aortic valve and ascending aortic root modeling from 3d and 3d+ t ct*, in SPIE Medical Imaging, San Diego, USA, February 2010.
- [63] I. R. GREENSHIELDS, *Extended superquadric models of elastic hollow viscera*, in Computer-Based Medical Systems, IEEE Symposium on, Los Alamitos, CA, USA, 1999, IEEE Computer Society, p. 98.
- [64] B. GRIFFITH, D. MCQUEEN, AND C. PESKIN, *Simulating cardiovascular fluid dynamics by the immersed boundary method*, in 47th AIAA Aerospace Sciences Meeting, 2009.
- [65] E. GRUBE, J. LABORDE, U. GERCKENS, T. FELDERHOFF, B. SAUREN, L. BUELLESFELD, R. MUELLER, M. MENICHELLI, T. SCHMIDT, B. ZICKMANN, S. IVERSEN, AND G. W. STONE, *Percutaneous implantation of the corevalve self-expanding valve prosthesis in high-risk patients with aortic valve disease*, Circulation, (2006), pp. 1616–1624.
- [66] E. HALPERN, *Clinical Cardiac CT: Anatomy and Function*, Thieme Medical Publishers, New York, NY , USA, 2008.
- [67] T. HERTZ, *Learning distance functions: algorithms and applications*, PhD thesis, The Hebrew University of Jerusalem, 2006.
- [68] B. K. P. HORN, *Closed-form solution of absolute orientation using unit quaternions*, Journal of the Optical Society of America A, 4 (1987), pp. 629–642.

-
- [69] P. J. HUNTER AND M. VICECONTI, *The vph-physiome project: Standards and tools for multiscale modeling in clinical applications*, Biomedical Engineering, IEEE Reviews in, 2 (2009), pp. 40–53.
- [70] R. IONASEC, V. MIHALEF, B. GEORGESCU, N. NAVAB, AND D. COMANICIU, *Patient-specific modeling of left heart anatomy, dynamics and hemodynamics from 4d images*, in BMT Biomedizinische Technik 2010, Rostock, Germany, October 2010.
- [71] R. I. IONASEC, B. GEORGESCU, D. COMANICIU, S. VOGT, U. SCHOEPF, AND E. GASSNER, *Patient specific 4d aortic root models derived from volumetric image data sets*, in Radiological Society of North American (RSNA), Chicago, USA, November 2008.
- [72] R. I. IONASEC, B. GEORGESCU, E. GASSNER, S. VOGT, O. KUTTER, M. SCHEUERING, N. NAVAB, AND D. COMANICIU, *Dynamic model-driven quantification and visual evaluation of the aortic valve from 4d ct*, in Proc. Int’l Conf. Medical Image Computing and Computer Assisted Intervention, 2008, pp. 686 – 694.
- [73] R. I. IONASEC, A. TSYMBAL, D. VITANOVSKI, B. GEORGESCU, S. K. ZHOU, N. NAVAB, AND D. COMANICIU, *Shape-based diagnosis of the aortic valve*, in SPIE Medical Imaging, Orlando, USA, February 2009.
- [74] R. I. IONASEC, I. VOIGT, B. GEORGESCU, H. HOULE, J. HORNEGGER, N. NAVAB, AND D. COMANICIU, *Modeling and assessment of the aortic-mitral valve coupling from 4d tee and ct*, in International Conference on Medical Image Computing and Computer-Assisted Intervention (MICCAI), London, USA, September 2009, pp. 767 – 775.
- [75] R. I. IONASEC, I. VOIGT, B. GEORGESCU, Y. WANG, H. HOULE, F. VEGA-HIGUERA, N. NAVAB, , AND D. COMANICIU, *Patient-specific modeling and quantification of the aortic and mitral valves from 4d cardiac ct and tee*, in IEEE Trans. Medical Imaging, in press, 2010.
- [76] R. I. IONASEC, Y. WANG, B. GEORGESCU, I. VOIGT, N. NAVAB, AND D. COMANICIU, *Robust Motion Estimation Using Trajectory Spectrum Learning: Application to Aortic and Mitral Valve Modeling from 4D TEE*, in Proceedings of 12th IEEE International Conference on Computer Vision 2009, I. C. Society, ed., 2009, pp. 1601–1608.
- [77] M. ISARD AND A. BLAKE, *C-conditional density propagation for visual tracking*, Int. J. Computer Vision, 29 (1998), pp. 5–28.
- [78] G. JACOB, J. NOBLE, C. BEHRENBRUCH, A. KELION, AND A. BANNING, *A shape-space-based approach to tracking myocardial borders and quantifying regional left-ventricular function applied in echocardiography*, IEEE Trans. Medical Imaging, 21 (2002), pp. 226–238.

- [79] J. W. JAROMCZYK AND G. T. TOUSSAINT, *Relative neighborhood graphs and their relatives*, in Proc. IEEE, 1992, pp. 1502–1517.
- [80] J. JIRI, *Medical Image Processing, Reconstruction and Restoration Concepts and Methods*, CRC Press, 2006.
- [81] M. KASS, A. WITKIN, AND D. TERZOPOULOS, *Snakes: Active contour models*, Int. J. Computer Vision, 1 (1988), pp. 321–331.
- [82] J. KEMPFERT, V. FALK, G. SCHULER, A. LINKE, D. MERK, F. MOHR, AND T. WALTHER, *Dyna-ct during minimally invasive off-pump transapical aortic valve implantation*, Ann. Thorac. Surg., 88 (2009), p. 2041.
- [83] D. G. KENDALL, *Shape manifolds, procrustean metrics, and complex projective spaces*, Bull. London Math. Soc., 16 (1984), pp. 81–121.
- [84] S. KHAMBADKONE, L. COATS, A. TAYLOR, Y. BOUDJEMLINE, G. DERRICK, V. TSANG, J. COOPER, V. MUTHURANGU, S. HEGDE, R. RAZAVI, D. PELLERIN, J. DEANFIELD, AND P. BONHOEFFER, *Percutaneous pulmonary valve implantation in humans: results in 59 consecutive patients*, Circulation, 112 (2005), pp. 1189–97.
- [85] S. KRUCINSKI, I. VESELY, M. A. DOKAINISH, AND G. CAMPBELLS, *Numerical simulation of leaflet flexure in bioprosthetic valves mounted on rigid and expansile stents*, Journal of Biomechanics, 26 (1993), pp. 929–943.
- [86] K. KUNZELMAN, D. EINSTEIN, AND R. COCHRAN, *Fluid-structure interaction models of the mitral valve: function in normal and pathological states*, Philos. Trans. R. Soc. Lond., B, Biol. Sci., 362 (2007), pp. 1393–1406.
- [87] M. LABROSSE, *Geometric modeling of functional trileaflet aortic valves: development and clinical applications*, Journal of Biomechanics, 39 (2006), pp. 2665–72.
- [88] E. LANSAC, K. LIM, Y. SHOMURA, W. GOETZ, H. LIM, N. RICE, H. SABER, AND C. DURAN, *Dynamic balance of the aortomitral junction*, J Thorac Cardiovasc Surg, 123 (2002), pp. 911–918.
- [89] I. LARRABIDE, A. RADAELLI, AND A. F. FRANGI, *Fast virtual stenting with deformable meshes: Application to intracranial aneurysms*, in MICCAI (2), 2008, pp. 790–797.
- [90] R. LEVINE, M. HANDSCHUMACHER, A. SANFILIPPO, A.J. ANS HAGEGE, P. HARRIGAN, J. MARSHALL, AND W. A.E., *Three-dimensional echocardiographic reconstruction of the mitral valve, with implications for mitral valve prolapse*, Circulation, 80 (1989).
- [91] P. LIBBY, R. O. BONOW, D. L. MANN, AND D. P. ZIPES, *Braunwald's Heart Disease: A Textbook of Cardiovascular Medicine*, Elsevier, Philadelphia, PA, USA, 2008.

-
- [92] C. LIM, R. HARRISON, AND R. KENNEDY, *Application of autonomous neural network systems to medical pattern classification tasks*, in *Artificial Intelligence in Medicine*, 1997, pp. 215–239.
- [93] C. A. LINTE, A. D. WILES, N. HILL, J. MOORE, C. WEDLAKE, G. GUIRAUDON, D. JONES, D. BAINBRIDGE, AND T. M. PETERS, *An augmented reality environment for image-guidance of off-pump mitral valve implantation*, in *Medical Imaging 2007: Visualization and Image-Guided Procedures*, K. R. Cleary and M. I. Miga, eds., Proceedings of SPIE, San Diego, California, USA, 2007.
- [94] C. LIU, H. SHUM, AND C. ZHANG, *Hierarchical shape modeling for automatic face localization*, in *Proc. European Conf. Computer Vision*, 2002.
- [95] F. LIU AND R. PICARD, *Finding periodicity in space and time*, in *Proc. Int'l Conf. Computer Vision*, 1998, pp. 376–383.
- [96] D. LLOYD-JONES, R. ADAMS, M. CARNETHON, G. DE SIMONE, T. B. FERGUSON, K. FLEGAL, E. FORD, K. FURIE, A. GO, K. GREENLUND, N. HAASE, S. HAILPERN, M. HO, V. HOWARD, B. KISSELA, S. KITTNER, D. LACKLAND, L. LISABETH, A. MARELLI, M. McDERMOTT, J. MEIGS, D. MOZAFFARIAN, G. NICHOL, C. O'DONNELL, V. ROGER, W. ROSAMOND, R. SACCO, P. SORLIE, R. STAFFORD, J. STEINBERGER, T. THOM, S. WASSERTHIEL-SMOLLER, N. WONG, J. WYLIE-ROSETT, Y. HONG, AND AMERICAN HEART ASSOCIATION STATISTICS COMMITTEE AND STROKE STATISTICS SUBCOMMITTEE, *Heart disease and stroke statistics–2009 update: a report from the american heart association statistics committee and stroke statistics subcommittee.*, *Circulation*, 119 (2009), pp. e21–181.
- [97] Q. LONG, R. MERRIFIELD, G. Z. YANG, X. Y. XU, P. J. KILNER, AND D. N. FIRMIN, *The influence of inflow boundary conditions on intra left ventricle flow predictions*, *Journal of Biomechanical Engineering*, 125 (2003), pp. 922–927.
- [98] C. LORENZ AND N. KRAHNSTOVER, *Generation of point based 3D statistical shape models for anatomical objects*, *Computer Vision and Image Understanding*, 77 (2000), pp. 175–191.
- [99] C. LORENZ AND J. VON BERG, *A comprehensive shape model of the heart*, *Medical Image Analysis*, 10 (2006), pp. 657–670.
- [100] S. MAHAMUD AND M. HEBERT, *The optimal distance measure for object detection*, in *Proc. IEEE Conf. Computer Vision and Pattern Recognition*, vol. 1, 2003, pp. 248–255.
- [101] F. MAHMOOD, S. KARTHIK, B. SUBRAMANIAM, P. PANZICA, J. MITCHELL, A. LERNER, K. JERVIS, AND A. MASLOW, *Intraoperative application of geometric three-dimensional mitral valve assessment package: A feasibility study*, *Journal of Cardiothoracic and Vascular Anesthesia*, 22 (2006), pp. 292–298.

- [102] J. MAINTZ AND M. VIERGEVER, *A survey of medical image registration*, Medical Image Analysis, 2 (1998), pp. 1–36.
- [103] T. MANSI, S. DURRLEMAN, B. BERNHARDT, M. SERMESANT, H. DELINGETTE, I. VOIGT, P. LURZ, T. A. M., J. BLANC, Y. BOUDJEMLINE, X. PENNEC, AND N. AYACHE, *A statistical model of right ventricle in tetralogy of fallot for prediction of remodelling and therapy planning*, Intl Conf. Medical Image Computing and Computer Assisted Intervention, (MICCAI09), (2009), pp. 214–221.
- [104] T. MCINERNEY AND D. TERZOPOULOS, *Deformable models in medical image analysis: a survey. medical image analysis*, Medical Image Analysis, 1 (1996), pp. 91–108.
- [105] R. MEIR AND G. RÄTSCH, *An introduction to boosting and leveraging*, Advanced lectures on machine learning, (2003), pp. 118–183.
- [106] G. J. MIAO AND M. A. CLEMENTS, *Digital signal processing and statistical classification*, Artech House, 2002.
- [107] V. MIHALEF, R. IONASEC, P. SHARMA, B. GEORGESCU, M. HUBER, AND C. D., *Patient-specific modeling of left heart anatomy, dynamics and hemodynamics from 4d images*, in VPH Virtual Physiological Human - Annual Conference 2010, Brussels, Belgium, October 2010.
- [108] V. MIHALEF, R. IONASEC, Y. WANG, Y. ZHENG, B. GEORGESCU, AND D. COMANICIU, *Patient-specific modeling of left heart anatomy, dynamics and hemodynamics from high resolution 4d ct*, in IEEE International Symposium on Biomedical Imaging (ISBI), Rotterdam, Netherlands, April 2010.
- [109] V. MIHALEF, D. METAXAS, M. SUSSMAN, V. HURMUSIADIS, AND L. AXEL, *Atrioventricular blood flow simulation based on patient-specific data*, in FIMH, Berlin, Heidelberg, 2009, Springer-Verlag, pp. 386–395.
- [110] S. C. MITCHELL, B. P. F. LELIEVELDT, R. J. VAN DER GEEST, H. G. BOSCH, J. H. C. REIBER, AND M. SONKA, *Multistage hybrid active appearance model matching: Segmentation of left and right ventricles in cardiac MR images*, IEEE Trans. Medical Imaging, 20 (2001), pp. 415–423.
- [111] J. MONTAGNAT AND H. DELINGETTE, *4d deformable models with temporal constraints : application to 4d cardiac image segmentation*, Medical Image Analysis, 9 (2005), pp. 87–100.
- [112] D. MUTLAK, D. ARONSON, J. LESSICK, S. A. REISNER, S. DABBAH, AND Y. AGMON, *Functional tricuspid regurgitation in patients with pulmonary hypertension*, CHEST, 135 (2009), pp. 115–121.
- [113] A. NAFTEL AND S. KHALID, *Motion trajectory learning in the DFT-coefficient feature space*, in Proc. Int'l Conf. Computer Vision Systems, 2006, p. 47.

-
- [114] T. Z. NAQVI, *Echocardiography in percutaneous valve therapy*, JACC Cardiovasc Imaging, 2 (2009), pp. 1226–1237.
- [115] N. NGUYEN, D. PHUNG, S. VENKATESH, AND H. BUI, *Learning and detecting activities from movement trajectories using the hierarchical hidden Markov models*, in Proc. IEEE Conf. Computer Vision and Pattern Recognition, 2005, pp. II: 955–960.
- [116] D. NICKERSON, N. SMITH, AND P. HUNTER, *New developments in a strongly coupled cardiac electromechanical model*, Europace, Oxford Journals, 7 (2005), pp. 118–127.
- [117] L. NIFONG, V. CHU, B. BAILEY, D. MAZIARZ, V. SORRELL, D. HOLBERT, AND W. J. CHITWOOD, *Robotic mitral valve repair: experience with the da vinci system*, The Annals of thoracic surgery, 75 (2006), pp. 438–442.
- [118] V. NKOMO, J. GARDIN, T. SKELTON, J. GOTTDIENER, C. SCOTT, AND M. ENRIQUEZ-SARANO, *Burden of valvular heart diseases: a population-based study.*, Lancet, 368 (2006), pp. 1005–1011.
- [119] G. NOLLEN, K. SCHIJNDEL, J. TIMMERMANS, M. GROENINK, J. BARENTSZ, E. WALL, J. STOKER, AND B. MULDER, *Pulmonary artery root dilatation in marfan syndrome: quantitative assessment of an unknown criterion*, Heart, 87 (2002), pp. 470–471.
- [120] D. ORMONEIT, H. SIDENBLADH, M. BLACK, AND T. HASTIE, *Learning and tracking cyclic human motion*, in Advances in Neural Information Processing Systems, 2001, pp. 894–900.
- [121] R. O’ROURKE, R. WALSH, AND V. FUSTER, *Hurst’s the Heart Manual of Cardiology*, McGraw-Hill, New York, NY, USA, 2008.
- [122] C. M. OTTO AND R. O. BONOW, *Valvular Heart Disease: A Companion to Braunwald’s Heart Disease: Expert Consult - Online and Print*, Elsevier, Philadelphia, PA, USA, 2009.
- [123] C. P. PAPAGEORGIOU, M. OREN, AND T. POGGIO, *A general framework for object detection*, in ICCV ’98: Proceedings of the Sixth International Conference on Computer Vision, Washington, DC, USA, 1998, IEEE Computer Society, p. 555.
- [124] J. PARK, D. METAXAS, A. YOUNG, AND L. AXEL, *Deformable models with parameter functions for cardiac motion analysis from tagged mri data*, IEEE Trans. Medical Imaging, 15 (1996), pp. 278–289.
- [125] J. PARK, S. ZHOU, AND D. COMANICIU, *Automatic mitral valve inflow measurements from doppler echocardiography, int’l conf. medical image computing and computer assisted intervention*, in Int’l Conf. Medical Image Computing and Computer Assisted Intervention, (MICCAI’08), 2008.

- [126] K. PARK, A. MONTILLO, D. METAXAS, AND L. AXEL, *Volumetric heart modeling and analysis*, Communications of the ACM, 48 (2005), pp. 43–48.
- [127] J. PARR, J. KIRKLIN, AND E. BLACKSTONE, *The early risk of re-replacement of aortic valves*, The Annals of Thoracic Surgery, 23 (1977), pp. 319–322.
- [128] C. PELIZZARI, G. CHEN, D. SPELBRING, R. WEICHSELBAUM, AND C. CHEN, *Accurate three-dimensional registration of ct, pet, and/or mr images of the brain*, J Comput Assist Tomogr., 13 (1989), pp. 1–36.
- [129] C. S. PESKIN AND D. M. MCQUEEN, *Case Studies in Mathematical Modeling: Ecology, Physiology, and Cell Biology*, Prentice-Hall, Englewood Cliffs, NJ, USA, 1996.
- [130] N. PIAZZA, P. DE JAEGERE, C. SCHULTZ, A. BECKER, P. SERRUYS, AND R. ANDERSON, *Anatomy of the aortic valvar complex and its implications for transcatheter implantation of the aortic valve.*, Circulation. Cardiovascular interventions, 1 (2008), pp. 74–81.
- [131] R. POLANA AND R. NELSON, *Detection and recognition of periodic, nonrigid motion*, Int. J. Computer Vision, 23 (1997), pp. 261–282.
- [132] E. RIBNICK AND N. PAPANIKOLOPOULOS, *Estimating 3D trajectories of periodic motions from stationary monocular views*, in Proc. European Conf. Computer Vision, 2008, pp. III: 546–559.
- [133] R. ROHLINGA, A. GEEA, AND L. BERMANB, *A comparison of freehand three-dimensional ultrasound reconstruction techniques*, Medical Image Analysis, 3 (1999), pp. 339–359.
- [134] W. ROSAMOND, K. FLEGAL, G. FRIDAY, K. FURIE, A. GO, K. GREENLUND, N. HAASE, M. HO, V. HOWARD, B. KISSELA, S. KITTNER, D. LLOYD-JONES, M. McDERMOTT, J. MEIGS, C. MOY, G. NICHOL, C. J. O'DONNELL, V. ROGER, J. RUMSFELD, P. SORLIE, J. STEINBERGER, T. THOM, S. WASSERTHIEL-SMOLLER, AND Y. HONG, *Heart disease and stroke statistics—2007 update: a report from the american heart association statistics committee and stroke statistics subcommittee*, Circulation, 115 (2007), pp. 69–171.
- [135] D. RUECKERT AND P. BURGER, *Geometrically deformable templates for shape-based segmentation and tracking in cardiac mr images*, in EMMCVPR '97: Proceedings of the First International Workshop on Energy Minimization Methods in Computer Vision and Pattern Recognition, London, UK, 1997, Springer-Verlag, pp. 83–98.
- [136] N. SABER, N. WOOD, A. GOSMAN, R. MERRIFIELD, G. YANG, C. CHARRIER, P. GATEHOUSE, AND D. FIRMIN, *Progress towards patient-specific computational flow modeling of the left heart via combination of magnetic resonance imaging with*

- computational fluid dynamics.*, Annals of biomedical engineering, 31 (2003), pp. 42–52.
- [137] R. E. SCHAPIRE, Y. FREUND, P. BARTLETT, AND W. LEE, *Boosting the margin: A new explanation for the effectiveness of voting methods.*, The Annals of Statistics, 26 (1998), pp. 1651–1686.
- [138] T. SCHENKEL, S. KRITTIAN, K. SPIEGEL, S. HÖTTGES, M. PERSCHALL, AND H. OERTEL, *World Congress on Medical Physics and Biomedical Engineering, September 7 - 12, 2009, Munich, Germany*, Springer Berlin Heidelberg, 2010.
- [139] S. SCHIEVANO, L. COATS, F. MIGLIAVACCA, W. NORMAN, A. FRIGIOLA, J. DEANFIELD, P. BONHOEFFER, AND A. TAYLOR, *Variations in right ventricular outflow tract morphology following repair of congenital heart disease: Implications for percutaneous pulmonary valve implantation*, Journal of Cardiovascular Magnetic Resonance, 9 (2007), pp. 687–95.
- [140] S. SCHIEVANO, F. MIGLIAVACCA, S. COATS, L. KHAMBADKONE, M. CARMINATI, N. WILSON, J. DEANFIELD, P. BONHOEFFER, AND A. TAYLOR, *Percutaneous pulmonary valve implantation based on rapid prototyping of right ventricular outflow tract and pulmonary trunk from mr data*, Radiology, 242 (2007), pp. 490–49.
- [141] M. SERMESANT, F. BILLET, R. CHABINIOK, T. MANSI, P. CHINCHAPATNAM, P. MOIREAU, J.-M. PEYRAT, K. RHODE, M. GINKS, P. LAMBIASE, S. ARRIDGE, H. DELINGETTE, M. SORINE, A. RINALDI, D. CHAPELLE, R. RAZAVI, AND N. AYACHE, *Personalised electromechanical model of the heart for the prediction of the acute effects of cardiac resynchronisation therapy*, Proc. of Functional Imaging and Modeling of the Heart 2009 (FIMH’09), (2009), pp. 239–248.
- [142] M. SERMESANT, H. DELINGETTE, AND N. AYACHE, *An electromechanical model of the heart for image analysis and simulation.*, IEEE Trans Med Imaging, 25 (2006), pp. 612–625.
- [143] M. SERMESANT, P. MOIREAU, O. CAMARA, J. SAINTEMARIE, R. ANDRIANTSIMIAVONA, R. CIMRMAN, D. HILL, D. CHAPELLE, AND R. RAZAVI, *Cardiac function estimation from mri using a heart model and data assimilation: Advances and difficulties*, Medical Image Analysis, 10 (2006), pp. 642–656.
- [144] M. SERMESANT, J.-M. PEYRAT, P. CHINCHAPATNAM, F. BILLET, T. MANSI, K. RHODE, H. DELINGETTE, R. RAZAVI, AND N. AYACHE, *Toward patient-specific myocardial models of the heart*, Heart Failure Clinics, 4 (2008), pp. 289 – 301.
- [145] C. SMINCHISESCU, A. KANAUIA, Z. LI, AND D. METAXAS, *Discriminative density propagation for 3D human motion estimation*, in Proc. IEEE Conf. Computer Vision and Pattern Recognition, 2005, pp. I: 390–397.

- [146] D. SNOW, M. JONES, AND P. VIOLA, *Detecting pedestrians using patterns of motion and appearance*, in Proc. Int'l Conf. Computer Vision, 2003, pp. 734–741.
- [147] J. SONG, S. FUKUDA, T. KIHARA, M. SHIN, M. GARCIA, J. THOMAS, AND T. SHIOTA, *Value of mitral valve tenting volume determined by real-time three-dimensional echocardiography in patients with functional mitral regurgitation.*, American Journal of Cardiology, 98 (2006), pp. 1088–1093.
- [148] L. H. STAIB AND J. S. DUNCAN, *Boundary finding with parametrically deformable models*, IEEE Trans. Pattern Anal. Machine Intell., 14 (1992), pp. 1061–1075.
- [149] L. H. STAIB AND J. S. DUNCAN, *Model-based deformable surface finding for medical images*, IEEE Transactions on Medical Imaging, 15 (1996), pp. 720–731.
- [150] W. SUN, M. CETIN, R. CHAN, V. REDDY, G. HOLMVANG, V. CH, AND A. WILLSKY, *Segmenting and tracking the left ventricle by learning the dynamics in cardiac images*, in IPMI '05: Information Processing in Medical Imaging, 2005, pp. 553–565.
- [151] Z. SUN, G. BEBIS, AND R. MILLER, *On-road vehicle detection: A review*, IEEE Trans. Pattern Anal. Mach. Intell., 28 (2006), pp. 694–711.
- [152] L. TAYCHER, D. DEMIRDJIAN, T. DARRELL, AND G. SHAKHNAROVICH, *Conditional random people: Tracking humans with CRFs and grid filters*, in Proc. IEEE Conf. Computer Vision and Pattern Recognition, 2006, pp. I: 222–229.
- [153] A. M. TAYLOR, *Cardiac imaging: Mr or ct? which to use when*, Pediatric radiology, 38 (2008), pp. 433–438.
- [154] J. B. TENENBAUM, V. DE SILVA, AND J. C. LANGFORD, *A global geometric framework for nonlinear dimensionality reduction*, Science, 290 (2000), pp. 2319 – 2323.
- [155] D. TERZOPOULOS AND K. FLEISCHER, *Deformable models*, The Visual Computer, 4 (1988), pp. 306–331.
- [156] J.-P. THIRION, *Image matching as a diffusion process: an analogy with maxwell's demons*, Medical Image Analysis, 2 (1998), pp. 243 – 260.
- [157] T. TIMEK, J. GLASSON, D. LAI, D. LIANG, G. DAUGHTERS, N. INGELS, AND C. MILLER, *Annular height-to-commissural width ratio of annuloplasty rings in vivo*, Circulation, 112 (2005), pp. I-423 – I-428.
- [158] T. TIMEK, G. GREEN, F. TIBAYAN, F. LAI, F. RODRIGUEZ, D. LIANG, G. DAUGHTERS, N. INGELS, AND D. MILLER, *Aorto-mitral annular dynamics*, Ann Thorac Surg, 76 (2003), pp. 1944–1950.
- [159] C. TOMASI AND T. KANADE, *Detection and tracking of point features*, in Technical Report CMU-CS-91-132, 1991.

-
- [160] A. TSYMBAL, M. HUBER, AND S. K. ZHOU, *Discriminative distance functions and the patient neighborhood graph for clinical decision support*, Springer, 2010, ch. Advances in Computational Biology, p. (to appear).
- [161] A. TSYMBAL, G. RENDES, M. HUBER, AND S. K. ZHOU., *The neighborhood graph for clinical case retrieval and decision support within health-e-child casereasoner*, in Workshop "Wissens- und Erfahrungsmanagement" der Fachgruppe Wissensmanagement, 2009.
- [162] A. TSYMBAL, S. K. ZHOU, AND M. HUBER, *Neighborhood graph and learning discriminative distance functions for clinical decision support*, in Proc. IEEE International Conference on Engineering in Medicine and Biology, 2009.
- [163] A. TSYMBAL, S. ZILLNER, AND M. HUBER, *Ontology - supported machine learning and decision support in biomedicine*, in DILS, 2007, pp. 156–171.
- [164] Z. TU, *Probabilistic boosting-tree: Learning discriminative methods for classification, recognition, and clustering*, in Proc. Int'l Conf. Computer Vision, 2005, pp. 1589–1596.
- [165] Z. TU, X. S. ZHOU, A. BARBU, L. BOGONI, AND D. COMANICIU, *Probabilistic 3D polyp detection in CT images: The role of sample alignment*, in Proc. IEEE Conf. Computer Vision and Pattern Recognition, 2006, pp. 1544–1551.
- [166] H. C. V. ASSEN, M. G. DANILOUCHKINE, A. F. FRANGI, S. ORDAS, J. J. M. WESTENBERG, J. H. C. REIBER, AND B. P. F. LELIEVELDT, *SPASM: A 3DASM for segmentation of sparse and arbitrarily oriented cardiac MRI data*, Medical Image Analysis, 10 (2006), pp. 286–303.
- [167] A. VAHANIAN, H. BAUMGARTNER, J. BAX, E. BUTCHART, R. DION, G. FILIPPATOS, F. FLACHSKAMPF, R. HALL, B. IUNG, J. KASPRZAK, P. NATAF, P. TORNOS, L. TORRACCA, AND A. WENINK, *Guidelines on the management of valvular heart disease: The task force on the management of valvular heart disease of the european society of cardiology*, European heart journal, 28 (2007), pp. 230–268.
- [168] F. VANDEN-EYNDEN, D. BOUCHARD, I. EL-HAMAMSY, A. BUTNARU, P. DEMERS, M. CARRIER, L. PERRAULT, J. TARDIF, AND M. PELLERIN, *Effect of aortic valve replacement for aortic stenosis on severity of mitral regurgitation.*, Ann Thorac Surg, 83 (2007), pp. 1279–84.
- [169] V. N. VAPNIK, *Statistical Learning Theory*, John Wiley and Sons, New York, NY, USA, 1998.
- [170] M. A. O. VASILESCU AND D. TERZOPOULOS, *Multilinear analysis of image ensembles: Tensorfaces*, in ECCV '02: Proceedings of the 7th European Conference on Computer Vision-Part I, London, UK, 2002, Springer-Verlag, pp. 447–460.

- [171] M. A. O. VASILESCU AND D. TERZOPOULOS, *Multilinear subspace analysis of image ensembles*, in CVPR '03: Proceedings of the 2003 IEEE Computer Society Conference on Computer Vision and Pattern Recognition (CVPR'03), IEEE Computer Society, 2003, pp. 2–93.
- [172] M. A. O. VASILESCU AND D. TERZOPOULOS, *Multilinear independent components analysis*, in CVPR '05: Proceedings of the 2005 IEEE Computer Society Conference on Computer Vision and Pattern Recognition (CVPR'05) - Volume 1, Washington, DC, USA, 2005, IEEE Computer Society, pp. 547–553.
- [173] F. VERONESI, C. CORSI, L. SUGENG, V. MOR-AVI, E. CAIANI, L. WEINERT, C. LAMBERTI, AND R. LANG, *A study of functional anatomy of aortic-mitral valve coupling using 3d matrix transesophageal echocardiography*, *Circulation. Cardiovascular imaging*, 2 (2009), pp. 24–31.
- [174] F. VERONESI, C. CORSI, L. SUGENG, V. MOR-AVI, E. CAIANI, L. WEINERT, C. LAMBERTI, AND L. R.M., *A study of functional anatomy of aortic-mitral valve coupling using 3D matrix transesophageal echocardiography*, *Circ Cardiovasc Imaging*, 2 (2009), pp. 24–31.
- [175] P. VIOLA AND M. JONES, *Rapid object detection using a boosted cascade of simple features*, in Proc. IEEE Conf. Computer Vision and Pattern Recognition, 2001, pp. 511–518.
- [176] P. VIOLA AND M. JONES, *Robust real-time face detection*, *International Journal of Computer Vision*, 57 (2003), pp. 137–154.
- [177] D. VITANOVSKI, R. IONASEC, A. TSYMBAL, B. GEORGESCU, M. HUBER, J. HORNEGGER, AND D. COMANICIU, *Cross-modality assessment and planning for pulmonary trunk treatment using ct and mri imaging*, in International Conference on Medical Image Computing and Computer-Assisted Intervention (MICCAI), Beijing, China, September 20-24 2010.
- [178] D. VITANOVSKI, R. I. IONASEC, B. GEORGESCU, M. HUBER, A. TAYLOR, J. HORNEGGER, AND D. COMANICIU, *Personalized pulmonary trunk modeling for intervention planning and valve assessment estimated from ct data*, in International Conference on Medical Image Computing and Computer-Assisted Intervention (MICCAI), London, USA, September 2009, pp. 17 – 25.
- [179] I. VOIGT, R. IONASEC, B. GEORGESCU, J. BOSE, J. HORNEGGER, AND D. COMANICIU, *Computational decision support and intraoperative guidance for percutaneous aortic valve implantation*, in Medical Image Computing and Computer Assisted Intervention Workshop - MIAR 2010, Beijing, China, September 20-24 2010.
- [180] I. VOIGT, R. I. IONASEC, B. GEORGESCU, H. HOULE, M. HUBER, J. HORNEGGER, AND D. COMANICIU, *Model-driven physiological assessment of the mitral valve from 4d tee*, in SPIE Medical Imaging, Orlando, USA, February 2009.

-
- [181] I. VOIGT, D. VITANOVSKI, R. I. IONASEC, A. TSYMBAL, B. GEORGESCU, S. K. ZHOU, M. HUBER, N. NAVAB, J. HORNEGGER, AND D. COMANICIU, *Learning discriminative distance functions for valve retrieval and improved decision support in valvular heart disease*, in SPIE Medical Imaging, San Diego, USA, February 2010.
- [182] E. VOTTA, E. CAIANI, F. VERONESI, M. SONCINI, F. MONTEVECCHI, AND A. REDAELLI, *Mitral valve finite-element modelling from ultrasound data: a pilot study for a new approach to understand mitral function and clinical scenarios*, *Philos Transact A Math Phys Eng Sci.*, 366 (2008), pp. 3411–3434.
- [183] L. WANG, X. GENG, C. LECKIE, AND R. KOTAGIRI, *Moving shape dynamics: A signal processing perspective*, in Proc. IEEE Conf. Computer Vision and Pattern Recognition, 2008, pp. 1–8.
- [184] N. WATANABE, Y. OGASAWARA, Y. YAMAURA, T. KAWAMOTO, E. TOYOTA, T. AKASAKA, AND K. YOSHIDA, *Quantitation of mitral valve tenting in ischemic mitral regurgitation by transthoracic real-time three-dimensional echocardiography*, *J Am Coll Cardiol*, 45 (2005), pp. 763–769.
- [185] W. WEIN, E. CAMUS, M. JOHN, M. DIALLO, C. DUONG, A. AL-AHMAD, R. FAHRIG, A. KHAMENE, AND C. XU, *Towards guidance of electrophysiological procedures with real-time 3D intracardiac echocardiography fusion to c-arm CT*, in MICCAI 2009 Proceedings, Lecture Notes in Computer Science, Springer, Sept. 2009.
- [186] W. R. WELLS, P. VIOLA, H. ATSUMI, S. NAKAJIMA, AND R. KIKINIS, *Multimodal volume registration by maximization of mutual information*, *Medical Image Analysis*, 1 (1996), pp. 35–51.
- [187] M. WELS, Y. ZHENG, G. CARNEIRO, M. HUBER, J. HORNEGGER, AND D. COMANICIU, *Fast and robust 3d mri brain structure segmentation*, in Int’l Conf. Medical Image Computing and Computer Assisted Intervention, (MICCAI’09), 2009.
- [188] B. R. WILCOX, A. C. COOK, AND R. H. SURGICAL, *Surgical Anatomy of the Heart*, Cambridge University Press, New York, NY, USA, 2004.
- [189] B. WU AND R. NEVATIA, *Detection and segmentation of multiple, partially occluded objects by grouping, merging, assigning part detection responses*, *Int. J. Comput. Vision*, 82 (2009), pp. 185–204.
- [190] Y. WU, G. HUA, AND T. YU, *Tracking articulated body by dynamic Markov network*, in ICCV’03, 2003, pp. 1094–1101.
- [191] L. YANG, B. GEORGESCU, Y. ZHENG, P. MEER, AND D. COMANICIU, *3d ultrasound tracking of the left ventricle using one-step forward prediction and data fusion of collaborative trackers*, in IEEE Conference on Computer Vision and Pattern Recognition, 2008.

- [192] M.-H. YANG, D. J. KRIEGMAN, AND N. AHUJA, *Detecting faces in images: A survey*, IEEE Trans. Pattern Anal. Machine Intell., 24 (2002), pp. 34–58.
- [193] A. YILMAZ, O. JAVED, AND M. SHAH, *Object tracking: A survey*, ACM Comput. Surv., 38 (2006), p. 13.
- [194] J. YU, J. AMORES, N. SEBE, AND Q. TIAN, *Toward robust distance metric analysis for similarity estimation*, in Proc. IEEE Conf. Computer Vision and Pattern Recognition, vol. 1, 2006.
- [195] L. ZELNIK MANOR AND M. IRANI, *Temporal factorization vs. spatial factorization*, in Proc. European Conf. Computer Vision, 2004, pp. II: 434–445.
- [196] T. ZHAO AND R. NEVATIA, *3D tracking of human locomotion: a tracking as recognition approach*, in ICPR, 2002, pp. I: 546–551.
- [197] Y. ZHENG, A. BARBU, B. GEORGESCU, M. SCHEUERING, AND D. COMANICIU, *Four-chamber heart modeling and automatic segmentation for 3d cardiac ct volumes using marginal space learning and steerable features*, IEEE Trans. on Medical Imaging, 27 (2008), pp. 1668–1681.
- [198] Y. ZHENG, B. GEORGESCU, H. LING, S. ZHOU, M. SCHEUERING, AND D. COMANICIU, *Constrained marginal space learning for efficient 3d anatomical structure detection in medical images*, Computer Vision and Pattern Recognition, IEEE Computer Society Conference on, 0 (2009), pp. 194–201.
- [199] S. ZHOU, J. SHAO, B. GEORGESCU, AND D. COMANICIU, *Boostmotion: Boosting a discriminative similarity function for motion estimation*, in Proc. IEEE Conf. Computer Vision and Pattern Recognition, 2006.
- [200] S. K. ZHOU, B. GEORGESCU, X. S. ZHOU, AND D. COMANICIU, *Image based regression using boosting method*, in ICCV, 2005.
- [201] Y. ZHU, X. PAPADEMETRIS, A. J. SINUSAS, AND J. S. DUNCAN, *A dynamical shape prior for lv segmentation from rt3d echocardiography*, in MICCAI '09: Proceedings of the 12th International Conference on Medical Image Computing and Computer-Assisted Intervention, Berlin, Heidelberg, 2009, Springer-Verlag, pp. 206–213.
- [202] B. ZITOVA, *Image registration methods: a survey*, Image and Vision Computing, 21 (2003), pp. 977–1000.